



HAL
open science

Parametric optimisation of 3D printed architected materials: application to the morphing of boat's appendages

Malik Spahic

► **To cite this version:**

Malik Spahic. Parametric optimisation of 3D printed architected materials: application to the morphing of boat's appendages. Materials. Université de Bretagne Sud, 2022. English. NNT : 2022LORIS635 . tel-04016583

HAL Id: tel-04016583

<https://theses.hal.science/tel-04016583>

Submitted on 6 Mar 2023

HAL is a multi-disciplinary open access archive for the deposit and dissemination of scientific research documents, whether they are published or not. The documents may come from teaching and research institutions in France or abroad, or from public or private research centers.

L'archive ouverte pluridisciplinaire **HAL**, est destinée au dépôt et à la diffusion de documents scientifiques de niveau recherche, publiés ou non, émanant des établissements d'enseignement et de recherche français ou étrangers, des laboratoires publics ou privés.

THÈSE DE DOCTORAT DE

L'UNIVERSITÉ DE BRETAGNE SUD

ÉCOLE DOCTORALE N° 602
Sciences pour l'Ingénieur
Spécialité : *Génie Mécanique*

Par

Malik SPAHIC

**Optimisation paramétrique de matériaux architecturés imprimés
3D : application au morphing des appendices de navire**

Thèse présentée et soutenue à Lorient, le 5 Juillet 2022
Unité de recherche : Institut de Recherche Dupuy de Lôme
Thèse N° : 635

Rapporteurs avant soutenance :

Anita CATAPANO Maître de Conférences, I2M, INP Bordeaux
Loïc DARIDON Professeur des Universités, LMGC, Université de Montpellier

Composition du Jury :

Président :	Jacques-André ASTOLFI	Professeur des Universités, Institut de Recherche de l'École Navale
Examineurs :	Sylvie RONEL	Professeure des Universités, LBMC, Université Lyon 1
	Justin DIRREBERGER	Maître de Conférences, PIMM, CNAM
Dir. de thèse :	Vincent KERYVIN	Professeur des Universités, IRDL, Université de Bretagne-Sud
Co-dir. de thèse :	Antoine LE DUIGOU	Maître de Conférences HDR, IRDL, Université de Bretagne-Sud
Co-encadrante de thèse :	Noëlie DI CESARE	Maître de Conférences, LMC2, Université Lyon 1

ACKNOWLEDGEMENT

Tout premièrement, je tiens à remercier mes encadrants Vincent Keryvin, Antoine Le Duigou et Noëlie Di Cesare pour m’avoir conseillé, encadré et accompagné au cours de ces trois ans et demi de thèse. Merci à eux également pour les nombreuses relectures de mon papier de journal et de mon manuscrit de thèse. Un merci tout particulier notamment à Noëlie qui a été, au-delà de son travail d’encadrement, comme une grande sœur pour moi à Lorient. Merci pour tous ces fous rires que l’on a eu tous les deux et merci aussi pour toutes ces discussions que l’on a eues sur des sujets divers et variés, comme les évènements de la vie, le fonctionnement de la recherche, ou encore les relations amoureuses.

J’aimerais également remercier Anita Catapano et Loïc Daridon d’avoir accepté d’être les rapporteurs de mon mémoire de thèse. Je remercie aussi chaleureusement Sylvie Ronel, Jacques-André Astolfi et Justin Dirrenberger d’avoir accepté d’être les examinateurs durant ma soutenance de thèse. Je les remercie également d’avoir pris le temps de se d’être présents physiquement pour ma soutenance à Lorient.

Je remercie aussi chaleureusement les différents membres de l’IRDL qui m’ont aidé et accompagné pendant mon travail de thèse. Merci à William Berckmans, Anthony Margueresse et Isabelle Pillin pour m’avoir aidé au cours de mes travaux expérimentaux et de m’avoir aidé lorsque j’ai rencontré des soucis avec mes manip. Je tiens particulièrement à remercier Hervé Bellegou, Antoine Kervoelen et Anthony Jegat pour m’avoir accompagné dans la mise en place de mes manip expérimentales.

Merci à Hervé d’avoir eu la patience de m’expliquer le fonctionnement des différentes machines de traction et d’avoir pris le temps de configurer les systèmes d’acquisition pour moi. Merci à Antoine pour ses nombreux conseils pour m’aider dans la mise en place de mes tests mécaniques pour caractériser mes échantillons imprimés 3D. Merci également à Anthony Jegat qui m’a laissé utiliser et surutiliser l’imprimante 3D Ultimaker 2 située à côté de son nouveau bureau.

Je tiens également à remercier chaleureusement ma famille pour son soutien indéfectible et pour avoir cru en moi depuis toujours. Merci à mes parents, Mulaz et Hajrija Spahic, de m'avoir soutenu tout au long de ma thèse, merci à eux pour les discussions que l'on a eues dans les moments les difficiles, de m'avoir toujours accueilli les bras ouverts chez eux et de m'avoir nourri pendant les moments où il était difficile pour moi de cuisiner. Merci également à mes sœurs, Mersiha Rozic et Merima Kupidura, d'avoir toujours pris le temps de discuter avec moi, de rigoler et de me conseiller dans les moments difficiles. Et cela, malgré le peu de temps qu'elles ont eu à me consacrer en raison de leur travail et de la charge de travail liée à leur responsabilité de jeunes parents. Merci à elles également, de toujours m'avoir accueilli les bras ouverts chez elles pendant des vacances et des week-end. Merci également à mes neveux et nièces : Rania, Ferran, Hanna et Rayan (dans l'ordre de naissance) pour la joie qu'ils m'ont apporté dans les moments éprouvants. Si vous lisez ces lignes quelques années plus tard, sachez juste que tonton vous aime.

Je tiens également à remercier ma chérie, Maxime Pesonen, dont j'ai fait la rencontre au cours de ma thèse, qui m'a toujours soutenue pendant les moments les plus difficiles de la thèse : les périodes de rédaction d'articles et de mon mémoire. Merci à elle pour ces longues discussions au téléphones, ces moments où on s'est balladé dans les paysages de Bretagne et merci à toi aussi d'avoir toujours cru en moi et de m'avoir soutenu. Je t'aime.

Je tiens également à remercier tous mes amis qui m'ont soutenu et avec qui j'ai partagé beaucoup de bons moments. Je remercie mon meilleur ami Paul Chambault avec qui j'ai partagé de nombreux très bons moments en vacances et avec qui je me suis tapé les meilleurs fous rires au téléphone. Si tu lis ça, t'es le sang khey ! Merci également à Corentin Guellec et Riadh Al Zubaidi pour être venu jusqu'à Lorient pour assister à ma soutenance. Vous êtes des potes en or ! J'aimerais également remercier toutes les personnes avec qui j'ai partagé le bureau 024, Dihya Mezi, Ayoub Zerhouni, Ajinkya Pawar, Hamza Issa, Guruprasad T. (My love, mon chéri!), Antoine Le Palabe, Mikaël Riou, Nihel Ketata et Rachel Azulay. Merci pour votre bonne humeur et les bonnes discussions que l'on a eu autour de la machine à café. Merci particulièrement à Dihya Mezi qui m'a bien intégré à son groupe d'amis, une fois que je suis venu sur Lorient. Merci à toi également pour tous les conseils que tu m'as donnés concernant mes manips et sur la gestion de la thèse. Un merci particulier à Ayoub Zerhouni également, avec qui j'ai eu l'occasion de partager énormément de bons moments, où nous avons beaucoup ris. Merci pour tous ces

échanges sur nos vies personnelles et professionnelles et sur nos moments de doute et de peine. Big thanks to Ajinkya Pawar also! (My people!!!!!!!) Thank you for all the trips, the debates, the discussions, the lunches and the good time we had during my time to Lorient. Thank to you, I now have a License 2 level in Indian history, Indian politics and Geopolitics after all our debates! Thank you also for being there with me when the times were harder! I hope we could make one days or trips to India/Bosnia together! Thanks also to you Guru! Thank you for sharing your experience, knowledge and thoughts with me about research and life. Thank you also for the good laughs and time I had with you. I hope to see you sson in India too! Thanks also to you Hamza for these good laughs and great discussions. I will always remember our football trolls and discussions! Hope to see you defend quickly too! Merci à toi aussi Antoine pour ces bons moments à rigoler et à discuter des performances de Liverpool. Merci pour ces discussions que l'on a eu sur la thèse et le monde professionnel en général. Un grand merci également à Flavien Lucas, merci pour ta gentillesse, ta bonne humeur et pour toutes les discussions que l'on a eu sur tous les thèmes possibles et imaginables (le seigneur des anneaux, le monde pro ou encore les jeux de sociétés). Merci à toi d'avoir toujours été là pour moi dans les moments difficiles et encore désolé de t'avoir tué en vélo sur la Presque-île de Rhuys... Et merci à Charles de Kergariou pour les bons moments que l'on a passé lorsque tu étais sur Lorient. C'était super sympa de refaire le monde avec toi le temps d'une soirée.

Un grand merci aussi à Yohan Rioual, Alisson Curly, Grégory Nayagom, Alix Le Tendre, Maxime Chassaing et la bande du LabSTICC (désolé si j'oublie des gens) pour m'avoir accueilli mes premiers jours à Lorient et pour m'avoir fait découvrir tous les coins sympas de Bretagne. Sans vous, mon expérience lorientaise n'aurait pas été la même. Pour finir, j'aimerais remercier tout le reste des personnes de l'IRDL avec qui j'ai passé du bon temps, cette liste ne pourra pas être exhaustive donc désolé d'avance si j'ai oublié votre prénom... Merci aux permanents Yann Guevel, Jean-Marc Cadou, Laëtitia Duigou, Grégory Girault (Allez Paris et aux chiottes l'OM !!!), Laurent Maheo, Christelle Combescure, Mikaël Kedzierski Alain Bourmaud, Thomas Pierre et Murielle Carin pour toutes les discussions, matchs de badminton et les bonnes rigolades que l'on a pu avoir. Merci aux post-doctorants que j'ai croisé au labo, Houdeyfa Ounis, Hassan Harb, et Pierre Lemechko pour les bonnes rigolades, les matchs de foot et les discussions que l'on a pu avoir sur le monde professionnel. Merci également aux doctorants, stagiaires et aux ingénieurs d'études avec qui j'ai également vécu de très bons moments que cela soit pour des

repas/apéros ou des matchs de foot ou de basket, un merci particulier à Thomas Fruleux, Delphine Ciréderf, Akanksha Singh, Anupam Glorious Lobo, Mathias Ziapkoff, Maxime Batard, Julien Gambade, Aïssata Bangoura, Machhour El-Assad, Kassem Saied, David Kerihuel, Ismahen Zaafouri, Kylian Mahé, Benjamin Cholet, Xavier Frias-Cacho, Marion Yvin, Lise Dugor et Aude Caillet-Gruet.

Ce fut une très bonne et riche expérience pour moi que je n'oublierai jamais. Une dernière fois, merci pour tout !

TABLE OF CONTENTS

Introduction	11
1 Morphing global presentation	19
1.1 Morphing challenges in the aeronautical field	20
1.1.1 Presentation of aerodynamic forces exerted on a plane	20
1.1.2 2D wing morphing devices	22
1.1.3 3D wing morphing devices	27
1.2 Morphing challenges in the marine field	32
1.2.1 Hydrodynamic forces present on foiling boats	32
1.2.2 Cavitation on hydrofoils	34
1.3 Structural elements characteristics needed for morphing	39
1.3.1 Airfoil and wing core for morphing	39
1.3.2 Skins for morphing	40
1.4 Morphing technological strategies	43
1.4.1 2D air- and hydrofoil morphing devices	43
1.4.2 3D wing morphing devices	50
1.4.3 Morphing devices for delaying cavitation	59
1.4.4 Summary of the different morphing technologies	64
1.5 Chapter summary	65
2 Multi-scale analysis of the morphing mechanism	69
2.1 Introduction	69
2.1.1 Cellular materials	69
2.1.2 Theory of homogenisation	75
2.1.3 3D printing processes	86
2.2 Materials and methods	96
2.2.1 Material	96
2.2.2 Manufacturing of tensile samples and cellular beams	97
2.2.3 Microscale: Experimental mechanical characterisation of the material	98

TABLE OF CONTENTS

2.2.4	Microscale: Experimental porosity measurement of the 3D printed material	98
2.2.5	Mesoscale: Selection of pattern	99
2.2.6	Mesoscale: Estimation of unit cells properties	101
2.2.7	Macroscale: Experimental mechanical characterisation of cellular beams	103
2.2.8	Macroscale: Numerical mechanical characterisation of cellular beams	104
2.2.9	Macroscale: Numerical investigation of the skin's rigidity effect . . .	105
2.2.10	Macroscale: Numerical investigation of the core's unit cell size effect	106
2.2.11	Macroscale: Numerical investigation of the differences in using a homogeneous equivalent material as the cellular core	107
2.3	Results	110
2.3.1	Microscale	110
2.3.2	Mesoscale	111
2.3.3	Macroscale	115
2.4	Discussion	124
2.4.1	Analysis of the cantilever beam's core	124
2.4.2	Skin rigidity effect	126
2.4.3	Cell size effect and comparison to a homogeneous core	128
2.5	Chapter summary	132
3	Fluid-structure interaction studies and hydrofoil's core parametric optimisation	137
3.1	Presentation of the fluid-structure interaction strategy	138
3.2	Presentation of meta-heuristic optimisation algorithms	144
3.2.1	Optimisation problems definition	144
3.2.2	Optimisation algorithms	147
3.3	Fluid dynamics insights and characteristic numbers	158
3.3.1	Reynolds number	158
3.3.2	Mach number	163
3.3.3	Boundary Layer	164
3.3.4	Aero- and hydrodynamic coefficients	172
3.3.5	Incompressible turbulent flow governing equations	177
3.4	Materials and Methods	179

3.4.1	Initial flow conditions	179
3.4.2	Hydrofoil selection and fluid flow’s boundary conditions	180
3.4.3	Fluid-structure interaction model development: the fluid model . . .	182
3.4.4	Fluid-structure interaction model development: the solid model . .	186
3.4.5	Fluid-structure interaction model development: spatial and tempo- ral interfacing	187
3.4.6	Fluid-structure interaction program operation	189
3.4.7	Sensitive core elastic coefficient identification protocol	191
3.4.8	Tailorability tests of the morphing hydrofoil	195
3.4.9	Parametric optimisation algorithm of the double arrow architecture	196
3.5	Results	203
3.5.1	Sensitive elastic coefficient identification	203
3.5.2	Tailorability tests of the morphing hydrofoil	203
3.5.3	Parametric optimisation algorithm of the double arrow architecture	206
3.6	Discussions	208
3.6.1	Sensitive elastic coefficient identification	208
3.6.2	Tailorability tests of the morphing hydrofoil	209
3.6.3	Parametric optimisation algorithm of the double arrow architecture	213
3.7	Summary	216
Conclusion		219
A Numerical modeling of a turbulent water flow around a hydrofoil		225
A.1	General overview	225
A.2	Key physical properties, concepts and dimensionless numbers	226
A.2.1	Viscosity	226
A.2.2	Conservation of mass: mass density and Reference Fluid Volume Element (RFVE)	231
A.2.3	Reynolds number	233
A.2.4	Kinematic viscosity	237
A.2.5	Mach number	238
A.2.6	Lagrangian and Eulerian descriptions	240
A.2.7	Boundary Layer	244
A.2.8	Aero- and hydrodynamic coefficients	252
A.3	Fluid dynamics governing equations	257

TABLE OF CONTENTS

A.3.1	Continuity equation	258
A.3.2	Navier-Stokes equations: the transport of momentum	260
A.3.3	The energy equation	263
A.3.4	Poisson’s pressure equation	265
A.4	Fluid dynamics closure equations	266
A.4.1	Turbulence modeling approaches	266
A.4.2	Reynolds time-averaging concept	270
A.4.3	Reynolds averaged Navier-Stokes (RANS) approach: time averaging governing equations	272
A.4.4	Turbulence closure equations	274
A.5	Methodology for numerical model development: validation test	285
A.5.1	Initial flow conditions	285
A.5.2	Material and methods	286
A.5.3	Results and discussion	293
A.6	Methodology for numerical model development: cambered hydrofoil test . .	297
A.6.1	Material and Methods	297
A.6.2	Results and discussion	300
A.7	Summary	304
A	Appendix	307
A.1	Appendix One: Spalart-Allmaras one equation model details	307
A.2	Appendix two: k-omega turbulence model	313
A.3	k-epsilon turbulence model	314

INTRODUCTION

General context of the PhD

Since the end of the 20th century to the beginning of the 21st century, the international maritime trade and the ship traffic has increased dramatically and is now reaching an important size and place in the modern globalised world. Indeed, as pointed out by the United Nations Conference on Trade and Development (UNCTAD, <http://unctadstat.unctad.or>), the tonnage of goods loaded worldwide increased linearly since the 1990s: in 1995, 4.4 Billions of tons of goods were loaded worldwide on cargo ships and in 2020 it rised up to 10.6 Billions of tons. This rise in goods loaded was also accompanied with a linear rise of the worldwide ship traffic [1]. Tournadre [1] counted 20 000 ships involved in the worldwide ship traffic for the year 1992. This number rised to 80 000 in year 2014, a fourfold increase of number. Economically, the maritime transport market's size was estimated at 2000 billions USD in 2020 and is expected to grow further in the following years.

This dense ship traffic has numerous consequences on the marine ecosystems and the environment. One of the most important nuisance of the maritime transport economy is the greenhouse gas emissions linked to the maritime exchanges. According to the fourth report of the International Maritime Organisation (IMO); a branch of the United Nations Organisation (UNO) responsible for regulating shipping; shipping emitted 1 billion of tons of CO₂ in 2020 corresponding to 2.89% of global anthropogenic CO₂ emissions [2]. In order to reduce the environmental impact of maritime exchanges, the IMO engaged in 2018 to reduce the international shipping's total greenhouse gases emissions by at least 50% by 2050 compared to the total emissions measured in 2008 (1.2 billions of tons of greenhouse gases) [2]. Again, according to this report, most of CO₂ and greenhouse gases emitted by ships are linked to the main and auxiliary engines used to propel the ship in water [2]. Thus, the efforts for reducing the ship's greenhouse gases emissions must be focused on the reduction of the fuel consumption of the main engine and the auxiliary engines while keeping similar shipping speeds.

To do that, one solution would be the use of the ship's **Engine Power Limitation (EPL)**. It consists in limiting the ship's engine power for reducing the ship's fuel consumption. Nonetheless, Rutherford *et al* [3] showed that the CO₂ reductions were not proportional to EPL, because the ships engines already operate on a range far below their maximum power. Thus, they showed that, in order to meet the IMO's engagements, EPLs needed to be significant: above 50% of the current engine power. Relying on EPL only might be difficult to reach those objectives. Thus, as it is done in the automotive industry with formula 1 competitions for example, new innovative solutions can be tested in racing yachting (*e.g.* Vendée Globe) or competitive powerboating (formula 1 power boating or P1 SuperStock contest for example) for being later introduced on industrial boats or ships.

Since the 2010s, most of racing yachts are equipped with exotic mustache shaped appendages that allow them to fly above water at high velocities (the verb 'foiling' is used for describing this flight). Those appendages are called foils, their operation mode is similar to an aircraft's wings. While the boat moves, the foil generates a lifting force that, at a sufficient speed, lifts the boat's hull above water. When the boat's hull is not in contact with the water surface anymore, the water's friction forces reduce dramatically allowing the sailing boat to reach higher speeds. Despite emerging in the early 2010s for racing sailboats, the foils are not new. The first foiling water vessel was built in the early 1900s by Enrico Forlanini [4], then the foil first appearance in sportive sailing was in 1980. This year, Eric Tabarly equipped his multi hull 'Paul Ricard' with foils and sailed across the Atlantic ocean [4]. From this period of time, it took another 30 years to appear in modern boat races in 2011. In the same way that foils progressively appeared in sportive sailing, the foils might be used on ships and cargos, in combination with EPL, for reducing the greenhouse gases emissions and respect the IMO's engagement for greenhouse gas reductions. Promising steps are taken towards this direction as boats used for passenger transportation already use hydrofoils (*e.g.* the TurboJET used on the Pearl River Delta between Hong Kong and Macau) [5]. The historical timeline shown in Figure 1 summarizes the evolution of the use of hydrofoils on water vehicles.

However, before reaching this point, many steps are needed for making this technology applicable to cargos. Indeed, if the introduction of foils on modern racing sailing boats took approximately 100 years it was because the foils needed to match numerous technical requirements, such as insuring a sufficient mechanical resistance for avoiding failure,

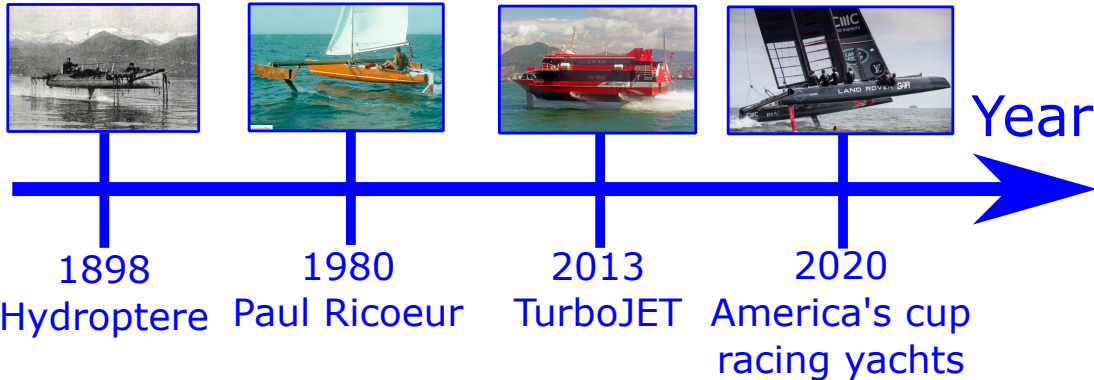


Figure 1. Historical timeline of the hydrofoil technology

insuring a good balance for the boat flight or producing enough lift forces for lifting the boats. Yet, the main challenge faced by foils, for all types of boats, is their current incapacity to adapt to the changes of navigation modes making them only efficient for a limited range of navigations. Similar problems are historically faced by aircraft wings. Indeed, they also need to change their aerodynamic properties when the aircraft changes its flight modes. Multiple solutions were found in the aeronautical field for solving this adaptability problem [6]–[8]. They all consist for the wings to change their geometries in function of the aircraft’s flight modes in order to tailor their resistance to air and/or tailor their capacity to lift the aircraft (*e.g.* makes the takeoff easier and reduce the air’s frictions). Many other issues faced by aircraft wings have been addressed with these technologies, such as flight instability. The boat’s hydrofoils operates in a similar manner and face similar issues as aircraft wing do. The navigation modes of water vehicles are similar to an aircraft’s different flight modes too.

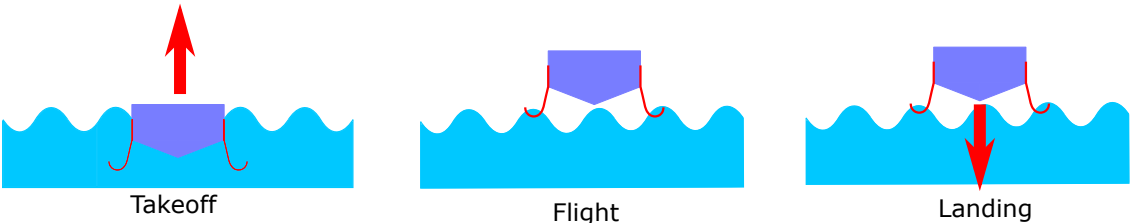


Figure 2. Three mains navigation modes for a foiling boat

For most of water vehicles equipped with foils, three navigation modes could be defined. These navigation modes are shown in Figure 2. For each navigation mode, a foil would require a dedicated shape to this particular navigation mode. The first mode corre-

sponds to the moments before the vehicle's hull takeoff, the second mode corresponds to the moments during vehicle's flight and the final mode corresponds to the moment when the vehicle is landing in the water. In the first navigation mode, the global aim is to help the vehicle to takeoff above water at the lowest speed possible, in order to make it as fuel efficient as possible. For that, the foil needs to have a geometric shape that maximises the lifting forces. Then, in the second navigation mode, the foils do not need to produce a high lifting force anymore, just enough to ensure the vehicle's flight and reduce to a minimum the water's friction forces. To do that, the foil needs to adopt a new geometry. In the last navigation mode, the vehicle needs to land back in the water. This needs to be done in the smoothest way possible, especially if the vehicle is cruising at a high speed. To do that, the hydrofoil needs to change back its shape to its original geometry, for providing enough lifting force to the vehicle so that the effect of weight could be reduced and a smooth hull landing can be ensured.

As said earlier, these different navigation modes depicted here are very similar to an aircraft's flight modes (takeoff, flight and landing) and the requirements expected with the variation of geometries are the same for foils and for aircraft wings. Yet, in the field of aeronautics, these issues have been continuously addressed and researched since the 20th century through what is called the **wing morphing technologies**. These technologies and concepts aim to modify and adapt an aircraft's wings geometry to the changes of flight conditions and of external loads. These morphing solutions are interesting for boats and can be adapted from aeronautics to marine engineering, as foils and aircraft wings share similar 2D geometries, operation modes and issues.

Currently, morphing concepts just started to appear for marine technologies at the end of the 2010s [9], [10]. These morphing technologies change effectively the shape of the hydrofoil; *i.e.* 2D section of a foil; nonetheless these shape changes are realized with heavy and complex actuation mechanisms that add weight to the boat and that are highly prone to maintenance (see Figure 3). To avoid these issues, an appropriate solution would be to use hydrofoils that passively change their shape through waterflow's pressure variations.

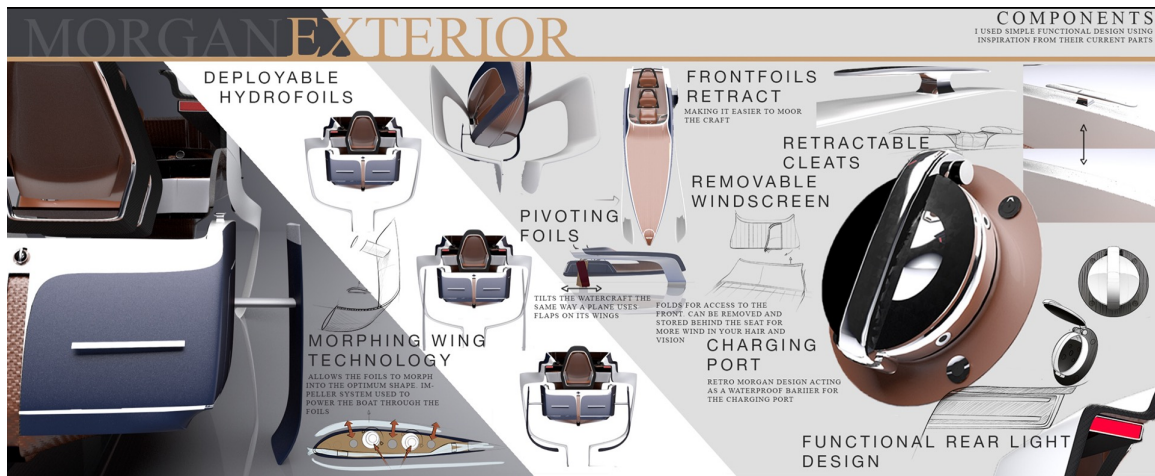


Figure 3. Example of commercial hydrofoil morphing mechanism available at Morgan Motors Company [11]

Objectives

The objective of this thesis is to design and develop an autonomously reconfigurable foil concept that could be manufactured quickly and whose deformations could be controlled. However, before reaching this final objective, multiple sub-objectives need to be fulfilled. Firstly, a state of the art of the different existing morphing strategies and technologies in the domain of aeronautics, *i.e.* aircraft wing morphing; and of marine engineering is made. Then, the second objective consists in deeply investigating the morphing operation mode of a selected strategy, a passive cellular morphing hydrofoil concept. The identification of the different parameters tailoring the foil's deformation is made. The third objective is to integrate the morphing concept into a section of the foil and to develop a reliable methodology for optimising the different parameters controlling the hydrofoil's deformations with the changes of navigation modes.

PhD Work's presentation plan

To fulfill these objectives, the following work will be divided into 3 chapters and one appendix:

Chapter 1 is devoted to the summary of the **state of the art** of the existing concepts and technologies in the **morphing** field. This chapter firstly defines what morphing is, then it depicts the different morphing strategies used in aeronautics; *i.e.* the domain where

morphing has been the most thoroughly researched; and then in marine engineering. It also lists a set of requirements that foils and wing morphing are expected to fulfill. Finally, a set of different existing technologies are presented in the final part of the chapter. As a chapter conclusion, the morphing concept selected for the rest of the work and the motivations for selecting this concept will be presented.

Chapter 2 presents the results of a **multi-scale analysis** performed on the selected morphing concept. This chapter presents the different parameters influencing the morphing capability of a structure where the morphing concept is implemented. The morphing concept selected uses the hydrofoil's core, constituted of a **cellular material**, and its **surrounding skin** as its operation core. Moreover a **3D printing** process, namely the *Fused Filament Fabrication*, is used as the manufacturing process of the morphing samples. To achieve this objective, multiple characterisation experiments and numerical models are developed.

Chapter 3 is devoted to the development of a new numerical model simulating the **interaction** between **fluid and solid numerical models**. This Fluid-Structure Interaction program is then used for investigating the effect of the parameters identified at the end of Chapter 2 on the bending performances of the morphing hydrofoil and their impact on its hydrodynamic properties. Then, a **parametric optimisation** with the meta-heuristic algorithm **PSO** (*Particle Swarm Optimisation*) is performed on the hydrofoil's core for finding a manufacturable cellular material that can ensure the good bending properties of the hydrofoil. For addressing all these topics, bibliographic elements on meta-heuristic optimisation and on fluid-structure interaction will be given at the beginning of this chapter.

The Appendix A depicts the development and the validation of the **Computational Fluid Dynamics (CFD)** numerical models used in Chapter 3 for simulating a turbulent water flow around a hydrofoil. The methods and results depicted in this appendix are not inherently needed for understanding the investigations and results made on the morphing hydrofoils (and this is the main reason why these results have been placed in appendix).

However, they provide meaningful insights on the robust methodology developed for modeling turbulent water flows. This appendix also show that the methodology developed here can predict precisely and reliably the lift and drag values of hydrofoils and the pressure distribution around it. The methods and results depicted in this appendix have

been developed by the PhD student on his own. Deep bibliographical elements and thorough explanations about the governing equations and the closure equations are detailed through the appendix for explaining the methodology used.

Finally, the conclusion and outlooks chapter of this thesis report summarises the approaches, the methods, the different results and the discussions presented in this work. This final section also opens new perspectives and further investigations that need to be done and that are related to the topic of hydrofoil morphing.

MORPHING GLOBAL PRESENTATION

In the research field, the word "morphing" refers to many different use cases. It can be associated to "image morphing" for instance [12], known also as "image metamorphosis". This use of the word morphing refers to a numerical technique that transforms one image into an another targeted image. The word morphing can also be applied to "shape morphing", "geometrical morphing" or "shape parametrical morphing" [13], [14]. This time, the word morphing refers to a numerical technique, once again, used in CAD for multiple purposes: transform a CAD object's shape or having a mesh that follows the deformation of a deformable object. This word can also refer to "morphing mechanisms", it describes a wide range of reconfigurable mechanisms that change the states, configurations or functional modes of objects [15]. Thus, through those multiple examples, it has been shown that the word "morphing" is not fixed to a domain yet. It might refer to several different objects. Nonetheless, most of applications where the word morphing was used related to objects that transform themselves to match an another form. The only things that changed between these several applications were the considered objects and the purpose that morphing had to fulfill. Having said that, for complex morphing structures (as morphing hydrofoils), the following definition paraphrased from Portela *et al*'s work [16] describes well the type of morphing that is considered.

Morphing

The capacity of a given structure to change its geometry macroscopically in order to better adapt to radically different external loading conditions

Morphing is currently used and researched in numerous fields and domains such as defense [17], civil engineering [18]–[20] or soft robotics [21]–[23]. Nonetheless, it is in aeronautics that morphing is currently the most advanced [7], [24], [25]. Due to the similarities

of the technological solutions used in these two fields, aeronautic morphing solutions start being tested in marine applications and sailing [9], [10], [26]. In this chapter, the aim will be to review the operation principles of aeronautic and hydraulic structures and identify the different problems morphing devices have to address and the solutions proposed for solving them. Then, from all these strategies, one will be chosen for deeper investigations. The chapter will be divided in four parts. In the first part, the requirements that morphing needs to fulfill in the aerodynamic field will be presented. These requirements are similar for a marine vehicle equipped with foils. In a second part, the same requirements listing will be done for morphing in the marine field. In a third part, the different morphing strategies used for both fields will be depicted. In this part, the pros and cons of the different solutions will also be addressed. In the final part, the selection of the morphing solution that will be investigated deeper will be discussed.

1.1 Morphing challenges in the aeronautical field

The operation mode, behavior and study of a sailing hydrofoil's hydrodynamic properties are very similar to aircraft's wings [27]–[29]. Moreover, morphing devices are currently the most developed for aircraft's wings. Hence, for determining the types of morphing devices fitted for sailing hydrofoils, investigating the existing morphing devices in aeronautics and the physical characteristics they target would be highly relevant. For aircraft's wing morphing, two types of morphing devices exists: the 3D wing morphing devices that target directly the whole wing and the 2D wing morphing devices that target the airfoil section of the wing. Both affect aerodynamic forces exerted on the aircraft.

1.1.1 Presentation of aerodynamic forces exerted on a plane

Before addressing the different morphing devices and technologies developed, one must list the different aerodynamic forces that are present on an aircraft during its flight. These forces are presented on Figure 1.1. The different geometrical elements that morphing devices will modify influences these different forces.

The list of present forces are the following:

- **The lift force L** , in aerodynamics, is defined as the force perpendicular to the aircraft's motion and oriented upward the plane. The equation governing the lift

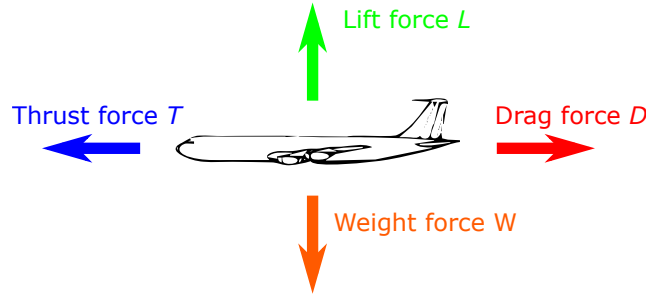


Figure 1.1. Aerodynamic forces exerted on the aircraft [30]

force is given below (see Equation 1.1). With C_L being the lift coefficient, ρ being the mass density, v being the aircraft's velocity and S being the wings surface viewed by the flow (the surface of the fuselage and of the engines are not considered here and are dealt separately). The lift coefficient C_L represents the impact of the geometry of the object on the generation of lift.

$$F_{Lift} = \frac{C_L}{2} \rho v^2 S \quad (1.1)$$

More details will be given to the origin of the lift force and the form of the Equation in section A.2.8 of Chapter 3.

- **The drag force D** , in aerodynamics, is defined as the force parallel and opposed to the aircraft's motion. The equation governing the lift force is given below (see Equation 1.2). All the terms of this equation are the same as Eq. 1.1 terms, except C_D being the drag coefficient. The drag coefficient C_D represents the impact of the geometry of the object on the generation of drag.

$$F_{Drag} = \frac{C_D}{2} \rho v^2 S \quad (1.2)$$

More details will be given to the origin of the drag force and the form of the Equation in section A.2.8 of Chapter 3.

- **The weight force W** , is the weight of the aircraft that tends to attract the aircraft downward and is opposed to the lift force.
- **The trust force T** , is given by the aircraft's propellers and is opposed to the drag force

The wing's geometrical characteristics can essentially influence the lift and the drag

forces but also the wing's weight in a secondary part. The thrust is influenced by the aircraft's engines only. Depending on the flight regime, the forces have to be maximised or minimised.

During takeoff, the aircraft has a low velocity and not enough lift to takeoff. The lift has to be maximised, to overcome the aircraft's weight, while keeping the drag at a reasonable level. While being on flight, lift must be provided to maintain that flight while minimising its drag. For doing this, the aircraft must maximise its lift/drag ratio. When the aircraft lands, it reduces its velocity and thus loses gradually its lift. At this stage, the lift coefficient C_L needs to be maximised for having a landing that is as smooth as possible.

The geometric features influencing those forces can be divided in two sub-categories: the 2D geometric features and the 3D ones. The change of these geometric features will either have a major impact on the lift coefficient C_L and the drag coefficient C_D that are highly influenced mainly by the 2D geometric features. The change of 3D geometric features influence the aerodynamic coefficients C_L and C_D , especially when the 3D change also impact the 2D geometric properties (e.g. wing twist/torsion), and the surface covered by the wings S .

The aerodynamic forces, lift and drag, strongly vary with the state of the flow: whether it is laminar or turbulent. This state can be known with the Reynold's number Re value (see Chapter A for more details).

In the next sections, these different types of morphing devices will be studied and their impact on the aerodynamic properties of the plane will be explained.

1.1.2 2D wing morphing devices

The 2D section of an aircraft's wing can be deformed or modified for influencing the aircraft's aerodynamic properties. This section is called an **airfoil**. Its geometric features and physical properties are given in Figure 1.2.

Physically, the airfoil is capable of producing lift thank to the third Newton's law: the principle of action and reaction. Cambered airfoil (i.e. airfoils with a camber line above the chord line on Figure 1.2a) repels air downside, which in return generates a reaction force that is commonly known as lift (see Figure 1.2b). So the more air an airfoil repels downwards, the more lift it has. If an airfoil does not generate enough lift from its fixed

geometric configuration, it is possible to increase the angle with which the air flow will encounter the airfoil. This angle is known as the **angle of attack α** and it is measured between the airfoil's chord line and the direction of the flow (see Figure 1.2b). The evolution of the lift coefficient C_L and the drag coefficient C_D in function of the angle of attack α is given in Figure 1.3.

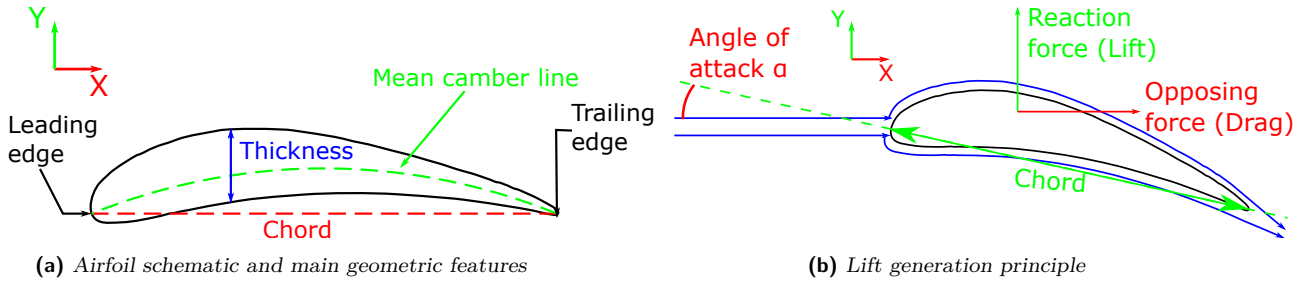
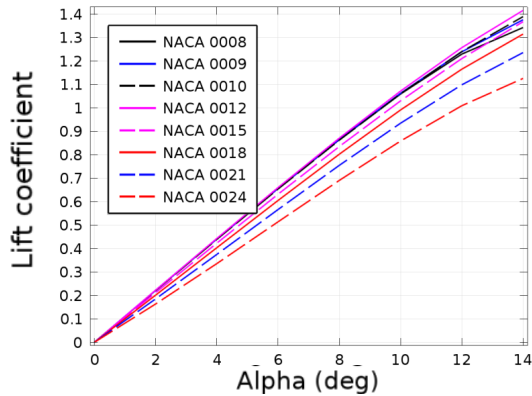
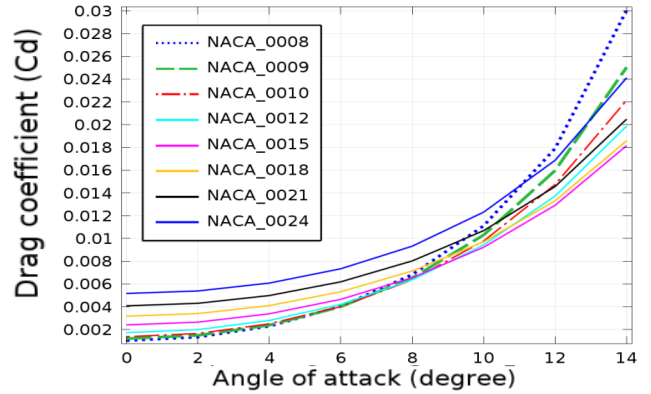


Figure 1.2. Presentation of an airfoil's geometric elements and of its operation

As shown in Figure 1.3, the increase or decrease of the angle of attack impacts directly the lift and drag coefficients C_L and C_D . Figure 1.3a shows that the lift coefficient C_L increases along with the angle of attack α and Figure 1.3b shows that the drag coefficient C_D also increases with the angle of attack α .



(a) Evolution of the lift coefficient in function of the angle of attack α for different profiles at $Re = 6$ millions [31]



(b) Evolution of the drag coefficient in function of the angle of attack α for different profiles at $Re = 6$ millions [31]

Figure 1.3. Aerodynamic coefficients C_L and C_D evolution in function of the angle of attack α at $Re = 6$ millions [31]

Looking at Figures 1.3, it can also be seen that the drag coefficient increases in a quadratic manner while the lift increases in an almost linear trend. Thus, the drag being

the principal source of fuel consumption, the increase of the lift through the angle of attack leads to an increase of fuel consumption. During the flight, it is relevant for an aircraft to tailor its wing's airfoils **angle of attack** for keeping the fuel consumption to a minimum. To achieve that, some morphing solutions were developed for inducing rigid rotations to the wing; i.e. without deforming the 2D airfoil; and thus adjusting the airfoils angle of attack accordingly to the flight regime [32].

However, in modern aircrafts, wings and thus airfoils are designed rigid for minimising wing's deformations. Thus the geometric configuration of the airfoils and their angle of attack are fixed. But, they still tailor the lift and drag generation while changing flight regimes. These variations in lift and drag are obtained with external removable devices that modify the airfoil's geometry without deforming it. These external devices modify the **mean camber line** and the **thickness** of the airfoil (see Figure 1.2a).

On Figures 1.3a and 1.3b, the difference between the different airfoils is their **thickness**, the two last digits of the NACA profiles being the airfoil's thickness in percent of chord (the bigger it is, the thicker the airfoil is). on Figure 1.3a, it can be seen that the lift coefficient decreases when the airfoil's thickness is beyond a certain value (Beyond 15 % of chord). This decrease is particularly notable at high angles of attacks and lower at low angles of attack (below $\alpha = 2$ deg). On Figure 1.3b, the drag coefficient has a more complicated relation with the airfoil's thickness. At low angles of attack, the drag coefficient is strictly proportional to the airfoil's thickness. On the contrary, at high angles of attacks, the thinnest and thickest profiles generate the most important drag (profiles below 12 % of drag and the NACA0024). Whereas, the other airfoils display a drag coefficient that is inferior to the prior profiles.

For modern aircrafts, the thickness tailoring is used for drag regulations at high angles of attack. The wing's thickness must be adjusted to an optimum value that would minimise the drag while keeping enough lift. This device exists already on modern aircraft, it is called **slats** (see Figure 1.6).

The second geometrical parameter tailored in an aircraft's wing is its camber. Figure 1.4 presents the evolution of the lift coefficient C_L as a function of the angle of attack α for a cambered profile and a symmetric profile (i.e. non-cambered one). On Figure 1.4,

it can be seen that an airfoil's cambering does not change fundamentally the relation between the lift coefficient C_L and the angle of attack α . The lift coefficient still increases linearly with the angle of attack for a cambered airfoil. The linear Lift coefficient versus angle of attack curves are parallel for cambered and symmetric airfoils. By cambering the airfoil, the curve is just offsetted from a fixed value of angle of attack α_{L_0} . This value α_{L_0} becomes the new $\alpha = 0$ where no lift is generated. This implies that cambered profiles generate lift for negative angles and increase the lift generation, compared to a symmetric profile.

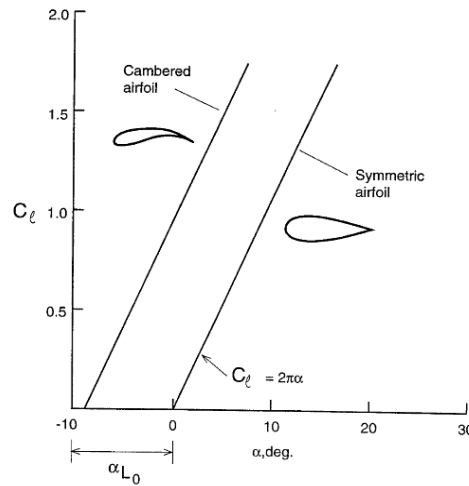


Figure 1.4. Lift coefficient C_L as a function of the angle of attack α for a cambered and symmetric airfoil [33]

On Figure 1.5, the evolution of drag coefficient C_D , for different cambered profiles, as a function of the angle of attack α can be observed. For small and large angle of attacks, the drag coefficient is inversely proportional to the camber value. The more cambered it is, the more drag it generates. Nonetheless, compared to the lift increase the drag increase is smaller: no major drag differences are observed between the profiles at lower and higher angle of attack. Yet, for average angles of attack, the drag coefficient is significantly less important when the camber and the Reynolds number are high.

Thus, from all these observations, it can be concluded that the airfoil cambering is essentially increasing the wing's lift production. By increasing significantly the lift while keeping the drag low, the lift drag ratio $\frac{C_L}{C_D}$ can also be increased significantly. Having a high lift/drag ratio is interesting for an aircraft, as it takes less energy to maintain the

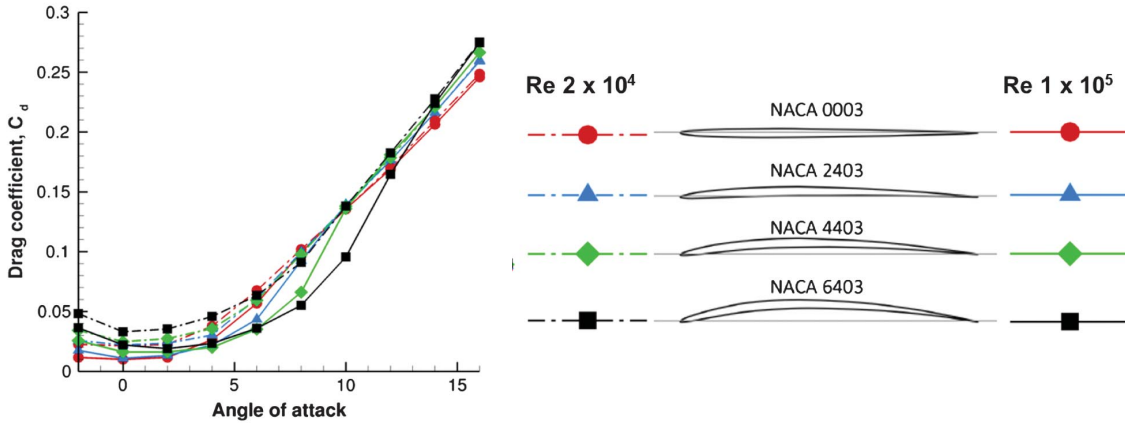


Figure 1.5. Drag coefficient C_D as a function of the angle of attack α for different cambered airfoils [34]

flight and thus leads to considerable fuel economy.

Tailoring the airfoil’s camber depending on the flight regime would be therefore relevant for an aircraft. As it was the case for **camber control**, devices already exist for this purpose. They are called **flaps** and **leading-edge flaps** (see Figure 1.6).

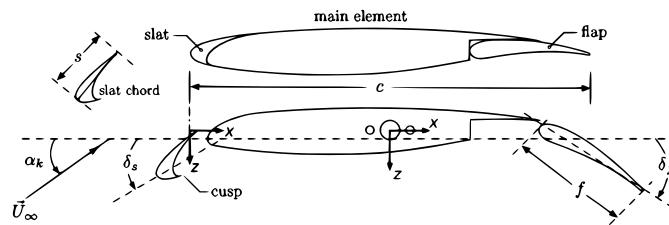


Figure 1.6. Slats and flaps on an airfoil [35]

Despite the advantages given by these different devices, they all suffer from numerous drawbacks. First of all, it can be seen on Figure 1.6 that, during operation, these devices induce non-continuous surfaces for the airfoil [36]. The gaps on the airfoil’s surface lead to wings vibration and noise. Moreover, these devices actuation systems are highly complex and makes the wing heavier. Finally, the servo-motor actuators are prone to maintenance inducing a loss of time and money.

Morphing solutions are developed for providing better performances in C_L and C_D tailoring. Some solutions are designed for thickness tailoring [37], others for camber tai-

loring [16], [38], [39]. But they all provide gapless continuous deformable surfaces and less complex actuation systems, compared to slats and flaps, leading to a decrease of wing's weight and thus increasing the aircraft's performances.

1.1.3 3D wing morphing devices

In order to enhance aerodynamic properties of a 3D wing, in addition to the former 2D parameters applied to airfoils, two 3-Dimensional geometric properties can be tailored: the span of the wing and the sweep angle of the wing (see Figure 1.7).

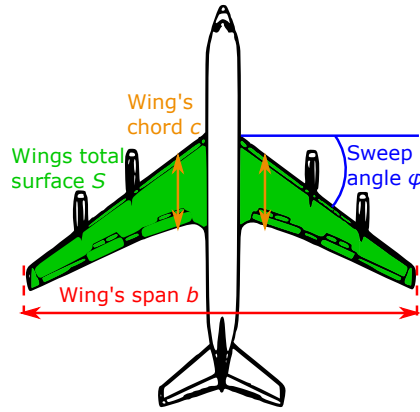


Figure 1.7. Wing's span, sweep and total surface area on a commercial plane [30]

Wing span morphing

The wing's span b is defined as the straight-line distance measured from wing tip to wing tip [29] (see Figure 1.7). The wing's span alone is not the only geometric parameter that influences the aerodynamic forces. Other properties such as the wing total area S , the average chord line \bar{c} or the wing's aspect ratio AR have to be introduced. It represents the ratio between the span b and the mean chord \bar{c} .

$$AR = \frac{b^2}{S} \quad (1.3)$$

The wing total surface area S is the projected area of the wing (see Figure 1.7, the green portion). The average chord line \bar{c} is represented by the ratio between the wing's total area and the wing's span ($\bar{c} = \frac{S}{b}$). This quantity is particularly useful, while the

majority of current aircrafts have a chordline that changes along the wing (see Figure 1.7). With these quantities, a new parameter can be introduced, the wing's aspect ratio AR (see Equation 1.3).

In the lift and drag forces equations (Equations 1.1 and 1.2) the wings surface S is the only parameter that can be influenced by the geometric parameters listed above. The aim for an aircraft is to be able to sustain his own weight force for being able to fly. Thus, for a constant velocity, the bigger the surface S of the wings is, the easier the aircraft can take off or maintain its flight. However, by increasing the wings surface, not only the lift force rises but so does the drag force. Hence, increasing the wing's surface helps to take off easier but the energy needed for motion would also be greater. By looking at Figure 1.1, it can be seen that for modifying the wings surface, it is easier to change the wing's span b , i.e. the aspect ratio AR , rather than changing the wing's chord c .

Indeed, most of gliders targeting this objective of having a maximum lift maximise their span [40]. However, for being truly effective, a high span winged aircraft would have to find an operation velocity where the lift force gains are not overshadowed by the massive drag increase leading to very high fuel consumption. The operation velocity for high aspect ratio wings lies in low cruise speeds for a commercial aircraft [36], at this operation point a maximum ratio of lift over drag $\frac{Lift}{Drag}$ can be found. This leads to high fuel efficiency, which can be interesting for middle or long hauls.

Nonetheless, for very high velocities, this configuration is not fuel efficient anymore but becomes fuel consuming with the drag increases in a quadratic manner with the velocity. Moreover, high aspect ratio aircrafts lack also in maneuverability [36]. On the contrary, at high velocities, low aspect ratio wings are more fuel efficient and have a higher maneuverability, but low aspect ratio wings show poor aerodynamic efficiency [36]. On current aircrafts, there are no devices that can switch efficiently from a low to a high aspect ratio. However, numerous morphing solutions are researched to adapt the wing's span and the aspect ratio at the flight's needs [8], [41].

In addition to aerodynamic benefits earned by the use of tunable span devices, reducing wings span can also be important for avoiding collision and failures of this structure in tight environments. This is particularly true for Micro Air Vehicles [42], [43].

In addition to the wing's span b and the aspect ratio AR , another parameter can be tailored for modifying the wings aerodynamic properties through morphing. This parameter is the wing's sweep angle Φ , this angle corresponds to the amount of translation of the tip chord made from the root chord of the wing (see Figure 1.7). Originally, the idea of sweeping wings originated from the 1950s for military fighter aircrafts [36]. Sweeping the wings was useful for better mastering the changes of flight conditions that occurred when an aircraft approached or surpassed the velocity of sound. Sailing and motor boats using foils never attain such extreme velocities and conditions, thus morphing technologies developed for aircraft fighters will not be of interest.

However, tuning the sweep angle of an aircraft found promising applications for the Micro Air Vehicles (MAVs), especially vehicles operating in air and water [44], [45]. Indeed, sweeping strongly the wings of an aircraft pitches the front side of the aircraft down towards the ground. Figure 1.8 shows the application points of the different forces applied to the aircraft. It can be seen that the center of gravity of the aircraft (i.e. where the weight of the aircraft is applied) is located at the front of the aircraft, whereas the center of pressure (i.e. where the aerodynamic forces of the aircraft are applied) is located behind it. This delay results in a nose-down pitching moment for the aircraft. This pitching moment exists for all aircrafts, it is corrected with other flight devices of the aircraft located on its tail [29]. Sweeping the aircraft's wings back moves the center of pressure to the back of the aircraft which increases this pitching moment. This concept is used on hybrid MAVs for penetrating water more easily [44].

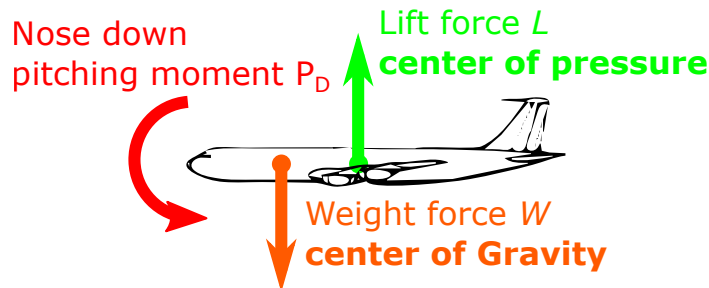


Figure 1.8. Aircraft forces application points

Wing twist morphing

Besides tailoring the wing's span for influences external aerodynamic forces, one can also tune the twist angle along the wing. Figure 1.9 displays a twisted wing with a twist angle θ . A twist angle is defined as the rotation observed by a 2D airfoil element of the wing compared to the root of the wing. This type of morphing is relevant for aircrafts because, along the span, the relative angle of attack and the intensity of the wind changes influencing the generation of lift and drag (see Figure 1.9). Thus, by being able to control the wing's airfoil orientation while being on cruise, one tailor dynamically the wing's lift and drag forces efficiency. Indeed, important changes in aerodynamic properties can be achieved with small wing's surface or geometry changes [36].

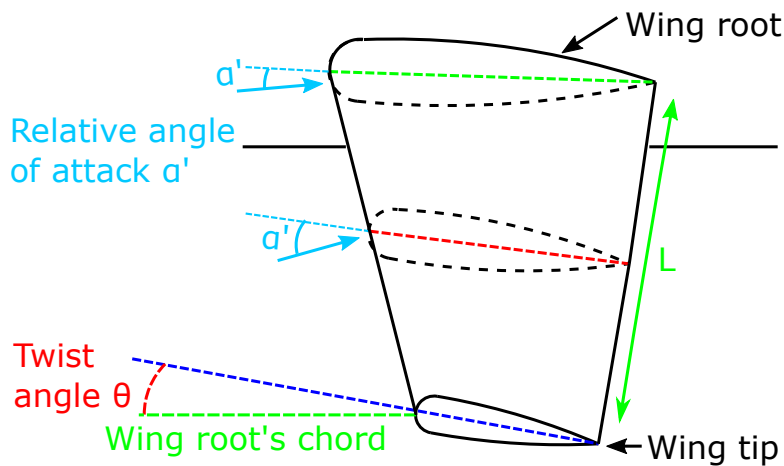


Figure 1.9. Twisted wing example

These changes does not require complex and heavy mechanisms, as the sweep or span morphing do, while having similar size effects on the lift and the drag [36]. Because of these features, the twist morphing is the oldest form of morphing developed for aircrafts. It originated with the "wing warping" developed by the Wright brothers at the end of the XIXth century that provided roll control for their flying vehicle [46], [47]. Despite those advantages, the rise in flight performance and speed went along with stiffer structures that minimise wings deformations for avoiding aeroelastic instabilities and permit to withstand the dynamic loads [46].

Nonetheless, during the last decades, it became possible to predict and limit the effects of the aeroelastic instabilities of the wing [48]. Moreover, new technical solutions have been developed for finding a compromise between wing compliance allowing twist

morphing, and sufficient wing stiffness for avoiding aeroelastic instabilities [25], [32].

Some are designed for giving enough compliance to the wing for torsional deformations, while keeping sufficient stiffness for withstanding aerodynamic loads [32]. Others can tailor the rigidity of parts of the wing for inducing torsional deformations.

Table 1.1 summarises all the **types of morphing** encountered, the **aerodynamic characteristics** they can improve and the **complexity level** of the solution (called the **Morphing level** in the Table). The **Morphing level** depends essentially on the type of morphing targeted (2D, span or twist wing tip morphing) and denotes the complexity level of actuation systems needed for this type of morphing. The higher the morphing level is, the heavier the wing becomes [36].

Morphing strategy	Purpose	Morphing level
Camber morphing (2D morphing)	Performance Lift/Drag (C_L/C_D) Noise reduction Flight control	Low
Thickness morphing (2D morphing)	Performance Lift/Drag (C_L/C_D) Low-speed performance improvement	Low
Twist wing tip morphing (3D morphing)	Flight control Drag reduction at low speeds Performance Lift/Drag (C_L/C_D)	Medium
Span morphing (3D morphing)	Performance Lift/Drag (C_L/C_D) Flight control	High
Sweep (3D morphing) morphing	Supersonic performance Flight control	High
Folding wing	Performance Lift/Drag (C_L/C_D)	High

Table 1.1. Mapping between morphing strategies and objectives copied from [36]

1.2 Morphing challenges in the marine field

Now that the different characteristics targeted for morphing in the field of aeronautics have been presented, it is the time to focus on the field of marine engineering. The challenges encountered are very similar to those of aeronautical morphing, making most of the solutions developed for the aeronautic engineering applicable to the marine field. Nonetheless, two important differences are present for water flows, compared to airflows, the dynamic pressure applied to structure due to the dramatical viscosity difference ($\mu_{water}/\mu_{air} = 1000$) and the presence of a physical phenomenon called **cavitation**. Dealing with this phenomenon implies having new requirements for having an effective effect of morphing on the hydrodynamic properties of a structure.

1.2.1 Hydrodynamic forces present on foiling boats

While using hydrofoils, the hydrodynamic forces are very similar to the ones applied to an aircraft and depicted in paragraph 1.4.2. Being subjected to the same forces, the 2D and 3D morphing solutions have the same effect on the boat's lift and drag performances. The only differences that exist between the aero- and hydrodynamic flows are the density and viscosity differences that are three times higher for water, inducing stronger absolute pressures fields applied to the structure; i.e. despite having stronger pressure fields, the relative pressure field distribution remains similar to aerodynamic flows.

Nonetheless, these stronger absolute pressures fields leads to a significant difference: the absence of 3D morphing solutions that is mostly due to the geometries of the foils. Figure 1.10 presents the different existing geometries of foils used on water vehicles: *V*, *T* and *U* shaped foils.

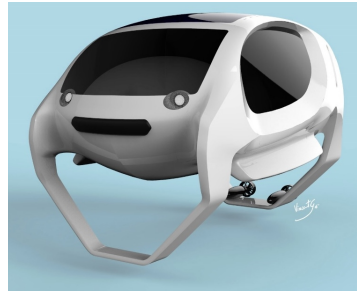
Figure 1.10a shows **V-shaped foils** used on racing sailing boats, by looking at this Figure, it can be seen that this foil geometry has a structural weakness: the elbow bend. When the boat is foiling, this area is subjected to out-of-plane stress concentration [52]. Because of the important waterflow's dynamic pressure forces, the risk of failure has to be well mastered for foils. Thus, adding 3D twisting deformations for morphing might increase the stress concentration in this region and increase the chances of failure [53]. Moreover, in the span morphing case, the heavy actuation systems used might weaken this structural point further [54]. For these reasons, 3D morphing designs are not desired



(a) Foils in a "V" shape [49]



(b) Foils in a "T" shape, mostly used on kitesurfs or windsurfs [50]



(c) Foils in a "U" shape [51]

Figure 1.10. Different existing geometries of foils used on water vehicles

for foils.

Figure 1.10b shows **T-shaped foils** used on surfboards, here no particular structural weakness is to be pointed out. However, these foils are small sized in length (few centimeters) and the hydrodynamic loads exerted on those are still important. Hence, there would be not enough space to put strong servo-motored actuated systems for being able to do 3D morphing.

Figure 1.10c shows **U-shaped foils** used on new water vehicles or large passenger transportation boats, in this configuration it is clear that span morphing would be inapplicable as the hydrofoils form a closed continuous structure. Indeed, enlarging or reducing the span of these hydrofoils would lead to the parts of the hydrofoil bearing the vehicle's load. Moreover, the same issue encountered for V shaped hydrofoils, the presence of multiple elbow bends, makes the implementation of 3D twisting deformations impossible.

Hence, only 2D morphing applications are implemented for hydrofoils. Yet, being subjected to the same hydrodynamic forces and having the same flight regimes as aircrafts,

the same objectives are targeted for foils. That is to say: maximising the lift coefficient C_L for the takeoff, maximising the lift and drag ratio $\frac{C_L}{C_D}$ during the flight and finally maximising the lift coefficient C_L for the landing. However, in the case of foils, an additional parameter has to be taken into account: the presence of cavitation.

1.2.2 Cavitation on hydrofoils

Despite these similarities, one major difference can be noted, 2D and 3D hydrofoils are subjected to a physical phenomenon known as cavitation. Cavitation is a physical phenomenon that has a negative impact on the hydrodynamic properties of an hydrofoil and it needs to be controlled for having functional foiling structures [55]. As it will be explained later, morphing has a positive impact on the delay of cavitation. Most of the bibliographical work presented here is taken from Arbab's PhD manuscript, consult the following reference [55] for more information.

Cavitation

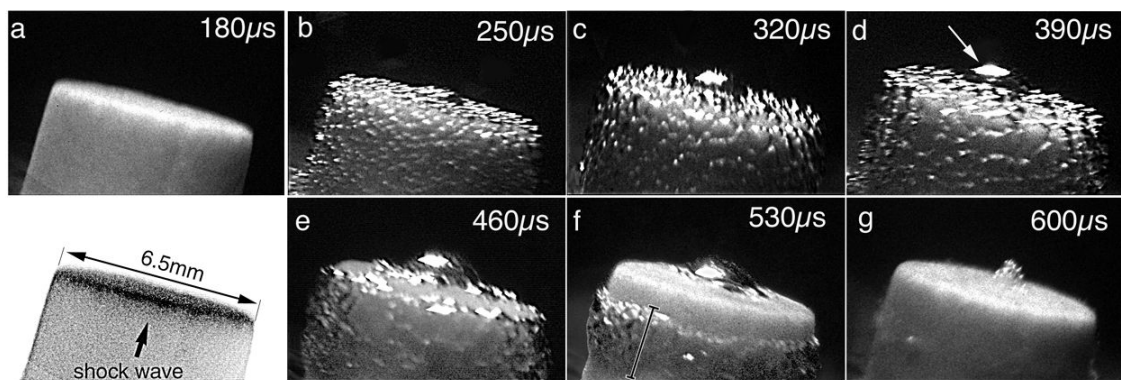
Cavitation is defined as the vaporisation of a liquid, when this liquid's pressure becomes lower than the vapour pressure P_v [55]. This physical phenomenon creates a diphasic flow composed of water's vapor and liquid water around the hydrofoil

Cavitation is influenced by various sets of physical conditions: the vapor pressure value (depends strongly on temperature), the flow's state (turbulence, laminar boundary layer detachment, flow separation...), the nature of the marine structure (geometry, angle of attack, roughness...) or the water's quality (salinity, presence of air bubbles, temperature...).

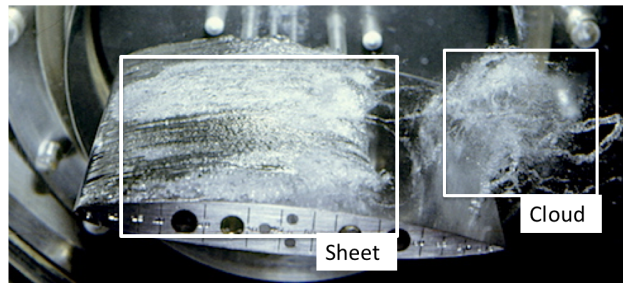
Different steps are observable while cavitation occurs. The first step is known as **inception**, where the first cavitation area (cavities) are start to arise. The second step corresponds to the **cavity's growth**, where the vapor volume increases. The last step is the **cavity collapse**, where the pressure surrounding the cavity becomes too important and makes the vaporous area collapse. This collapse is mostly responsible of surface erosion and structural damage.

Cavitation can be observed in four main forms:

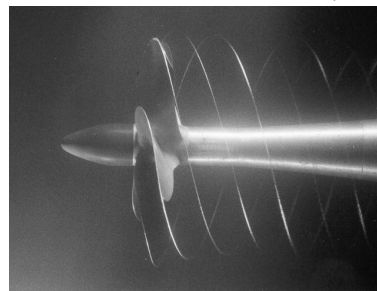
- **Bubble cavitation** can be seen as vaporous bubbles apparition at many points of the structure [56], [57] (See Figure 1.11a).
- **Sheet cavitation** can be seen as an important cavity attached to the structure [58], [59] (See Figure 1.11b).
- **Cloud cavitation** is an unstable state of cavitation where the interface between the liquid and the vaporous state is hard to distinguish [58] (See Figure 1.11b).
- **Vortex cavitation** is observed for high vorticity regions, like water turbines or hydrofoil wakes [58], [60] (See Figure 1.11c).



(a) Bubble cavitation example for a kidney stones into water submitted to Lithotripter Shock Waves [61]



(b) Sheet and cloud cavitation over a hydrofoil [62]



(c) Vortex cavitation around a marine helix for a water flow at 4 m.s^{-1} and $\sigma = 0.596$ (see Equation 1.4) [63]

Figure 1.11. Different types of cavitation

Cavitation has various negative effects on marine structures, that are mainly due to

cavitation bubbles or cavities collapse under water pressure leading to having small water jets hitting the structure's surface:

- Generation of vibration and noise on thrusting devices
- Marine structure damaging, leading sometimes to failure (see Figure 1.12)
- Erosion of marine devices surfaces (see Figure 1.12)
- Loss of hydrodynamic properties

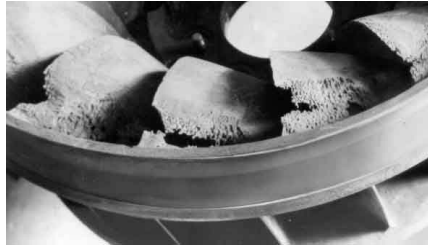


Figure 1.12. *Cavitation damage on a propeller [64]*

Being intrinsically linked to the vaporous pressure P_v , the cavitation can be studied through pressure gradients prediction. Hence, two dimensionless pressure coefficients have to be introduced for quantifying pressure variations, σ and C_p . σ is known as the cavitation number (see Equation 1.4), this coefficient represents the dimensionless reference pressure of the fluid at steady state. P_{ref} is the reference pressure of the fluid, usually this value is the fluid's pressure when it is at steady state. ρ is the fluid's density and v is the flow's velocity.

$$\sigma = \frac{P_{ref} - P_v}{\frac{1}{2}\rho v^2} \quad (1.4)$$

The C_p is known as the pressure coefficient (see Equation 1.5), it represents the dimensionless pressure at a given location. P is the pressure at a given location.

$$C_p = \frac{P - P_{ref}}{\frac{1}{2}\rho v^2} \quad (1.5)$$

For cavitation to occur at a certain point of the flow, its local pressure P_i needs to be inferior to the vapor pressure P_v . This condition is fulfilled if $\sigma < -C_{pi}$ for any point in the flow.

Usually, cavitation is expected when the cavitation number σ is inferior to the opposite value of the minimal pressure coefficient of a given flow $-C_p^{min}$ ($\sigma < -C_p^{min}$). This condition is given in Equation 1.6.

$$\sigma < -C_{pi} \quad (1.6)$$

Many authors have investigated the apparition of cavitation for hydrofoils in a water tunnel [58], [65]. To do that, they have chosen two variables to be tested, the cavitation number σ and the hydrofoil's angle of attack α . The experimental protocol for determining the apparition of cavitation is the following: the cavitation number σ is fixed and the angle of attack α is varied from an initial value of 0 deg to a final value of 8 deg of a step of 0.5 deg. While increasing the angle, cavitation appears for a given angle of attack.

Figure 1.13 displays the cavitation inception and development on a NACA0066-312 profile at a Reynolds number of $Re = 0.8 \times 10^6$ obtained by Leroux *et al.* [65]. The behaviors displayed on this Figure are also observed experimentally and numerically by other authors [58]. On this figure, a $-C_p^{min}$ line can be seen just below the **cavitation inception** points. This line corresponds to the moment cavitation starts occurring ($\sigma = -C_p^{min}$), the surface formed by this curve is also known as the **cavitation bucket**. The **cavitation bucket** is the area where $\sigma > -C_p^{min}$, so no cavitation is to be observed if the cavitation number and the angle of attack are located in the **cavitation bucket**. This area is called a **sub-cavitant domain**. On the opposite, if σ and α are located outside the cavitation bucket, than $\sigma < -C_p^{min}$ and some form of cavitation is present. Thus, it is called the **cavitant domain**.

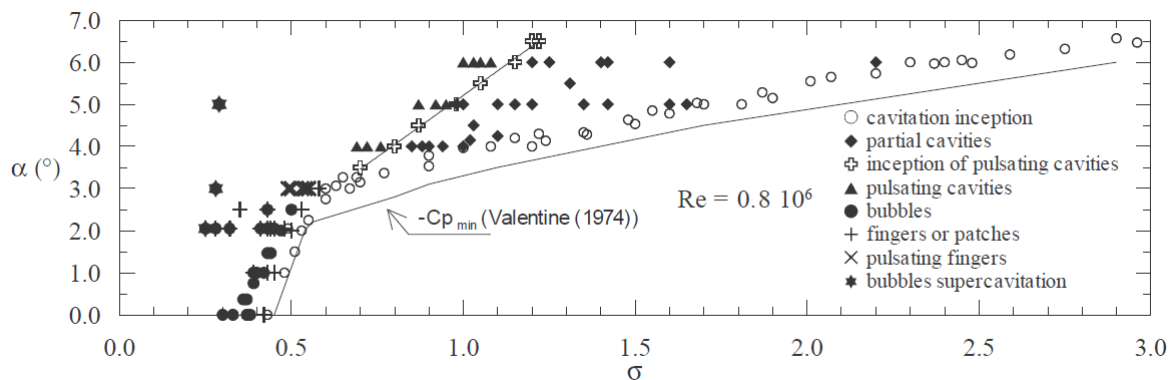


Figure 1.13. Cavitation profile of a NACA66-312 hydrofoil [65]

On Figure 1.13, it can be seen that the types of cavitation occurring change slightly depending on the cavitation numbers and the angle of attacks observed. For low cavitation

numbers ($\sigma < 0.8$) and low angle of attacks ($\alpha < 2^\circ$), the dominant mode of cavitation is the **bubble cavitation**, the cavitation generation strongly depends on the presence of initial undissolved microbubbles within the liquid that grows unbounded when they are exposed to regions of under-pressure (i.e. $C_p < 0$) [55]. Then, for low cavitation numbers ($\sigma < 0.8$) and average angle of attacks ($2^\circ < \alpha < 5^\circ$), small **sheet cavitation** starts to appear through **fingers or patches of cavitation** at the leading edge of the hydrofoil [55]. For higher cavitation numbers ($0.8 < \sigma < 1.2$), these **sheet cavitation fingers** transform themselves into **cavitation clouds** for $\alpha > 3^\circ$; i.e. **pulsating fingers and pulsating cavities** on Figure 1.13. Cloud cavitation arises for regions generating pressure or velocity instabilities in the liquid flow [55]. Finally, for higher cavitation numbers $\sigma > 1.2$, the instability region is passed and the dominant form of cavitation becomes **sheet cavitation partial cavities** at the leading edge of the hydrofoil.

For a NACA0015 profile, Wang *et al* showed that for angles of attack extremely high ($\alpha > 20^\circ$) and cavitation numbers of $\sigma = 1.0$ and $\sigma = 1.5$, the main type of cavitation is the **vortex cavitation** occurring in the wake of the hydrofoil, near the hydrofoil's trailing edge [58].

Thus, for foiling boats, cavitation control mechanisms or devices might be crucial for an optimal operation of 3D hydrofoils. Being a complicated phenomenon to solve, the topic just starts to be thoroughly researched now. However, in the literature, different ways were investigated for avoiding or limiting hydrofoil cavitation. One of these ways consist in perturbing the regular hydrofoil flow by adding other water flows, like water jets or small air bubbles for example, that leads to total cavitation suppression or a limitation of cavitation negative effects. For instance, it can promote **sheet cavitation** and suppress **cloud cavitation** that is more damaging for the structure [66]–[68].

Other examples included the geometry tailoring of hydrofoils. Indeed, to some extends, hydrofoils with higher thickness and camber tend to delay the apparition of cavitation [55].

Flexible airfoils also reduce cavitation negative effects, especially vibration, by deforming under cavitation bubbles collapse leading to vibration damping effects [9].

Morphing solutions can be developed in one of those three axes for tailoring hydrofoil cavitation.

1.3 Structural elements characteristics needed for morphing

In order to be able to develop structures fulfilling the aforementioned requirements, suitable constitutive structural elements must be identified. In most of the morphing strategies developed, two constitutive structural elements are considered: the wing's core and skin [9], [32], [69], [70]. For each constitutive elements, their mechanical characteristics needs to be specified.

1.3.1 Airfoil and wing core for morphing

The core of the airfoil is the constitutive element that must ensure the structural integrity of the wing or the hydrofoil. The core is the element that sustain the external dynamic loads applied on the structure and it is also the element that hosts the actuation systems. The core is generally the structural section that initiates the deformations for the structure's morphing [32], [38], [71].

Thus, the core must have **tailorable mechanical properties in the morphing directions, high mechanical properties in the other directions and a low density**. The direction where mechanical properties need to be tailorable, i.e. changing from a stiffer state where deformations are negligible to a compliant state allowing directed deformations, is different depending on the type of morphing targeted. Figure 1.14 shows the direction where the deformations need to be done, and thus where the mechanical properties need to be tailored, depending on the morphing type targeted. For 2D morphing, the deformations need to be done in a direction parallel or orthogonal to the chord, hence the in-plane stiffness of the airfoil needs to be tailorable (see Figure 1.14a). This type of deformations allows to change the camber line of the airfoil. For 3D morphing, the deformations need to be done along the wing (see Figure 1.14b).

While deforming in one direction, the core must have a **zero Poisson's ratio** for avoiding unnecessary deformations in the other directions [41]. When authorized, the deformation must be **reversible** for being able to switch from one configuration to the other. Thus the core must be constituted of an elastic material or a mechanism [41]. Finally, all these characteristics have to be met while ensuring a **low structural weight**.

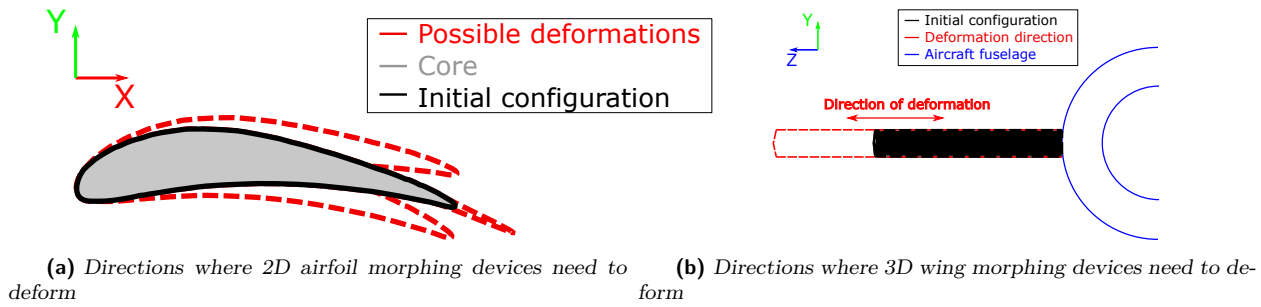


Figure 1.14. Directions of deformations for 2D and 3D morphing concepts

All these characteristics are summarized below:

- The mechanical properties must be stiff enough for minimizing deformations in all directions, except one direction where the mechanical properties can be changed from stiff to compliant for enabling deformations.
- While being deformed by morphing, it must also deform only in this direction (i.e. Poisson's ratio of zero).
- The core's deformations must always be reversible, no yielding must occur and no failure in the skin must be observed.
- The core must also have a light weight.
- The skin must be resistant to different weather conditions: humid, cold, high UV exposition...

1.3.2 Skins for morphing

For operating efficiently, the wing's core needs to have an appropriate skin that is fitted to its operation mode. Here the skin acts as a gapless continuum for ensuring a uniform flow at the wing's surface. Usually, all the skin requirements are not explicitly formulated, but are implied in the various solutions proposed. Figure 1.15 shows different patents for 2D morphing. The first thing that can be noticed is that the mechanism is way more detailed than the related skin. On this Figure, the skin is expected to be **perfectly elastic**, deforming only chordwisely (in the direction of the airfoil's deformation) and perfectly fitting the airfoil's shape with **no skin warping**; i.e. skin local buckling.

Mechanically, these requirements can be translated into the following features: first of all, for enabling chordwise deformations, **the skin must have compliant in-plane mechanical properties**; i.e. low longitudinal elastic rigidity E_L and low transversal rigidity

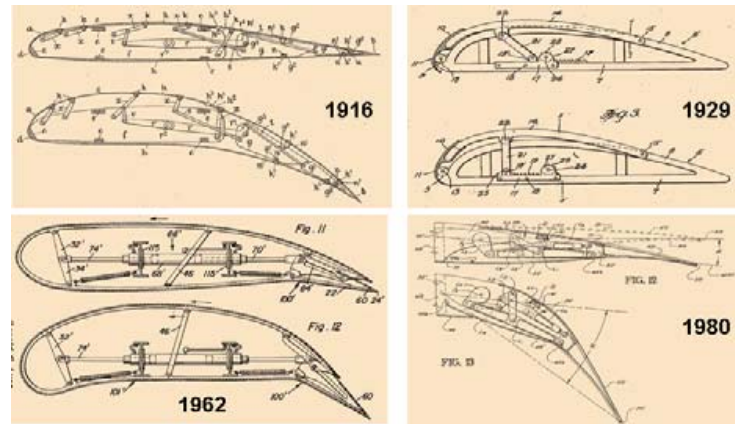


Figure 1.15. Morphing patents dating from 1916 to 1980 [38]

E_T (see Figure 1.16a) [38], [72]. Moreover, for having deformations in this direction only, the material must not deform in transverse and out of plane directions, thus it must have a **Poisson's ratio of zero in all directions** [38], [72]. The last requirement is having a skin that **has recoverable deformations (i.e. remains in the elastic domain)**.

In addition to this, it is expected for the wing to resist to out-of-plane deformations (see Figure 1.16b). To do this, the wing's core must bring enough structural stiffness. Hence, **the skin is supposed to transfer efficiently the aerodynamic loads to the wing's core** [72]. The skin can also be used for damping purpose, especially when the beam bends in its vibratory frequency [73].

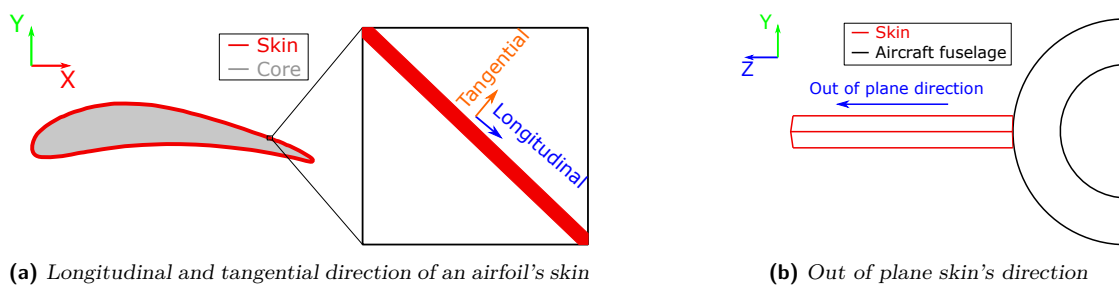


Figure 1.16. Different directions of a wing's skin rigidities

From these observations, it can be seen that these mechanical characteristics are very hard to reach for a continuous closed elastic skin. Indeed, a closed continuous elastic skin gives a problem of **adverse requirements**: if the airfoil deforms downward, for example, the upper side of the skin is submitted to tensile loading and the lower side of the skin

is submitted to compression loading [38]. Being a continuous structural element, these loading lead to **local deformations** or problems to **spouse the airfoil’s deformed shape**.

To overcome these issues, some morphing solutions used **slotted discontinuous skins** [47], [74], [75]. Nonetheless, using this type of solution leads to new issues: an important stiffness reduction of the wing, implying the use of heavy actuators. The use of such solutions enters in contradiction with the purposes targeted with 2D morphing; i.e. **Wing continuity and reduction of weight** [38]. Thus, having **continuous skins** seems to be necessary to avoid a high structural weight. Yet, special mechanisms dealing with this problem of **adverse requirements** are needed for ensuring the absence of local skin warping [39], [76], [77].

In addition to these operational requirements, skins suitable for morphing need to have the same requirements demanded for any aeronautical structure: **resistance to different weather conditions (humidity, low temperatures, high UV exposition...)** and **high toughness for preventing crack propagation**. For twist morphing, very similar requirements are needed for the skin [32].

For the span morphing, the stiffness requirements for the skin are different, as the **out of plane stiffness needs to be low** for stretching the wing’s skin and ensuring a homogeneous continuum along the wing with a minimum of actuation power. The structural stiffness avoiding the wing’s bending in the YZ plan (see Figure 1.16b) is ensured by the wing’s core rigidity, hence reducing the skin’s stiffness will not foster wing bending and instabilities. The longitudinal and transversal stiffnesses can be either stiff for adding supplementary structural stiffness for avoiding aeroelastic instabilities [24], [41] or low for enabling deformations and being coupled with twist morphing [8].

So far, no concept for skin adapted to morphing proposed in the literature is able to fulfill sufficiently all these requirements altogether. This is one of the main reasons why morphing is still not used on modern aircrafts. Moreover, deeper insights are still needed, for the suitable skins for morphing and the morphing devices, to assess their reliability during long times of operation [36].

All these requirements are summarised below:

- The in-plane XY elastic rigidities of a morphing wing skin need to be low for enabling airfoil 2D deformations (see Figure 1.16a), but must still be higher than a minimum affordable stiffness for avoiding excessive deformations.
- While being deformed by morphing, it must also deform only in this direction (i.e. Poisson's ratio of zero).
- The skin must have great out-of-plane elastic rigidity for avoiding the 3D wing bending in the direction Y and be able to keep and transfer the aerodynamic loads to the airfoil's (see Figure 1.16b).
- Local skin warping must be avoided.
- Aero-elastic instabilities must be partially or totally damped by the skin.
- The skin's deformations must always be reversible, no yielding must occur and no failure in the skin must be observed.
- The skin must also have a light weight.
- The skin must be resistant to different weather conditions: humidity, cold, high UV exposition...
- The skin's out of plane mechanical properties (along the Z axis) needs to be small for having low actuation costs (**Span morphing**)

1.4 Morphing technological strategies

In the previous sections, most of the different challenges and requirements met in the morphing airfoil and hydrofoil fields have been presented. In this section, various technological solutions fulfilling these requirements will be presented. These solutions will be discussed and analysed on the advantages and the limits they bring. At the end of the chapter, a morphing solution will be proposed for further development, in the light of the information provided in this section. Morphing mechanism investigations and manufacturing induced issues will not be treated in this chapter, they will be covered in chapter 2.

1.4.1 2D air- and hydrofoil morphing devices

As explained in section 1.1.2, compared to the current high lift devices used, such as slats or flats, the 2D morphing solutions could tailor the lift and drag properties of the air-

craft with similar or higher efficiency, while providing gapless surfaces, being light weight and being less prone to maintenance. To do that, the solutions either play on camber line or thickness variations.

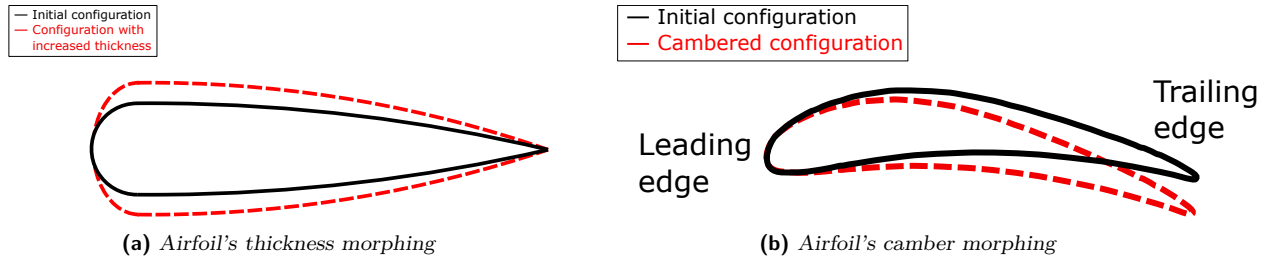


Figure 1.17. Thickness and camber morphing variations on an airfoil

Figure 1.17 presents the two geometric parameters tailorable for airfoil morphing: the thickness morphing solutions (see Figure 1.17a) and camber morphing solutions (see Figure 1.17b). Thickness morphing solutions are less investigated than camber tailoring morphing solutions, because this geometric parameter has less direct impact on aerodynamic forces than camber variations. In addition, the technology needed for tailoring this parameter requires complex systems. Most of those use shape memory alloys (SMA) as actuators coupled with complex systems of wires, a flexible composite or aluminum skin and sensors that convert electrical signals into mechanical movements [78], [79]. These solutions provide better flight conditions (reduction of aero-elastic effects, delaying stall, drag reductions at high angle of attacks...) but they have a limited impact on lift and drag tailoring.

The most common solutions found in the literature are targeting camber control [16], [69], [74], but various solutions are employed for this target. Among these camber control strategies, the most investigated ones are solutions coupling mechanically actuated structures in the airfoil's core and an adapted skin. These structures can either target camber variations at the leading-edge [80]–[82] or at the trailing-edge [47], [75], [83].

Leading edge morphing devices are mostly servo-actuated mechanisms combined to very flexible skins and specific structural solutions for skin deformations [38], [81], [82]. Leading edge morphing devices are very effective on lift and drag tailoring. Li *et al.* have showed that with their leading-edge morphing devices, the lift/drag ratio $\frac{C_L}{C_D}$ can be doubled and even quadrupled for positive angle of attacks [82].

Trailing edge morphing devices are the most popular and most studied devices. Most of those are mechanically actuated through servo-motors and combined to an adapted structural design [7], [84], [85], as the leading-edge morphing does. The most common structural encountered is called the **finger concept** and it was theorised and tested by Monner [71]. It has been called "finger concept" because this solution was inspired from the roll of human fingers. Figure 1.18 depicts the **finger concept** used for trailing edge morphing. Its operation is simple, a front hydraulic actuator, fixed on the leading edge pulls a first plate element connected to a chain of plate elements fixed altogether with prismatic and cylindrical joints. Under the stroke of the actuator, the morphing structure cambers thanks to the plate's rotation around the cylindrical joints [71] (see Figure 1.18).

The morphing airfoil's skin is divided in two: a superior and an inferior skin (see Figure 1.18). Both skins are fixed to the core with slide bearings (see Figure 1.18) and fixed at the trailing edge. When the airfoil is deforming, the upper and lower skins slide along the structure and in the trailing edge. Numerous recent mechanically actuated 2D morphing solutions are based on this concept [7], [86]. In this study, Monner demonstrated a good operational range of the device. Indeed, the trailing edge 2D deformations are included in an interval of $\Delta = \pm 11\%$ of the total airfoil's chord. Furthermore, this solution displayed a good capacity to support the aerodynamic loads [74].

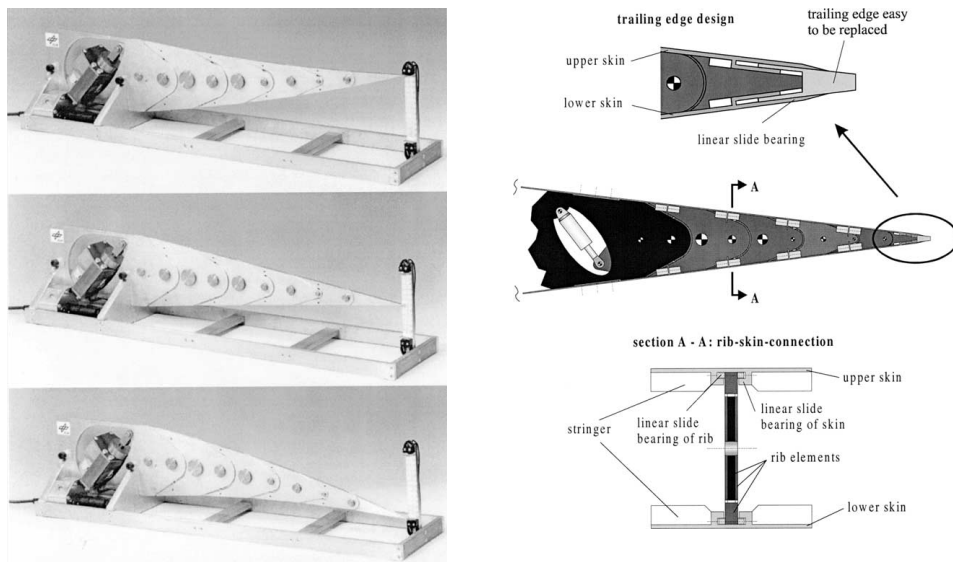


Figure 1.18. Finger concept structure (on the left) and skin (on the right) developed by Monner [71]

Nonetheless, one of the limits of this actuated device is the management of a discontinuous skin. It requires numerous critical parts as bearings that must not fail during operation. Moreover, the **finger concept** is developed with **mechatronics**, i.e. the actuation system and load bearing system are separate, which makes the actuation system more complex and hence heavier [39]. Thus, some other solutions have been developed that used continuous skins while being able to perform morphing that need less actuation. One of the most popular approach is known as the **Belt-Rib Concept** developed by Campanile and Dachau [39] that used **structonics**, i.e. the structural load bearing system and the actuator are in the same entity.

Figure 1.19 shows the operation mode of the **Belt-Rib Concept**, the belt-rib morphing airfoil is composed of a compliant shell (*belt*) on which the closed skin will be applied and is reinforced by in-plane stiffeners (*spokes*). The spokes and the skin are connected through solid states hinges, except the two actuated strokes that are connected through ball joints. When the actuator induces a rotation on the ball jointed strokes locally, the local rotation is transferred through the belt to the other hinged strokes. Having a relatively low bending stiffness, the hinges deform in bending and the strokes remain loaded in tension and compression.

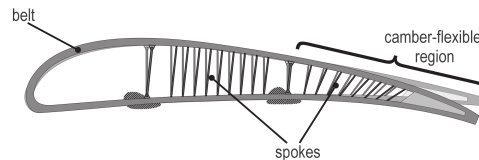


Figure 1.19. *Belt-rib concept developed by Campanile et al [39]*

With this concept, it was possible to induce a displacement of ± 2.7 mm to the airfoil's trailing edge tip, for a chord length of 500 mm which corresponds to a tailoring interval of $\Delta = 0.5\%$ of chord. Comparatively to the finger concept, the performances displayed gives less tailoring possibilities. Nonetheless, the belt-rib concept was then further investigated in the following years, for optimising the inner strokes structure for enhancing the tailorability range of the belt-rib concept [87], [88].

All the morphing solutions depicted here are active ; i.e. they require the use of an actuation system combined with transducers that convert electrical input into mechanical output. The presence of actuators induces numerous issues: because of strong dynamic

pressures, the actuation power needed is important. If mechanical actuators are used, the wing deformations often require complex systems of actuation such as hydraulic jacks, numerous wires or servo-actuators, which adds considerable weight to the wing. Moreover, such complex systems are prone to maintenance and complex to maintain over time [39].

To overcome these problems, numerous alternative morphing solutions were proposed. One of those was the use of smart materials: **piezoelectric actuators**. Piezoelectric actuators are devices that deforms or changes shape when subjected to an electric current. Various forms of piezoelectric actuators exist. The most common ones are the **piezoelectric ceramics**, they are widely used on helicopter rotor systems for enhancing their aerodynamic properties, but also for reducing the vibration and noise caused by these systems [85]. These piezoelectric actuators have also the advantage of deforming quickly when activated [89].

An other family of piezoelectric actuators are **piezoelectric composites**. Here, the actuators are embedded inside the composite materials or are the composite material itself. The composite starts actuating when an electric current passes through it (see Figure 1.20) [16]. Mostly, **piezoelectric composites** are used on airfoil skins. It is the skin itself that induce the airfoil's cambering or decambering to the core [90]. Using piezoelectric actuators as morphing systems provides major advantages over mechanically actuated composites. Indeed, they have a low volume and are low weight as the actuation system is embed within the composite. Other advantages are to be noted such as simplicity of the overall system, reliability and continuous deformation [83]. In terms of performance, the trailing edge 2D deformations tailoring can be pushed up to $\Delta = \pm 18\%$ of the total airfoil's chord [91]. That is more than any other mechanically actuated devices investigated so far.

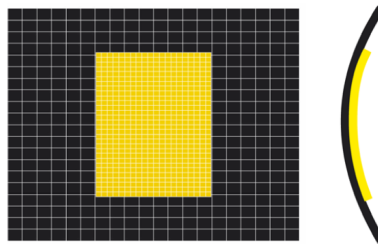


Figure 1.20. Piezoelectric actuator (yellow) on a composite plate (black) [16]

Nevertheless, piezoelectric actuators are generally applied to small or averaged size vehicles [83], [89], [91] and are not well fitted to bigger scales vehicles. The reason behind that is the limited strain output provided by those actuators leading to limited shape change [16], [83]. A risk of structural failure exist, if the vehicle's strains while deforming becomes higher than the strain output scope.

An another emerging solution for solving mechanical actuation issues is the use of **passive morphing devices**. For passive morphing devices, the actuation system and the servo-actuated electronics are embedded within the structure and the structure adapts its shape autonomously to the changes of external conditions. In order do that, one characteristic of the environment must be targeted by the morphing device. The variation of this characteristic in this environment is the morphing trigger of this device. The characteristics targeted are often the temperature [92] and the moisture of the environment [93]. Nonetheless, other more original environmental characteristics can be used as trigger as light [94] or **external loading** [47]. In the literature, these characteristics are known as "external stimulus". Passive morphing structures actuated by external loading are the most interesting ones for marine morphing. These **passive solutions** are categorised as **structonics**, where the structural load bearing system and the actuation system are embedded within the core (e.g. **Belt-rib concept**).

Passive morphing for airfoil morphing is barely investigated in the literature, currently only one system has been researched (see Figure 1.21). This system was initially developed by Bornengo, Scarpa and Remillat [47]. This solution is composed of a combination of cellular materials (it can be either polymeric or metallic) and composite materials: the airfoil's core is made out of a hexachiral architected cellular material and a glass fiber composite skin, with a piece of rubber for assessing skin's discontinuity (see Section 1.3.2). The hexachiral structure was chosen for its auxetic properties (i.e. negative Poisson's ratio), which, combined to its transverse isotropic properties, gives a relatively high shear modulus to the structure compared to their tensile modulus. Moreover, hexachiral lattices have a unique deformation mechanism exhibiting large deformations for low strains, while maintaining a decent torsional stiffness [95].

Shape reconfiguration is triggered by change of surrounding pressure. Indeed, by combining the aerodynamic pressure distribution along the airfoil with the tailoring cellular

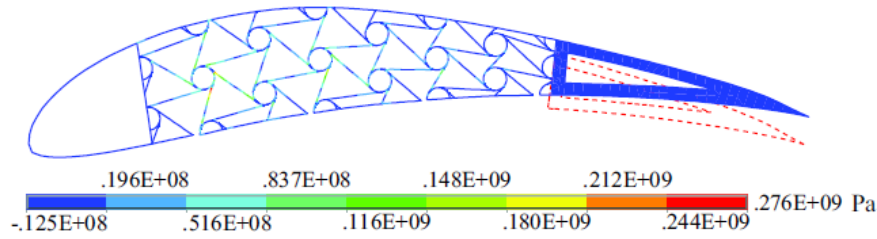


Figure 1.21. Cellular morphing airfoil with a hexachiral structure [96]

core, the airfoil decambering can be controlled (see Figure 1.21). Initially, the cellular core in Bornengo *et al*'s device was at a **material scale**; i.e. the cellular material's cells are very small compared to the structure, and they can be considered as a homogeneous material in the airfoil's core [47]. Yet, other researchers modified this concept. For instance, Spadoni and Ruzzene reused the hexachiral architected material, but the cellular core was designed at a **structural level**, where unit cells are large, leading to a non-homogeneous mechanical behavior of the cellular structure that cannot be considered as a continuous material anymore (see Figure 1.21) [96]. Heo *et al*, then reused Spadoni *et al*'s concept, but they compared the hexachiral cellular core to different architected cellular cores (regular hexagons and reentrant hexagons) [76].

The tailorability of 2D trailing edge displacements displayed by these concepts are respectively in a range of:

- $\Delta = 1.6\%$ of the airfoil's chord for Bornengo's concept [47]
- $\Delta = 2.5\%$ of the airfoil's chord at max for Spadoni's concept [96]
- $\Delta = 0.4\%$ of the airfoil's chord for Heo's concept [76]

The performances obtained with these concepts are very close to the ones obtained with the **belt-rib concept** ($\Delta = 0.5\%$ of the airfoil's chord). From these results, it seems that structonic solutions tailorability ranges are at lowest around 0.5% of chord's length up to 1 or 2% of chord's length, which is considerably lower than mechatronics or piezoelectric solutions that can undergo deformations beyond 10% of chord's length.

Thus, the advantages of those passive solutions compared to mechatronic or piezoelectric solutions are their low wing weight and low maintenance costs, due to the absence of external actuators systems. The disadvantages of these passive devices compared to the other types of morphing devices are their lower tailorability and the difficulty to precisely

control the airfoil's deformations.

Indeed, the different papers investigating the **passive cellular morphing airfoil** efficiency seem to identify different parameters tailoring the cellular airfoil's deformations. For Bornengo and Spadoni, the core's main deformation mechanism is the tensile-compressive one [47], [96]. Three parameters tailor the flexural behavior of the airfoil: the cells size inside the core, the hexachiral unit cell's geometric parameters and the skin's stiffness [47], [69], [96]. The cells size and the unit cell geometry influencing the tensile deformation mechanisms [69], [96] and the skin tend to oppose to the airfoil's deformation [96]. On the contrary, Heo *et al* highlighted that the shear rigidity exhibited by the cellular core is the main mechanism tailoring the airfoil's flexural deformation [76]. These contradictory conclusions tend to confirm that the mechanism controlling the passive airfoil's decambering is yet not well understood and makes the decambering control inaccurate.

Nonetheless, these final contradictory conclusions highlight one supplementary reason, in addition to the airfoil/wing skins, why commercial aircraft manufacturers are reluctant to use morphing technologies: their reliability. This ascertainment is particularly true for technologies based on novel **smart materials** (e.g. piezoelectric composites, architectures materials, smart structures...). As demonstrated above, currently, there are several critical points that present severe commitment issues for airplane manufacturers (high maintenance needed, high risk of failure, issues for controlling the airfoil's displacement...). Thus, there is a need of deepening the study of these new materials for being able to have a deep understanding of these different issues and finding ways to solve them [36].

1.4.2 3D wing morphing devices

In Section 1.1.3, it has been showed that during the flight tailoring the airfoil's span and twist can significantly improve the aircraft's performances and control over the lift and drag forces. This section will present the different morphing solutions proposed for that purpose in two different subsections, one dedicated to span morphing and an another one dedicated to twist morphing.

Span morphing technology

For achieving a tailorable aspect ratio for wings, many morphing solutions are based on deployable structures (see Figure 1.22). Deployable wings have two different states: folded and unfolded states (see Figure 1.22a). Deployable structures used as morphing solutions are usually bio-inspired, for instance the solution proposed in Figure 1.22b is inspired from seagulls wings and the one proposed in Figure 1.22d is inspired from a beetle's wing.

These solutions involve soft materials and soft parts of their bodies in opposition with modern aircrafts that are designed in a rigid way. The idea of integrating foldable structures in aircraft wings is to soften the overall structure for having a better adaptability and maneuverability for the aircraft, as it is already the case for flying animals. The objectives of high maneuverability and high adaptability are especially important for micro air vehicles (MAVs) like drones that have to navigate in close proximity with obstacles.

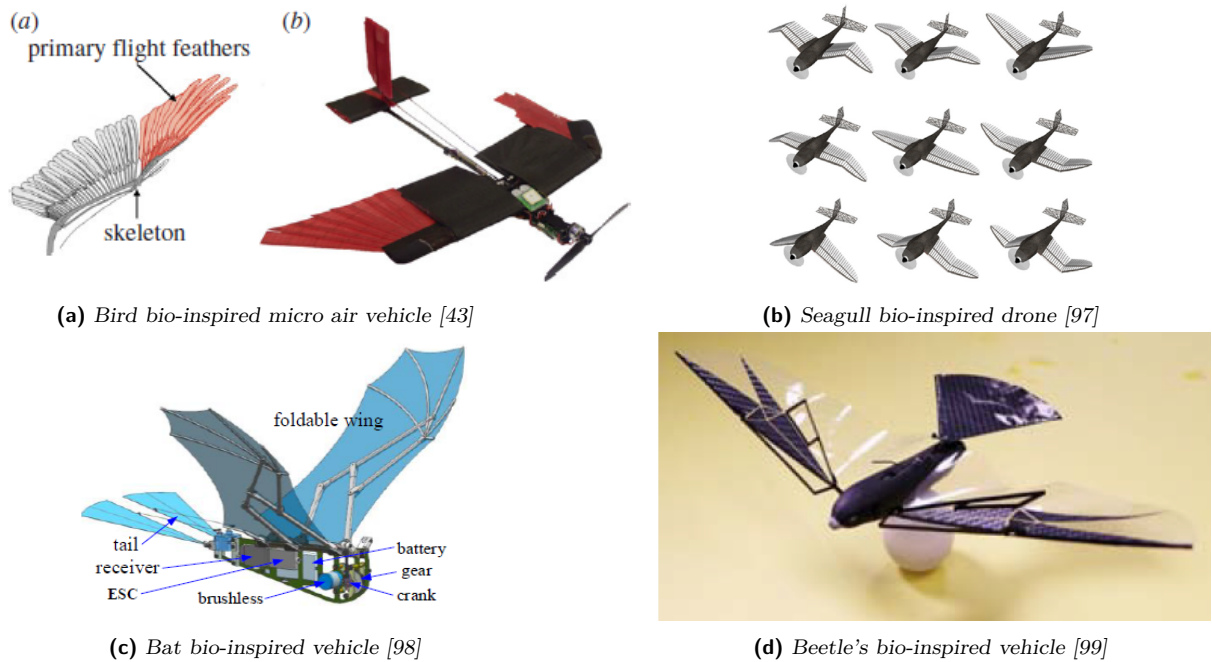


Figure 1.22. Bio-inspired deployable wings and devices

For operating, these deployable span morphing devices for MAVs use rigid materials (e.g. rigid polymer or carbon composite) as load bearing structures combined with soft deployable structures. These soft deployable structures are composed of tendons and

hinges linking the rigid load bearing parts with the deployable ones. These are, most of the case, combined with small electronic servo-actuated systems for enabling structural displacement when needed. The deployable structure's continuous external surfaces are made with compliant membranes. Depending on the wings deformations targeted, the tendons can be either in a stretched or a loose configuration depending on the flight type targeted. The bird inspired MAV's wings showed in Figure 1.22a and the beetle inspired MAV's wings on Figure 1.22d, for example, have a similar operation.

In both cases, tendons are stretched if the wing tip needs to be folded. This configuration stands for closed spaces (e.g. caves), where a high maneuverability is needed and the wings need to be as small as possible. And, for both MAVs, the tendons are looser if the wing tips need to be deployed for assuring a high lift over drag ratio for efficient flights in open spaces.

Being composed from similar structural elements, yet, bat inspired MAV presented in Figure 1.22c and seagull inspired MAV presented in Figure 1.22b operate in a different manner. Indeed, in this case, the wings are not meant to stay horizontal, vertical upward and downward wings movements are needed for repelling air downward and generating lift. For being able to do that, regular tendons are accompanied with rotative mechanisms for enabling the vertical displacement of the deployable structure. In the same way as the previous mechanisms, tendons are stretched for folding the structure and unfolded for deploying the structure.

Deployable structures can tailor the wings aerodynamic properties in a very effective way. For instance, in Di Luca *et al's* work [43], the authors showed that in a fully deployed configuration, an increase of 32% of lift force can be observed. When fully folded, the minimum drag reduces from 40% [43].

Despite these good results, other requirements are needed for having reliable wings span morphing for larger scale aircrafts. When the wingspan increases, so does the wing's weight and the aerodynamic forces applied to it. Uncontrolled 3D wings bending displacements can damage the structure. Usually, deployable wings are actuated with very fragile systems such as hinges and tendons [43], [99]. Thus, it implies to put the right material at the right place.

As a solution, rigid frameworks can be used for insuring sufficient stiffness against wing bending. For instance, in the work of Vale *et al.*, an actively actuated span morphing device was developed [8]. This device is composed from an inner and an outer wing, the inner wing is a hollow wing where the inner wing slides in and out from it [8]. To make the structure stiffer, the leading and the trailing edges are made of composite carbon fiber reinforcement. Moreover, carbon reinforced lattices are added along the span for bearing the flexural loads (see Figure 1.23d) [8]. The solution proposed here is to reinforce the inner structure of the wing for bearing the bending and aerodynamic loads. However, one another solution is to reinforce the wing's surrounding skin for resisting these loads.

VockeIII *et al.* for instance have chosen another solution, they designed a mechanically actuated zero Poisson's ratio core and skin that stretches easily along the span but that resists to bending loads [41], [70]. The wing is designed for only being able to stretch in the span wise direction and not in other directions and loading modes. The core is designed with a cellular structure that exhibits a zero Poisson's ratio when stretched in-plane (see Figure 1.23b), it also provides most of the stiffness for resisting out of plane deformations [70]. The skin is made out of an elastomeric carbon reinforced composite (see Figure 1.23d). This skin was designed for exhibiting a Poisson's ratio of zero in the plane parallel to the span's direction [70], in addition to this purpose, the skin could provide additional stiffness for resisting the out-of-plane deformations and it could also undergo reversible deformations [70]. The overall results given by this configuration were quite interesting: the wings span could be increased by 100 % (see Figure 1.23a). This morphing concept was then validated as functional for helicopter rotor blade tips morphing [41]. On the contrary of the solution above, the span morphing properties are not given by the core alone but also by the wing's skin.

Despite being functional, those morphing systems often require complex and high power actuation systems for deploying these wings on flight [36]. Indeed, for delivering a high actuation power, servo-actuated devices are often used.

Wing tip twist morphing technology

Multiple concepts were developed for achieving a wing with a tailorable twist. Most of these solutions proposed flexible cores with sufficient stiffness for withstanding aerodynamic loads combined with flexible zero-poisson's ratio skins. For example, Jenett *et*

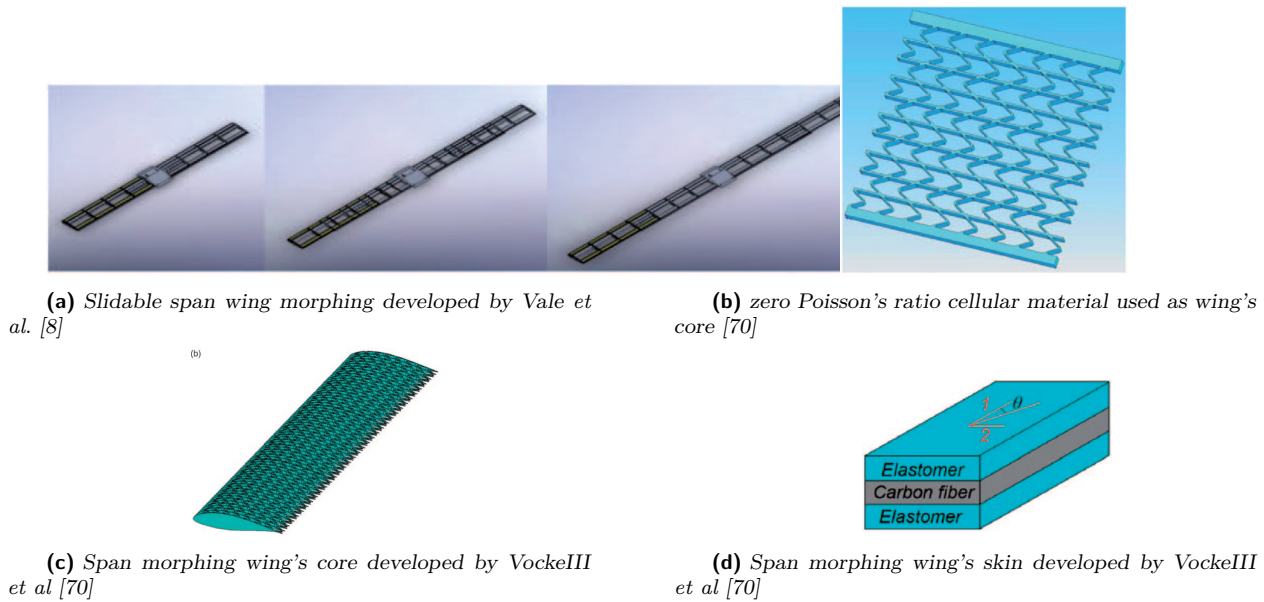


Figure 1.23. Span morphing device developed by VockeIII et al [70]

al developed an actuated morphing device for MAVs that was able to find this good compliance over stiffness ratio [32]. For that, they used carbon fiber reinforced polymers (CFRP) struts that were assembled to form a cellular material with a prismatic pattern as the wing's core. A compliant aluminum alloy was used as the wing's skin and assembled on the cellular core [32]. The structure and the skin are actuated with a servo-motor flexural arm that applied a given torque to the structure (see Figure 1.24). For deforming the wing, the morphing device operates as following: the root of the wing's cellular core is embedded in the vehicle and its tip is embed to the servo-motored arm. The servo-actuated arm's torque is transferred to the cellular wing leading to smooth rotation around the arm's axis leading to morphing (see Figure 1.24).

In a flight configuration, the external loads are essentially supported by the cellular structure of the wing, as the skin is soft and not stiff [32]. Hence in this study, Jenett *et al* investigated the evolution of the flexural stiffness and the torsional stiffness of the cellular core, while considering the requirements the cellular core needed to meet for morphing [32]. The results obtained showed that the flexural modulus remained approximately constant with the variation of thickness while the torsional stiffness increased or decreased dramatically with a more or less dense cellular wing [32]. This lead Jenett *et al* to consider that the wing's core's overall stiffness must be constrained in a fixed interval. The

lower bound of the interval represents the minimum flexural stiffness needed for allowing the wing to withstand the aerodynamic loads, the upper bound represents the maximum torsional stiffness over which the actuated arm cannot transmit its couple anymore [32]. Then, to assess the efficiency of the device, this morphing solution was assembled on a MAV and tested in a wind tunnel. The results obtained were compared to a MAV with rigid wings, tested with various sweep angles, wind velocities or twist. Results demonstrated that the active morphing wing was able to replicate the performance of the rigid wings with several additional benefits such as, reduction of drag [32].

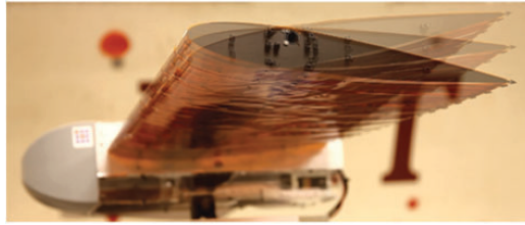


Figure 1.24. Twist morphing wing developed by Jenett *et al* [32]

Passive morphing solutions are also developed for twist morphing. For an example, another twist morphing concept was developed by Raither *et al* [25]. Here a semi-passive device was adopted, this solution arised from a concept developed in the same study. The morphing concept was developed for a cantilever beam configuration with a hollow rectangular section (see Figure 1.25a). On Figure 1.25a it can be seen that, three out of four faces of the beam were made out of a normal material 1, with a thickness t_1 and a shear rigidity G_1 and the last face of the beam is replaced by a thermo-activated smart-material that has a thickness of t_2 and a shear rigidity G_2 [25]. The face made out of the smart material is parallel to the bending load (see Figure 1.25a). Under bending loads, if the product $G_1 t_1$ of the regular material face parallel to the bending loads is equal to the product $G_2 t_2$ of the smart material face, no displacement of shear center occurs and the bending deformation occurs without torsion (see Figure 1.25a). However, if $G_1 t_1 > G_2 t_2$ or $G_1 t_1 < G_2 t_2$ the center of shear of the beam is displaced towards the regular material face's size or the smart material sheet's size inducing beam torsion (see Figure 1.25a). No changes in bending rigidity was to be observed as only one sheet of the beam was replaced by a smart material [25].

This morphing concept was then adapted for a 3D wing section (see Figure 1.25b),

several tests on this device’s bending and torsional stiffness tailoring was then carried out experimentally by Raither *et al* [25]. The objectives of these tests were to see to what extent the wing’s tip rotation could influence the aerodynamic properties of the wing and to see whether the bending stiffness remained constant while changing the torsional stiffness of the airfoil [25]. Results demonstrated that this device could tailor the lift’s coefficient C_L (i.e., the link between the lift force and the lift coefficient is the following for this study $F_{Lift} \propto C_L$) in an interval of a minimum value of 0.4 going up to a value of 1.2. Moreover, this study demonstrated also that tailoring the lift coefficient through torsional stiffness of the wing has a minor impact on the bending stiffness of the wing [25]. This implies that a good compromise can be found between enough compliance for morphing and enough stiffness for withstanding the aerodynamic loads [25]. Nonetheless, Rathier *et al* also warned the readers that the power needed for deforming the wing in torsion increased also dramatically with the increase of torsional rigidity and the twist morphing could lead to flight control issues [25].

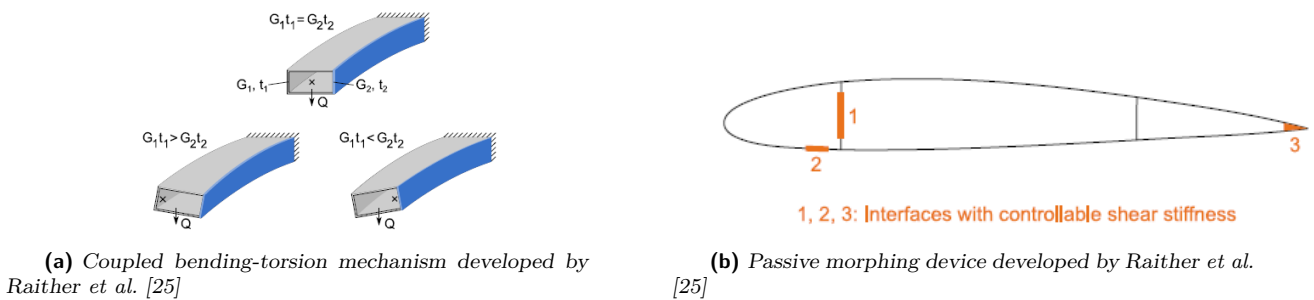


Figure 1.25. Raither *et al*'s study on passive twist morphing

Last but not least, a fully passive wing tip twist morphing concept is currently widely used on wind turbines. This twist morphing concept is similar to Raither’s *et al* concept [25] and it is based on the application of composites skins that display a bend-twist coupling [100]. For operating, the composite material’s stack plies sequences orientation is engineered to deform in torsion when the structure is subjected to bending deformations. it is said that **torsional deformations are coupled with bending deformations.**

Figure 1.26 illustrates this concept, it shows a tidal turbine blade that can exhibit either bend-twisting deformations or stretch-twisting deformations [101]. Depending on the stack plies sequence orientation, it is also possible to couple twisting deformations with stretching displacements, it is also possible to couple more than two deformations mode if the composite is well engineered [102]. The coupled deformation is not necessar-

ily proportional to the imposed displacement (e.g. the bending deformation is the main displacement, and twist is the coupled one). Through, the sequencing of the stack plies, it is possible to control the direction and the intensity of the coupled deformations [100].

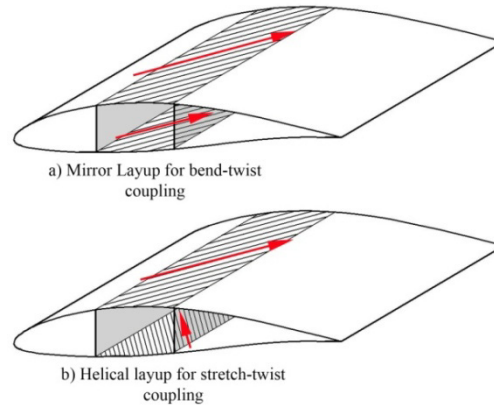


Figure 1.26. Tidal turbine blade designs for bend-twist or stretch-twist morphing [101]

By using this concept, many benefits have been attained: the dynamic loads have been reduced on the blade while keeping similar power output, the efficiency of the wind turbine can be adapted to changes of external dynamic loads and the wind turbine's rotation can also be stopped when needed [100], [103]. Gains in aerodynamic performances can also be obtained with bend-twist composites if they are combined to the optimisation of other parameters. For instance, Vesel *et al* optimised multiple parameters of a wind turbine blade, including the bend-twist coupling effect [103]. After optimisation, the average maximum lift coefficient C_{Lmax} of the blade was increased by 33% and the maximum lift and drag ratio was increased by 65%. In addition to these benefits, the passive nature of the solution inducing an absence of servo-motor actuated systems and the inherent lightweight properties of composites materials make this solution lighter compared to servo-actuated solutions.

However, the passive nature of the solution is also one of its biggest lock. Indeed, tailoring the coupled deformation is a challenging task. It has been well mastered for wind turbines, however the complexity needed for implementing this concept and controlling reasonably the coupled deformations still hinder its wider application for other types of applications [100]. Hence, to solve this problem, many solutions are investigated

in the literature: some studies develop numerical models and new design tools for predicting coupled twisting deformations [100], other studies optimise the coupling deflections for maximising the hydro or aerodynamic properties of its system [103] and others add lightweight electronic devices, transforming the **bend-twist passive composite** into **active piezoelectric composites** [104].

From these three studies, it can be seen in fact that, the twist morphing solutions have a deep correlation with airfoil 2D-morphing mechanisms seen in Section 1.4.1. Indeed, if 2D-morphing deformations are used only on the wing's tip while keeping a rigid root, 2D deformations can be transformed into 3D deformations and wing tip twist morphing can occur. This was confirmed by Monner *et al*, in their study where the finger concept was developed, where they also specified that their solution was fitted to 3D wing tip twist morphing [71]. Moreover, as demonstrated by the two studies above, tailoring the torsional stiffness of the beam has only a small influence on the beam bending properties [25], [32]. So all the solutions presented in the 2D morphing section, such as the belt-rib concept [39], pneumatic actuated morphing [75] or passive cellular morphing [96] can be used as a twist morphing mechanism, while keeping enough bending stiffness for withstanding the loads.

Nonetheless, despite showing such promising results and applications, twist morphing suffers from several issues, one of those was pointed out in the former studies, that is the need of very high actuation power if the torsional stiffness of the wing becomes too high [25], [32]. As it was the case for previous morphing technologies, important actuation powers induced heavy wings and high maintenance.

Yet, wing tip twist morphing devices suffer from an another issue that is common to other types of morphing too: skin local deformation or buckling [6]. Providing enough compliance to the wing for targeting aeroelastic effects increases the chances of having undesired aeroelastic deformations and effects [6]. While developing their prototypes, Jenett *et al* also added pressure actuated patches on the wing's skin for avoiding its local aeroelastic deformations [32].

Vos *et al* also mentioned those initiatives, however they pointed out their limits, most of the energy used by the actuators in the wing was directed for avoiding those local

deformations. This lead to an increase of weight, volume and power consumption [6]. The twist deformations imposed by wing tip twist morphing devices induce skin warping [6], hence the development of suitable skin for wing morphing and the need of high actuation powers are major problems for seeing these technologies appear on modern aircrafts.

1.4.3 Morphing devices for delaying cavitation

In marine applications, the major concern is the control or the delay of cavitation over hydrofoils, then the second major objective is to tailor the lift and drag properties of the hydrofoil for being able to lift the boat's hull at low velocities. Indeed, cavitation disturbs the flow so much that the lift and drag forces produced are no more effective for lifting the vehicle. Thus, for marine applications the primary objective is to delay or control cavitation and then tailor the lift and drag properties of the hydrofoil.

Regular morphing as seen so far, i.e. a hydrofoil that can change its geometry macroscopically for adopting a better reconfiguration to external loading, has just started to arise in the marine field for controlling cavitation [9], [10], [105]. However, before morphing was introduced in the marine field, different fixed geometries of hydrofoils have been proposed for reducing cavitation issues. All the solutions proposed were 2D solutions acting on the hydrofoil section instead of the full 3D hydrofoil [66]–[68]. Some of these solutions, if they are actuated, they can be categorised as morphing.

For suppressing or delaying cavitation, the most popular solutions employed are the use of active or passive fluid injection systems. The most investigated injection systems, are active systems where a fluid (water or air) supplier is embedded in the hydrofoil's core and is connected to small holes or cavities on the hydrofoil's surface expelling this fluid [68], [106]. The aim of fluid injection is to suppress one or multiple forms of cavitation or to limit the damages of cavitation.

In some cases, like the study of Wang *et al*, several types of cavitation can be totally suppressed [68]. In this study, a *NACA66* hydrofoil was tested in a water tunnel with a flow in conditions where cavitation can occur. Figure 1.27 shows how the anti-cavitation device operates. On the top of the hydrofoil, holes communicating with a water supply cavity injected water in the water flow. In their study, Wang *et al* showed that this solution could totally suppress the cavitation occurring along the hydrofoil. In an another study,

it was shown that adding water injection cavities at the tip of marine propellers could also suppress vortex cavitation [106].

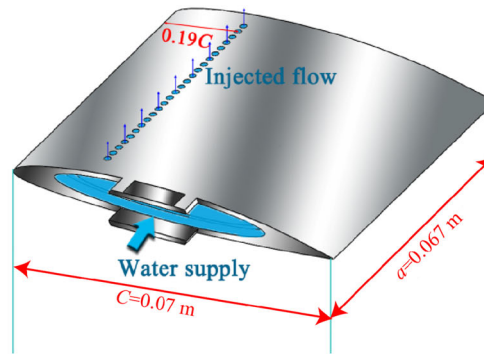


Figure 1.27. Active anti-cavitation device developed by Wang *et al* [68]

As it was the case for morphing already, using active devices implies actuation mechanisms synonym with maintenance and heavier systems. Thus, some passive ways for delaying or suppressing cavitation are researched. For example, Liu *et al.* tried to use a slotted *Clark-Y* hydrofoil design injecting water in the hydrofoil's flow (see Figure 1.28) [66]. This device showed promising results, as it was able to delay the sheet cavitation on the slotted leading edge only, which resulted in the suppression of cloud cavitation and cavitation instabilities. The authors also said that with few improvements, this device could suppress cavitation totally [66].

Other passive solutions consists in putting obstacles in the water flow. If those obstacles could be mechanically actuated, it could provide an interesting morphing solution. Indeed, in the study of Kadivar *et al.*, small cylindrical obstacles were placed at the top of a *CAV2003* hydrofoil [67]. The results of this study demonstrated that the sheet cavity could not be erased, but it was able to suppress the apparition of cloud cavitation due to sheet cavitation.

These different solutions show very promising results for suppressing cavitation around a hydrofoil. Nevertheless, these solutions suffers from some limits. Firstly, these solutions do not prevent cavitation occurrences, but just suppress it after it appeared. Moreover, these solutions do not modify the Lift and Drag coefficients C_L and C_D of the hydrofoil, thus the problem of non-adaptative devices remains. However, recently, hydrofoil morphing solutions have been investigated for being able to do both: prevent cavitation and

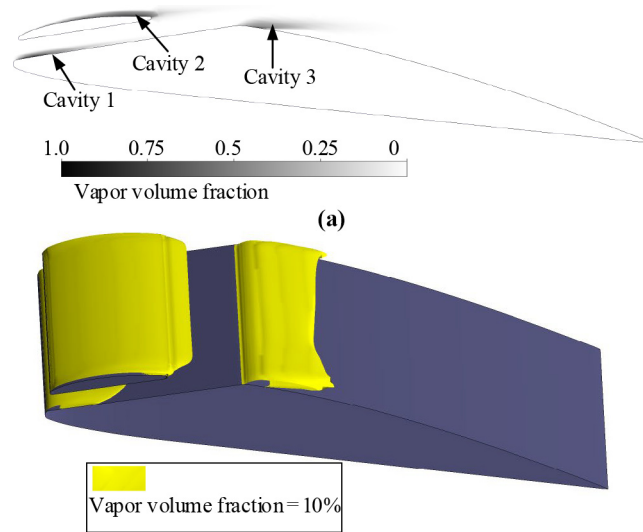


Figure 1.28. Passive slotted anti-cavitation device developed by Liu *et al* [66]

tailor the hydrodynamic properties of the hydrofoil [9], [10].

These morphing solutions applied to water flows have appeared very recently and most of them are based on the use of flexible composite structures. Composites materials start appearing in marine engineering for replacing metallic structures used for propellers [107]. While using these structures, engineers noticed that their flexibility allowed to obtain several non-expected benefits such as vibration damping [105] or passive deformations due to bend-twist coupling [107].

Hence, flexible composites started to be used for shape control in order to adapt the hydrofoil's geometry to the changes of loading conditions. However, in addition to regular morphing technologies, those devices have to take into account the apparition of cavitation. Two different types of hydrofoil morphing devices have been investigated in the literature, active [9] and passive [10] morphing devices.

Active morphing devices are very similar to the ones encountered for aerodynamic morphing. For an example, the new morphing concept developed and tested by Fatiha *et al* on a *NACA0012* profile was composed of two skins, a lower rigid composite skin, composed of 5 carbon plies, and an upper flexible composite skin, composed of 1 carbon ply and 1 glass fiber ply at the leading and trailing edge and 3 carbon plies on the rest of

the upper skin [9] (see Figure 1.29).

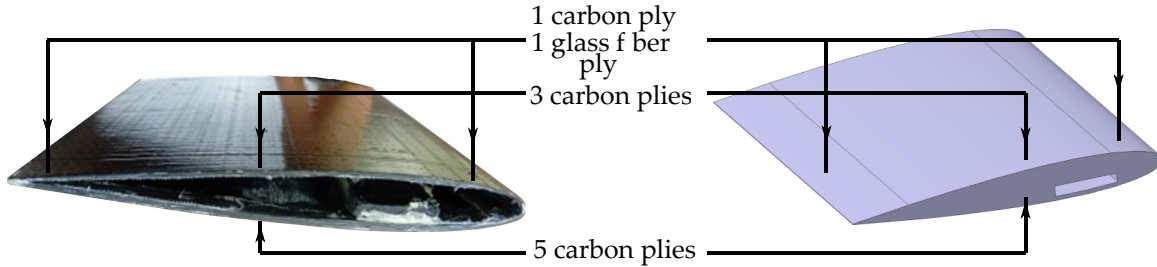


Figure 1.29. Active hydrofoil morphing concept [9]

The core of the hydrofoil is empty, but it is connected to a pump that varied the internal pressure, through the variation of internal pressure, the flexible skin bends accordingly to the pressure variation (see Figure 1.30). The results obtained by this new concept were very promising as it was able to improve the lift/drag ratio of the hydrofoil. Moreover, it is able to prevent cavitation on the morphing hydrofoil by tailoring the lower skin deformations [9].

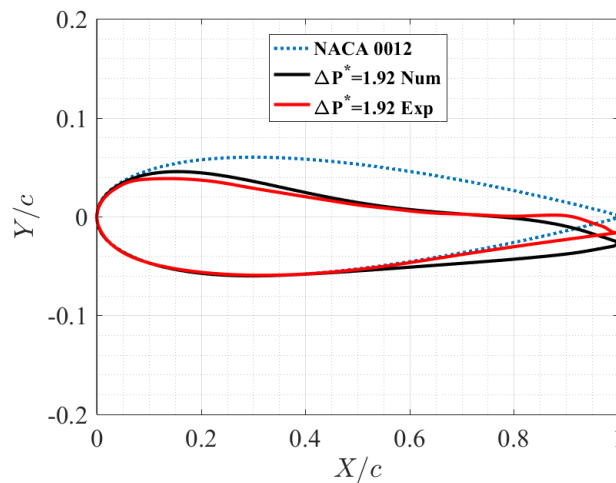


Figure 1.30. Deformed hydrofoil geometry after actuation [9]

Passive morphing devices numerically developed by Sacher *et al* [10] for hydrofoils operate in a similar manner to the concept developed by Bornengo *et al* [47]. This device is presented in Figure 1.31. In this concept, the hydrofoil is divided in two major regions, a rigid undeformable region and a compliant deformable one. The rigid region

represents approximately 90% of the hydrofoil's chord and does not deform under pressure (see Figure 1.31). The compliant region is at the trailing edge and represents 10% of the hydrofoil's chord (see Figure 1.31), this region is composed of materials of various elastic properties.



Figure 1.31. Passive morphing hydrofoil regions: meshed colorful regions represent the elastic region [10]

Similarly to Bornengo's morphing concept [47], the trailing edge is supposed to deform with external dynamic pressure variation, making this concept a pressure actuated **passive morphing device**. Nonetheless, the primary aim of the study is to be able to find the optimum hydrofoil's shape for minimising drag without cavitation inception [10]. To ensure that, the authors coupled their numerical model with an optimisation program that would optimise the different elastic properties of the materials located in the elastic region for minimising the drag, while verifying that there is no cavitation as optimisation constraint.

The results obtained by Sacher *et al* were promising, for some velocities (e.g. 30 knots), the program designated the original hydrofoil shape as the optimal solution (see Figure 1.32a). Which means that the elastic properties of the elastic region were optimised for having a rigid region. Whereas, it was able to find an optimal solution for other velocities (e.g. 40 knots) (see Figure 1.32b). At 40 knots, the displacement of the trailing edge was $\Delta = 5\%$ of the hydrofoil's chord. For this case, the optimisation was able to find a deformed configuration where the drag was minimal and where no cavitation occurred. Moreover, the authors showed that the optimal shape showed a better cavitation bucket than the original shape [10].

Compared to other regular methods for suppressing or delaying cavitation, many advantages are obtained by using flexible hydrofoils. Firstly, with these solutions, it is possible to extend the **sub-cavitant domain** directly and thus prevent cavitation to occur at values of **angle of attack** α and **cavitation numbers** σ . This can be referred as a **passive solution for delaying cavitation**. On the contrary, other solutions suppress

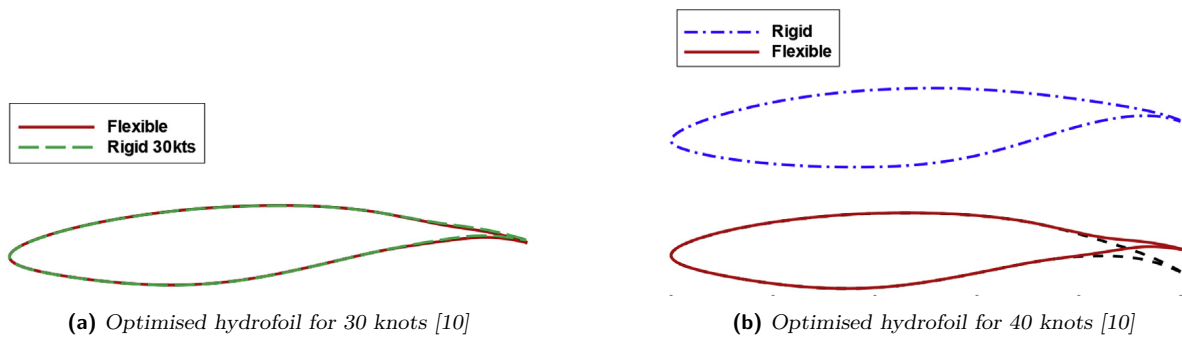


Figure 1.32. Two optimised hydrofoils geometry configurations for 30 and 40 knots

cavitation when it starts occurring instead of preventing it. These solutions are **active solutions for suppressing cavitation**.

Secondly, in addition to delaying cavitation, it is possible to maximise the hydrodynamic properties of the hydrofoil (lift coefficient, drag coefficient, lift and drag ratio...), a thing that is not possible with formerly presented solutions. Nonetheless, despite showing very promising results these **passive anti-cavitating solutions** have a limited range of application.

Indeed, the passive solutions are suited for small angle of attacks where the **sub-cavitant domain** can be tailored with camber variations. According to the results obtained by Fatiha *et al.*, the camber domain can be shifted in a range of $\pm 40\%$ [9]. Outside this range, cavitation will necessarily occur. Thus, if the hydrofoil's operation condition is out of this range, this technique will be ineffective. Moreover, the efficiency of this concept has been only tested for small angle of attacks $\alpha < 4^\circ$ [9], [10].

1.4.4 Summary of the different morphing technologies

This part aims to summarise the different technologies encountered in this section, the morphing type they belong to (2D or 3D morphing, passive or active) and provide information on their advantages and their drawbacks. Table 1.2 summarises all these points and will be reused in the conclusion for choosing a morphing technology to deepen.

Morphing strategy	Morphing Type	Advantages	Drawbacks
Servo-motor actuated camber morphing	Active 2D morphing	High tailorability range Ability to resist loads	Heavy actuation system Highly prone to maintenance
Structonic camber morphing	Passive or active 2D morphing	Lightweight solution Autonomous adaptation to external loads	Low tailorability range Difficulty to control
Piezoelectric camber morphing	Active 2D morphing	-High tailorability Lightweight solution	Fragility, prone to failure Low actuation force
Deployable span wing morphing	Active 3D morphing	Lightweight solution High tailorability	Fragility, prone to failure Low actuation force
Servo-actuated span morphing	Active 3D morphing	-Ability to resist dynamic loads Absence of local skins deformations	Heavy solution Prone to maintenance
Servo-actuated wing tip twist morphing	Active 3D morphing	High tailorability Ability to resist dynamic loads	Heavy solution Local skin warping
Bend-twist coupling wing tip twist morphing	Passive or semi-passive 3D morphing	Autonomous adaptation to external loads High tailorability	Difficulty to control Difficult to implement
Water injection anti-cavitation solution	Active 2D morphing	Disappearance of cavitation Lightweight solution	No increase in lift/drag Fixed geometric shape
Compliant hydrofoil morphing	Passive or active 2D morphing	Prevent totally cavitation Lightweight solutions	Low tailorability Difficult to control

Table 1.2. *The different morphing technologies encountered in this section*

1.5 Chapter summary

To conclude with, in this chapter, all the different challenges and requirements for morphing in the aeronautical and the marine field were presented. In addition, most of the existing solutions in the literature fulfilling these requirements were also reviewed and

analysed in this chapter. Their strengths and weaknesses were also discussed in their different sections. Our aim was to select a morphing concept for investigating and optimising its operative mechanisms. Moreover, that concept must present the most promising characteristics for being implemented in future marine applications (sailing races, industrial applications, passenger transport...).

As showed in Table 1.2, 3D morphing concepts face currently numerous limits that prevent their future use in marine engineering. These limits are essentially linked to the complex actuation system needed for guaranteeing a good operation, that adds undesirable weight to the structure and that are prone to maintenance, and the fact that 3D deformations are not desirable for 3D sailing foils. Most of the 2D active morphing solutions showed also many limits in the aeronautical morphing. These limits were linked, again, to the actuation system complexity, but also to limited actuation force output and the risk of failure of some solutions such as piezoelectric actuators.

To avoid facing similar problems in the future, the study of passive morphing solutions is relevant. So far, two interesting pressure actuated passive morphing concepts have been proposed. One in the aeronautic field, developed by Bornengo *et al*, based on a combination of an elastic skin combined to an architected material core [47] and an another one, in the marine field developed numerically by Sacher *et al* [10]. In addition to our previous requirements, we would also like to optimise the morphing solution while considering the morphing concept's manufacturing. Indeed, we would like to develop a concept that could be manufactured and tested in a water tunnel. The concept proposed by Sacher *et al*, despite showing highly interesting results, is still only numerical, while the morphing concept of Bornengo has already been manufactured and mechanically tested [69].

Thus, the morphing concept chosen for deeper investigation will be the **passive morphing concept from Bornengo *et al***. This morphing concept will be adapted from aeronautics to the marine field. This solution is constituted of a cellular architected polymer core combined with a continuous or discontinuous skin, depending on the variations of the concept. To operate, this solution takes advantage of external hydrodynamic loads for deforming. The deformation is tailored by the cellular core. Our first objective with this morphing concept is to investigate it thoroughly for identifying and understanding the different mechanisms governing the hydrofoil's morphing. Indeed, as highlighted

in this chapter, the mechanisms controlling the hydrofoil's morphing are still not well understood. Furthermore, as highlighted by Li *et al* [36], for this concept it would be a step towards gaining reliability for convincing marine engineers to integrate these solutions in their structures.

The other main objective is to optimise the different parameters identified in the previous section for controlling the hydrofoil's decambering and maximising the ratio $\frac{C_L}{C_D}$. This optimisation will be done by constraining this optimisation into manufacturable results. To be more precise, the final optimised concept must be manufacturable with **3D printing**, process chosen for its ability to manufacture complex geometries. This optimisation work will be done by coupling a **fluid-structure interaction (FSI)** with an **optimisation** program. In this work, cavitation will not be modeled, but it will be taken into account by verifying that $-C_p^{min} > \sigma$. Indeed, as highlighted by Fatiha, cavitation is very complicated to model numerically [55], we do not have the capacity to model this behavior.

The next chapter is dedicated to the investigation of the different parameters tailoring morphing for a **passive polymeric cellular hydrofoil**.

MULTI-SCALE ANALYSIS OF THE MORPHING MECHANISM

As stated in the last chapter's conclusion, the morphing strategy studied is a **passive pressure actuated cellular hydrofoil**. In this concept, the different parameters governing the morphing mechanism's performances are not precisely identified in the literature. The only thing that is known is that the main actuation device is the cellular core of the hydrofoil, who is actuated by external pressure variations. Before establishing an investigation strategy, in the first section of this chapter, the various properties and characteristics of a cellular material have to be presented. Moreover, the different ways of analysing their mechanical behavior and of manufacturing them need to be addressed in this section. At the end of this section, a manufacturing process is chosen for fabricating experimental specimens to be characterised.

In a second section, a numerical and experimental protocol is presented for identifying the morphing mechanism's governing parameters. In this protocol, in addition to this main objective, the effect of the manufacturing process on the morphing structure's mechanical behavior and the ways for taking them into account in a numerical model is also investigated.

In a third section, the results obtained with this protocol are displayed and in a last section, these results are discussed with regard to the literature.

2.1 Introduction

2.1.1 Cellular materials

Cellular materials are defined as an assembly of cells with solid edges or faces, packed together so that they can fill space [108]. One cell is a heterogeneous combination of material and space [109]. Some cellular materials can have a random cell-shape and distribution

in space; this is generally the case for foams. Some other shapes, such as 2D honeycombs, have a unit cell that repeats itself. This leads to **periodic cellular materials**. The geometric pattern of some periodic cellular materials are purposely designed for achieving particular targeted properties that is not present in the natural world. These types of materials have different names in the literature. They are either called **metamaterials** or **architected materials**, or sometimes they are referred to regular **cellular materials**. Thus, the architected geometry of these cellular materials brings them unique physical and mechanical properties [110]. Some are shared by all cellular materials, *e.g.* low density, high energy absorption ability or high compliance [46], [108]. Others are unique, purposely targeted through the engineering of their pattern's design. The properties attainable are various, some can control the propagation of soundwaves and deflect them [111], others can absorb electromagnetic waves [112] or microwaves [113]. However, the most popular architected materials are used for targeting some specific mechanical properties, and are called **mechanical metamaterials** in the literature [114]–[116]. However, in the remaining parts of the chapter, these materials will be referred as **mechanical cellular materials** or just **cellular materials** in short. Currently, mechanical cellular materials have found their way to the industry. They are used as cores of **sandwich composites**. Figure 2.1 depicts the different layers composing a sandwich composite, which are usually made out of (i) two sheets of light and rigid material located, *i.e.* **skins**, on their top and bottom faces; *e.g.* carbon or glass fiber composites or aluminum alloy sheets; And (ii) a thick cellular core which is often a regular honeycomb or a polymeric foam. These two heterogeneous materials are assembled together with adhesive films. These structures exhibit very high mechanical properties, such as good specific stiffnesses. Many use cases of sandwich composites can be found in aeronautics [117], in the naval industry [118]–[121] and in the automotive industry [122], [123].

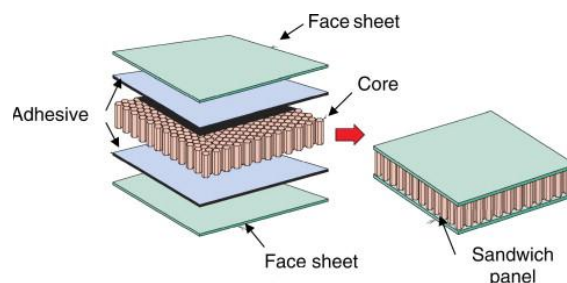


Figure 2.1. Sandwich composite constituents [124]

Sandwich composites are mostly submitted to bending loads. For these applications, cellular materials are mainly used for their low density. Indeed, this specific property enables the addition of high volumes of material, without increasing too much the weight, to increase the beam's flexural stiffness (increase in height), through the increase of the 2nd moment of area, without increasing the sandwich composite's mass. In addition to their low density, cellular materials are also used for their good out of plane specific rigidity E/ρ in the direction parallel to the 2D pattern extrusion of honeycombs of Figure 2.1, it allows them to resist the shear force applied to the sandwich composite. When subjected to bending, the sandwich's rigid skins concentrate the tensile and the compressive stresses. By doing so, this allows to spread the remaining shear stress uniformly in the sandwich's core.

Despite this broad use in industry, research is still carried out on these regular sandwich composites. Some researches tend to find the optimum geometric pattern for the core and/or the optimum material for the skin in order to minimise the sandwich's weight and maximise its stiffness [125]–[127]. Other studies tend to investigate their mechanical behavior in particular applications [128], in elasto-plasticity [129] and fatigue [130]. Some also investigate the failure mechanisms of these structures [131]. Studies in these areas are particularly numerous and dynamic as sandwich composites behavior is mostly known in elastic regime as a bending device.

Aside from beam bending, sandwich composites are also used for energy dissipation. These sandwich composites have the same architecture as regular sandwich beams. However, in this case, the core has a different orientation. Indeed, it is not contained in the same plane as the skin anymore, the geometric pattern is now perpendicular to the skins. Figure 2.2 shows regular patterns used for energy dissipation; usually corrugated pattern are used for this application (*e.g.* packaging boxes layers). In this application, the aim of orienting the patterns perpendicularly to the skins is to benefit from their deformation mechanisms to dissipate energy [46].

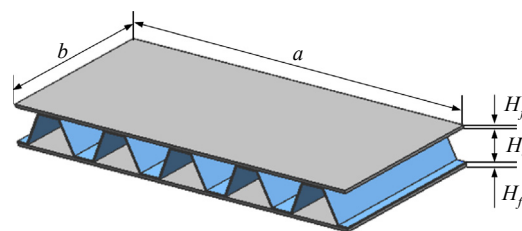


Figure 2.2. Sandwich composite with a corrugated core [132]

Thus, most of the research, for this application, focuses on finding patterns with compliant deformation mechanisms that might dissipate energy effectively and avoid stiff patterns that quickly fail [46], [133]–[135]. Some research have shown that cellular materials displaying **auxeticity** tend to absorb energy better than regular hexagonal or corrugated shaped cores [46], [133]. Auxetic cellular materials are materials with a negative Poisson’s ratio. Indeed, in their work, Li *et al.* showed that, when submitted to 3 points bending tests, auxetic reentrant shaped cores combined with thick carbon composite skins exhibited an interesting buckling mechanism [46]. This mechanism leads to progressive global core failure with respect to the increase of applied stress, which increases considerably the absorbed energy. On the contrary, regular trusses and regular hexagons exhibited local stress concentration and failure which lead to poor energy absorption properties [46].

Having said that, architected material buckling and non-linear deformations are not well understood nowadays and are subjected to extensive research [136], [137]. From these articles, it seems that the apparition of buckling is geometry dependent with specific types of buckling and non-linear instabilities [136].

Coming back to morphing, mechanical cellular materials are interesting for two types of applications: morphing skins and morphing core. As a reminder, morphing skins require three characteristics for a good operation: a zero Poisson’s ratio, a low in-plane stiffness (the 2D hydrofoil plane of a 3D extruded wing) and a high relative out of plane stiffness. These three requirements can be fulfilled with **mechanical cellular materials**. Indeed the Poisson’s ratio can be tailored with the design of particular patterns.

Most of the research of new morphing skins are directed toward the development of zero Poisson’s ratio skins [24], [70], [138]. The skin’s operation is close to the sandwich composites used for energy absorption, the skin needs to have deformation mechanisms as compliant as possible for opposing minimal resistance to morphing. Thus, corrugated patterns have been used extensively for matching these requirements [77], [139].

In the case where mechanical cellular materials are used in the core as a morphing mechanism, the structure’s behavior is in a mid-step between a sandwich composite beam and an energy absorption sandwich composite. Indeed, the morphing structure needs compliance for adapting its shape to external environments while maintaining a minimum stiffness for withstanding dynamic loads and avoiding aero- (or hydro-) elastic instabilities.

Nevertheless, the characteristics that need to be targeted by the cellular core depend on the type of morphing sought. For instance, if a spanwise morphing is targeted, the core property needed would be a zero Poisson's ratio core [41]. On the other hand, if a 2D morphing is needed, the core would need different characteristics: high deformation ranges with low strains and compliant deformation mechanisms. For instance, in the cellular hydrofoil morphing concept, the hexachiral pattern was selected for its auxetic properties conferring it a relatively high shear modulus compared to its tensile modulus. This property combined with the unique deformation mechanism of hexachiral lattices allows the airfoil to undergo large deformations, while maintaining a good torsional stiffness [47], [69].

The hexachiral structure was originally developed by Prall and Lakes [95]. Figure 2.3 depicts the deformation mechanism of this structure: when loaded in compression, the cell's walls wind around the structure's nodes which makes them bend. This unique deformation mechanism grants a theoretical Poisson's ratio of -1, which, combined with the transverse isotropic property of the structure, provides a theoretical infinite shear rigidity in the plane of transverse isotropy [95]. Moreover, the deformation mechanism guarantees recoverable deformations that can go up to 25% [95].

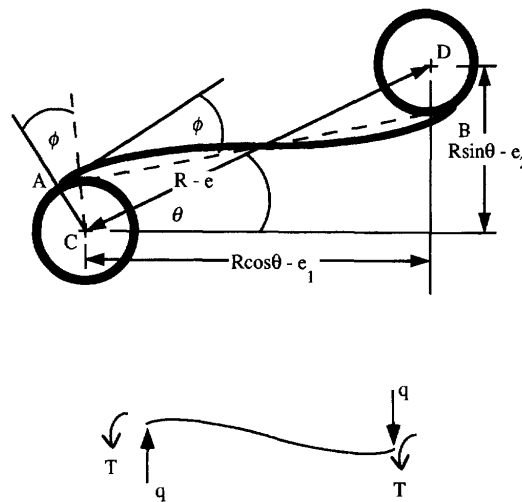


Figure 2.3. Hexachiral cellular material's deformation mechanism [95]

In Heo's morphing concept [76], the pattern that shows the best performance is the reentrant pattern. The reentrant and its shear deformation are showed in Figure 2.4, on this Figure, it can be seen that the vertical walls tend to bend when loaded. The pattern

is shear compliant. Other core morphing concepts use buckling structures for ensuring enough compliance [140] or select patterns that enables high rotations [141].

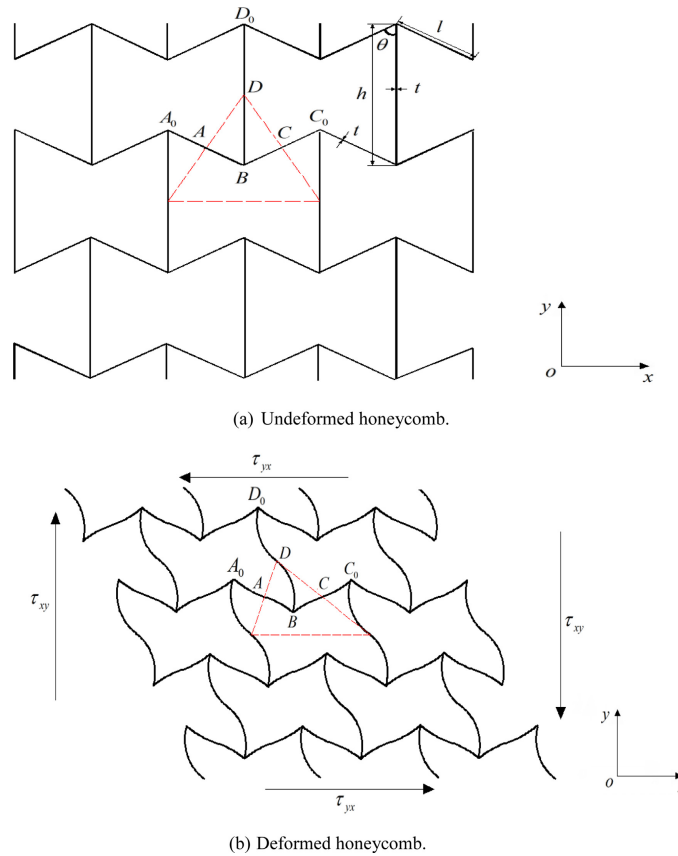


Figure 2.4. Shear deformation mechanisms of reentrant honeycomb [142]

Hence, one must be able to estimate the deformation mechanism efficiency by being able to predict the cellular material’s mechanical properties. In their work, Gibson and Ashby highlighted the fact that the cellular material’s mechanical properties depend on various parameters located at different scales [108].

The deformation mechanisms depend on the constitutive material’s properties. Indeed, the cellular material inherits the properties of its constitutive material [108]. Thus, having elastic isotropic, elasto-plastic anisotropic or elasto-plastic at the **microscopic scale** changes the material’s mechanical properties and its deformation mechanisms. Then, the geometry of the cellular material, at the **mesoscopic scale**, changes the deformation mechanisms and is linked to the apparition of buckling [108]. Finally, the deformation mechanism is highly influenced by the loading at the **structural scale**.

Thus, for investigating the properties of a structure composed of cellular materials, one must perform a **multi-scale analysis** for quantifying and characterising the influence of each scale. Now at **the mesoscopic scale**, *i.e.* the cellular material's scale, one needs to find a method able to take into account the bulk material properties and the local deformations for estimating the average mechanical properties of the cellular solid.

2.1.2 Theory of homogenisation

Representative Volume Element (RVE) and homogenisation methodology

The method that allows to estimate the mean mechanical properties of a cellular material is called the **theory of homogenisation**. This methodology is not reserved to architected materials, but it can also be applied to any media presenting multi-scale characteristics. The methodology depicted here is presented in details in the book of J. Yvonnet [143]. In this theory, several scales are considered and presented in Figure 2.5. They are in the number of three: the **macroscopic scale**, the **mesoscopic scale** and the **microscopic scale**. For each scale, a fictive observer will be considered.

For the observer located at the **macroscopic scale**, only the mean mechanical fields can be observed: the **mean stress** $\bar{\sigma}$, the **mean strain** $\bar{\varepsilon}$ and the **mean displacement** \bar{u} . The local microscopic fields cannot be noticed by this observer.

On the contrary, the observer located at the **microscopic scale** has no idea of how the macroscopic mean mechanical fields look like. The only thing noticeable for this observer are the microscopic mechanical fields: the **local stress** $\sigma(x)$, the **local strain** $\varepsilon(x)$ and the **local displacement** $u(x)$. At a microscopic level, those quantities are space dependent: they vary inside the microstructure.

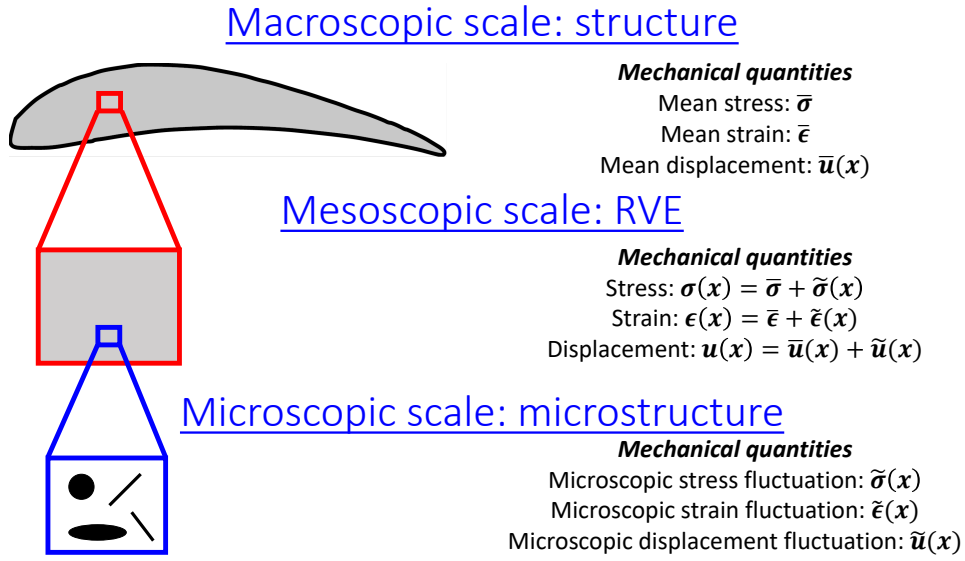


Figure 2.5. The different scales considered in homogenisation theory

Despite not being noticeable by observers at the two different scales, the microscopic mechanical fields influence the macroscopic ones and *vice-versa*. The common scale where those fields encounter is the **mesoscopic scale**. The observer at the **mesoscopic scale** is at a scale big enough for starting to see the macroscopic mechanical fields in addition to the microscopic ones. Thus, the mesoscopic mechanical fields are expressed as a combination of the mean mechanical fields $\bar{\sigma}$, $\bar{\epsilon}$, \bar{u} and local field fluctuations originating from the microscopic scale $\tilde{\sigma}(x)$, $\tilde{\epsilon}(x)$, $\tilde{u}(x)$:

- **The mesoscopic stress** $\sigma(x) = \bar{\sigma} + \tilde{\sigma}(x)$
- **The mesoscopic strain** $\epsilon(x) = \bar{\epsilon} + \tilde{\epsilon}(x)$
- **The mesoscopic displacement** $u(x) = \bar{u}(x) + \tilde{u}(x)$

At this scale, if the mesoscopic strain or stress is averaged, the microscopic stress and strain fluctuations should start to be less predominant than the mean macroscopic quantities. This scale is commonly referred as the **Representative Volume Element (RVE)**, it is the minimum microstructural volume sample containing enough informations for representing the material's mechanical behavior [143]. Having said that, a homogenisation problem can be defined as the research of the mesoscopic quantities verifying the set of Equations 2.1 for a given volume Ω . With $\mathbb{C}(x)$ being the local elasticity tensor of a material at a given location and V being the RVE's volume. When the mesoscopic quantities are defined, the final goal would be to find an expression for the mean elastic tensor $\bar{\mathbb{C}}$

that links the mean stress field $\bar{\sigma}$ and the mean strain field $\bar{\varepsilon}$.

$$\begin{aligned}
\operatorname{div}(\sigma(u(x))) &= 0 \quad \forall x \in \Omega \\
\sigma(u(x)) &= \mathbb{C}(x) : \varepsilon(u(x)) \\
\varepsilon(u(x)) &= \frac{1}{2} (\nabla u(x) + \nabla^T u(x)) \\
\bar{\sigma} &= \frac{1}{V} \int_V \sigma(x) \cdot dv \quad \text{OR} \quad \bar{\varepsilon} = \frac{1}{V} \int_V \varepsilon(x) \cdot dv
\end{aligned} \tag{2.1}$$

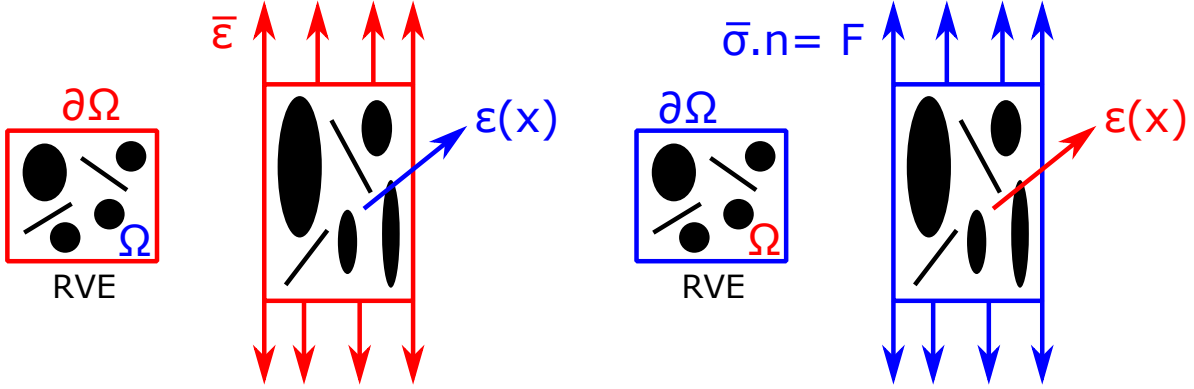
As supposed by the last set of equations of Equation 2.1, multiple solutions exist for a homogenisation problem. In fact, multiple homogenisation problems exist depending on the type of boundary conditions chosen: the problem where, the volume averaging of the mesoscopic stress field is equal to the mean stress field, is different from the problem where, the volume averaging of the mesoscopic strain field is equal to the mean strain field. Thus, for finding a solution for two different homogenisation problems, two different methods are used for solving each problem. These methods are presented in Figure 2.6.

In both cases one RVE is considered and its domain is noted Ω . The boundary of this RVE is noted $\partial\Omega$. The first way for solving one problem is shown in Figure 2.6a, it consists in imposing a mean displacement field $\bar{u}(x) = \bar{\varepsilon} \cdot x$ on $\partial\Omega$. The mean strain field used $\bar{\varepsilon}$ in the former equation is supposed to be equal to the mean strain field of the **macroscopic scale** (see Figure 2.5).

The second solution, depicted in Figure 2.6b, consists to impose a stress vector $\bar{F} = \bar{\sigma} \bar{n}(x)$ on the boundary of the domain $\partial\Omega$. With \bar{n} being the normal of the boundary surface. The mean stress field used for the boundary condition is supposed to be equal to the mean strain field of the **structural scale** (see Figure 2.5). Equation 2.2 shows mathematically the implications of these imposed boundary conditions.

$$\langle \varepsilon(x) \rangle = \bar{\varepsilon} \quad \text{or} \quad \langle \sigma(x) \rangle = \bar{\sigma} \quad \forall x \in \partial\Omega \tag{2.2}$$

Imposing the boundary conditions of Equation 2.2 to the boundary of the domain $\partial\Omega$ implies that the average of the local fluctuations $\widetilde{\sigma}(x)$, $\widetilde{\varepsilon}(x)$ and $\widetilde{u}(x)$ are null, depending on the loading mode selected. There are two possibilities for nullifying these fluctuations



(a) Kinematically uniform boundary conditions (KUBC) with an imposed strain (b) Statically uniform boundary conditions (SUBC) with an imposed stress

Figure 2.6. Kinematically and statically uniform boundary conditions

on the boundaries, presented in Equation 2.3.

$$\begin{aligned} \text{if } \langle \epsilon(x) \rangle = \bar{\epsilon} &\implies \widetilde{\epsilon(x)} = 0 \implies \widetilde{u(x)} = 0 \quad \forall x \in \partial\Omega \\ \text{if } \langle \sigma(x) \rangle = \bar{\sigma} &\implies \widetilde{\sigma(x)} = 0 \quad \forall x \in \partial\Omega \end{aligned} \quad (2.3)$$

A third possibility can also nullify these quantities, the **condition of periodicity** presented in Equation 2.4. The implications of this last condition will be explained in detail later.

$$\text{if } \widetilde{u(x)} \text{ is periodic on } \partial\Omega \quad (2.4)$$

The two first boundary conditions are respectively called the **Kinematically Uniform Boundary Conditions (KUBC)** and the **Statically Uniform Boundary Conditions (SUBC)**. These are defined more precisely below.

Kinematically Uniform Boundary Conditions (KUBC): the displacement $\bar{u}(\mathbf{x})$ is imposed at for all points $\mathbf{x} \in \partial\Omega$ such that:

$$u(x) = \bar{u}(x) = \bar{\epsilon}x \quad \forall x \in \partial\Omega \quad (2.5)$$

Statically Uniform Boundary Conditions (SUBC): the tensile vector is prescribed at the boundary such that:

$$\sigma(x)\mathbf{n} = \bar{\sigma}\mathbf{n} \quad \forall x \in \partial\Omega \quad (2.6)$$

After applying these boundary conditions, one must find the mesoscopic physical quantities σ and ε in the RVE and then being able to identify the mean elasticity tensor $\overline{\mathbb{C}}$ of the structural scale. To identify this tensor, the RVE must be loaded in all spatial directions in order to identify all of its components. Thus, the mean strain tensor $\overline{\varepsilon}$ for the KUBC conditions presented in Eq. 2.5 and the mean stress tensor $\overline{\sigma}$ for the SUBC conditions presented in Eq. 2.6 must have the form depicted in Equation 2.7, represented in a matrix rotation system axis 1,2,3.

$$\overline{\varepsilon} = \begin{bmatrix} \overline{\varepsilon}_{11} & \overline{\varepsilon}_{12} & \overline{\varepsilon}_{13} \\ \overline{\varepsilon}_{12} & \overline{\varepsilon}_{22} & \overline{\varepsilon}_{23} \\ \overline{\varepsilon}_{13} & \overline{\varepsilon}_{23} & \overline{\varepsilon}_{33} \end{bmatrix} \quad (2.7)$$

$$\overline{\sigma} = \begin{bmatrix} \overline{\sigma}_{11} & \overline{\sigma}_{12} & \overline{\sigma}_{13} \\ \overline{\sigma}_{12} & \overline{\sigma}_{22} & \overline{\sigma}_{23} \\ \overline{\sigma}_{13} & \overline{\sigma}_{23} & \overline{\sigma}_{33} \end{bmatrix}$$

If the tensors depicted in Equation 2.7 are applied directly on the RVE, the mesoscopic stress σ and the mesoscopic strain ε would be very hard to find. Thus, using the fact that the problem is linear, the superposition principle can be used to decompose the original complicated problem into several other problems that are more simple to solve. The mesoscopic displacement field $u(x)$ and the mesoscopic stress field $\sigma(x)$ can be rewritten in new forms dependent on $\overline{\varepsilon}$ and $\overline{\sigma}$. The solutions are presented in Equation 2.8.

$$\begin{aligned} u(x) &= u^{(11)}\overline{\varepsilon}_{11} + u^{(22)}\overline{\varepsilon}_{22} + u^{(33)}\overline{\varepsilon}_{33} + u^{(12)}\overline{\varepsilon}_{12} + u^{(13)}\overline{\varepsilon}_{13} + u^{(23)}\overline{\varepsilon}_{23} \\ \sigma(x) &= \sigma^{(11)}\overline{\sigma}_{(11)} + \sigma^{(22)}\overline{\sigma}_{(22)} + \sigma^{(33)}\overline{\sigma}_{(33)} + \sigma^{(12)}\overline{\sigma}_{(12)} + \sigma^{(13)}\overline{\sigma}_{(13)} + \sigma^{(23)}\overline{\sigma}_{(23)} \end{aligned} \quad (2.8)$$

The $u^{(ij)}$ terms are solutions to the problem depicted in Eq. 2.1 with regard to the simplified KUBC loading $\overline{\varepsilon}_{ij}$ applied on the RVE (see Figure 2.6a and Eq. 2.5). The $\sigma^{(ij)}$ terms are solutions to the problem depicted in Eq. 2.1 with simplified SUBC loading $\overline{\sigma}_{ij}$ (see Figure 2.6b and Eq. 2.6).

The $u^{(ij)}$ and $\sigma^{(ij)}$ are fourth order tensors. The initial problem is split in six simpler problems for 3D homogenisation problems and in 3 simplified problems if the problem is 2D. The form of the 2D mean strain and stress loading are shown respectively in Equations

2.9 and 2.10.

$$\bar{\varepsilon}_{11} = \begin{bmatrix} 1 & 0 & 0 \\ 0 & 0 & 0 \\ 0 & 0 & 0 \end{bmatrix} \quad \bar{\varepsilon}_{22} = \begin{bmatrix} 0 & 0 & 0 \\ 0 & 1 & 0 \\ 0 & 0 & 0 \end{bmatrix} \quad \bar{\varepsilon}_{12} = \begin{bmatrix} 0 & \frac{1}{2} & 0 \\ \frac{1}{2} & 0 & 0 \\ 0 & 0 & 0 \end{bmatrix} \quad (2.9)$$

$$\bar{\sigma}_{11} = \begin{bmatrix} 1 & 0 & 0 \\ 0 & 0 & 0 \\ 0 & 0 & 0 \end{bmatrix} \quad \bar{\sigma}_{22} = \begin{bmatrix} 0 & 0 & 0 \\ 0 & 1 & 0 \\ 0 & 0 & 0 \end{bmatrix} \quad \bar{\sigma}_{12} = \begin{bmatrix} 0 & \frac{1}{2} & 0 \\ \frac{1}{2} & 0 & 0 \\ 0 & 0 & 0 \end{bmatrix} \quad (2.10)$$

Once all the $u^{(ij)}$ solution tensors and all the $\sigma^{(ij)}$ solution tensors are found, for respectively the KUBC and the SUBC loading, they can be assembled in a global tensor $\mathbb{A}(x)$ for strains (see Eq. 2.11) and $\mathbb{B}(x)$ for stresses (see Equation 2.12).

$$\varepsilon(x) = \mathbb{A}(x) : \bar{\varepsilon} \quad \forall x \in \Omega \quad \text{with} \quad A_{ijkl}(x) = \varepsilon_{ij}^{(kl)} \quad \text{KUBC} \quad (2.11)$$

$$\sigma(x) = \mathbb{B}(x) \bar{\sigma} \quad \forall x \in \Omega \quad \text{with} \quad B_{ijkl}(x) = \sigma_{ij}^{(kl)} \quad \text{SUBC} \quad (2.12)$$

After finding these tensors, the expression of $\varepsilon(x)$ (Eq. 2.11) and $\sigma(x)$ (Eq. 2.12) can be injected in Equation $\sigma(x) = \mathbb{C}(x) : \varepsilon(x)$ (see Equation 2.1). Equations 2.13 and 2.14 show the final expressions of mesoscopic strain and stress fields. It also shows the expression of the mean elasticity tensor $\bar{\mathbb{C}}$ after volume averaging the mesoscopic fields.

$$\sigma(x) = \mathbb{C}(x) : \mathbb{A}(x) : \bar{\varepsilon} \implies \bar{\sigma} = \langle \mathbb{C}(x) : \mathbb{A}(x) \rangle : \bar{\varepsilon} \quad (2.13)$$

$$\varepsilon(x) = \mathbb{C}(x)^{-1} : \mathbb{B}(x) : \bar{\sigma} \implies \bar{\sigma} = \langle \mathbb{C}(x)^{-1} : \mathbb{B}(x) \rangle^{-1} : \bar{\varepsilon} \quad (2.14)$$

In these two last equations, the mean stress tensor $\bar{\sigma}$ and the mean strain tensor $\bar{\varepsilon}$ are linearly linked by a new tensor. This tensor can be identified as the mean elasticity tensor $\bar{\mathbb{C}}$. Equations 2.15 and 2.16 show the final expression of the mean elasticity tensor obtained respectively with the KUBC method or the SUBC method.

$$\bar{\mathbb{C}}^{KUBC} = \langle \mathbb{C}(x) : \mathbb{A}(x) \rangle \quad (2.15)$$

$$\bar{\mathbb{C}}^{SUBC} = \langle \mathbb{C}(x)^{-1} : \mathbb{B}(x) \rangle^{-1} \quad (2.16)$$

It can be observed that both methods give a different final result for the mean elasticity tensor. As expected, KUBC and SUBC loaded RVEs are two different homogenisation problems imposing that respectively, the microscopic fields $\widetilde{\varepsilon}(x)$ and $\widetilde{\sigma}(x)$ are null on the domain's boundary $\partial\Omega$. Thus in each configuration, there are quantities that are nullified, while they are non-null in the reality. Such strong hypotheses lead to differences when the mean elastic tensor is estimated. The mean elasticity tensor is rather limited in an interval defined by the KUBC and SUBC solutions, than properly estimated by these methods.

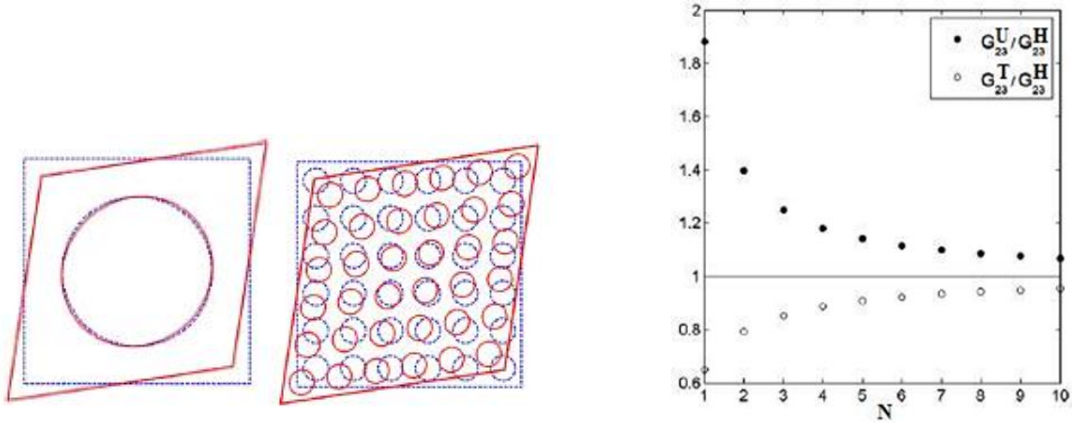
Indeed, the mean elastic mechanical properties obtained with KUBC loading always overestimates the real elastic properties, *i.e.* obtained with **periodic boundary conditions**, and are considered as **an upper boundary**. On the contrary, the mean elastic mechanical properties obtained with SUBC loading always underestimates the real elastic properties. Hence, it is considered as **a lower boundary**. Equation 2.17 summarises this paragraph, in terms of positive-definite quadratic forms of fourth order elasticity tensors.

$$\overline{\mathbb{C}}^{SUBC} \leq \overline{\mathbb{C}}^{PERIODIC} \leq \overline{\mathbb{C}}^{KUBC} \quad (2.17)$$

The values obtained with the KUBC and SUBC loading are strongly dependant on the RVE's size. Indeed, despite being bounded, the upper and lower bounds of the elastic properties get closer to the periodic solution as the size of the RVE grows. As a matter of fact, when the RVE size increases, the microscopic mechanical fields intensity decreases until becoming negligible compared to macroscopic fields and thus reducing the difference between the bounds. Figure 2.7b obtained from Czech [144] shows a typical homogenised mechanical property evolution with regard to size. Figure 2.7a shows the homogenised pattern's size evolution: a unidirectional composite with an increasing number of fibers and with its matrix.

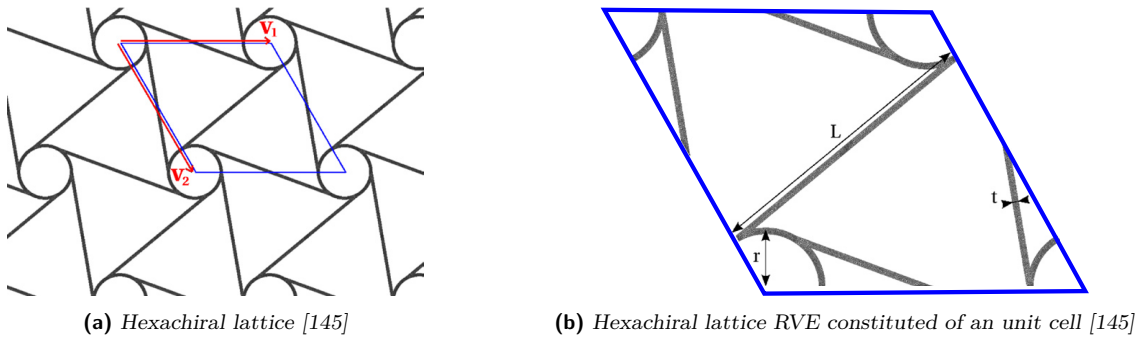
The KUBC and SUBC methods are very useful for determining the minimum size needed for a random media to start having mean mechanical fields, where microscopic field effects start being negligible. Nonetheless, for periodically organised materials such as architected materials, their properties can be just determined with one unit cell used as a RVE [145], [146]. Figure 2.8 shows an example of a RVE composed of one unit cell with a hexachiral lattice. However, for homogenising the properties of an architected material unit cell, periodic boundary conditions need to be applied on the boundaries of the cell.

Periodic Boundary Conditions: The displacement field $\mathbf{u}(\mathbf{x})$ over the boundary



(a) Composite fiber and matrix homogenisation unit cell and 6x6 size composite RVE (b) Homogenised elastic rigidity coefficient G_{23} ratio: KUBC and SUBC value over the periodic value G_{23}^H

Figure 2.7. Homogenisation of a composite material [144]



(a) Hexachiral lattice [145] (b) Hexachiral lattice RVE constituted of an unit cell [145]

Figure 2.8. Hexachiral lattice and its associated RVE [145]

$\partial\Omega$ takes the form:

$$u(x) = \bar{\varepsilon}x + \tilde{u}_P(x) \quad \forall x \in \partial\Omega \quad (2.18)$$

Contrarily to the KUBC boundary conditions, the microscopic displacement fluctuation $\tilde{u}_P(x)$ is non-null. However, this microscopic displacement field is expected to be canceled on the whole domain's boundary $\partial\Omega$. The stress vectors are also considered to be anti-symmetric on the whole domain's boundary $\partial\Omega$ under periodic boundary conditions.

The methodology used for solving periodic homogenisation problems is the same as the methodology used for solving KUBC and SUBC problems: selection of a strain or stress uniform loading, division of the problem into six simpler problems, solving the small problems and finally estimating the mean periodic elastic tensor $\bar{\mathbb{C}}^{PERIODIC}$. The only difference is the presence of periodic boundary conditions on the domain's bound-

ary. These periodic boundary conditions purpose is to mimic the reaction to the uniform loading of an infinite number of neighboring cells.

For showing how, in practice, periodic boundary conditions are to be applied, a periodic homogenisation problem of a regular hexagonal honeycomb will be considered. Figure 2.9 shows the homogenisation problem. When applying periodic boundary conditions, the RVE must have periodicity vectors (red and blue vectors on Figure 2.9b) that show the periodicity directions and link the two faces that have periodic points (red and blue faces on Figure 2.9b). On associated periodic faces, each point on a face and its symmetric associated point on the other face have a constraint displacement. On Figure 2.9b, the points A and B on the red faces will be taken as examples.

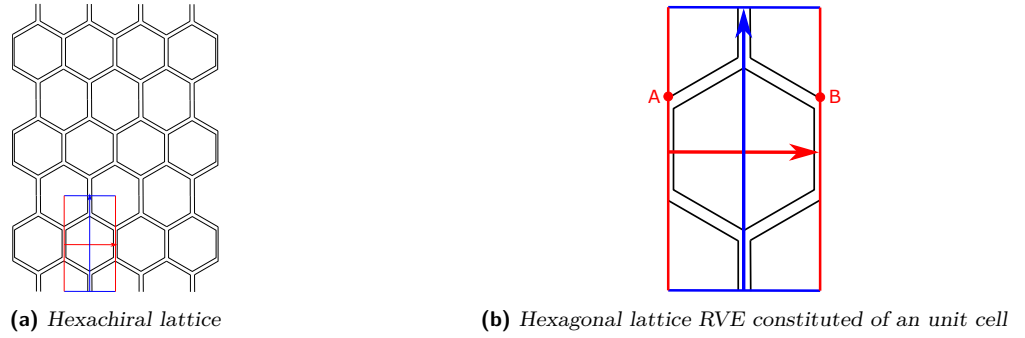


Figure 2.9. Hexagonal lattice and its associated RVE

By applying conditions of periodicity on points A and B, Equation 2.19 can be obtained.

$$\begin{aligned} u(x^A) &= \bar{\varepsilon}x^A + \widetilde{u}_P(x^A) \\ u(x^B) &= \bar{\varepsilon}x^B + \widetilde{u}_P(x^B) \end{aligned} \quad (2.19)$$

Nevertheless, because both points have their displacement constrained, the microscopic displacement of these points nullify each other (see Equation 2.20). Thus, the final displacement constraint between the two points can be written in the form presented in Eq. 2.21. Hence, by combining the application of these constraints on the hexagonal RVE's boundaries, in addition to regular mean strain or stress boundary conditions and the application of the KUBC or SUBC homogenisation method, the mean periodic elastic tensor $\overline{\mathbb{C}}^{PERIODIC}$ can be estimated.

$$\widetilde{u}_P(x^A) = -\widetilde{u}_P(x^B) \quad (2.20)$$

$$u(x^A) - u(x^B) = \bar{\varepsilon}(x^A - x^B) \quad (2.21)$$

The KUBC, SUBC and Periodic boundary conditions methods for solving homogenisation problems have been implemented on the commercial software *Abaqus* through the addition of a plugin called *Micromechanics* developed by Dr. Ross McLendon [147]. This plugin has been tested essentially for RVEs of composites [148]–[150], but it was not tested for RVEs of cellular materials yet, at the best knowledge of the author at the moment of the thesis’ writing.

Thus, in the next section, the predictive abilities of the *Micromechanics* plugin will be tested with a test case from the literature.

Abaqus Micromechanics periodic homogenisation validation

To validate the efficiency of a new homogenisation strategy that we developed on the Abaqus Micromechanics plugin, it has been chosen to homogenise periodically a hexagonal cell with thick vertical walls (see Figure 2.10a). The geometric parameters of this hexagonal cell are given in Table 2.10b. The 9 coefficients of elasticity have already been homogenised by Catapano and Montemurro and they have already compared them to the literature [151].

This model was reproduced in Abaqus. The material used for this simulation and in the paper of Catapano *et al* is aluminum [151], for which the mechanical properties are given in Table 2.1. 39 060 quadratic hexaedric elements were used for developing the finite element mesh of this model, on which periodic boundary conditions were applied.

Mechanical property	Young’s modulus	Poisson’s ratio
	(MPa)	(-)
value	70 000	0.33

Table 2.1. Mechanical properties of isotropic aluminum

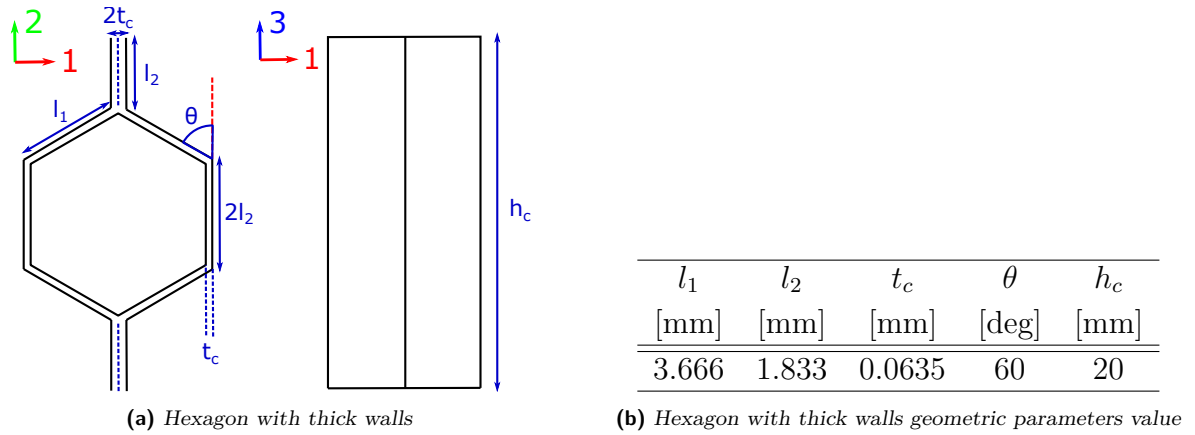


Figure 2.10. Hexagon with thick walls geometry and parameters value [151]

The results of this homogenisation model are shown in Table 2.2, where these results are compared with Catapano *et al* [151]. From Table 2.2, it can be seen that most of the elastic coefficients obtained with Micromechanics have a difference located between 0% and 6% compared to the results of Catapano *et al*, which represents a small difference for elastic coefficients. Only the shear coefficient G_{12} has a difference of 12% compared to values obtained by Catapano *et al*. This difference can be considered as acceptable for engineering problems.

Elastic coefficient	Micromechanics values	Catapano <i>et al</i> [126] values	Difference (in %)
E_1 [MPa]	0.938	0.884	6.1
E_2 [MPa]	0.954	0.918	3.9
E_3 [MPa]	1835	1812	1.3
G_{12} [MPa]	0.558	0.640	12
G_{23} [MPa]	260	263	1.1
G_{13} [MPa]	394	391	1.0
ν_{12}	0.990	0.980	1.0
ν_{23}	1.69×10^{-3}	1.61×10^{-3}	5.0
ν_{13}	1.71×10^{-3}	1.67×10^{-3}	2.4

Table 2.2. Results of the homogenisation numerical model

Thus, it can be concluded that the plugin Micromechanics is reliable for estimating

the mean elastic coefficients of a RVE. Micromechanics can be reused later on for homogenising the mechanical properties of new patterns. Nevertheless, **if the patterns are used inside a structure, what would be the difference in macroscopic structural properties (e.g. the structure’s stiffness) if a continuous homogenised material is used instead of the original architected material?** If differences are observed, **how many pattern would be needed to obtain a negligible difference between a continuous homogenised material and the original architected material?**

Before being capable to answer these questions, one must be able to know the microscopic elastic tensor $\widetilde{\mathbb{C}}(x)$, *i.e.* the bulk material’s mechanical properties and manufacturing processes influence over it, for being able to carry out homogenisation successfully. To do that, the manufacturing process of mechanical cellular materials has to be explored in the literature.

2.1.3 3D printing processes

In the literature, most of promising mechanical cellular materials have been manufactured through **additive manufacturing** also called **3D printing** [46], [152]. Since the 2000s, multiple technologies arised using multiple types of materials. Additive manufacturing is being popular for manufacturing cellular materials for its ability to create complex geometric shapes [46]. Moreover, the other advantages of additive manufacturing processes compared to regular manufacturing processes are the low manufacturing cost per part and the wide choice of materials available for building structures.

For instance, some cellular materials are manufactured by using metals as bulk materials [152]–[154]. The most popular process for metal 3D printing is known as the **laser powder bed fusion**. For manufacturing a part with this process, metal powder layers are added on the printer’s plate and melted with a laser. The advantages of parts manufactured with this process compared to other additive manufactured parts are their good mechanical properties processes [155]. Indeed, material rigidities close to 100 GPa are currently only attainable with 3D printed composite parts [156], [157]. However, the main drawbacks of this process are its parts rough surface quality, the local geometry distortion of these parts and more importantly the presence of porosity decreasing the parts mechanical properties. To overcome those issues, alternative chemical based metal additive manufacturing processes are being developed and tested [153]. These processes

are being widely used for aeronautical structure manufacturing [158], because of the good mechanical properties of the manufactured parts. It can be interesting to use this process for manufacturing our cellular morphing hydrofoil; using metal as the bulk material can give enough stiffness to the structure to withstand hydrodynamic pressure. However, using metal as the bulk material makes the cellular hydrofoil heavy.

Yet, the most popular 3D printing technologies are polymeric based additive manufacturing processes [159]–[161]. The popularity of the process can be explained by the low price of 3D-printing machines and materials needed for polymeric 3D-printing and also by the printers size variability. These sizes can go from small home-scaled printers to factory-scaled printers used for manufacturing large parts. However, this process is essentially used for prototyping and manufacturing small lightweight parts. There are multiple types of existing processes, but the two most common ones are stereolithography (SLA) and the **Fused Filament Fabrication (FFF)** also called the **Fused Deposition Modeling (FDM)**. The **FFF** manufacturing process is shown on Figure 2.11. The polymer material used for printing is wound up a spool as a filament. This filament is then brought up in the extruder with gear wheels. Afterwards, the filament is moved to the nozzle where the filament is heated to its melting temperature to transform it into a viscous fluid state. Finally the filament goes out the nozzle and is deposited on a heated plate, which is set at a temperature close to the glass transition temperature T_g of the polymer.

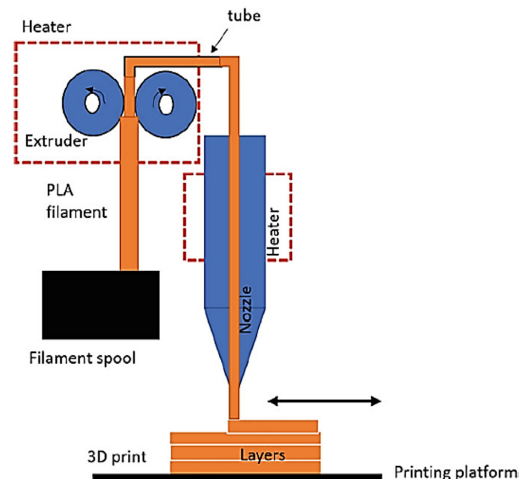


Figure 2.11. Fused Filament Fabrication (FFF) process [162]

Stereolithography (SLA) process is closer to metal 3D printing where a liquid resin

is brought up to a laser with a piston-and-platform system. The laser then solidifies progressively the resin to fabricate the part [163]. The parts manufactured with these two processes exhibit radically different mechanical properties: the polymeric parts manufactured with stereolithography exhibit isotropic mechanical properties with low porosity, whereas FFF parts exhibit a strong anisotropy and high porosity [164]–[166]. Compared to metal and concrete 3D printing, a decrease in mechanical properties is exhibited by these 3D-printed polymeric parts [164], [165].

Nevertheless, the mechanical properties of SLA and FFF processed parts can be enhanced by adding reinforcements such as short glass or carbon fibers or nano-compounds [167]–[169]. Despite the increase of mechanical properties, 3D-printed parts with nano- or short fibers reinforcements are still far from the mechanical properties of metal 3D printed parts or of more conventional processed parts [167]–[169]. For that reason, continuous fibers such as carbon, glass or basalt are now combined to polymeric 3D printed parts for improving their mechanical properties [168], [170]. However, it is for the **FFF** process that the neatest increase in mechanical properties are obtained [170]–[172]. These parts exhibit very good mechanical properties, close to metal 3D printed parts, and have the advantage of being more lightweight than the latter. In addition, the price of manufacturing machines and materials are less important for continuous fiber-reinforced polymer (CFRP) parts than metallic printed parts. For these reasons, the **Fused Filament Fabrication (FFF)** process seems to be the more promising process for manufacturing the cellular passive hydrofoil concept and will be considered and studied deeply for being able to manufacture this concept.

Before investigating the manufacturing of the morphing concept, the different parameters tailoring a part 3D printed by the FFF process must be known. For identifying those parameters, it is important to know the different procedures that are needed for parameterising the 3D printing process of a part. Figure 2.12 shows the overall procedure. Figure 2.12 shows that, in a first step, the part is designed in a **CAD software** where its geometry and size are defined. Then, in a second step, this CAD file is saved in an STL format that will be read by a software called **Slicer**. The slicer is used for partitioning the part into a finite number of layers and to define several manufacturing parameters of the part. These manufacturing parameters are numerous: the layer height, the printing speed, the presence and orientation of printing infill, the presence of part supports or the

nozzles trajectory paths.

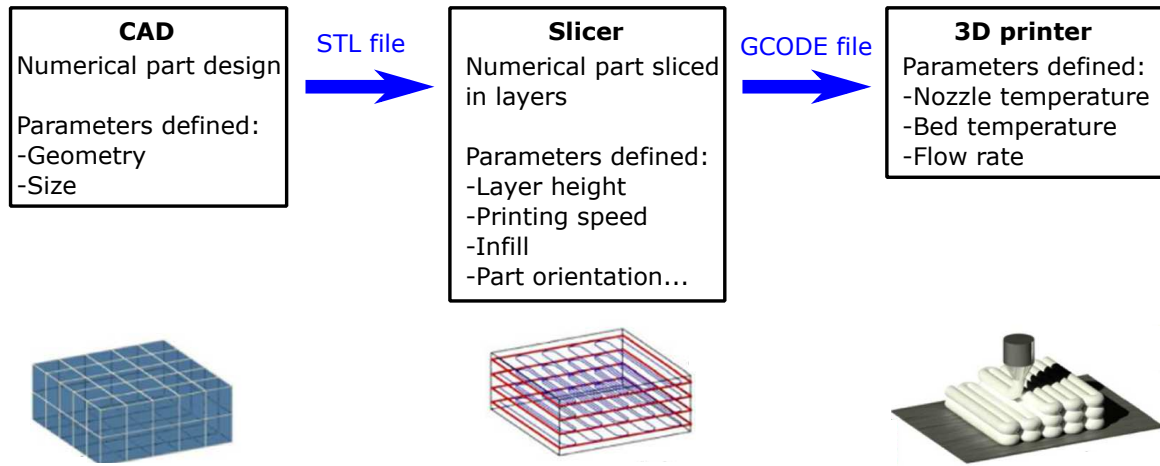


Figure 2.12. Procedure for parametrizing 3D printing [173]

Figure 2.14 tries to illustrate and summarise the different parameters involved here. The final aim is to define a manufacturing strategy for the 3D printer. Once finished, this strategy is stored into a GCODE file that has numerous instructions following the manufacturing strategy. Finally, this GCODE file is sent to the 3D printer for manufacturing. Depending on the type of printer used (*e.g.* Ultimaker 2), several parameters are tunable directly on the printer such as the nozzle temperature, the bed temperature or the flow rate.

As stated above, multiple parameters can be tuned in the slicer and the printer for 3D-printing a part: the filaments layer height (see Figure 2.14d), the nozzle temperature, the plate temperature, the nozzle displacement speed, the flow rate or the presence of fan cooling (see Figure 2.14c). These parameters have broad impacts on the final part obtained, going from final part's manufacturing quality to the part's mechanical properties [162], [174]–[177]. Some of these parameters have a role in the apparition of geometric defects. Figure 2.13 shows common 3D printing defects. The most common defect is depicted in Figure 2.13a, it is **3D printed part warping**, this warping is mostly present because of internal residual stresses developing in the printed layer, while it is cooling just after deposition [174]. However, it can also be caused by low bed temperature that leads to poor part adhesion [175]. Indeed, if the bed's temperature is below the polymer's glass transition temperature, a poor adhesion between the part and the plate is observed. Thus,

the parameters influencing this warping are the nozzle temperature, the bed temperature, the printing speed and the presence of fan cooling [174], [178]. For avoiding it, one strategy consists in avoiding to set the bed temperature to be high enough for releasing the material's residual stress, but not too much for avoiding material's creep, and using small fan cooling for controlling stress relaxation speed rate [178].



(a) Local 3D printed part warping [178]

(b) 3D printed part stringing issues [179]

(c) 3D printed part dimensional inaccuracies [180]

Figure 2.13. Most common 3D printing manufacturing defects

Figure 2.13b shows an other very common defect known as **oozing or stringing**. This defect appears during the nozzle's travel between two parts (*e.g.* on Figure 2.13b, between the two pillars). During the travel the polymer remains in a too liquid state and still comes out of the nozzle, without being pushed by the printer's gears. This leads to the appearance of white strings where the nozzle traveled, hence the name **stringing**. This defect is fixable through the adjustment three parameters: the material's weight, temperature and the filaments retraction length [179].

Indeed, if the material is printed at a high temperature (*i.e.* generally above 220°C), the filament is in a liquid state and goes out of the nozzle more easily [179]. Moreover, in a state where the filament is heated at a high temperature, the heavier the filament is, the more stringing is to be observed [179]. To overcome these issues and being able to print at high temperatures, the retraction length of the filament can be tailored (see Figure 2.14a). This parameter controls the length of filament that is rolled up by the gears, after finishing a layer or before starting to travel. The study of Haque showed that if this parameter is well chosen, according to the temperature and the filament's weight, the stringing effect decreases [179].

Finally, Figure 2.13c shows another common defect of 3D printed parts, which is the dimensional inaccuracies. Indeed, printed parts do not have the same dimensions as the ones displayed on the slicing software after being manufactured. The geometric parameters control is a complex issue where multiple parameters are involved. The first major sources of dimensional imprecision are the printer's bad calibration, such as improper bed leveling, extrusion miscalibration or bad part tessellation when exported into an STL file [175].

Apart of these miscalibration issues, Hernandez pointed out the influence of four other parameters influencing part precision: outer shells thickness (see Figure 2.14b), the printing speeds, the part's size and the part's geometry [175]. Considering only the two first parameters' influence on the final part precision is not statistically significant, however they become significant when they are coupled with variation of size or geometry [175]. Indeed, in this study, it was shown that for small objects with large outer shells (relatively to the part's size), faster printing speeds give a better dimensional precision to the part. On the contrary, for bigger parts slower printing speeds and small outer shells gave a better dimensional precision to the part [175].

Even if it can be considered as counter-intuitive at first sight, this can be explained by the fact that for smaller parts, lower printing speeds make the hot printhead linger next to the previously deposited material. Hence, the proximity of the heated nozzle with previously deposited material leads to its melting and thus, the dimensional expansion of this material [175]. This effect is even more emphasized with geometry variations. Indeed, it is statistically more pronounced for circular shapes, rather than straight lines. There is an inherent inaccuracy of the FFF 3D printing process when arcs are manufactured: more material is deposited in the inside of the circle rather than on the outside [175]. This effect becomes less significant when part's size increases [175].

When cellular materials are manufactured through the FFF process, mastering these manufacturing defects is crucial, especially the dimensional errors. Actually, compliant cellular material's walls often behave like thin Bernoulli beams [108], with a width located between 0.5 mm and 2 mm and with a cell length located between 5 mm and 30 mm. Thus, the dimensional inaccuracies depicted earlier impact the cellular materials importantly. Former articles have estimated the absolute precision of FFF printed part to 0.16 ± 0.009 mm at best [186]. The relative error of the 3D printed parts width, according

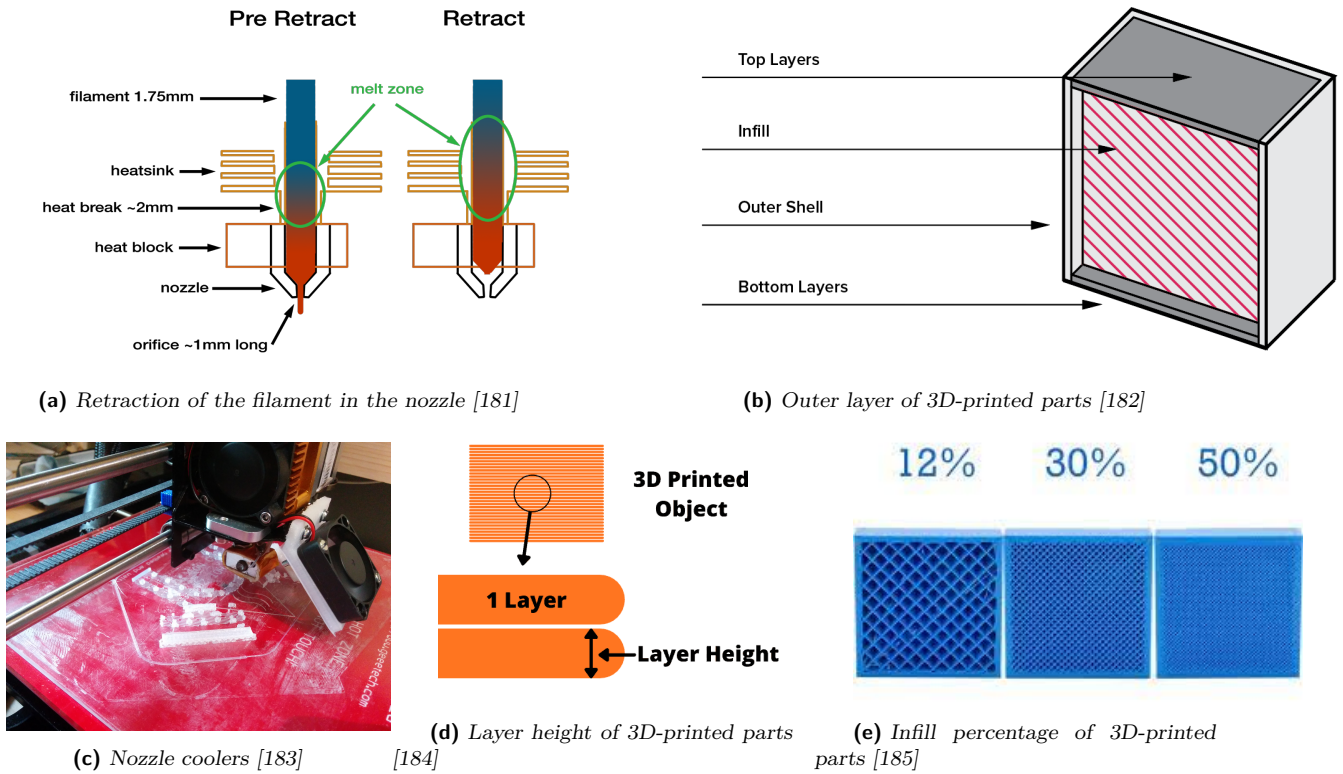


Figure 2.14. Summary of the main 3D-printing parameters influencing the part's dimensional quality or its mechanical properties

to the previously fixed interval, is located in an interval of [8%, 32%]. Assuming that the cell wall has a rectangular section, according to Equation 2.22, when the beam is submitted to an external force, its flexural stiffness EI depends on the cube value of the beam's width b . In Equation 2.22, d is the beam's displacement, E is the bulk material's rigidity, I is the beam's second moment of inertia, b is the beam's width and c is the beam's depth. Depending on the manufacturing error value, the displacement error value and thus the cellular material's final rigidity error value varies from 25% up to 130% of the expected displacement or rigidity value.

$$d = f(EI)$$

$$I = \frac{b^3c}{12} \tag{2.22}$$

Thus, when a 3D printed cellular material or cellular structure is manufactured through

FFF and is then characterised experimentally and modeled numerically, the variability of its walls width needs to be estimated precisely. Nonetheless, in addition to these geometric defects, the 3D printing process induces the presence of porosity inside the 3D printed material and induces anisotropy through the filament directional deposition [187], [188]. These two process induced properties are interdependent and have an impact on the mechanical properties of the 3D printed material [187], [188]. Furthermore, the presence of porosity and the degree of anisotropy are influenced by numerous slicing and printing parameters [189]–[191].

The temperature extrusion, the temperature bed and the cooling conditions stated above as influencing part warping also influence the level of cristallinity of the polymer for thermoplastics, the polymer filaments bonding and thus the mechanical properties [174]. However, the nozzle temperature must be adjusted carefully, as too high nozzle temperatures can lead to dimensional inaccuracies [174]. For manufacturing cellular structures, the printing speed is also a crucial parameter as it has a direct impact on the cellular material's dimensions precision. In addition to this, the printing speed also affects the mechanical properties of the 3D printed part, the part's tensile and flexural modulus and strength decrease with the increase of printing speed [176]. This decrease in tensile and flexural properties with printing speeds seems to be due to the increase in porosity in the 3D-printed part's structure [187]. Indeed, when the printing speed increases, the part is less exposed to high temperatures, resulting in a lower material expansion and thus more void [187]. Hence, the printing's parameters value must be set precisely, when printing cellular structures, in order to minimize dimensional errors while maintaining decent mechanical properties.

Nevertheless, in the same study, Christiyan *et al.* showed that the effect of printing speed can be overshadowed by the effect of a higher layer thickness [176]. As a matter of fact, the maximum tensile and flexural strengths decreased with the increase of the layer height [162], [176]. Besides the layer height, slicing parameters in general have a critical importance for ensuring good mechanical properties to the 3D printed parts [174]. The most important ones being the layer height, the infill percentage (see Figure 2.14e), and the infill raster angle (see Figure 2.15) [174].

The infill has a direct link with the part's mechanical strength and stiffness. Indeed,

multiple parameters are tailorable with the infill: the density and the pattern. Obviously, the infill density directly dominates the mechanical properties of the 3D-printed part [192]. The denser the infill is, the better the mechanical properties are [192]. Indeed, the best mechanical properties are attained for infill density superior to 100%, where the polymer filaments of printed layers overlap, reducing the part's porosity [174]. In FFF, multiple pattern geometries are available in slicing softwares: hexagonal, or linear patterns [192]. The infill's pattern seems to play a significant role in the mechanical properties exhibited by 3D-printed parts [192], [193].

Finally the infill's raster angle is also widely studied in the literature [194]–[196]. The raster angle is defined as the angle between the X-axis of the 3D printer and the deposited filament as shown in Figure 2.15. The best mechanical properties are obtained when the 3D-printed part is loaded along the raster angle orientation [177], [197]. When the loading is not parallel to the raster angle orientation, the bonding areas between deposited polymer beads get loaded which affects mechanical properties negatively [174], [177]. These mechanical properties disparities are due to the process induced anisotropy [174], [177].

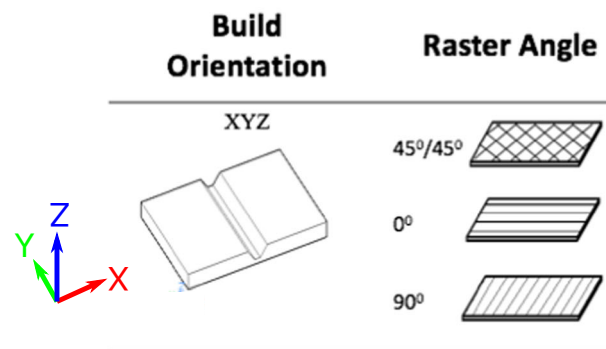


Figure 2.15. Raster angle of a 3D printed layer [198]

In this section, the *Fused Filament Fabrication* process has been presented. It induces multiple changes to the final manufactured part, such as microstructure changes, by introducing porosity and anisotropy, and it also alters the part's final dimensions and geometry. These elements are influenced by a great number of printing parameters. Furthermore, these altered bulk material's mechanical properties and the part's geometry have a tremendous impact on global mechanical properties of the 3D-printed part. Thus, if cellular materials are manufactured with the FFF process, according to what has been

said in this Section and in Sections 2.1.1 and 2.1.2, this can have tremendous effects on their global mechanical properties. **Thus, it would be interesting to know how to quantify and control these different process induced properties on the final cellular structure. And also to seek how these process induced properties can be taken into account in a numerical model.** Indeed, while developing our morphing concept, taking the porosity and process induced anisotropy in the cellular morphing hydrofoil into account is essential to predict and to simulate reliably its mechanical behavior.

To summarise the objectives of this chapter, the global aim of this section is to investigate the passive morphing mechanism developed by Bornengo [47]. This morphing concept is constituted of a cellular architected core and a surrounding skin. Depending on the concepts considered, the cellular core can be at a material level scale [47] or a structure level scale [69], [76] (cf. Section 2.1.2) and the surrounding skin can be continuous around the core [76] or discontinuous [47], [69]. Depending on the concepts, different core behaviors of the core can be observed: the main deformation mechanism governing morphing is either tensile dominated [47], [69] or shear dominated [76]. Thus, the global objective of this chapter will be to address two questions: **what are the critical parameter(s) influencing the core's deformation mode when the morphing structure is bent? What are the observable differences for the tension (compression) dominated deformation core and the shear dominated deformation core?**

As shown in this introductory section, for investigating the behavior of structures with cellular materials, a multi-scale approach is needed to take into account the impact of the bulk material and the geometric pattern of the cellular material on the global structural mechanical properties. Here, three scales are considered:

- **The microscopic scale**, where the mechanical properties of the bulk material are characterised
- **The mesoscopic scale**, where the influence of the cellular pattern's geometry on local deformation mechanism and on elastic properties is studied
- **The macroscopic scale**, where the global behavior of cellular beams is analysed, compared and discussed through the different scales

The passive morphing airfoil problem exposed before can be reduced to a cantilever beam bending problem [141], [199]. In this study, a two-step-investigation-strategy is con-

ducted. In a first step, a numerical and experimental multi-scale analysis is performed with four different patterns and 3D printed cellular beams tested in a 3 points bending configuration. This analysis is used to study the beam's flexural behaviour by isolating and quantifying all internal parameters that have an influence on the beam's flexural properties. The three scales previously presented are studied. In a second step, the numerical models developed at the macroscopic scale are used on cantilever beams, as representation of morphing airfoils cambering and decambering. The effect of the skin's stiffness and of the cellular core's cell size is discussed with these results.

To do that, minor issues have to be solved. The first one consists in finding **how to take into account the process induced porosity and anisotropy in the 3D printed structures**. Thus, the data obtained experimentally at the microscopic scale will be used in the numerical model used for the multi-scale analysis. Then, the results obtained numerically at the macroscopic scale for the cellular beams tested in a 3 points bending will be compared to the experimental results obtained at this scale for assessing of the effectiveness of the modeling method employed. The second one consists in knowing **if a homogeneous equivalent material used for modeling the cellular core is able to display similar mechanical behavior as the non-homogeneous cellular core**. Cellular beams with various unit cell size of the core and with different skin rigidities are tested numerically in a cantilever configuration to provide enlightenment on this issue. The results obtained will then be compared to a beam with a homogeneous equivalent material used as the beam's core.

2.2 Materials and methods

2.2.1 Material

We use an injection moulded co-Polyester (CPE) polymer supplied by Ultimaker. Its mechanical properties can be found in Table 2.3.

Young's modulus (MPa)	Yield strength (MPa)	Poisson's ratio (-)	Density (g.cm ⁻³)
1900	50	0.44	1.27

Table 2.3. Mechanical properties of isotropic injection molded CPE's [200]

2.2.2 Manufacturing of tensile samples and cellular beams

The process used for sample fabrication is a fused filament fabrication (FFF) process, a 3D printing technique. The 3D printing machine is an Ultimaker 2 and the slicing software is Cura 4.0. The printing parameters of the samples are given in Table 2.4.

Layer height	Nozzle temp.	Plate temp.	Cooling	Flow	Print speed	Nozzle diameter	infill overlap
0.2 mm	255 °C	85 °C	OFF	108 %	60 mm/s	0.4 mm	6 %

Table 2.4. Printing parameters used (<https://ultimaker.com/> last connection on September 9th 2020)

As explained in Section 2.1.3, dimensional precision is very important for cellular materials. Thus, these printing parameters were chosen to print a sample as fast as possible while keeping unit cells dimensional inaccuracies low, without defects and with smooth surfaces. In the parameters shown in Table 2.4, the *Flow* (flow rate) and *infill overlap* values were set for different reasons. They were set to guarantee that the infill density is theoretically superior to 100% and guaranteeing a good cohesion between the different polymer strings. Indeed, the *infill overlap* value of 6% means that 6% of the printed filament's volume will be shared with other filaments. In the same way, the *Flow* value ensures that supplementary materials will be extruded for promoting this bonding. The printing duration varied from 30 minutes up to 1 hour for tensile samples and from 8 hours up to 12 hours for beams. The dimensions of the beams were set to $250 \times 50 \times 10$ mm³ (see Figure 2.16). The beam's length L and its height d were set to maximise the beam's aspect ratio L/d , in the technical limits available, *i.e.* the printer's plate size of 200×200 mm², and for having three unit cells in the vertical direction.

Figure 2.16 shows the dimensional parameters of the cellular beam and their numerical values. The depth t was set to optimise the printing time. In addition, CPE polymer

skins have been set on the top and the bottom of the beam. These skins act as continuous surfaces for the rollers to apply loads efficiently for the 3 points bending tests. Their thickness b is 2 mm.

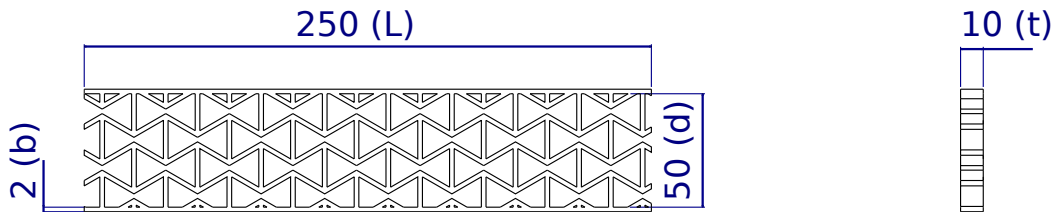


Figure 2.16. Dimensions of all cellular beams (reentrant pattern example)

2.2.3 Microscale: Experimental mechanical characterisation of the material

The elastic properties of the 3D-printed CPE have been characterised in longitudinal tension, transverse tension and in-plane shear with filaments oriented at 0 , 90 and $\pm 45^\circ$ with respect to the loading direction. Three types of samples were printed following ISO-527-B (tensile tests) and ISO-14129 (shear tests). For each filament orientation, 5 specimens have been manufactured and tested (Instron 5566; load cell 1 kN). A biaxial extensometer was fixed on tensile samples to measure longitudinal and transverse displacements and compute classically the associated strains. According to ISO-527-B, the 0 and 90° samples tensile moduli were calculated by linearly fitting the stress and the strain measured values. The Poisson's ratios were determined by dividing the measured values of the transverse and longitudinal strains (strain interval between 0.05% and 0.25%). The Yield strength $R_p^{0.2\%}$ was classically determined from the stress-strain curve with a 0.2% offset. For shear samples, the shear strain is $\gamma = \epsilon_1 - \epsilon_2$, where ϵ_1 and ϵ_2 are the axial and transverse tensile strains, respectively. The results of these tests are presented in §2.3.1.

2.2.4 Microscale: Experimental porosity measurement of the 3D printed material

Porosity measurements were also conducted in this experiment. To measure it, for each filament orientation, 5 small 3D printed blocks were cut in tensile samples, whose

dimensions were set to $10 \times 4 \times 20 \text{ mm}^3$. After being cut, the density of the 3D printed sample was measured with specific gravity analysis measurements. Figure 2.17 shows how specific gravity analysis measurements are carried out.

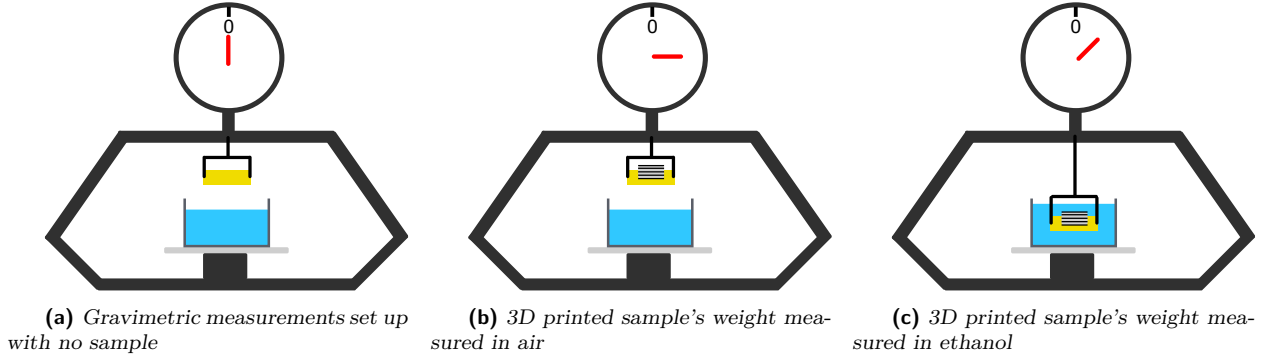


Figure 2.17. Gravimetric measurements experimental set-up

Firstly, the 3D printed rectangle's mass M_{air} (see Figure 2.17b) is measured in air and then the mass $M_{ethanol}$ is measured in ethanol (see Figure 2.17c). With the help of Equation 2.23, the experimental 3D printed part density is calculated with the previously measured data. In Equation 2.23, $\rho_{3D \text{ printed}}$ is the density of the 3D printed material, $\rho_{ethanol}$ is the density of ethanol estimated at 789 g.cm^{-3} at 20°C and ρ_{air} is the density of air estimated at 1.3 g.cm^{-3} .

$$\rho_{3D \text{ printed}} = \frac{M_{air}}{M_{air} - M_{ethanol}}(\rho_{ethanol} - \rho_{air}) + \rho_{air} \quad (2.23)$$

Finally, this density is compared to the theoretical density value $\rho_{CPE \text{ th}}$ of the transparent CPE given in Table 2.3 and is used for calculating the porosity p in Equation 2.24.

$$p = 1 - \frac{\rho_{3D \text{ printed}}}{\rho_{CPE \text{ th}}} \quad (2.24)$$

2.2.5 Mesoscale: Selection of pattern

Four types of cellular patterns were selected: a hexagonal re-entrant honeycomb, a swastika pattern, a double-arrow shaped pattern and a hexachiral pattern (see Figure 2.18).

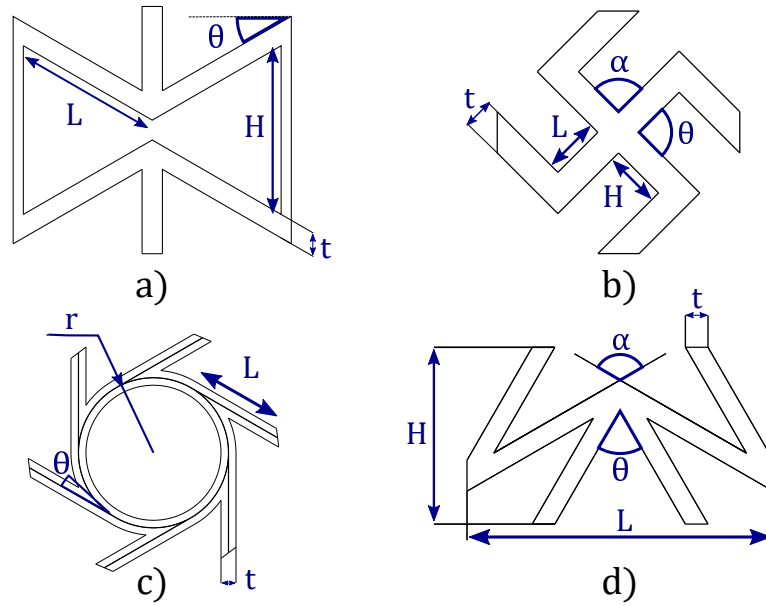


Figure 2.18. Cellular material's unit cells tested a) Reentrant b) Swastika c) Hexachiral d) Double-arrow head

The designs of the four cellular patterns were selected for: (i) their auxetic properties (except for the swastika pattern, all cellular materials exhibit a negative Poisson's ratio); (ii) their different shear rigidities that are related to auxeticity [47], [69]; (iii) their compliance for morphing [47], [69], [76]. The pattern compliance was estimated with the Maxwell's connectivity and stability criterion [201]. This criterion is regularly used to determine the structural stability of rigid truss structures. Eq. (2.25) gives the condition for 2D pin-jointed frames made out of b struts and j joints to be both statically and kinematically determinated, Eq. (2.26) gives the same kind of information for the 3D case.

$$M = b - 2j + 3 = 0 \quad (2.25)$$

$$M = b - 3j + 6 = 0 \quad (2.26)$$

The structural behaviour of the cellular solid is then determined with the obtained results from Eq. (2.25) or (2.26) (see Figure 2.19).

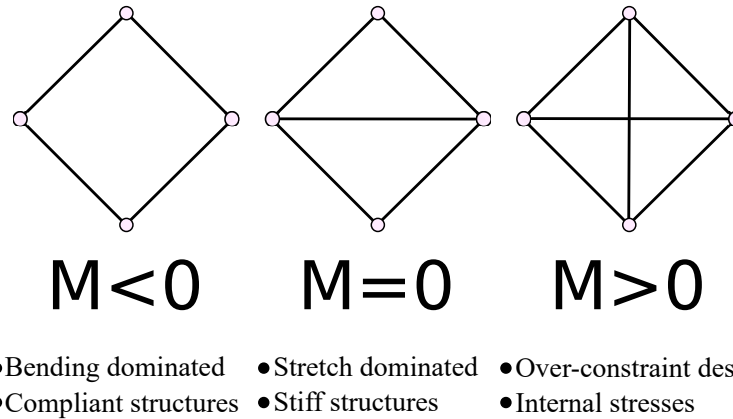


Figure 2.19. Structures type determination with Maxwell's criterion, image adapted from [109]

All previously cited cellular patterns exhibit a negative M value (see Figure 2.19). After selecting these cellular materials, their geometrical parameters have been precisely set so that every unit cell has a relative density of approximately 0.3 (see Table 2.5). This was done to reduce the contribution of mass on the mechanical properties. The limit value of 0.3 for the relative mass has been chosen for manufacturing constraints.

	b	j	M	L	t	α	θ	H	R
	-	-	-	(mm)	(mm)	(deg)	(deg)	(mm)	(mm)
Reentrant	6	6	-3	15	2.05	-	-30	17	-
Swastika	12	12	-9	5	1.7	-	90	5	-
Double arrow	4	4	-1	25	1.6	120	60	-	-
Hexachiral	6	6	-3	16	1.6	-	30	-	6

Table 2.5. Geometrical properties of different shapes, see main text for the definition of parameters

2.2.6 Mesoscale: Estimation of unit cells properties

For every cellular pattern, numerical homogenisation was used to estimate their elastic properties: E_x , E_y , G_{xy} and ν_{xy} (in the axis system presented in Figure 2.20) using Abaqus software v.6.17.

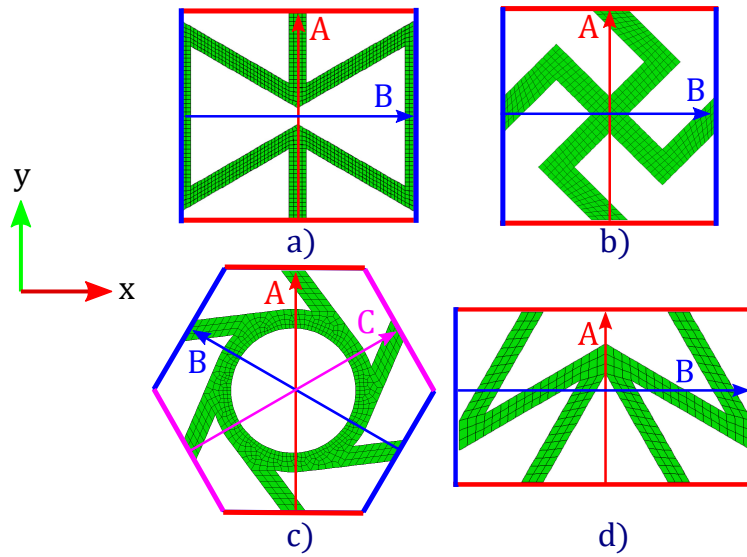


Figure 2.20. The different Representative Volume Elements, their vectors of periodicity (A,B and C) and their periodic boundaries. a) Reentrant b) Swastika c) Double-arrow d) Hexachiral

Periodic and stress driven boundary conditions have been set on the unit cell of each pattern. The mechanical homogenisation was carried out with the Abaqus Micromechanics Plugin. This plugin automatically sets the periodic boundary conditions and the stress-driven boundary conditions. It also automatically solves the finite elements models and post-treats the finite elements results to display the patterns deformations and elastic coefficients. However, for that to work, it is needed to provide an already meshed pattern and specified locations for applying periodic boundary conditions. Figure 2.20 displays the different vectors of periodicity and the periodic boundary conditions. 3D quadratic finite elements with full integration were used. For the reentrant, swastika, double arrow and hexachiral cellular patterns, the number of quadratic elements used for each pattern is 19 194, 10 600, 3 354 and 9 588 respectively. The stress driven boundary conditions values imposed at periodic boundaries are 23 MPa, 18 MPa, 11 MPa and 30 MPa respectively.

The material properties of the different Representative Volume Elements (RVE) were modelled in two steps to account for anisotropy. Firstly, local coordinate systems have been set on each RVE to suit the anisotropic properties of printed polymer. For each RVE, Figure 2.21 displays local axis systems. The longitudinal direction corresponds to the direction of the fused filament filling. Secondly, the material elastic properties are those of a linear transversely isotropic elastic behaviour introducing 5 independent elastic constants (see § 2.2.3).

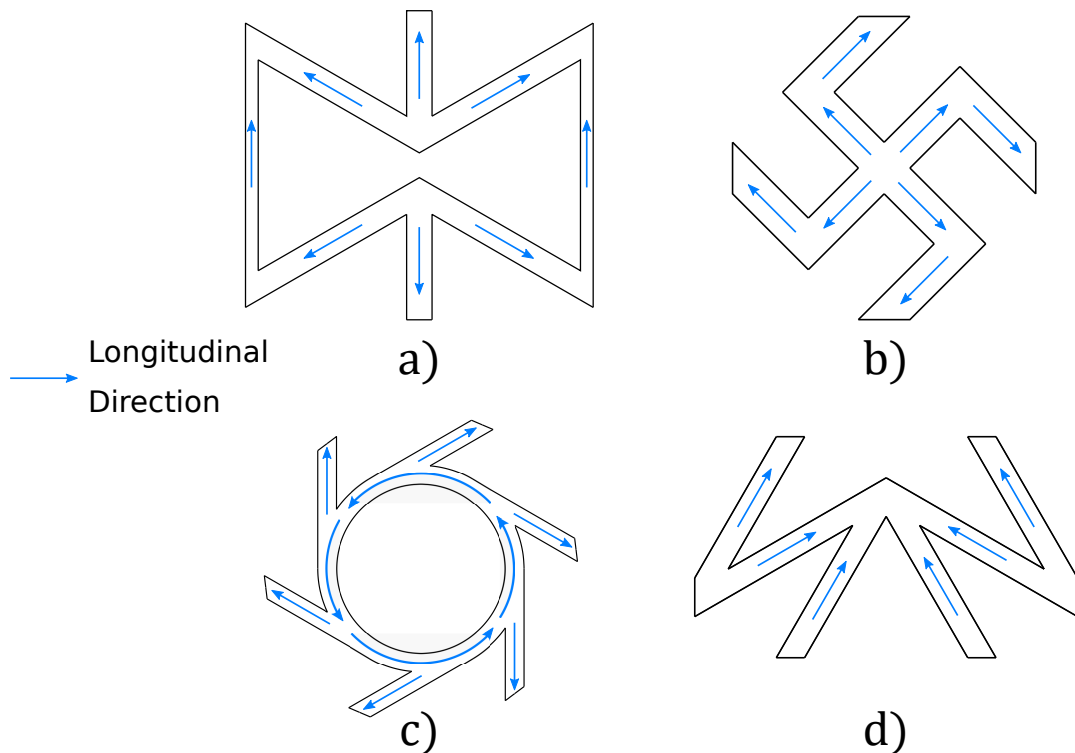


Figure 2.21. Local 3D printing longitudinal directions a) Reentrant b) Swastika c) Double-arrow d) Hexachiral

2.2.7 Macroscale: Experimental mechanical characterisation of cellular beams

At this scale, an experimental 3 points bending test is conducted to validate the numerical model (see next Section). The reasons for making an experimental 3 points bending test instead of an experimental cantilever beam test lie in the difficulty to obtain a proper clamping at one edge of the beam. Figure 2.22 shows the four types of manufactured cellular beams. Each cellular beam was manufactured 5 times, then these beams were tested in 3 points bending. The loading rate is 1 mm/s and the distance between the lower rollers is 190 mm. The loading rate is kept low to avoid visco-elastic effects of the 3D printed material. The testing room temperature was 20°C, and the humidity rate in the room was about 40%.

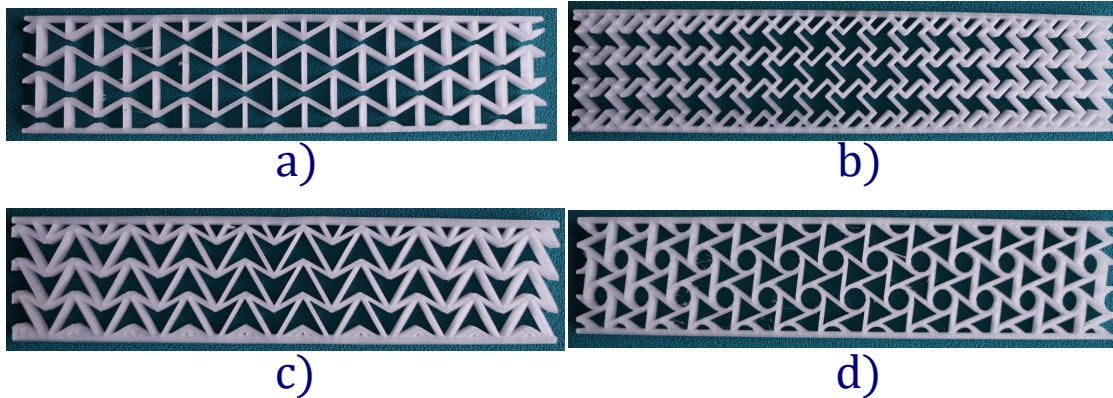


Figure 2.22. Pictures of different 3D printed cellular beams a) Reentrant b) Swastika
c) Double-arrow d) Hexachiral cellular solids

For each beam, the test consisted in a displacement of 1 mm of the upper roller. This low value of displacement ensures the beam to remain in the elastic domain. While testing, the reaction force was then measured by a load-cell of 1 kN. A LVDT Gefran sensor was used under the beam’s lower surface to measure the beam’s deflection. Having a linear mechanical response for these mechanical tests, the beam’s stiffness was then calculated by linearly fitting the force and the displacement. The linear regression range used for determining the beam’s stiffness starts at 0.2 mm and finishes at 1 mm.

2.2.8 Macroscale: Numerical mechanical characterisation of cellular beams

This numerical model of 3 points bending test aims at precisely describing the experimental beam bending behaviour. The beam is considered as a deformable solid, whereas the rollers are specified as rigid bodies. The contact between the beam and the rollers is modelled as a hard frictionless contact. A vertical displacement of 1 mm is imposed on the upper rollers. The beam stiffness is then calculated. Figure 2.23 shows the numerical model used for the numerical 3 points bending test.

The finite elements used are 3D quadratic elements with full integration. For the reentrant, swastika, double arrow and hexachiral cellular patterns, the number of quadratic elements used for each pattern is 30 902, 29 994, 31 030 and 57 588 respectively.

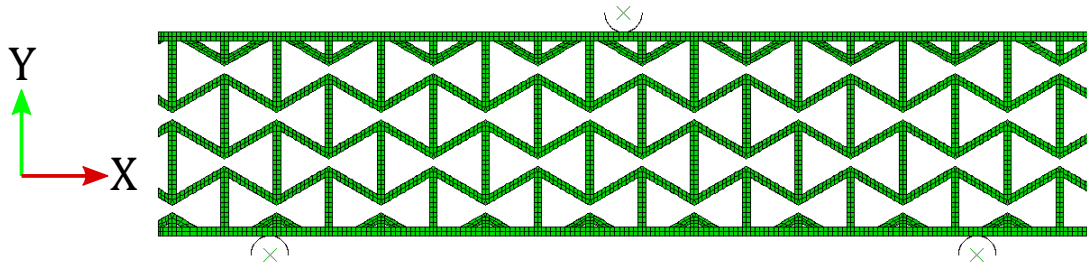


Figure 2.23. 3 points bending numerical model (Reentrant pattern example)

2.2.9 Macroscale: Numerical investigation of the skin's rigidity effect

The numerical model described above is then employed again to model a cantilever beam configuration. One edge of the beam is clamped and the other edge is assigned with a vertical displacement of 3 mm. Two configurations are considered: one where the skin's material is the 3D printed material ($E = 1900$ MPa, $\nu = 0.44$) and one where the skin's material is taken as a compliant isotropic material with a Young's modulus of 0.02 MPa and a Poisson's ratio of 0.3 (see Figure 2.24). This material is not referred to any existing specific material; these coefficients are used to represent a configuration where the skin does not affect the stiffness and the deformation mode of the beam.

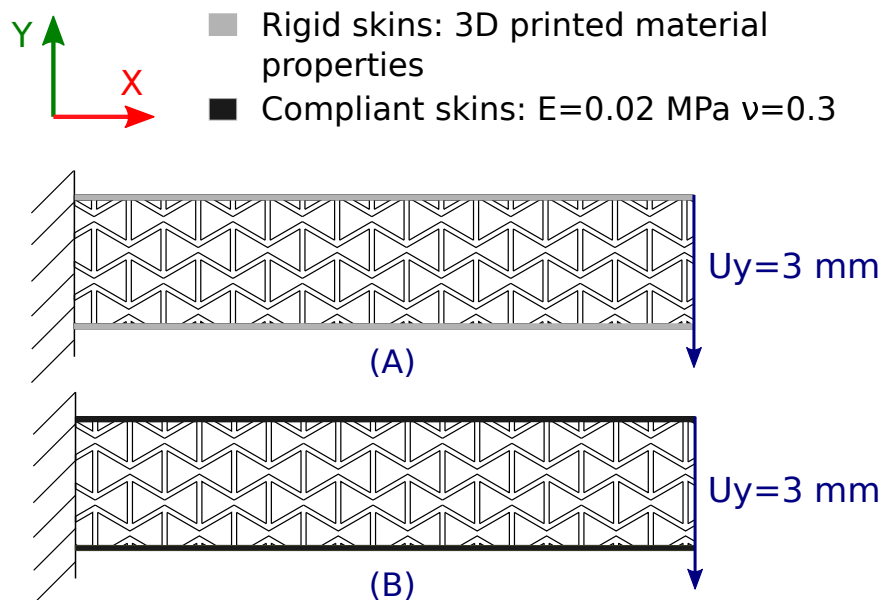


Figure 2.24. Cantilever beams simulation configuration (A) Rigid skins (B) compliant skins

2.2.10 Macroscale: Numerical investigation of the core's unit cell size effect

The numerical model developed in § 2.2.8 is used once again for investigating the impact of the core's cell size on the mechanical behavior of the structure. To do that the same cantilever beam experiment with two distinct skin rigidities, as depicted in § 2.2.9 and shown in Figure 2.24, is reused in this section. However, in this new experiment, out of the four patterns previously tested, only the double-arrow geometric pattern is chosen in this numerical experiment. The pattern choice is arbitrary and any other pattern could have been convenient for this experiment.

The material used as the beam's bulk material is an isotropic CPE polymer with a Young's modulus of $E = 1900$ MPa and a Poisson's ratio of $\nu = 0.44$. These data are the ones given by the supplier, Ultimaker, and given in Table 2.3. Here the 3D printed CPE is replaced by the isotropic CPE, because the method used to take into account the process induced anisotropy becomes time consuming and complicated for a number of cell superior to 4.

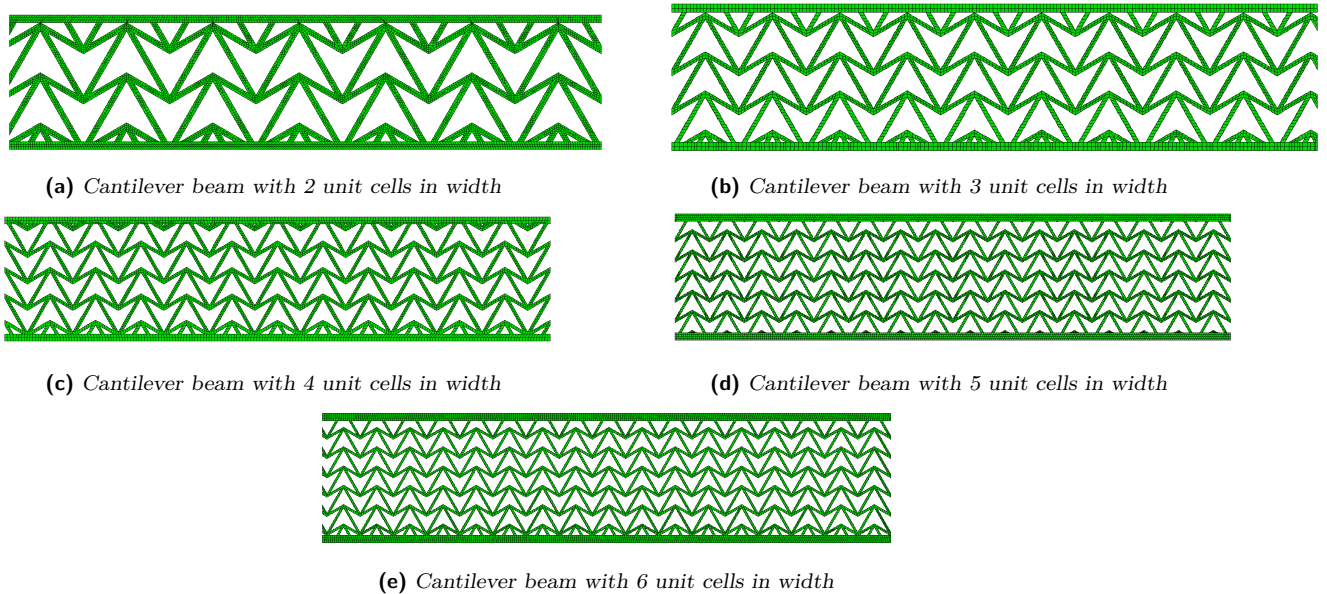


Figure 2.25. Different cantilever beam configurations for investigating the effect of the unit cells number on the structure's behavior

The geometric parameters used for earlier experiments and given in Table 2.5 of §2.2.5

correspond to a 3 double arrow unit cells present in the beam's thickness. The number of cells is changed from 3 to 2, 4, 5 and 6 cells by changing the double-arrow unit cell geometric parameters. These parameters are given in detail in Table 2.6 of the next section where these unit cell geometries are reused (§ 2.2.11). While changing the geometric parameters and the unit cell's size, its relative density was kept constant. Calculations are provided in the next section at Equation 2.27. For each beam configurations, the number of quadratic elements used is respectively 47 792, 19 488, 149 279 and 189 120. Figure 2.25 shows the four cantilever beams tested in this section.

For each beam, the numerical stiffness is estimated in a soft skin configuration and a rigid skin configuration. The soft skin mechanical properties is the same as the one presented in § 2.2.9. For one skin rigidity configuration, the evolution of the beam stiffness is presented in function of the number of cells present in the beam's height.

2.2.11 Macroscale: Numerical investigation of the differences in using a homogeneous equivalent material as the cellular core

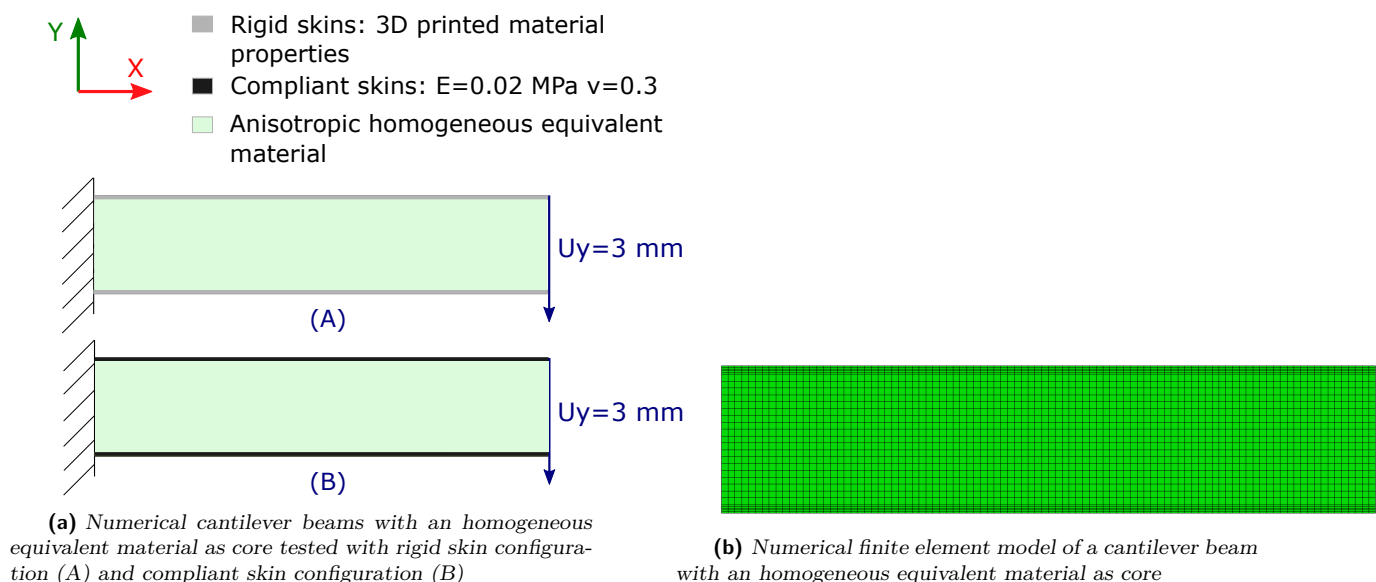


Figure 2.26. Different cantilever beam configurations for investigating the effect of the unit cells number on the structure's behavior

For being able to observe if the mechanical behavior of a morphing structure using a homogeneous equivalent material as the beam’s core, a new numerical model is developed. This model is presented in Figure 2.26. The homogeneous equivalent material used in the core is anisotropic and its elastic coefficients change for each skin configurations. The elastic coefficients values used in the homogeneous equivalent core are determined by homogenising the cellular unit cells used in the cellular beams of § 2.2.10 and showed in Figure 2.25. To do that, the homogenisation method used in § 2.2.6 was applied to each modified cellular pattern. Yet, for being able to homogenise them, the geometric parameters of each unit cells must be known precisely.

Figure 2.27 depicts the different geometric parameters that defines a double-arrow shape. Table 2.6 shows the values of these geometric parameters for each cantilever beam’s number of cells in the direction of width and their respective relative density values.

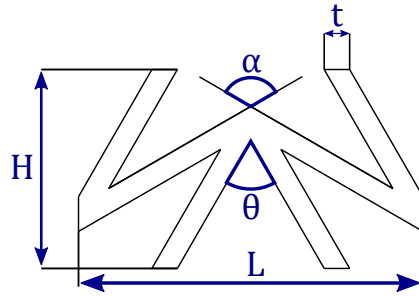


Figure 2.27. Geometric parameters defining a Double-arrow unit cell

These geometric parameters were selected for keeping a constant relative density for each unit cell. Equation 2.27 shows how the relative density $\frac{\rho^*}{\rho_s}$ is calculated with the help of the geometric parameters of the double-arrow pattern depicted in Figure 2.27.

$$\begin{aligned}
 H_1 &= \frac{L}{4\sin\left(\frac{\theta}{2}\right)} \\
 H_2 &= \frac{L}{2\sin\left(\frac{\alpha}{2}\right)} \\
 H &= 2H_1\cos\left(\frac{\theta}{2}\right) - H_2\cos\left(\frac{\alpha}{2}\right) \\
 \frac{\rho^*}{\rho_s} &= \frac{4H_1t + 2H_2t}{H.L}
 \end{aligned}
 \tag{2.27}$$

Because, it has to be compared to the results of the previous section, the bulk material of the unit cells is also made out of isotropic CPE polymer.

Numbers of cells in width	L (mm)	t (mm)	α (deg)	θ (deg)	H (mm)	relative density
2 cells	35	2.25	120	60	-	0.185
3 cells	25	1.6	120	60	-	0.185
4 cells	20	1.3	120	60	-	0.187
5 cells	15	1.0	120	60	-	0.192
6 cells	14	0.9	120	60	-	0.185

Table 2.6. Geometric values of the different parameters of the Double-arrow shape used in cantilever beams with different unit cells size

Table 2.7 shows the homogenised elastic coefficients of the different double-arrow pattern configurations. Once the beams with a homogeneous core are tested in a cantilever test, their numerical stiffness is estimated. The stiffnesses obtained in this section are then compared to the stiffnesses obtained in § 2.2.11.

Numbers of cells in width	E_x (MPa)	E_y (MPa)	ν_{xy} (-)	G_{xy} (MPa)
2 cells	23.7	17.0	-0.99	42.1
3 cells	23.3	16.7	-0.99	41.9
4 cells	24.7	17.6	-0.99	42.7
5 cells	27.1	18.9	-0.98	43.9
6 cells	23.7	17.0	-0.99	42.1

Table 2.7. Numerical values of homogenised elastic coefficients for each double-arrow pattern configuration

For comparing them, The relative difference in bending stiffness for each skin configuration between is then calculated with Equation 2.28. In this Equation, K_{Hom} corresponds to the numerical bending stiffness for beams with homogeneous cores and K_{struct} corresponds to the numerical bending stiffness for beams with cellular structures used in the core.

$$r = \frac{|K_{Hom} - K_{struct}|}{K_{struct}} \quad (2.28)$$

2.3 Results

2.3.1 Microscale

Figure 2.28 shows representative stress-strain plots for the three types of CPE printed samples. The difference in behaviour between 0° and 90° samples is an evidence of the anisotropy induced by the 3D printing manufacturing process.

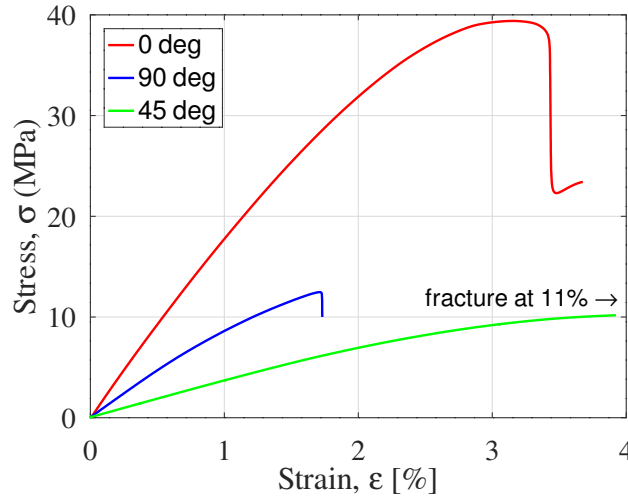


Figure 2.28. Representative engineering stress-strain curves for 0° specimens, 90° 3D printed specimens and $\pm 45^\circ$ specimens

Table 2.8 shows the experimental elastic coefficients. By comparison to Table 2.3, a decrease in rigidity ($\sim 10\%$) and yield strength ($\sim 60\%$) properties of the 3D printed material can be observed with respect to the injection molded material. A drop in rigidity and strength is also observed in the literature for other polymers, like ABS 3D printed parts. The rigidity decrease is in the range of 11-37% [188] and the strength decreasing is in the range of 20-80% [197] comparing to the isotropic ABS.

Moreover, from Table 2.8 the anisotropy ratio between the transverse modulus E_t and the longitudinal modulus E_l can be calculated and it is equal to $\frac{E_t}{E_l} = 0.55$. In the

literature, the anisotropy ratio measured varies a lot depending on the studies, in some studies this ratio is close to 1 and the 3D printed material is almost isotropic [190], in other studies a medium range of anisotropy is observed and this ratio is close to 0.80 [202], [203] and in other studies, a high degree of anisotropy is observed with ratios close to 0.6 [204]. The anisotropy degree observed for the 3D-printed samples of this study is very high and is close to high anisotropy ratios found in the literature.

Test	Elastic modulus (MPa)	Yield strength ($R_p^{0.2\%}$) (MPa)	Poisson's ratio (-)
Longitudinal tension	$1720 \pm 55 (E_l)$	30 ± 1	$0.436 \pm 0.006 (\nu_{lt})$
Transverse tension	$940 \pm 73 (E_t)$	7 ± 1	$0.241 \pm 0.022 (\nu_{tl})$
In-plane shear	$420 \pm 95 (G_{lt})$	10 ± 3	

Table 2.8. Mechanical properties of the 3D printed transparent CPE

Indeed, depending on the various processing parameters that were used (raster angles, part orientation, layer height...), the internal cohesion and the porosity inside the 3D printed material may considerably vary [205]. They have a direct impact on the bonding between layers and the building orientation [206]. Thus, we think that the high orthotropy observed in this 3D printed material is due to a difference of porosity between the 0° samples and the 90° samples.

Figure 2.29 shows the porosity present in the three types of CPE printed samples. On this Figure, it can be seen that the porosity level of 90° samples is almost twice more important than 0° samples.

Table 2.9 shows the mean porosity values observed for the different types of samples. The porosity ratios between the 90° samples and 0° samples is close to 0.60. Hence, the strong anisotropic ratio observed earlier is majorly due to the difference in porosity content.

2.3.2 Mesoscale

Table 2.10 presents the in-plane numerical values of homogenised elastic coefficients for every cellular material. We also check for a possible transverse isotropy of each pattern

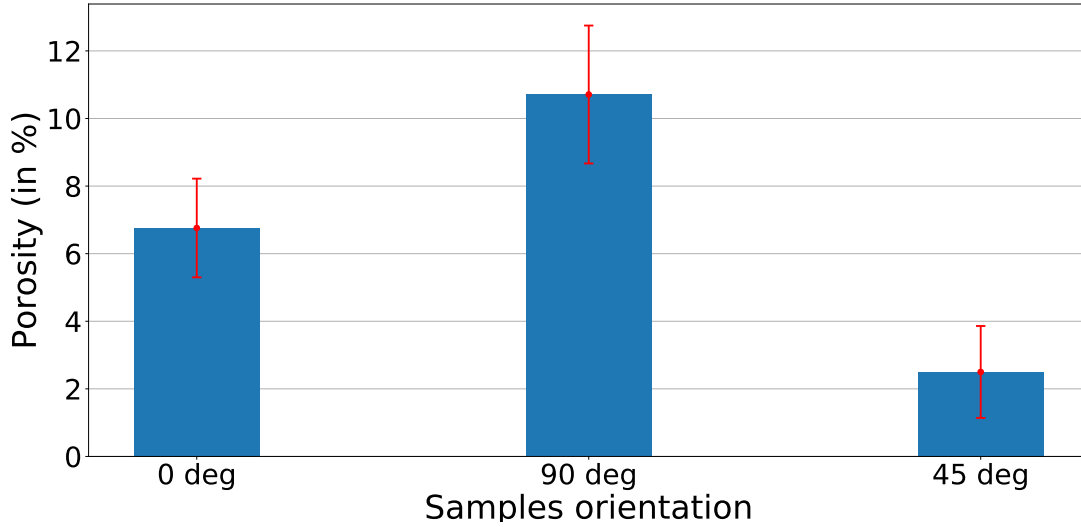


Figure 2.29. Porosity measurements for 0° specimens, 90° specimens and ±45° specimens

Sample orientations	Porosity mean value (in %)
0 deg	6.76 ± 1.46 (E_l)
90 deg	10.71 ± 2.04 (E_t)
45 deg	2.50 ± 1.36 (G_{lt})

Table 2.9. Porosity values of the 3D printed transparent CPE

(plane x-y in Fig. 2.20). For checking the transverse isotropy, the equivalence between E_x and E_y and the validity of Eq. 2.29 were sought. Following those conditions, the reentrant and double arrow are clearly not transversally isotropic since their two tensile elastic moduli are different. The swastika and hexachiral patterns, on the contrary, have the same moduli. But only the hexachiral pattern fulfils the transverse isotropy relationship given in Eq. (2.29) and yet is transversely isotropic.

$$G_{xy} = \frac{E_x}{2(1 + \nu_{xy})} \quad (2.29)$$

Figures 2.30 to 2.33 show the different deformation mechanisms for each pattern depending on the loading mode (tension or shear).

Pattern	E_x (MPa)	E_y (MPa)	ν_{xy} (-)	G_{xy} (MPa)	Transverse isotropy?
Reentrant	20.3	5.0	-0.45	0.76	No
Swastika	9.23	9.23	0	1.19	No
Hexachiral	37.2	37.1	-0.32	27.1	Yes
Double Arrow	17.4	12.7	-0.99	33.6	No

Table 2.10. Numerical values of homogenized elastic coefficients for every cellular material, see § 2.2.6 for the definition of parameters

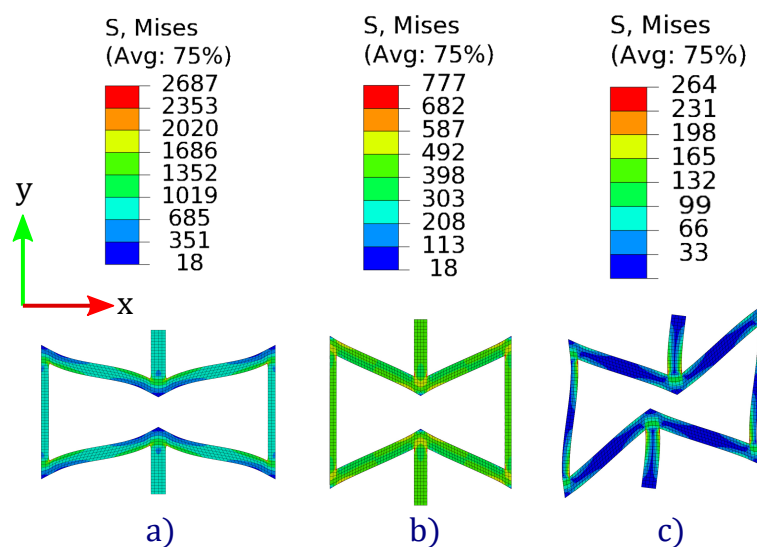


Figure 2.30. Deformation of the Reentrant pattern and Mises stresses associated under an imposed stress of 23 MPa a) under tensile loading in direction x b) under tensile loading in direction y c) under shear (x,y) loading

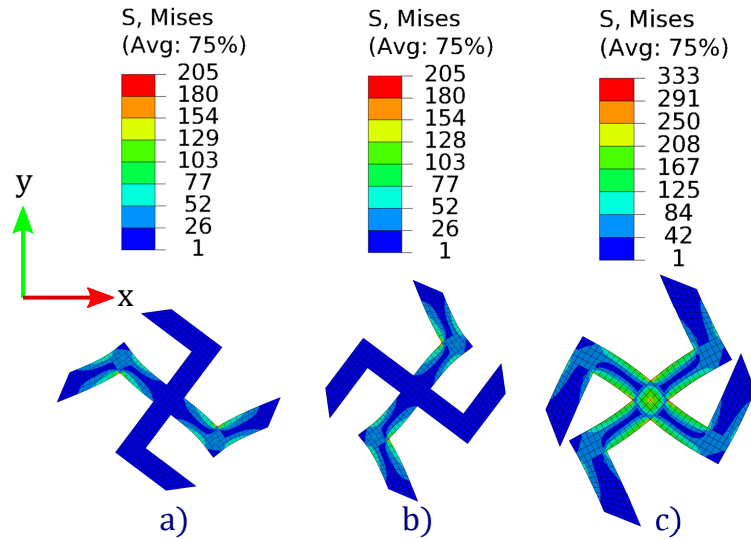


Figure 2.31. Deformation of the Swastika pattern and Mises stresses associated under an imposed stress of 18 MPa a) under tensile loading in direction x b) under tensile loading in direction y c) under shear (x,y) loading

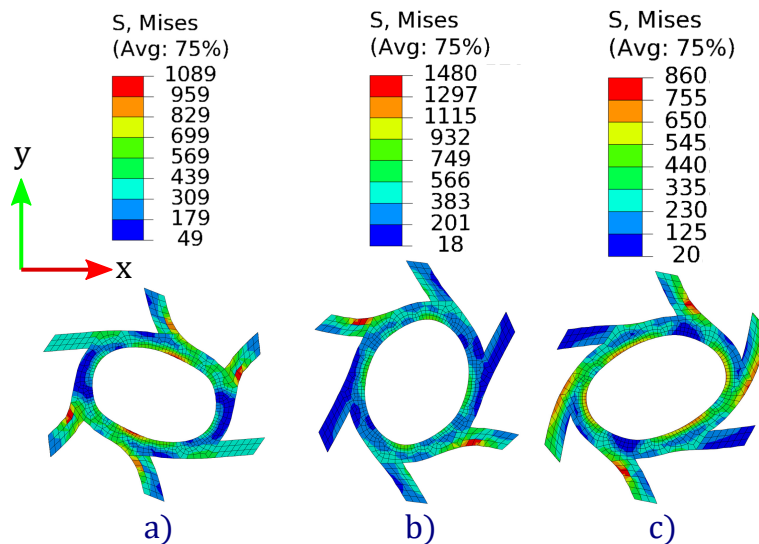


Figure 2.32. Deformation of the Hexachiral pattern and Mises stresses associated under an imposed stress of 11 MPa a) under tensile loading in direction x b) under tensile loading in direction y c) under shear (x,y) loading

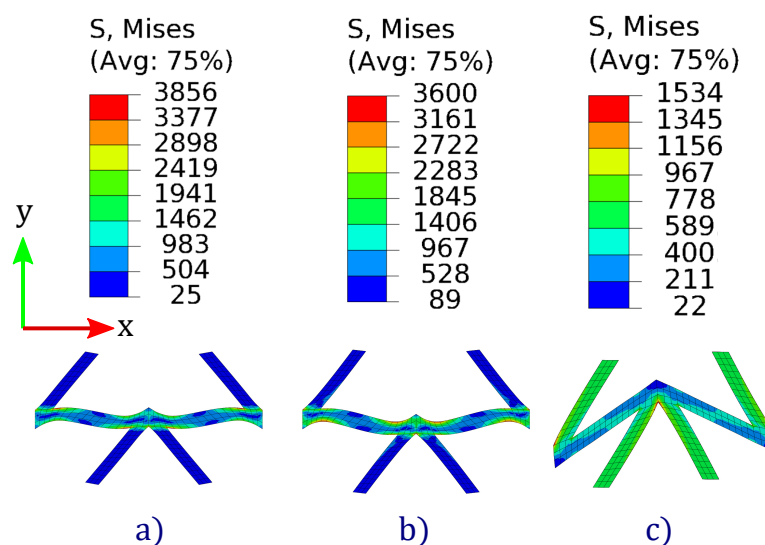


Figure 2.33. Deformation of the double arrow pattern and Mises stresses associated under an imposed stress of 30 MPa a) under tensile loading in direction x b) under tensile loading in direction y c) under shear (x,y) loading

2.3.3 Macroscale

Macroscale: Experimental mechanical characterisation of cellular beams

Figure 2.34 shows the evolution of the force applied by the upper roller as a function of the beam's deflection. It can be described by a linear elastic behaviour (see Figure 2.34). This result is in accordance with the results obtained at the microscopic scale where the mechanical behaviour of the printed CPE was also linear elastic. Figure 2.34 and Table 2.11 also show that the numerical model describes perfectly (Reentrant and Swastika) or adequately (Hexachiral and Double-Arrow) the experimental data.

In addition, by comparing the results obtained in Table 2.10 and Table 2.11, it can be observed that the macroscopic beam's stiffnesses and the mesoscopic pattern's shear rigidities are sorted equally. In both tables, the two same groups of stiffnesses and rigidities can be observed: a low rigidity group composed of the reentrant and the swastika patterns and a high rigidity group composed of the hexachiral and the double arrow patterns. As expected, these results highlight that the core of the beam is loaded in shear (sandwich structure).

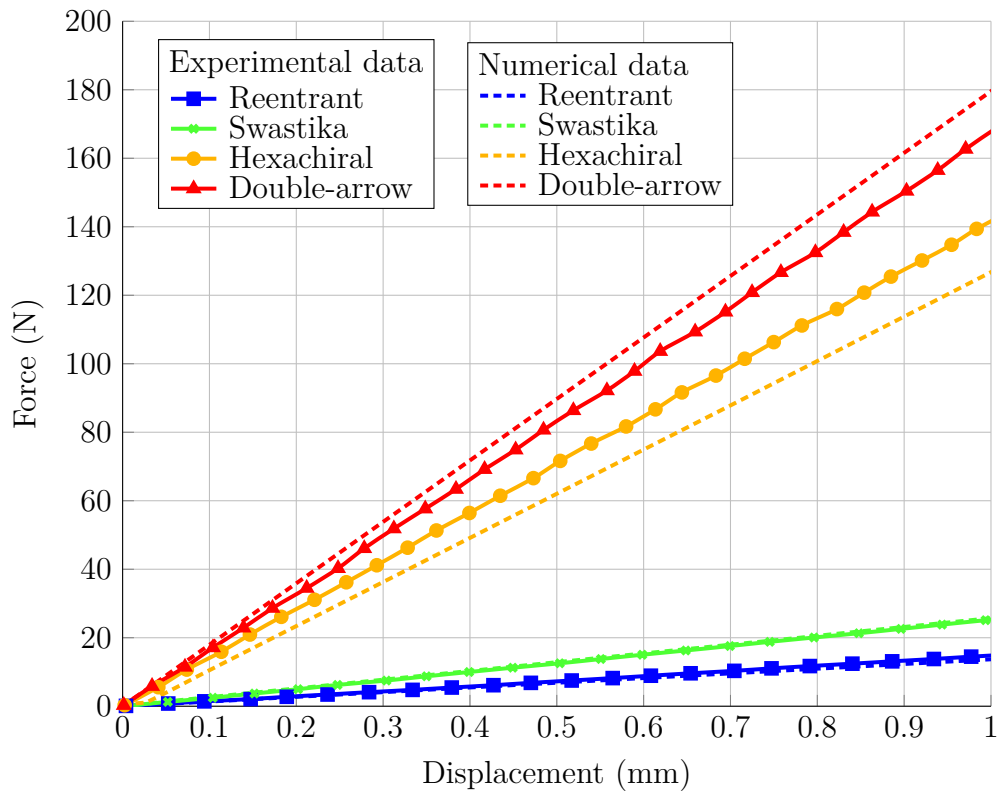


Figure 2.34. Comparison between experimental and numerical 3 points bending force-displacement curves for the four patterns (experimental error-bars are superimposed)

Macroscale: Numerical investigation of the skin's rigidity effect

Table 2.12 shows the numerical stiffnesses of the different cellular beams tested in a cantilever configuration with compliant and rigid skins. This table highlights that the stiffness order of each cantilever beam with stiff skins is the same as the 3 points bending tested beam. The rigidity groups of each pattern are also the same. Thus, the main deformation mechanism of the cantilever beam's core with rigid skin is also shear. Hence, this cantilever beam behaves as a sandwich structure.

Pattern	Experimental stiffness (N/mm)	Numerical stiffness (N/mm)	Deviation (in %)
Reentrant	14.4 ± 0.5	13.7	4.9
Swastika	25.5 ± 0.9	25.6	0.4
Hexachiral	131 ± 2	137	4.6
Double arrow	173 ± 17	181	4.6

Table 2.11. *Experimental and numerical bending stiffness of cellular beams (3 points bending)*

On the contrary, the beams with compliant skins exhibit different stiffnesses that are ten to hundred times lower than the cantilever sandwich composites. Moreover, their bending stiffness order is different compared to the previously cited cantilever beams and does not follow any rigidity order from Table 2.10. These results indicate that the deformation mode of these beams is dramatically different from standard sandwich composites.

Figures 2.35 and 2.36 show the different mechanical behaviour of cellular beams with rigid and compliant skins and their core's stress state. Cellular beams with rigid or compliant skins exhibit very different mechanical behaviours. Cellular beams with rigid skins have a higher maximal stress usually located in the rigid skin. This means that the rigid skin opposes to beam's deflection. On the contrary, structures with compliant skins have lower maximal stress and the whole stress concentration is within the structure, whereas the skin remains quasi unloaded. The skin is not stiff enough to prevent the beam's deflection. Thus, in response to the beam's deflection, the compliant skin deforms locally. These results also confirm that the beams with compliant skins behave in a more complex way than the classical sandwich structure.

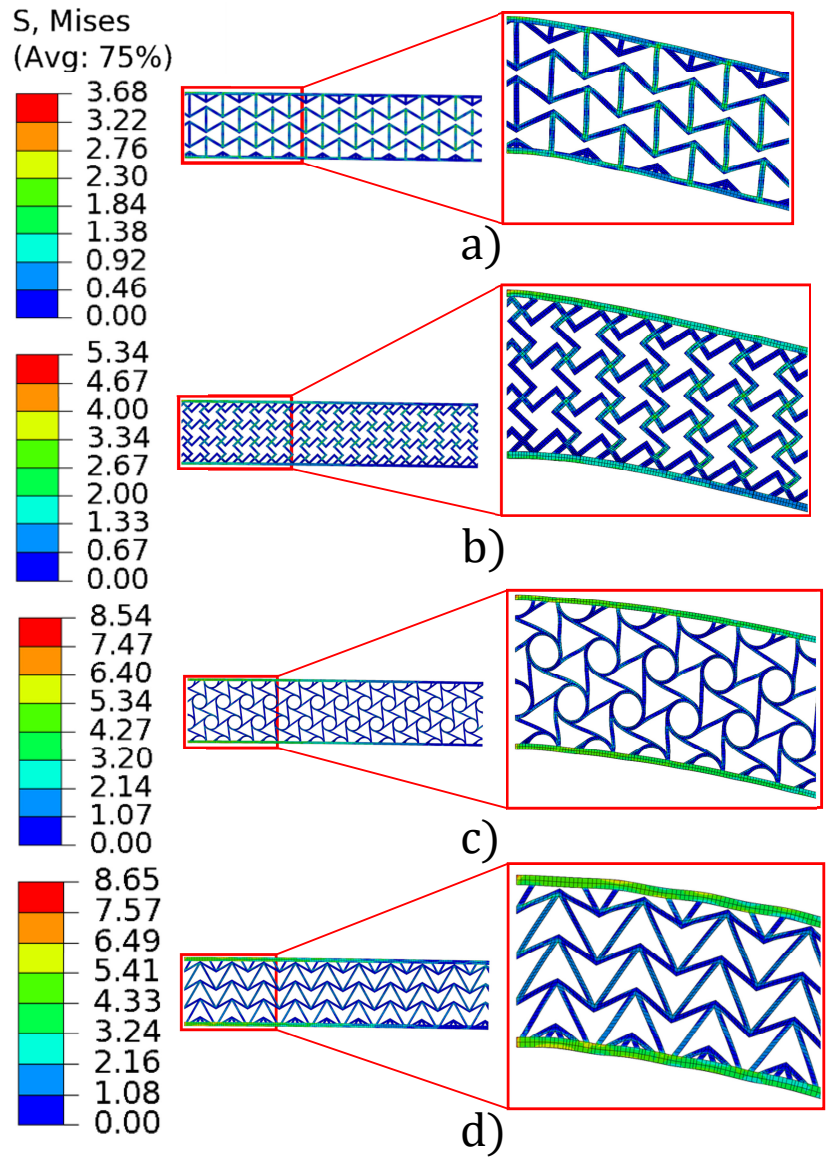


Figure 2.35. Mises stress distribution in rigid skins cantilever cellular beam's core with 20 times amplified zoomed deformations a) Reentrant b) Swastika c) Hexachiral d) Double-Arrow

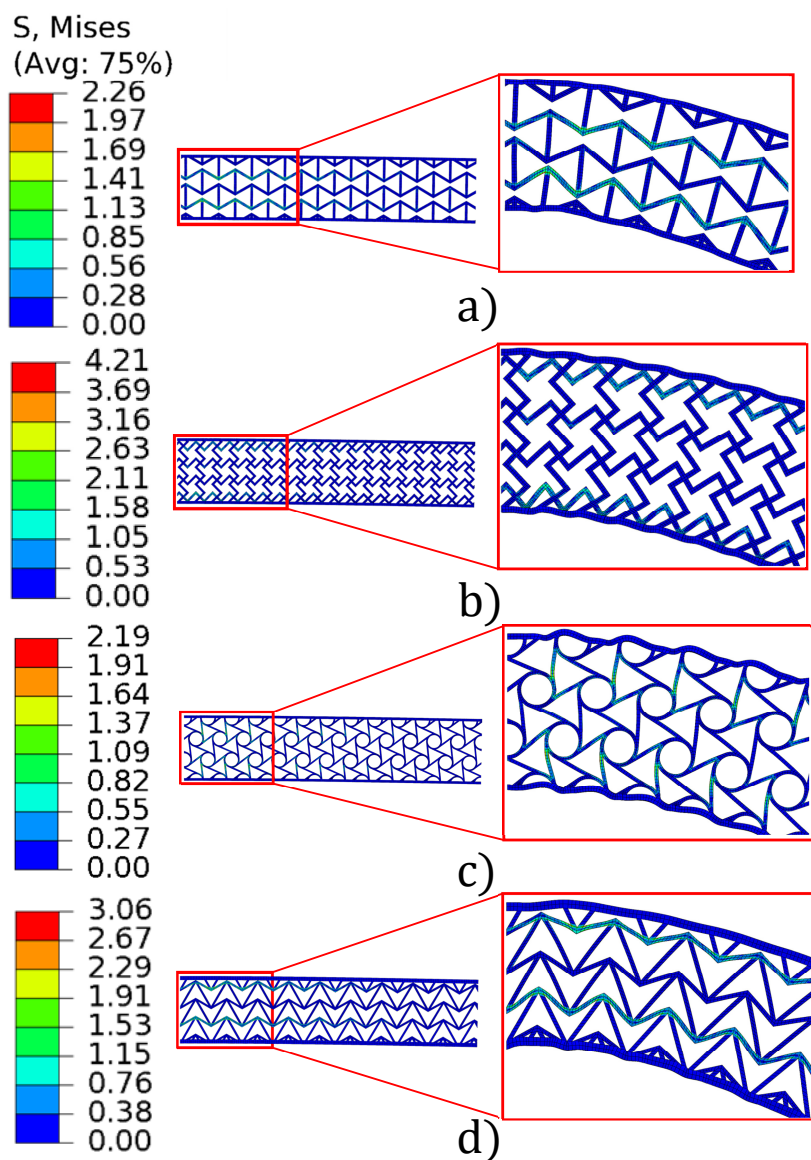


Figure 2.36. Mises stress distribution in compliant skins cantilever cellular beam's core with 20 times amplified zoomed deformations a) Reentrant b) Swastika c) Hexachiral d) Double-Arrow

Pattern	Rigid skins stiffness (N/mm)	Compliant skins stiffness (N/mm)
Reentrant	1.95	0.14
Swastika	3.28	0.25
Hexachiral	9.03	0.09
Double arrow	11.3	0.24

Table 2.12. Numerical bending stiffness of cellular cantilever beams with rigid and compliant skins

Macroscale: Numerical investigation of the core’s unit cell size effect

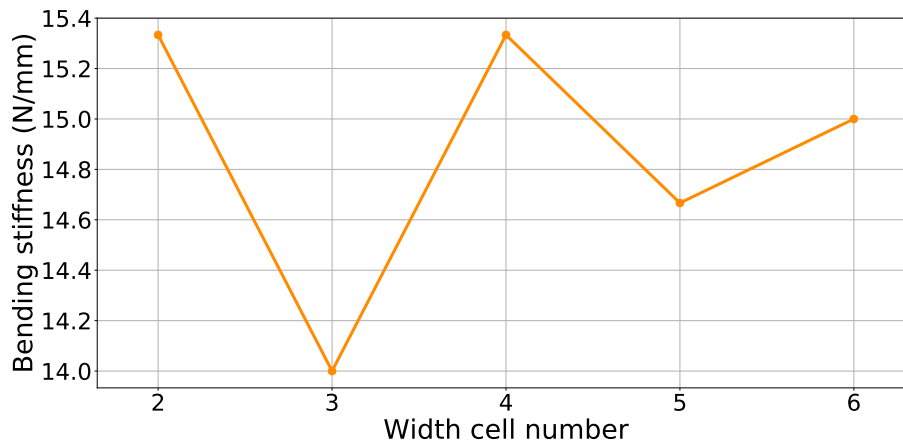
Figure 2.37 shows the evolution of the bending stiffness of cellular beams with rigid and soft skins in regard to the beam’s cell number in its width.

For the rigid skin configuration, on Figure 2.37a, it can be seen that the bending stiffness oscillates between 14 N/mm and 15.3 N/mm. Having variations that are that small, the bending stiffness of rigid beams can be considered constant. The mean stiffness value is 14.9 N/mm and it oscillates in an interval of $\pm 5\%$. Thus, it can be concluded that the cell size have not a significant impact on a rigid skined cellular beam’s mechanical behavior; *i.e.* the bending stiffness of a beam with rigid skin is independent of the number of cell in its width.

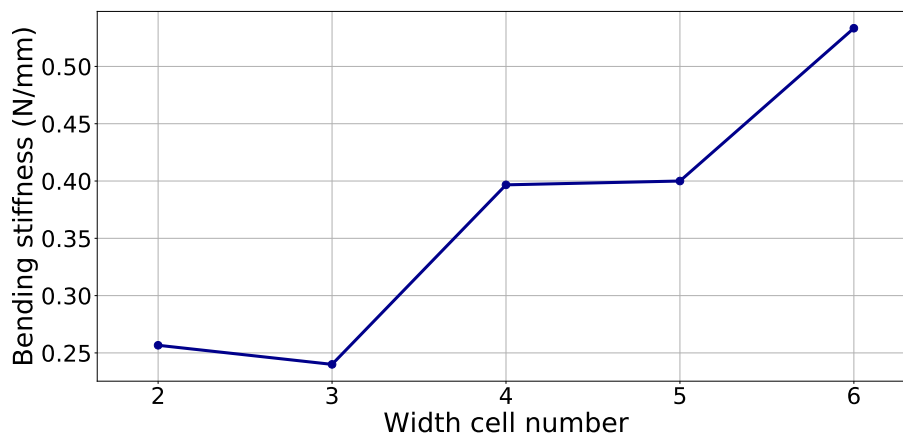
For the soft skin configuration, on Figure 2.37b, it can be seen that the bending stiffness increases with the number of cells in the direction of width. Indeed, when the number of cell passes from 2 to 6, the bending stiffness is doubled. The cell size seems to have a more important impact than the mechanical properties of the pattern for beams with soft skins. Thus, in Table 2.12 of § 2.3.3, the beams with soft skin exhibiting a lower bending stiffness must have a lower number of cells in the direction of width compared to the beams with higher bending stiffnesses.

Macroscale: Numerical investigation of the differences in using a homogeneous equivalent material as the cellular core

Figure 2.38 shows the evolution of the relative difference of bending stiffness between a beam with homogeneous core and with a cellular structural core in function of the beam’s



(a) Evolution of the numerical beam bending stiffness of a beam with rigid skins in function of the beam's cell number in width



(b) Evolution of the numerical beam bending stiffness of a beam with soft skins in function of the beam's cell number in width

Figure 2.37. Evolution of the numerical beam bending stiffness of beams with rigid and soft skins in function of the beam's cell number in width

cell number in width for two different configurations: a beam with rigid skin and with soft skin. It can be seen that for the rigid skin, for all width cell number, the relative difference of stiffness between the beam with the homogeneous core and the beam with the cellular core is inferior to 5%. Table 2.13 depicts the bending stiffness values of rigid skinned beams with a cellular core, beams with a homogeneous core and the relative difference in bending stiffness between the two beam configurations calculated with Equation 2.28. On this Table, it can be seen that the difference oscillates from 4.5 % to 1.1 %, which is a low difference value. Thus from these results, it can be concluded that, when the skins used

are rigid, a cellular structure can be replaced by a homogeneous material for modeling the behavior of a morphing structure.

Cell number	2	3	4	5	6
Cellular core bending stiffness (in N/mm)	15.3	14	15.3	14.7	15
Homogeneous core bending stiffness (in N/mm)	14.7	14.7	14.7	14.8	14.7
Bending stiffness relative difference (in %)	4.3	4.5	4.1	1.1	2.2

Table 2.13. Numerical bending stiffness of cellular cantilever beams with increasing cell number in direction of width with rigid skins and different core configurations

On the contrary, on Figure 2.38, it can be observed that the relative difference of stiffness for the beams with soft skins dramatically decreases with regard to the cell number in width. When the cell number in width is 2 or 3, the relative bending stiffness difference between the cellular and the homogeneous core is close to 100 %. Then when the cell number in width is increased up to 6, the relative difference of stiffness between the beams with homogeneous and cellular cores is below 10%. Thus, it can be supposed that when the cell number is significantly important, the relative difference between the cellular and homogeneous cores becomes small. From these results, it can be concluded that the use of a homogeneous material for numerically modeling the cellular core of a morphing structure gives non-reliable results. The cellular structure’s geometry must be modeled directly into the numerical model.

Table 2.14 depicts the bending stiffness values of soft skinned beams with a cellular core, beams with a homogeneous core and the relative difference in bending stiffness between the two beam configurations calculated with Equation 2.28. The results from this table highlight a new point, the sensitivity of the numerical bending stiffness values obtained with the homogeneous core to the geometric parameters and the relative stiffness of the unit cell. Indeed, a relative density value of 0.185 couldn’t be ensured for beams with 4 and 5 unit cells in the direction of width (see Table 2.6). A relative increase of respectively

1.1 % and 3.8 % was observed for the 4 and 5 number of cells. This increase in relative density resulted in an increase of respectively 4 % and 14 % in bending stiffness for the homogeneous core. This sensitivity with regard to the geometric parameters and the relative density increases the unreliability of the use of a homogeneous core for modeling the bending behavior of a cellular morphing structure.

Cell number	2	3	4	5	6
Cellular core bending stiffness (in N/mm)	0.26	0.24	0.40	0.40	0.53
Homogeneous core bending stiffness (in N/mm)	0.49	0.48	0.51	0.56	0.49
Bending stiffness relative difference (in %)	92.2	101.4	29.1	40.0	7.5

Table 2.14. Numerical bending stiffness of cellular cantilever beams with increasing cell number in direction of width with soft skins and different core configurations

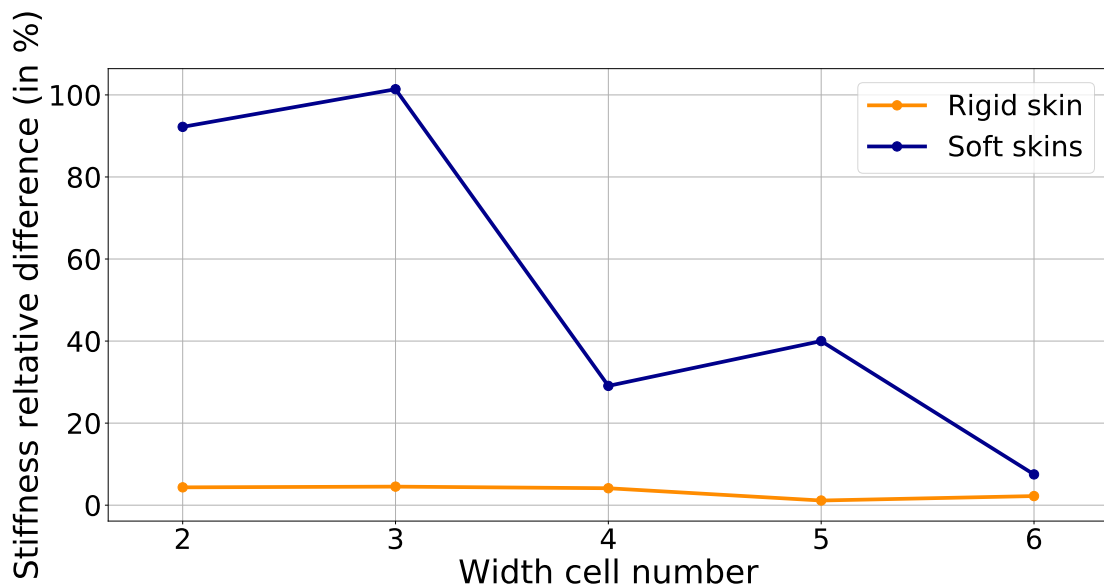


Figure 2.38. Evolution of the numerical relative difference of bending stiffness between a beam with homogeneous core and a cellular structural core in function of the beam's cell number in width

2.4 Discussion

2.4.1 Analysis of the cantilever beam's core

As mentioned in § 2.3.3, the behaviour of the cantilever beam with rigid skins is the same as a sandwich structure: the rigid skin concentrates all the tensile (or compressive) stresses and opposes to the cellular beam flexural deformation (see Figure 2.35). The core's main deformation mode is dominated by shear. By comparing the results of Figure 2.35 to the shear deformation of the various patterns (c case of Figures 2.30, 2.31, 2.32 and 2.33), it can be seen that the core deforms uniformly in shear. By concentrating all the tensile stress, the rigid skin distributes all the shear loading equally and uniformly to the core. This uniform distribution implies that the pattern size does not have a major impact on the global mechanical behavior observed, only its shear rigidity and deformation modes matter. Moreover, the comparison of the values of Maxwell's criterion from Table 2.5 and the values of shear rigidities from Table 2.10 shows that the shear rigidity cannot be predicted by Maxwell's criterion. This criterion is only qualitative for identifying compliant structures. For instance, the Maxwell's stability criterion is -3 for the reentrant honeycomb and -9 for the swastika, while the shear rigidity of the latter is higher than that of the former. These behaviours seem to be similar to the one observed by Heo *et al.* [76] on their morphing airfoil decambering. The conclusions of this study also highlights the qualitative efficiency of the Maxwell's criteria in determining compliant shear patterns, the shear deformation dominance in the airfoil's cellular core and the lack of effect of cell size on global stiffness. The behavior of Heo *et al.*'s morphing airfoils is similar to that of cantilever beams with rigid skins, *i.e.* sandwich structures.

Therefore for tuning the core's mechanical behaviour, one must tune the shear rigidity of the cellular pattern. Many authors linked the cellular shear rigidity with the auxeticity of a cellular pattern. The closer the Poisson's ratio is to -1, the higher the shear rigidity is [47], [48], [207]. Nonetheless, the results obtained in this study are not in complete agreement with these observations. By observing the values of the Poisson's ratios and shear rigidities of the reentrant and swastika pattern in Table 2.10, it can be seen that, despite being auxetic and sharing the same relative density of 0.3, the shear rigidity of the reentrant pattern is lower than that of the swastika pattern. Thus, there seems to be no complete link between auxeticity and shear rigidity. Some authors made this connection with the hexachiral lattice [47], [48], [207]. However, this pattern is the only one of our four patterns that is transversely isotropic in addition to being auxetic. Only in this case,

the shear rigidity is directly linked to auxeticity, not in other cases. An alternative sorting of the interplay between resistance to shear force and resistance to pure bending could be made with the ratio G_{xy}/E_x . The latter is found to be 0.037, 0.13, 0.73 and 1.93 for reentrant, swastika, hexachiral and double arrow patterns, respectively. This sorting is in complete agreement with the stiffness of Table 2.12.

For the cantilever beam with compliant skin, the exhibited behaviour is totally different. It is not stiff enough for concentrating tensile (an compressive) loads. Hence, the beam's cellular core deforms non-uniformly because of that loading. This is observable along and across the beam axis, where the stress is concentrated at the clamped edge of the beam and decreases at the other end of the beam. Across the beam's axis, only some struts of the cellular core concentrate the stress and deform. The rest of the struts are in a lower stress state and deform less. Because of this non-uniform state, the unit cells deformation is complex. However, by comparing the results of Figure 2.36 and a) cases of Figures 2.30, 2.31, 2.33 and 2.32, it can be noted that the dominant deformation mode of the loaded struts is the tensile / compressive deformation mode.

For the reentrant core (see Figure 2.36 a)), the diagonal struts loaded on the middle-bottom and the middle-top of the beam bend under loading. In addition, the stress concentrates inside these struts, while the vertical struts have low stress concentration. This deformation mode is similar to the tensile (and compressive) deformation modes of the reentrant geometry (see a) and b) cases of Figure 2.30), where the diagonal struts concentrates the stress and bend under the tensile loading. This tensile loading mode is thoroughly explained by Gibson and Ashby [108].

For the swastika core (see Figure 2.36 b)), the only deformation mode observable is the tension and compression of the cells located at the top and the bottom of the beam. By comparing those deformation modes to the tensile deformation of the swastika's pattern in Figure 2.31.a, it can be seen that in both cases the central vertex of the pattern remains unloaded, whereas the horizontal branches bend around the vertex in the center of the branches. This tensile mode is similar to the one depicted by Smith *et al.* for the swastika pattern [208].

For the Hexachiral core (see Figure 2.36.c), it is harder to confirm the loading state of the core by comparing those results to Figure 2.32. This difficulty might come from the fact that, unlike the other patterns, the hexachiral pattern has a hexagonal geometry and

has not been packed the same way as other patterns. Thus, the complex loading state of the core deforms the pattern in a non-expected way. However, comparing those results to the one obtained by Spadoni *et al.* [96], the loaded ligaments seem to rotate around the nodes of the hexachiral cellular cell. This deformation mode is the same as the one theorised by Prall *et al.* [95] for hexachiral honeycombs.

For the Double arrow core (see Figure 2.36 d)), the top and the bottom loaded struts clearly display a tensile deformation mode when compared to Figure 2.33 a) and b) case's deformation mode. Indeed, the outer struts of one arrow remain rigid and undeformable, whereas the inner struts are compliant and deform under the tensile load like predicted by many theoretical and experimental models [209], [210].

The behavior of the beam's core with compliant skins is similar to the behavior of the cellular core of morphing airfoil observed by Spadoni *et al.* and Bettini *et al.* [69], [207], [211]. In their studies, the airfoil cellular core was also non-uniformly deformed. Thus, the mechanical behavior of cantilever cellular beams with compliant skins is the same as the morphing airfoils depicted by Bornengo *et al.* and Spadoni *et al.* [47], [69].

The apparent contradiction between [76] and other authors [47], [69], [211] lies in their skin rigidity. All the authors previously cited used rigid skins around airfoils, composed of carbon or glass fiber composites or aluminium, in combination with more compliant materials or rigidity disruption solutions. For instance, [47] used a rubber skin section in the middle of their glass fiber composite skin for creating a rigidity disruption. [69] had little holes on the bottom skin of the airfoil and Bettini *et al.* used a compliant material for the bottom skin of their airfoil [211]. These disruptions in rigidity allowed the morphing airfoil to behave like the beam with compliant skins. On the contrary, Heo *et al.* [76] did not mention any disruption in rigidity in their morphing airfoil skin leading to a behavior which is similar to a sandwich composite.

2.4.2 Skin rigidity effect

In this paragraph, we investigate quantitatively the influence of the skin's rigidity on the behavior of the cantilever beam. To do that, th numerical model was used again. The skin is still modeled as an isotropic material (see Figure 2.24), with values of Young's modulus ranging from 0.01 MPa to 1000 MPa. Simulations are made to find the order of magnitude where the skin starts to oppose to the beam's deflection, and thus when the global behavior tends towards a sandwich structure behavior. Results are displayed

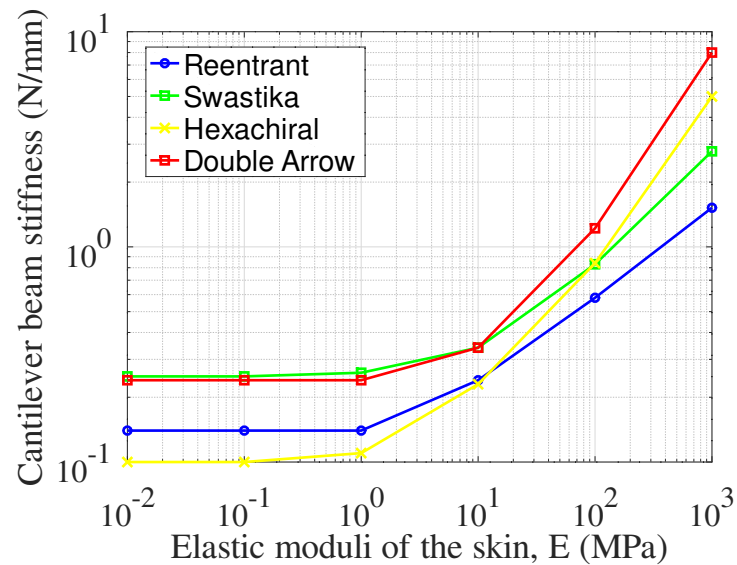


Figure 2.39. Numerical cellular cantilever beam's stiffness variation in function of skin rigidity

in Figure 2.39, which displays the variation of the cantilever beam stiffness as function of the skin's elastic modulus. It can be observed that below 1 MPa, the skin does not influence the bending stiffness of the cellular beams. The behavior of the beam is the same as the one depicted in § 2.4.1 (morphing beam). Above 1 MPa, the bending stiffness of all cellular beams increases, which means that the skins carry loads. The shear loading mode starts is the predominant deformation mode in the cellular core and the beam behaves like a sandwich structure. This threshold of 10 MPa actually corresponds to the elastic tensile and shear rigidities orders of our cellular materials (see Table 2.10). This means that the skin starts to oppose to the structure's deflection when its axial rigidity reaches the rigidity of the cellular core. Thus, for morphing applications, the axial rigidity of the constitutive material of the skins must be at least an order lower than the rigidity order of the core of the cellular structure, if the compressive core deformation mode is sought. As for the sandwich structure deformation mode, the skin's rigidity order must be comparable or higher than that of the cellular core. Practically, apart from rubbers, such homogeneous compliant materials can hardly be found in nature. Thus, research of in-plane highly compliant skins, is an active research subject in airfoil morphing [72], [212], [213]. Most of this research investigates mechanisms that do not oppose to the airfoil decambering for being able to reach such low axial rigidities and respect the other requirements needed for the morphing skin [77], [212].

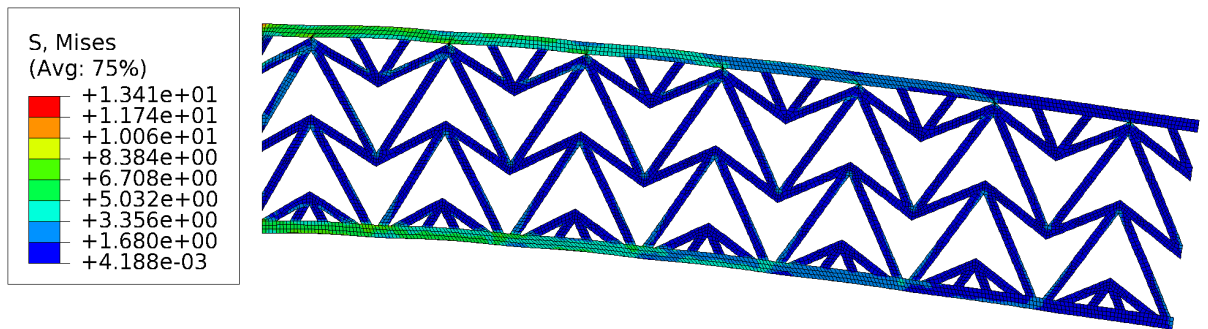
2.4.3 Cell size effect and comparison to a homogeneous core

The results obtained in § 2.3.3 for beams with soft skins are in a good agreement with the results found in the literature. Spadoni and Ruzenne showed that the bending stiffness of cellular airfoils increased with the increase of the hexachiral unit cell size [69], [207]. The results observed for the beams with rigid skin seem also to be in a good agreement with the results of Heo *et al* [76]. Indeed, the number of cells in the airfoil's width are different for each geometric pattern tested and apart of the core's shear stiffness, no other mechanism was highlighted as tailoring the airfoil's decambering. Therefore, these results suppose that the cell size has also a negligible impact on the airfoil's stiffness [76].

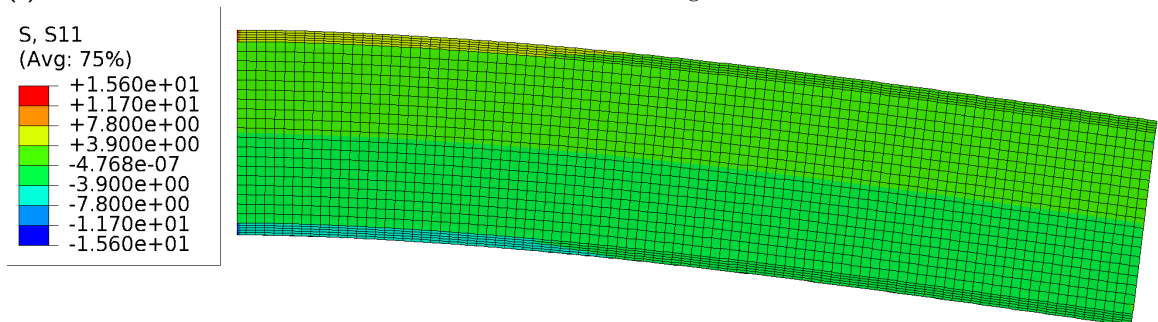
This paragraph aims to investigate the reasons why the cell size has an impact on the beams with soft skins and not for a beam with rigid skin. Figure 2.40 shows the comparison of the mechanical behavior between cantilever beams with rigid skins and with 2 cells in the direction of width, where one beam has a cellular core and the other has a homogeneous core. On Figure 2.40a, it can be seen that the stress mainly concentrates in the skins. The stress state of the core is lower than the skins, thus the skins are the structural element tailoring the bending stiffness of the cellular beam. As stated above, this mechanical behavior observed proves that those beams behave like a sandwich composites.

In Figures 2.40b and 2.40c, it can be seen that the homogeneous beam's mechanical behavior is similar to the one with the cellular core presented in Figure 2.40a: The skin concentrates the stress and the homogeneous core has a negligible stress state compared to them. Indeed, the stress in the skins is approximately 100 times more important than the one of the core. In § 2.3.3, it has been shown that the relative difference of stiffness exhibited by beams with rigid skins are small, thus this difference of stress concentration between the skin and the core must be the same for beams with cellular cores.

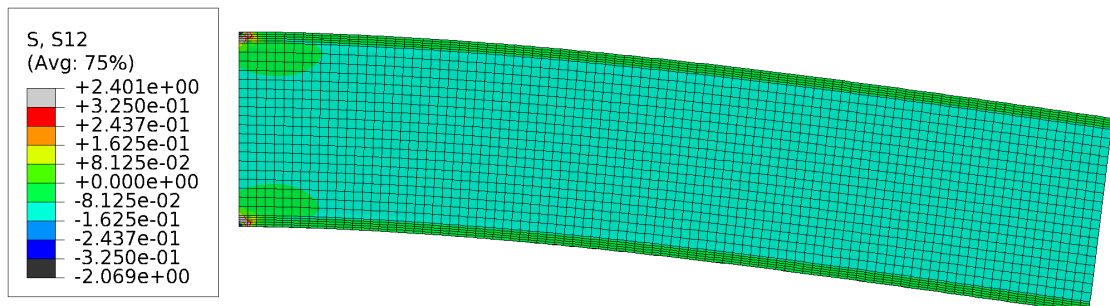
By looking more carefully at the shear stress distribution in the homogeneous core at Figure 2.40c, it can be seen that the homogeneous material used in the core is homogeneously and fully loaded in shear. Because of the homogeneity of this loading, if the homogeneous material is replaced by a cellular structure of any size, all the unit cells will be loaded equally in shear as showed in Figure 2.36 of § 2.3.3. Hence, the number of cell will matter less than the shear properties of the pattern.



(a) Von Mises stress distribution in a cantilever cellular beam with rigid skin and with 2 unit cells in its width



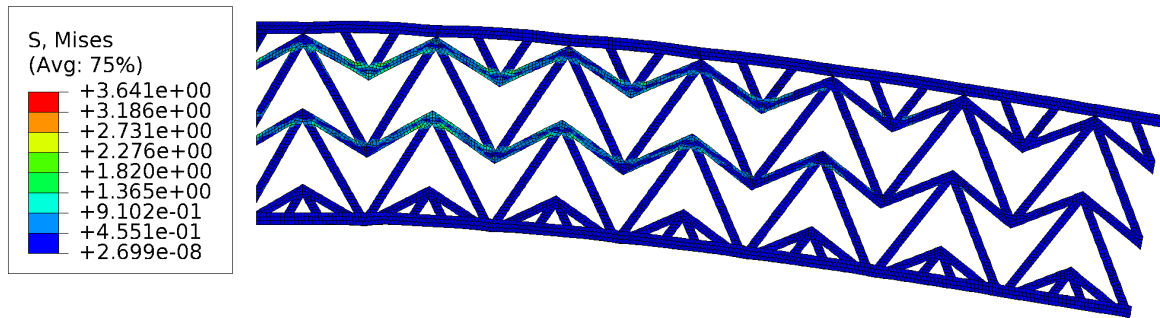
(b) Tensile and compressive stress distribution in a cantilever homogeneous beam with rigid skin



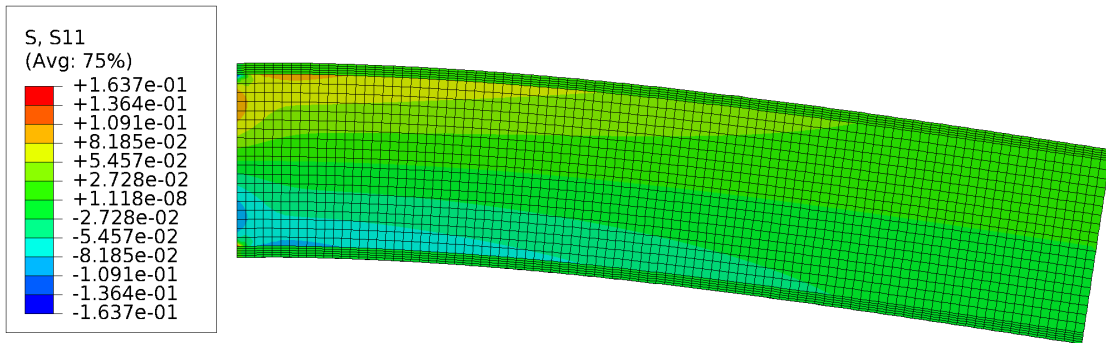
(c) Shear stress distribution in a cantilever homogeneous beam with rigid skin

Figure 2.40. Cantilever cellular beams with rigid skins and with 2 cells in the direction of width: comparison of mechanical behavior between a beam with a cellular core and a beam with a homogenised core

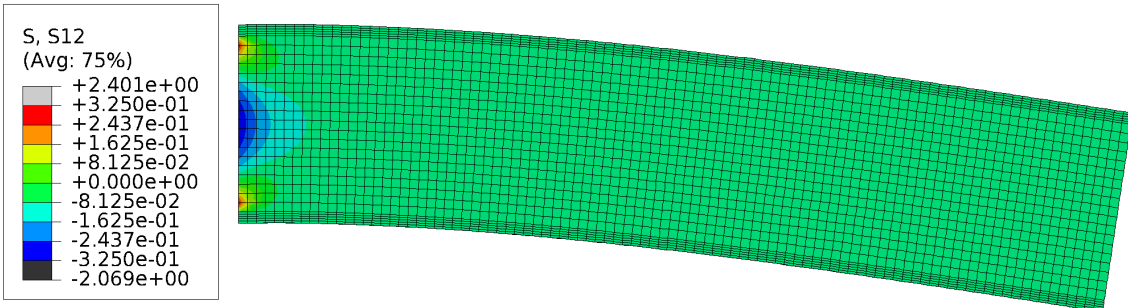
Figure 2.41 shows the comparison of mechanical behavior between cantilever beams with soft skins and with 2 cells in the direction of width, one beam has a cellular core and the other has a homogeneous core. By looking at Figure 2.41a, it can be seen that the core is non-homogeneously loaded: the two rows of cells located near the clamping at the top regions of the core seems to be loaded in tensile/compressive mode. Being soft, the skins do not concentrate stress and are unloaded.



(a) Von Mises stress distribution in a cantilever cellular beam with soft skin and with 2 unit cells in its width



(b) Tensile and compressive stress distribution in a cantilever homogeneous beam with soft skin



(c) Shear stress distribution in a cantilever homogeneous beam with soft skin

Figure 2.41. Cantilever cellular beams with soft skins and 2 cells in the direction of width: comparison of mechanical behavior between a beam with a cellular core and a beam with a homogenised core

Now, if these observations are compared to the mechanical behavior of beams with homogeneous core, by looking at Figure 2.41b, it can be seen that the upper part of the core of the beam, near the clamping, is submitted to tensile loading and the lower part of the core, near the clamping, is submitted to compressive loading. These regions width, near the clamping, corresponds to 2/3rd of the total width of the core. The tensile region's

width takes 1/3rd of the core's total width and the compressive region takes the other 1/3rd part. Hence, in the cellular core, the upper cells seems to correspond to the tensile region and the lower cells to the compressive region.

Figure 2.41c shows the distribution of shear stress in the core, the shear stress seems to be located in the center of the beam, close to the neutral fiber of the beam. The width of this shear stress region corresponds to 1/3rd of the total width of the core.

The non-homogeneity of the loads applied to the core is the reason why the bending stiffness of beams with soft skins depends strongly on the number of unit cells in the beam's width direction. Indeed, if the number of cells in the width direction is low as presented here, the unit cell's size is large compared to the core's width. Therefore the cell becomes so large that it is in between tensile/compressive regions and the shear region of the beam (see Figure 2.41a), thus the different cells of the cellular core are not recognised as a **cellular material** but as a **structure**. Then, only a limited number of compliant struts actually deforms under the dominant loading mode, the tensile loading mode (see Figure 2.41a). Indeed, most of the material is constituted by void that is not submitted to stress. Hence, by enlarging the size of the unit cell in the beam, the amount of non-loaded void in the beam is increased and the loads are distributed to few compliant struts leading to a reduced structural stiffness and thus promoting structural deformation.

On the contrary, if the number of cells in the core's width is high, *e.g.* 6 cells in width, the unit cell's size is small compared to the core's width. Hence, the number of cells in the tensile and compressive regions will be higher (2 for each region for 6 cells in width), the remaining two cells will be submitted to shear loads (see Figure 2.41). By increasing the number of cells in each region and reducing their size, the amount of void is reduced and the number of struts sustaining the loads are increased leading to an increase of stiffness and smaller deformations. Hence, the decrease of the relative difference between the bending stiffness of a cellular core and the homogeneous one on Figure 2.38.

These observations explain the strong relative differences observed between the bending stiffness of beams with a cellular core and beams with a homogeneous core seen in Figure 2.38 of § 2.3.3: in a homogeneous material, the cell's size, the amount of void and load bearing struts are not represented. Thus, the numerical results obtained with

a homogenised core and the soft skins are just a mathematical abstraction and do not represent reality when the cell size becomes big, on the contrary of beams with rigid skins. Thus, the results obtained by the passive airfoil with a homogeneous core developed by Bornengo *et al.* could be only numerical and would not be reproducible experimentally if the hexachiral cell size is too big compared to the core size [47]. This might be the reason why Spadoni *et al.* worked on a cellular core instead of a homogenised one [69], [207].

2.5 Chapter summary

In this chapter, multiple numerical methods were developed to understand the morphing mechanism in a beam with architected materials as the core. this section aims to summarise all the different information identified and introduce the next chapter.

Firstly, **a method was developed for reliably simulating numerically 3D printed parts and structures.** With the use of the *polymeric Fused Filament Fabrication* 3D-printing process for manufacturing structures and parts, porosity and anisotropy are introduced in the processed material leading to an anisotropic behavior.

Thus, to characterise the mechanical properties of the 3D printed polymer, tensile specimens were 3D printed to identify four elastic coefficients: **the longitudinal rigidity coefficient E_l , the transverse rigidity coefficient E_t ,** the longitudinal-transverse Poisson's ratio ν_{lt} and the shear rigidity G_t . In addition to this, porosity measurements were carried out in the 3D-printed samples.

Results demonstrated a strong anisotropy, with a longitudinal vs transverse rigidity ratio $\frac{E_l}{E_t} = 60\%$. The porosity measured for the longitudinal and transverse samples also demonstrated a ratio of 60%, suggesting that the difference of mechanical behavior might mostly originate from porosity differences. Furthermore, it proves that **the coefficients measured took into account the process induced porosity and anisotropy.**

Afterwards, these coefficients were introduced in a numerical model simulating the 3 points bending test of a cellular beam with 3D-printed polymer skins. Local orientations for the bulk material were set in the beam for taking into account anisotropy. The numerical results of the 3 point bending test were compared to experimental data, the comparison showed that the numerical model was able to fit accurately the experimental data. Thus, **the method developed here is reliable for simulating 3D-printed structures and parts.**

Secondly, this numerical model developed above was re-used to identify and investigate a tailoring morphing parameter: the beam's skin rigidity. In this experiment, **the cellular beam is considered as an idealised geometry for the hydrofoil, thus it is tested in a cantilever configuration.** Two configurations of skins are considered: in the first configuration, it has the properties of the 3D printed CPE, it is considered as a rigid skin, and in an other configuration, the skin's bulk material is softer ($E = 0.02 \text{ MPa}$ and $\nu = 0.3$).

The results of this experiment pointed out that **when the skin is rigid, the beam behaves as a sandwich composite.** The core is loaded homogeneously in shear loading and the bending stiffness of the beam is tailored by the shear rigidity of the core. This type of behavior is the one depicted by Heo *et al.* for his morphing cellular airfoil [76]. When the skin is soft, the beam has an other mechanical behavior. The loading of the core is non-homogeneous, the loads are concentrated on the upper and the lower regions of the core near the clamping. Its predominant loading is tensile and compressive loading. This type of behavior is the one encountered in Bornengo *et al.*'s study and Spadoni *et al.*'s studies [47], [69], [207].

Results also demonstrated that, **for the beam to behave as a sandwich composite, the rigidity of the skin must be superior to 10 times the rigidity of the core. For behaving in a compliant manner, the rigidity of the skin must be inferior to the rigidity of the core.**

In a third step, another parameter was identified and investigated: the cell number along the beam's width. To do that, the cantilever beam bending model with two skin rigidities configurations depicted above was reused here. Only the bulk material was changed to isotropic CPE. In this experiment, five number of cells in the beam's width are tested: 2, 3, 4, 5 and 6 cells in the beam's width. These beams are tested in a cantilever configuration with soft and rigid skins.

Result demonstrated that, for the rigid skin configuration, no significant difference in bending stiffness is observed with the increase of the cell number in width. In this configuration, the shear rigidity of the core remains the biggest parameter tailoring the beam's stiffness. **The cell number impact on the stiffness is negligible compared to the geometry for the rigid skin configuration.**

For the soft skin configuration, **the beam's bending stiffness increases dramat-**

ically with the cell number in the beam's width. This dependence on the cell number is due to the non-homogeneous loading of the core: the upper third region of the core's width, near the clamping, is loaded in tension, the middle third region is loaded in shear and the bottom third region of the core's width is loaded in compression. this non-homogeneity of the loading makes the cell's size important for the global beam's core mechanical behavior and its bending stiffness.

In a final step, the results obtained in the experiment designed for investigating the impact of the cell number in width are compared to the results obtained by testing a beam with a homogeneous material as the core in a cantilever configuration. The homogeneous beam is tested with a soft and rigid skin configuration. The mechanical properties of the cellular materials used for investigating the cell size impact (2, 3, 4, 5 and 6 cells in width) are homogenised and attributed to the homogeneous core.

Results demonstrated that in the rigid skin configuration, the cantilever homogeneous beam's bending stiffness is very close to the cellular beam's bending stiffness. Thus, **homogenised cores can reliably be used for modeling the mechanical behavior of the beam with rigid skins.** On the contrary, important differences were observed between beams with an homogeneous core and beams with a cellular core when the skin is softer. Nevertheless, the difference seemed to decrease when the number of cells in the beam's width increased. Thus, **in a soft skin configuration, for a small number of cells, a cellular core must be used numerically for faithfully modeling the beam's mechanical behavior.**

Thus, after finding those results, we must chose one configuration for optimising the decambering of the cellular passive morphing hydrofoil: the rigid or soft skin configuration. The configuration chosen is the **hydrofoil with rigid skin configuration**, two reasons drive this choice. Firstly, the hydrofoil is supposed to be submitted to important hydrodynamic loads, thus using a rigid skin for stiffening the structure and avoiding aero-elastic instabilities is a good idea. Moreover, using a stiff skin enables us to model the cellular core with a homogeneous equivalent material (HEM). The use of the HEM reduces the simulation time needed for modeling the hydrofoil's decambering. This last reason is the main reason for choosing this configuration as optimisation algorithms are often time-consuming.

In addition to the beam configuration, a geometric pattern out of the four investigated ones needs to be chosen for the hydrofoil's optimisation. The pattern chosen is the double-arrow pattern that can provide high shear rigidity needed for avoiding aero-elastic instabilities for a low relative density. Now that the hydrofoil deformation configuration and the geometric pattern to use in the hydrofoil's core are chosen, we need to select the hydrofoil's shape and test this morphing mechanism into a fluid-structure interaction while ensuring the manufacturability of this hydrofoil. This new issue will be investigated in the next chapter.

FLUID-STRUCTURE INTERACTION STUDIES AND HYDROFOIL'S CORE PARAMETRIC OPTIMISATION

In the former chapter, methodologies have been developed for accurately modeling the mechanical behavior of a morphing structure using a cellular core in combination with skins stiffer than the core. Now, an interaction must be set between the surrounding fluid and the structural numerical models for fulfilling the thesis main objective. The aim of this chapter is to assess the control of a manufacturable morphing cellular hydrofoil's deformation submitted to hydrodynamic loading, by using parametric optimisation algorithms.

The full methodology detailing how the turbulent fluid flow is modeled numerically with a CFD model around the hydrofoil is given in Appendix A. Originally, it was written to be the third chapter of this thesis. However, because of its size and because of the fact that the manuscript focuses on solid mechanics, and thus can mostly be understood without it, it has been changed into an appendix. The CFD numerical model developed for simulating the turbulent water flow will still be presented in this chapter. Thus, for being able to understand it, some bibliographic element from the appendix will be provided at the beginning of this chapter. The main accomplishment achieved in this chapter is the validation of the CFD model used in this thesis. That was done by modeling a turbulent airflow around a NACA0012 airfoil and finding similar pressure, lift and drag coefficients as it can be found in the literature [214].

To investigate the deformation tailorability of our morphing hydrofoil concept, the evolution of the displacement of the trailing edge of the hydrofoil will be studied with regard to the skin's rigidity. The aim of this study will be to match or to outperform the trailing edge displacement of structonic concepts encountered in Chapter 1. The targeted

morphing concepts are the belt-rib concept [39], Heo’s morphing concept [76], Bornengo’s morphing airfoil concept [47] and Spadoni’s morphing concept [69]. The numerical hydrofoil will be made out of an isotropic skin and a homogeneous anisotropic core. The manufacturability of the morphing cellular hydrofoil will numerically be ensured by using a parametric meta-heuristic optimisation algorithm, that will optimise the geometric parameters of a double-arrow shaped cellular material for reaching homogenised properties close to the homogeneous core. Thus, for doing that, the fluid-structure interaction method, some fluid dynamics literature and the optimisation algorithms will be presented in the first sections. Then, in the following section, the methods and algorithms used for the fluid-structure interaction and for the optimisation process will be presented. In a third section, the results obtained with the fluid-structure interaction program and the optimisation program will be presented. In a fourth section, the results displayed in the former section will be discussed and analysed. In a fifth section, the limits of the chosen approach will be discussed. The final section is dedicated to the conclusions and the perspectives of the investigations presented in this chapter.

3.1 Presentation of the fluid-structure interaction strategy

The mechanics of interactions between a fluid system and a structural system, also called **Fluid-Structure Interaction (FSI)**, can be defined as the interaction of a movable or a deformable structure with an internal or surrounding flow.

As an example, Figure 3.1 depicts a regular fluid-structure interaction problem. In this problem, the domain of study Ω is constituted of three sub-domains: the fluid domain Ω_f , the solid domain Ω_s and the interface between the solid and the fluid domain Γ_s . Mathematically, the global domain Ω and the interface Γ_s can be defined as $\Omega = \Omega_f \cup \Omega_s$ and $\Gamma_s = \Omega_f \cap \Omega_s$.

For being able to couple the behavior of the fluid and the solid domains, one must solve the governing equations of the three sub-domains. The governing equations of the solid domain Ω_s are given in Equations 3.1. In this set of Equations, ρ^S is the solid’s density, u_i^S is the solid’s displacement field, σ_{ij}^S represents the solid’s stress field, ϵ_{ij}^S represents the strain field and f_i represents the body forces applied to the solid. In this problem, the

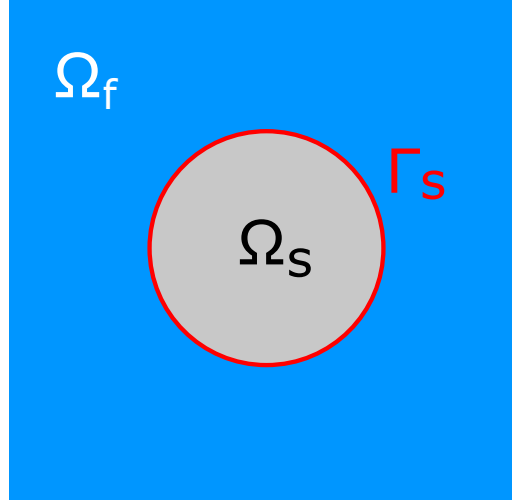


Figure 3.1. Example of a fluid-structure interaction problem

material is considered as being linear elastic, hence it is modeled with an elastic constitutive law where C_{ijkl} represents the elasticity tensor of the material.

Solid domain governing equations

$$\rho^S \frac{d^2 u_i^S}{dt^2} - \frac{\partial \sigma_{ij}^S}{\partial x_j} + f_i = 0 \text{ on } \Omega_S$$

$$F_j = \sigma_{ij}^S n_i \text{ on } \Gamma_S$$

With :

(3.1)

$$\sigma_{ij}^S = C_{ijkl} \epsilon_{kl} \text{ on } \Omega_S \text{ (Material's constitutive model)}$$

$$\epsilon_{ij} = \frac{1}{2} \left(\frac{\partial u_i^S}{\partial x_j} + \frac{\partial u_j^S}{\partial x_i} \right)$$

The governing equations of the fluid domain Ω_f are given in Equations 3.2. In this set of Equations, ρ^F is the fluid's density, v_i^F is the fluid's velocity field, σ_{ij}^F represents the fluid's stress field, f_i represents the body forces applied to the fluid, P represents the fluid's pressure field, τ_{ij} represents the fluid's shear stress field and e_{ij} is the fluid's strain rate. In this problem, the fluid is considered Newtonian, thus μ represents the dynamic viscosity.

Fluid domain governing equations

$$\begin{aligned}
 \rho^F \frac{dv_i^F}{dt} - \frac{\partial \sigma_{ij}^F}{\partial x_j} + f_i &= 0 \text{ on } \Omega_F \\
 \frac{\partial^2 P}{\partial x_i^2} + \rho^F \frac{\partial v_j}{\partial x_i} \frac{\partial v_i}{\partial x_j} &= 0 \text{ on } \Omega_F \\
 \text{With :} & \\
 \sigma_{ij}^F &= -P\delta_{ij} + \tau_{ij} \text{ on } \Omega_F \\
 \tau_{ij} &= 2\mu e_{ij} \\
 e_{ij} &= \frac{1}{2} \left(\frac{\partial v_i^F}{\partial x_j} + \frac{\partial v_j^F}{\partial x_i} \right)
 \end{aligned} \tag{3.2}$$

The governing equations of the fluid-solid interface Γ_s are given in Equation 3.3. At the interface, three conditions have to be met: the fluid’s velocity is equal to the solid’s velocity, the fluid and solid forces are equal at the interface and the dimensions of the fluid’s wall and the solid’s wall are homogeneous at the interface. For respecting the last condition, the dimensions of the solid’s and the fluid’s numerical models are $N.m^{-1}$.

Fluid-solid interface governing equations

$$\begin{aligned}
 v_i^S &= v_i^F \text{ on } \Gamma_S \text{ (Wall boundary conditions)} \\
 \sigma_{ij}^S n_i &= \sigma_{ij}^F n_i \text{ on } \Gamma_S \text{ (Equality of forces at the wall)} \\
 x_i^S &= x_i^F \text{ on } \Gamma_S \text{ (Dimensional homogeneity)}
 \end{aligned} \tag{3.3}$$

In order to solve these equations, two coupling strategies are possible [215], [216]:

- **A Monolithic approach** where the discretised equations for the fluid and the structure are solved simultaneously inside the same system [215], [216] (see Figure 3.2a)
- **A partitioned approach** where the solid and fluid’s equations are sequentially solved and advanced in time, by using, eventually, different methods and different solvers [215], [216] (see Figure 3.2b)

The monolithic approach, at the beginning, was very popular because of its robustness [215], [217], [218]. However, this method is cumbersome and lacks of generality [215]. Indeed, monolithic methods are developed for a small range of problems and can hardly

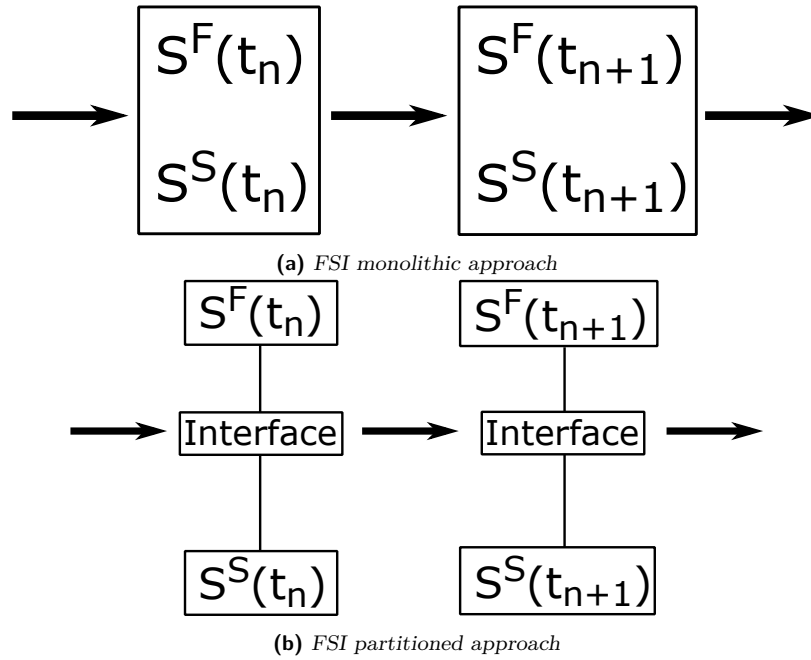


Figure 3.2. *FSI monolithic and partitioned approaches*

be adapted from one problem to the other.

On the other hand, the partitioned approach is more agile, it allows the use of different codes for the structural and the fluid calculations, separately. By doing so, it is possible to always use the latest updates of these programs. The exchange of data between the systems can be done either directly between the two codes or through a coupling interface [215]. These exchanges correspond to pressure forces applied to the object and to the structural displacement of the object [215]. In this thesis, the approached selected is the **partitioned approach**.

Four elements are necessary to develop these Fluid-Structure Interaction models [215]:

- A **Fluid dynamics solver**
- A **Structural mechanics solver**
- A **Space coupling interface**
- A **Time coupling interface**

The **fluid solver** is used for solving the fluid model's partial differential governing equations. It must also be able to read the information transmitted at its boundaries as inputs (in this study's case, the structure's displacements) and to transmit the exerted

forces on the fluid-structure interface in a precise format as an output (in this study’s case, the pressure) [215]. The fluid solver used in this study is **Abaqus CFD v.6.14**.

The **Structural mechanics solver** has a similar purpose as the fluid one, solving the structure model’s partial differential equations. This solver must be able to read the information relative to the dynamic forces generated by the fluid as an input (in this study’s case, the pressure) and transmit the structure’s reaction as an output (in this study’s case, the displacement) [215]. The structural solver used here is **Abaqus v.6.14**.

To link the data obtained with both solvers, an interface must be made in space and time. Indeed, the information sent by one solver might not be adapted to the other one. The **Space coupling interface’s** role is to **adapt the emitting server’s information to the receiving server**. Indeed, two major issues are to be considered in FSI problems: the mesh size between the structural and the fluid models are different at the fluid-structure interface and the walls of the object in the flow, for the fluid model, is deformed during the simulated time, leading to mesh displacements in the fluid model. For solving the first issue, several techniques are used for ensuring the information transmission despite the meshing difference [219]–[221].

These methods are classified in three types of methods: **Primal**, **Dual** and **Primal-Dual** methods [221]. The **primal method** is used on FSI problems where the mesh differences between the solid and the fluid is not important. In these cases, the information is shared without the aid of *additional interface variables (AIVs)* [221]. One popular method developed in this category is known as the Direct Force-Motion Transfer (DFTM) method [221].

The **dual methods** corresponds to add AIVs of dual types (*i.e.* Lagrangian multipliers) to the boundary [221]. In this category, the mortar method is the most popular numerical method used [220]. The **Primal-dual** methods consist in combining dual and primal types of methods. The Localised Lagrange-Multipliers (LLM) methods are popular numerical methods used, combining both of the approaches [221]. In this thesis, a primal method is essentially used, hydrodynamic pressures are directly applied to the object’s surface.

For the coupling of the structure's deformation and the fluid domain's mesh deformation issue, several numerical methods exist also [220], [222], [223]. The mortar method cited above can also be re-used for creating a coupling between the structural and the fluid model, so that the fluid model's mesh deforms with the solid's displacements [220]. An other very popular solution consists in the use of Arbitrary Lagrangian-Eulerian (ALE) methods where the fluid mesh is given a velocity and a displacement field that is coupled to the solid's displacement field, allowing it to move with the solid [222]. A last broadly used technique consists in the fluid domain remeshing, after a displacement is observed in the structure [223]. Out of these methods, the remeshing method will be used in this thesis.

The **Time coupling interface** is the element that *organises the exchange of information in time and functionally allows the structural and the fluid numerical models to be run in "parallel"* [215]. In reality, those exchanges happen all the time instantaneously, as they must verify the principle of action-reaction. In a FSI code, it is not the case because of the time discretisation and because of the solvers separation for solving fluid and structural problems. The efficiency of a time coupling algorithm is the better, the more the principle of action-reaction is respected [215].

In a FSI simulation, the precision and the stability of the coupling is lower than the time precision and stability of the fluid and solid solvers. Thus, the way the coupling in time is handled is the key of the stability and the precision of a FSI code. In terms of coupling, 3 main time coupling techniques exist [215]:

- The **explicit synchronised offseted algorithms**: Each sub-domain (fluid and structure sub-models) are *updated in time successively, one after the other*,
- The **parallel algorithms**: Each sub-domain is *updated at the same time*,
- The **iterative algorithms** (also called **implicit**): Several iterations of simulation are made between two offseted time steps for improving the temporal precision (see [215] for broader information).

The algorithm selected for managing the time interface in this thesis is a version of **explicit synchronised offseted algorithm**. Figure 3.3 shows the type of algorithm used in this thesis.

In algorithmic terms, the **time interface** shown in Figure 3.3 follows the following steps for advancing the simulation from a time t^n to a time t^{n+1} :

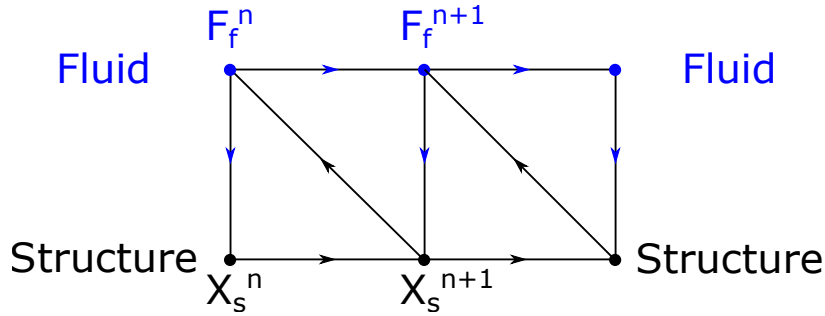


Figure 3.3. Explicit synchronised offsetted algorithm operation

- The **Fluid solver** calculates the pressure forces on the structure F_f^n ,
- The forces F_f^n are passed from the **Fluid solver** to the **Solid solver** by using the **Spatial interface**
- The **Solid solver** calculates the solid’s deformation from the geometry of the precedent iteration X_s^n to its final geometric form X_s^{n+1}
- The final geometric form X_s^{n+1} is transmitted from the **Solid solver** to the **Fluid solver** by using the **Spatial interface**
- The fluid domain is remeshed and the **Fluid solver** calculates the pressure forces on the structure F_f^{n+1}

3.2 Presentation of meta-heuristic optimisation algorithms

3.2.1 Optimisation problems definition

After presenting the FSI strategy, the optimisation methods will be depicted here. A regular optimisation problem of dimension D is defined in Equation 3.4 [224]. In this Equation, X is **the optimisation variables vector**. Its various components are the different variables to optimise.

$f(X)$ is called the **objective function**. f can also be called a **loss function**, a **cost function** or a **reward function**. This function’s aim is to map a certain value of **an optimisation variables vector** to a **cost value**. Usually, the lower the cost is, the more optimal the solution is. Thus, to find the optimal solutions to a problem, one must find the minimum value of the objective function (and vice-versa, if the maximal value is the more optimal one).

The $g_j(X)$ and the $h_k(X)$ functions are **constraint functions** that have to be fulfilled to validate the optimal solution. The $g_j(X)$ functions are n inequality type constraint functions, and $h_k(X)$ are equality type constraint functions.

$$\left\{ \begin{array}{l} X = \{x_1, x_2, \dots, x_i\} \text{ for } i = 1, \dots, D \\ \text{Min}(f(X)) \text{ or Max}(f(X)) \\ \text{Subjected to } g_j(X) \geq 0 \text{ for } i = 1, 2, \dots, n \\ \text{Subjected to } h_k(X) = 0 \text{ for } i = 1, 2, \dots, m \end{array} \right. \quad (3.4)$$

From this definition, different categories of homogenisation problems can be identified. First of all, a distinction can be made between **discrete optimisation problems** and **continuous optimisation problems** [224]. **Discrete optimisation problems** deal with discrete optimisation variables that can only take specific values. One of the most famous discrete optimisation problem is the traveling salesman problem. In this problem, the aim is to find the shortest possible loop that connects different dots [224]. This problem is regularly used for testing new optimisation algorithms [225]–[227].

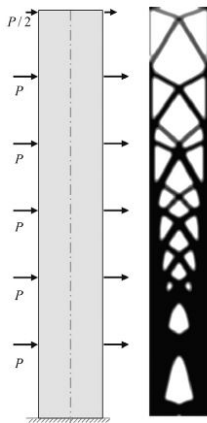
In solid mechanics, discrete optimisation problems can be encountered for **topology optimisation** problems and **shape optimisation** problems [228], [229]. However, continuous versions of these optimisation problems also exist. These studies [228], [229] critically discuss, which kind of techniques and problem formulations provide the best solutions for topology and shape optimisation problems. Topology and Shape optimisation are defined below.

Topology optimisation

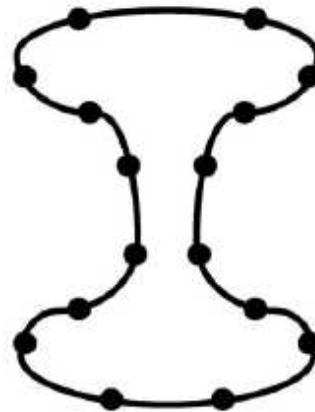
Topology optimisation problems is looking for an optimal minimal material distribution inside a volume that is submitted to external or internal loads (see Figure 3.4a)

Shape optimisation

Shape optimisation problems is looking for a part's optimal geometric shape to fulfill at best a particular task (see Figure 3.4b)



(a) Example of a topology optimisation problem [228]



(b) Example of a shape optimisation problem [224]

Figure 3.4. Motorised boat at full scale and at reduced scale

On the contrary, **continuous optimisation problems** deal with continuous variables located in a continuous interval. The most common continuous problem that can be solved is the research of the global minimum of a continuous differentiable function in a fixed interval.

In solid mechanics, **parametric optimisation problems** are usually continuous optimisation problems where some given parameters have to be optimised in a certain interval of values [48], [230], [231]. Parametric optimisation problems can also contain discrete variables only, or a mix of discrete and continuous optimisation variables. Parametric optimisation is defined below.

Parametric optimisation

Parametric optimisation problems is looking for finding optimal values of a different set of parameters in order to fulfill the most efficiently a particular task (see Figure 3.5)

In the group of discrete optimisation problems, specialised **heuristic algorithms** can provide approached solution to these problems. Nevertheless, these algorithms are often highly specialised and limited to a small range of problems. Problems that cannot be approached by such methods are called **hard optimisation problems** [224].

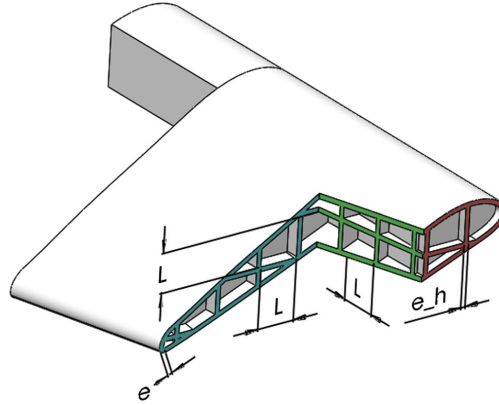


Figure 3.5. Parametric optimisation of a wind turbine blade internal structure [231]

Two types of distinct problems can be qualified as **hard optimisation problems** [224]:

- Some discrete optimisation problems cannot be solved with classical methods. Namely no solution is known for being able to solve the problem in a polynomial time ; *i.e.* the time needed for solving the problem takes the form of Equation 3.5 with $a_1, a_2, a_3, \dots, a_N \in \mathbb{R}$, N is the number of optimisation variables and $n \in \mathbb{N}$. These problems are known as **N-P hard problems**.

$$\text{Time} = a_1 + a_2N + a_3N^2 + \dots + a_NN^n \quad (3.5)$$

- Some continuous optimisation problems, for which no algorithm is known for identifying systematically a global solution to the problem. Typically, parametric optimisation problems encountered in solid mechanics, such as the one presented in Figure 3.5, enter this category of hard optimisation problems.

3.2.2 Optimisation algorithms

For solving these different optimisation problems, numerous algorithms have been developed [232]–[234]. However the most popular algorithms developed are based on **gradient descent algorithms** [224].

Gradient descent based algorithms

Originally, the gradient descent algorithms are **local optimisation algorithms** ; *i.e.* they are capable of finding the minimal value of an objective function in a local region but not in the global domain. The gradient descent algorithm is depicted in Algorithm 1.

Algorithm 1 Gradient descent algorithm

Require: An original point $X^0 = \{x_1^0, x_2^0 \dots x_n^0\}$ is arbitrary chosen

- 1: Calculation of the objective function $f(X^0)$
 - 2: Calculation of the gradient $\nabla f(X^0)$
 - 3: $k \leftarrow 0$
 - 4: $\varepsilon \approx 0$ ▷ Residual value of the gradient, must be set close to 0, *e.g.* $\varepsilon = 10^{-3}$
 - 5: **while** $\|\nabla f(X^k)\| > \varepsilon$ **do**
 - 6: $\alpha^k > 0$
 - 7: $X^k \leftarrow X^k - \alpha^k \nabla f(X^k)$
 - 8: **end while**
-

The operation of Algorithm 1 is simple, it first selects one initial point in the domain X^0 . Then, it estimates the objective function’s value and the gradient of this function at this particular point. Then, until the norm of the gradient becomes null the new point X^k is moved in the opposite direction of the gradient direction $\nabla f(X^k)$ from a step α_k . Here, the opposite direction of the gradient is selected, as the gradient points towards the maximum of the objective function.

The selection of the step α_k is important for the algorithm’s operation: it shouldn’t be too small for obtaining the solution in a reasonable amount of time and it either shouldn’t be too large for avoiding the objective function’s minimum. Thus, special techniques are developed for always finding an appropriate step for the gradient descent algorithms. These techniques will be detailed later in the paragraph.

This algorithm is considered as a **local optimisation algorithm**, because the final solution obtained is strongly dependent on the initial point X^0 selected. Figure 3.6 shows an example where a local minimum of an objective function is found instead of the global minimum. On Figure 3.6, if the initial point X_1 is taken, the algorithm will converge towards X_2 as the point where $\|\nabla f(X^k)\| = 0$. Whereas, if X_3 is taken as the initial point, the algorithm will converge towards X_4 .

To overcome this issue and make it a **global optimisation problem**, several origin

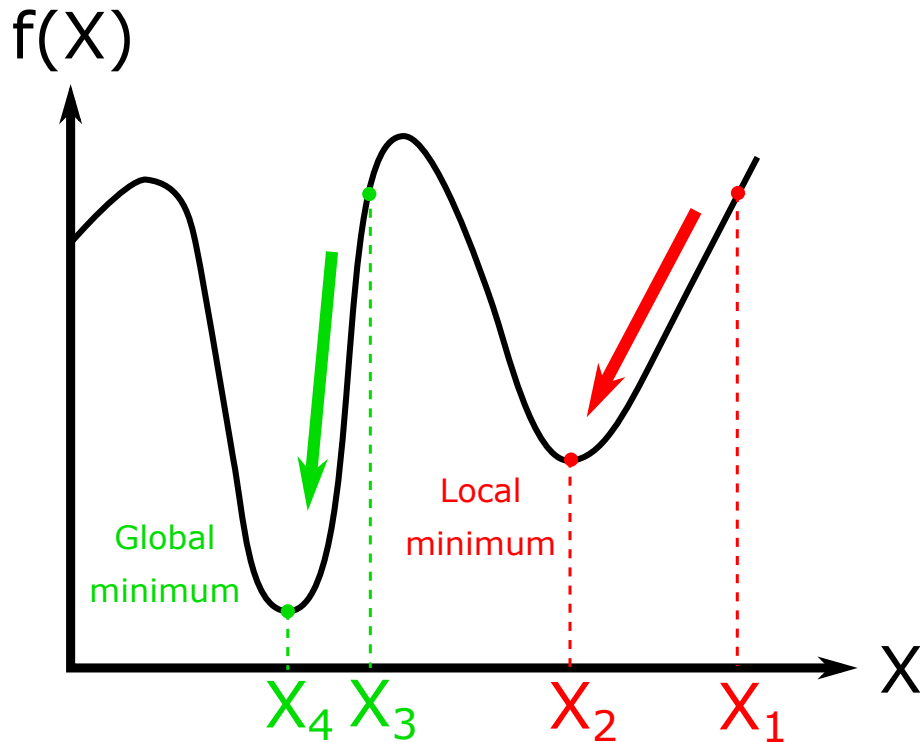


Figure 3.6. An example where the gradient descent algorithm finds a local optimum instead of the global one

points are taken in the considered domain. After all initial points converged to a solution, their **fitness** value ; *i.e.* the value of the objective function, is compared between them and the global minimum is then saved. This global optimisation algorithm is the most broadly used for solving optimisation problems [48], [235], [236].

Despite its popularity, this algorithm suffers from several limitations. The first major limitation is the fact that it is inherently a local optimisation algorithm. Thus, dispatching randomly origin points throughout the domain does not ensure that the global minimum value will be attained if the good area is not targeted. This limitation is strongly highlighted in the literature as the main improvement needed for gradient descent based optimisation algorithms [224], [237].

An other major challenge for gradient descend based algorithms lies in the choice of the descending step α_k . Indeed, as said above, if the step is too small, the convergence towards the objective function's minimum can be too slow, and if the step chosen is too big the minimum can be missed by the algorithm and the solutions can bounce around the

minimum [238]. In order to avoid that, in most modern gradient descent based algorithm, the choice of the step is automated for being able to converge towards the local minimum [238]. The most common method used adapting the step to the problem is the *Line Search* [238], [239]. The *Line Search* method consists in finding the smallest descending step α_k where the the fitness $f(X^k - \alpha_k \nabla f(X^k))$ becomes inferior to the current fitness $f(X^k)$ [239]. Equation 3.6 shows the condition that the step α_k needs to match. Despite operating well for most of the optimisation problems, the *Line Search* method can be too time-consuming. Thus, multiple research is carried out to increase the convergence speed, either by improving the *Line Search* method [239] or by developing new algorithms for finding a more adapted step [238].

$$f(X^k - \alpha_k \nabla f(X^k)) < f(X^k) \quad (3.6)$$

The last major challenge encountered by gradient descent based algorithms is the difficulty to estimate the gradient of the objective function for certain problems. This is especially the case for hard optimisation problems. Thus, for solving this issue, new methods are explored in the literature. The most popular one is known as the *Stochastic Gradient Descent* method [240]. Instead of directly calculating the gradient, the gradient is estimated through the addition and averaging of multiple points gradients (see Equation 3.7) [240]. Then, at particular points, the gradient can be estimated through finite differences.

$$\nabla f(X^k) = \frac{1}{n} \sum_{i=1}^n \nabla f_i(X^k) \quad (3.7)$$

Despite the various solutions proposed for fixing these issues, gradient descent based optimisation methods suffer from one of these three aforementioned problems. Thus, in order to totally overcome these issues and increase the convergence speed, new bio-inspired optimisation algorithms were developed: **Meta-heuristic optimisation algorithms**.

Meta-heuristic algorithms

In computer science and in optimisation, a **heuristic** can be defined as a set of methods designed for solving a problem more quickly when classical methods are too slow or for finding an approximate solution when classical methods fail to find any exact solu-

tion. Thus, **Meta-heuristic methods** are *higher-level* procedures of heuristics that can provide sufficiently good solutions to an **optimisation problem**.

The *higher level* properties of the **Meta-heuristic methods** come from the fact that there is no need to know prior information on the domain's shape nor the objective function's evolution for a good operation [224]. Thus, there is no need of gradient calculations for these algorithms. Moreover, these methods are intrinsically **global optimisation methods** that tend to find the global minimum of a considered objective function in its definition domain.

Despite encountering a great amount of various types of meta-heuristic methods in the literature, they all share some common properties according to Di Cesare [224]:

- Most of them are **stochastic** ; *i.e.* the algorithm's operation is strongly based on probabilities. This property enables to reduce the number of tested combinatory variables to the most interesting ones,
- A **population of solutions** is often considered instead of a **single solution** at every iteration of the optimisation process. This property gives to meta-heuristic potential solutions the possibility to explore the considered domain, hence avoiding them to be blocked in local minimums,
- These methods are **direct methods**; *i.e.* no sensitivity or gradient calculations are needed, which can be a source of nuisance,
- Meta-heuristic algorithms are bioinspired, making them straightforward to implement and easy to use for a given problem,
- The algorithms are dependent on various parameters, some being constant others being heuristic. These parameters have a strong influence on these methods operation, hence a prior knowledge of each parameters is needed for having a good operation of the method [241],
- The efficiency of these methods have been shown empirically only, no mathematical derivation of their efficiency is known.

Meta-heuristic algorithms also have two similar operation phases [224]:

- The first phase is called **the domain exploration** phase, the population is dispatched and moves throughout the domain for finding the best areas of the domain.
- The second phase is called **the convergence** phase, once the global minimum

region is found, all the population members converge towards it to try to find the global minimum.

These two phases induce that some parameters of the algorithm are modified during the optimisation for switching from a **domain exploration phase** to a **convergence phase**.

Out of the numerous metaheuristic optimisation algorithms present in the literature, the most popular ones are the Ant Colony Optimisation (ACO) [242]–[246], the Genetic Algorithms (GA) [231], [247]–[249] and the Particle Swarm Optimisation (PSO) [250]–[254].

Algorithm selection

For this thesis, Meta-heuristic algorithms will be preferred over gradient descent based algorithms. As exposed in the two former paragraphs, meta-heuristic algorithms are simpler to implement for mechanical optimisation problems as there is no need to explicit the objective function. This objective function can have an implicit form (for example, the objective function can be calculated by a black-box).

Between the three most popular meta-heuristic optimisation methods: ACO, GA and PSO, the Particle Swarm Optimisation (PSO) method will be preferred over the two latter, because it was initially designed for continuous optimisation problems [224], [255]. Indeed, the Ant Colony Optimisation (ACO) algorithm is best suited for discrete optimisation problems [226], [245]. The operation principle of this algorithm can be used for continuous optimisation problems, however the implementation becomes less straightforward [256]. Genetic Algorithms (GA) share the same issues as the ACO algorithms, they are mostly designed for discrete problems [257], [258].

Thus, the main reasons for selecting PSO as the main optimisation algorithm are its implementation simplicity for mechanical continuous problems, the capacity to easily control the algorithm’s behavior and the accessibility of PSO python open source packages and codes that makes code development for our mechanical problems easier [259], [260]. The PSO program will be presented in the next subsection.

Particle Swarm Optimisation (PSO)

The Particle Swarm Optimisation (PSO) algorithm has been developed based on the observation of groups of birds and shoals of fishes by Craig at the end of the 80s [261]. This algorithm is based on the sociologic behavior of animal groups or swarms, where individual members of the group have limited cognitive capacities and can access only **local** information but still manage to organise for finding food or avoiding a predator [224]. This type of societal organisation is called **self-organisation** and it is said that the global behavior **emerges** from local interactions.

Self-organisation

Self-organisation is a process where a global behavior of a system **emerges** only from multiple interactions between the different individual constituents of the lower-level of the system. Furthermore, these interactions are constituted of information available only locally, where no mentions to the global behavior is mentioned [224], [262].

Emergence

Emergent properties are properties that appears unintentionally, without being planed beforehand [224], [263].

Inspired by these principles, PSO was first developed by Kennedy *et al.* in 1995 [264]. Then this algorithm became, and stayed for decades, one of the best meta-heuristic algorithm within the field of hard optimisation problems.

For operating, a group of particles is considered in the optimisation domain. Each and every individual particle X_i in this domain are considered to be potential solutions to the optimisation problem. For each **individual particle** \mathbf{X}_i , a **fitness value** $f(\mathbf{X}_i)$ is associated to them in the space of solutions. In order to move, the individual particle has access to local information about its neighboring particles and to several information about the space of solutions: its former position in the space of solutions, its *speed* V_i and its fitness value at the current position $f(X_i)$. It is called speed in the literature, however

it is in fact the displacement of the particle in the optimisation variable domain.

Depending on these information, the individual particle X_i ’s displacement is influenced by:

- its own fitness value $f(X_i)$,
- the fitness value of its neighboring particles $f(X_j)$,
- the particle’s *inertial speed* V_i .

The idea here is to mimic the behavior of a group or a swarm of animals that move in group for converging together towards a given objective. Figure 3.7 shows the displacement of an individual particle according to this behavior.

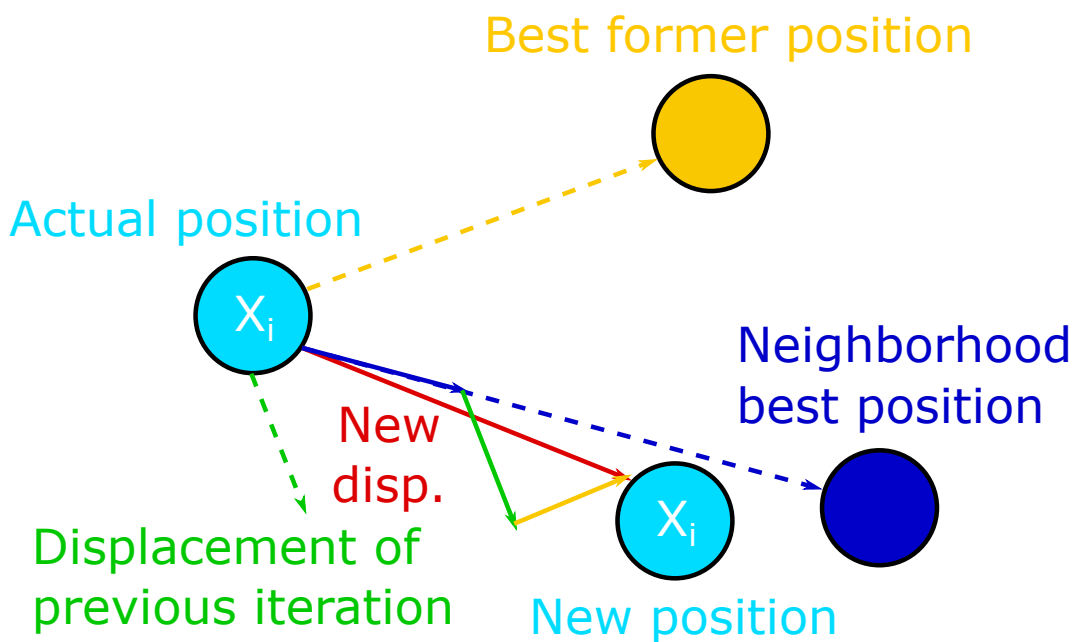


Figure 3.7. An individual particle displacement in the PSO algorithm

This movement is described mathematically in Equation 3.8. Actually, the Equation given here and the concept of inertia have been proposed by Shi and Eberhart [265]. Initially, in the concept proposed by Kennedy and Eberhart, the particle consciously followed its own speed. This is referred as *egoistic* in the literature. It was Shi who proposed the concept of particle inertia.

$$\begin{cases} V_i^k = \underbrace{\omega \times V_i^k}_{\text{Inertia}} + \underbrace{c_1 \times rand_1 \times (P_{i,best}^k - X_i^{k-1})}_{\text{Particle's best position memory}} + \underbrace{c_2 \times rand_2 \times (G_{i,best}^k - X_i^{k-1})}_{\text{Best position in the neighborhood}} \\ X_i^k = X_i^{k-1} + V_i^k \end{cases} \quad (3.8)$$

In Equation 3.8, the integer i represents an individual particle and k represents the iteration number. In this equation the different variables are:

- X_i^k is the position of a particle i at iteration k ,
- $P_{i,best}^k$ is the best position ever attained by a particle i at iteration k ,
- $G_{i,best}^k$ is the best position attained by the neighboring particles of i at iteration k ,
- V_i^k is the *speed* of a particle i at iteration k (but it is homogene to a displacement),
- ω is the inertial parameter, the greater it is the greater inertia the particle will have,
- c_1 and c_2 are the confidence coefficients, it representing the confidence a particle has for its best memory or its neighbor position. The greater those parameters are, the more confidence it has towards its position or its neighborhood's best position,
- $rand_1$ and $rand_2$ are random normal statistical numbers that were added by Shi and Eberhart for a better operation of the algorithm [265]. These random functions represent the shift of preference of the animals: sometimes they trust their former best position more than their neighbor's, on other times it is the opposite.

Thus, the different parameters governing the optimisation algorithm's behavior are:

- V_{min} is the minimal speed attainable by a particle's speed component,
- V_{max} is the maximum speed attainable by a particle's speed component,
- N is the total number of particles,
- ω is the inertial parameter,
- c_1 and c_2 are the confidence coefficients.

For ensuring a good convergence during a reasonable amount of time of the different particles, the values of these parameters must be set precisely. Or, they can be either changed through time to favor targeted operation modes. Earlier, two phases of operation were defined for meta-heuristic algorithms: a **domain exploration phase** and a **convergence phase**.

For promoting the exploration phase, the parameters ω , V_{min} and V_{max} can be set higher in order to give more inertia to a particle and permit it to have greater displacement amplitude for exploring the domain. Then, when interesting regions of the domain have been found, these parameters can be reduced for converging towards the global minimum.

The pseudo-code of the PSO algorithm is given in Algorithm 2 [224].

Algorithm 2 Particle Swarm Optimisation

```

1: N = Particles number
2: D = Problem dimension
3: while the stopping criterion is not met do
4:   for i=1,N do
5:     if  $f(X_i) > f(P_i)$  then      ▷  $P_i$  is the best individual position attained so far
6:       for d=1,D do
7:          $p_{id} = k_{id}$                 ▷  $p_{id}$  is the best individual fitness so far
8:       end for
9:     end if
10:     $g = i$ 
11:    for All the neighboring particles of  $i$  do
12:      if  $f(P_j) > f(P_g)$  then
13:         $g = j$                         ▷  $g$  is the best individual of the neighborhood
14:      end if
15:    end for
16:    for d=1,D do
17:      Updating speeds and positions with Equation 3.8
18:    end for
19:  end for
20: end while

```

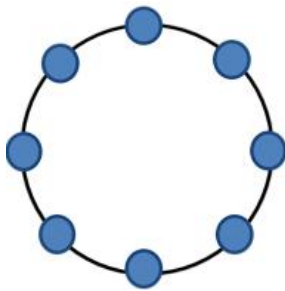
In Algorithm 2, the second part of the algorithm is dedicated to finding the best individual value of the neighborhood. A loop is made on *All the neighboring particles*, yet who are the neighboring particles of the considered individual particle ? For being able to answer this question, the links between all the particles must be specified; *i.e.* **the group topology**.

Indeed, the impact of the topology of the group is deeply investigated in the literature. In the work of Kennedy *et al* [266], it has been shown that the more connections the parti-

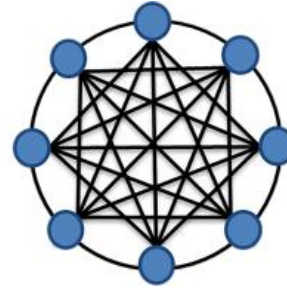
cles have, the fastest they converge towards a minimum. Actually, having a great number of connections make the information traveling faster between the different particles and accelerates convergence. Nevertheless, a faster convergence means that the domain exploration becomes more limited. And on the contrary, low particles connectivity enhances the domain exploration and obstructs convergence. Thus, for effectively managing the population topology, two different strategies exist: **static topologies** and **dynamic topologies**.

Various **static topologies** have been investigated, the most popular ones are the **LBEST** and the **GBEST** architectures [266], [267]. The **LBEST topology** is shown in Figure 3.8a, with this configuration the particles connectivity is low which leads to a slow information transfer between particles. This topology is well suited for exploring the domain and finding the region where the global minimum could be. Nonetheless, this lack of connectivity can lead to convergence issues if some parameters are badly chosen [241], [266].

On the contrary, the **GBEST topology** shown in Figure 3.8b connects all the particles between them. Thus, each individual particle knows the position and the fitness of all other particles at any given time. This topology ensures a very fast convergence towards a domain minimum as the information transits fast from one particle to the other. However, this topology violates **the local information rule**; *i.e.* each individual particle should have only the information of its local neighbor position, not of all the swarm. Thus, with this topology, there is a risk of early convergence towards a local minimum.



(a) *LBEST topology for Particle Swarm Optimisation*
[268]



(b) *GBEST topology for Particle Swarm Optimisation*
[268]

Figure 3.8. *LBEST and GBEST topologies*

Hence, for solving these issues, multiple **dynamic topologies** are researched. Sugathan, for instance, proposed to start with a LBEST topology at the beginning of the optimisa-

tion, in order to benefit from the topology’s capacity to explore the domain. Then, after some iterations, the topology is replaced by a GBEST topology for ensuring convergence [269]. Other methods consisted in classifying particles in a pyramidal hierarchy depending on their fitness value [270], [271]. For instance, the best particle i at an iteration k will be connected to the 2nd, 3rd and 4th best particles. Then the 2nd best particle will be connected to the 5th, 6th and 7th best particles, etc. At iteration $k + 1$, if a particle has a better fitness value than its superior particle, they switch their places in the hierarchy. Recently, other methods, inspired by artificial intelligence, dynamically modify the topology of the particles at each iteration. It is the case of the algorithm Inverse-PageRank-PSO (I-PR-PSO) [251], that combines the PageRank algorithm formerly used by Google for classifying the internet pages and PSO. At each iteration, the topology is optimised for ensuring a good domain exploration or a fast convergence [251].

3.3 Fluid dynamics insights and characteristic numbers

As said in the introduction of the chapter, some important literature elements from Appendix A are presented below in this section for the reader to understand the elements linked to the fluid model development section (see § 3.4.1, 3.4.2 and 3.4.3).

3.3.1 Reynolds number

In fluid dynamics, the fluid’s motion can be categorised in two types of flow: laminar flow and turbulent flow. The fluid’s motion state depends on the kinetic energy of the considered flow. When the kinetic energy is low, the flow particles follow rectilinear streamlines in the flow and the general state of the flow is non-chaotic. This state is called the laminar state (see Figure 3.9 on the bottom). When the kinetic energy of the flow is high, the momentum accumulated by the particles becomes too high to follow rectilinear streamlines. So the particles starts swirling and the motion of the fluid becomes chaotic and non-deterministic. This state of flow is called a turbulent state (see Figure 3.9 on the top). One third state exists, which is called transient. This state is only observable when a flow passes from a laminar to a turbulent state.

Now that these states are identified, how is it possible to determine qualitatively the state of the flow? The answer to this question is by using a fundamental number of

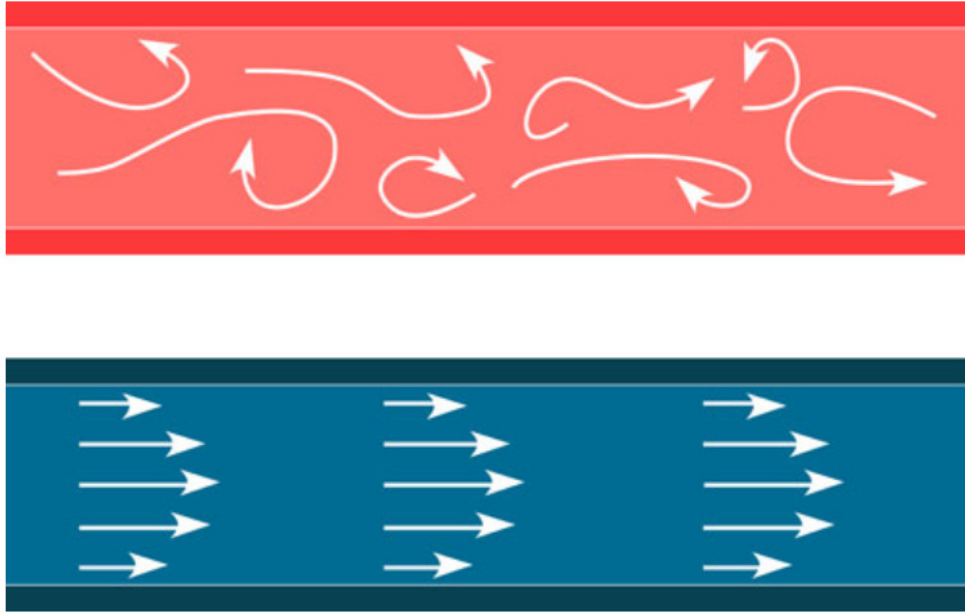


Figure 3.9. Turbulent flow (on the top) and laminar flow (on the bottom)

fluid dynamics: the Reynolds number. The Reynolds number was named after Osborne Reynolds, who evidenced in 1883 that a flow has 3 different states: laminar, transition from laminar to turbulent (transient) and turbulent state. He is also the one who publicised the use of this number. This number's most common expression is given in Equation 3.9, with Re being the Reynolds number, ρ being the fluid's density, V being the fluid's velocity, D being a characteristic length and μ being the dynamic viscosity.

$$Re = \frac{\rho V D}{\mu} \quad (3.9)$$

The expression of the Reynolds number given in Equation 3.9 is very interesting. The numerator of this number is the product of the momentum of the fluid ρV and the characteristic length D . This characteristic length will change depending on the object and problem considered. For instance, the characteristic length considered for a flow inside a pipe will be its diameter D instead of its length L (see Figure 3.10 a)). Whereas, for an airfoil, the characteristic length considered will be its chord c instead of its thickness d (see Figure 3.10 b)). By looking at Figure 3.10 a), it can be seen that alongside the pipe's length L the velocity profile does not change. However alongside the diameter D of the pipe, the velocity profile changes depending on the distance the particle of fluid is from the rims of the pipe. Thus, it is the diameter of the pipe that has to be considered as the

reference length governing the flow’s motion, not the length of the pipe. On the contrary, airfoil flows do not change because of airfoil’s thickness (see Figure 3.10 b)). The state of the flow changes depending on the position considered alongside the airfoil’s chord c . Hence, the length of the airfoil c will be preferred for being used as a reference length. In the Reynolds number’s expression, this quantity is used for describing "the quantity of fluid that must be set in motion". The bigger this length is, the more energy the fluid needs for getting in motion and the unsteadier the flow would be.

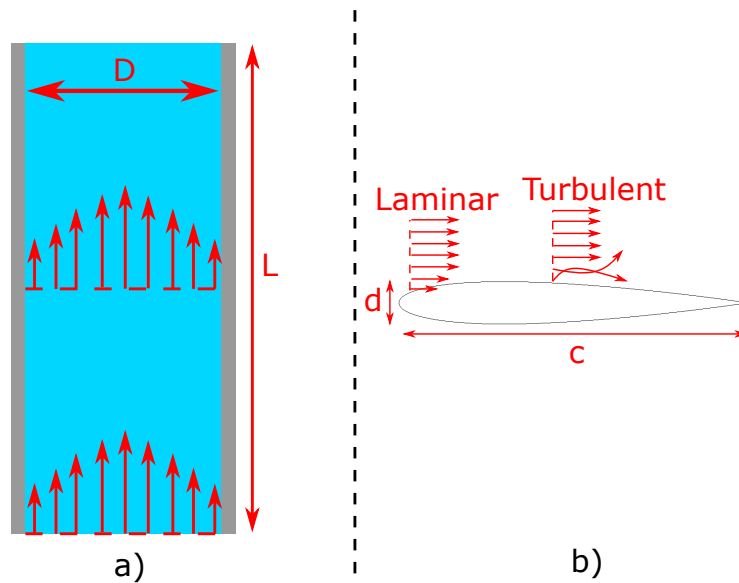


Figure 3.10. Different object characteristic length for a) a pipe flow b) an airfoil flow

The product of the momentum and the reference length are considered as being a representation of the "inertial forces of the fluid" in the Reynolds number. Indeed, the higher this numerator is, the higher inertial energy the flow has. On the contrary, the denominator is composed of the dynamic viscosity μ only (see Equation 3.9). This denominator is representing the viscous forces occurring inside the flow as depicted in the paragraph dedicated to viscosity. These forces tend to reduce the inertial velocity inside the flow and makes it steadier. Physically speaking, the Reynolds number is a ratio between the inertial forces and the viscous forces (see Equation 3.10).

$$Re = \frac{\text{inertial forces}}{\text{viscous forces}} \quad (3.10)$$

When this ratio is far less than 1. It means that the viscous forces dominate the flow’s behavior. This flow is called the Stokes flow and it has already been widely studied for

flows around spheres [272], [273]. When the value of the Reynolds number is far greater than 1 (which happens quite often in nature), the inertial forces dominate the flow. Depending on the value of this number, the state of the flow can be either a laminar flow, a transient flow or a turbulent flow. When the Reynolds number is below a certain limit, the flow has a low inertial energy which is observable as a laminar flow behavior (see Figure 3.9). This limit changes depending on the considered problem, for instance for pipe flows the Reynolds number limit value of a laminar flow is 2000, for an opened channel flow passing over a flat plate the limit value of the Reynolds number is $5 \cdot 10^5$ [274] and for flows passing over airfoils, the laminar limit depend on the type of the considered airfoil. This limit value varied from $3.5 \cdot 10^4$ to $1.1 \cdot 10^5$ [275]. However, if the limit is unknown, the laminar transition point will be taken at $Re = 5 \cdot 10^5$, the laminar limit value for a flat plate.

Beyond this limit value, there is an interval where the flow has a complex behavior for which turbulence and small vortices start appearing in the flow. Moreover, the speed and the pressure in the flow starts to be erratic. It is the transient flow status. As for the laminar limit, this interval changes depending on the problem considered. For pipe flows, this interval is between a Reynolds number of 2300 and 4000 and for a flat plate, this interval is between $5 \cdot 10^5$ and $1 \cdot 10^6$ [274].

If the Reynolds number is greater than the upper boundary of the interval, the inertial forces of the flow are so important that an infinite number of chaotic vortices are present inside the flow, the speed and the pressure of the flow become chaotic and brutally oscillate non-periodically. This state is called the turbulent state of the flow (see Figure A.4).

Besides being able to predict the state of a given flow and qualitatively estimating the inertial forces present in it, the Reynolds number is also very popular because of its ability to link geometric and kinetic quantities of two different scaled flows. Figure 3.11 shows a motorised boats models, one is a full scale model with a length L_1 that moves at a velocity v_1 . The other model is a small scale model with a length L_2 that moves at a velocity v_2 . A motorised boat is usually 8m long ($L_1 = 8$ m) and moves at a velocity of 8.2 m/s ($v_1 = 8.2$ m/s).

Before manufacturing the boat, a smaller scale prototype is tested on water. This

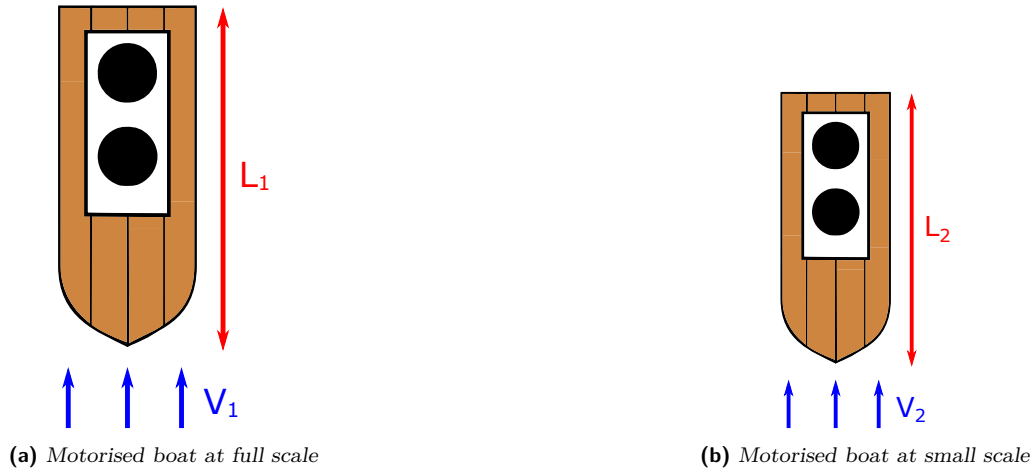


Figure 3.11. Motorised boat at full scale and at reduced scale

smaller scale prototype is designed at 1/4th scale of the full boat. This small scale boat will be tested in a water tunnel, *i.e.* large tubes where water is expelled at controlled high velocities for testing boats in cruising conditions. According to the Vaschy-Buckingham similitude principle, the small and the bigger scale problems can be put in the same conditions of navigation. However, because of the difference of scale size, the speed must be modified accordingly to have a flow that is in the same state for the full scale and small scale models.

As explained earlier, the Reynolds number is a mean of qualitatively estimating the inertial forces inside a flow for a given fluid dynamics problem. So for two problems having the same boundary conditions but where only the scale of the considered objects change, having a similar Reynolds for the two problems means that the state of the flow, and thus its inertial energy, are the same for the both considered problems. So, it said that the two problems are in a dynamic similarity. Equation 3.11 shows the dynamic similarity between the full scale boat 1 and the small scale boat 2.

$$Re_1 = Re_2$$

$$\frac{\rho V_1 L_1}{\mu} = \frac{\rho V_2 L_2}{\mu} \quad (3.11)$$

The dynamic similarity is not only used for boats, but also for aircrafts and other complex industrial systems [276]. Nevertheless, as implied previously by studying the

Reynolds number, the dynamic similarity of different scales depends strongly on the considered problem. Thus, having only a similar Reynolds number is not enough, for some problems, to have a dynamic similarity. For instance for problems where the flow velocity is close enough or superior to the speed of sound, the Mach number must also be checked to be sure that the flow is in the same conditions on the scaling model and in reality.

The Mach number will be later introduced in § 3.3.2. For the problems encountered in this work, checking the Reynolds number and the Mach number similarity is sufficient for having a dynamic similarity.

3.3.2 Mach number

As said in the paragraph devoted to the Reynolds number, many dimensionless numbers can be used for describing and comparing the states of different flows submitted to different conditions. They are also used to scale up or down fluid flow problems by having similar dimensionless numbers. The Mach number is one of these dimensionless numbers.

The Mach number compares the velocity of a flow to the speed of sound in this fluid. Its expression is given in Equation 3.12. With V being the velocity of the flow and a being the velocity of sound in the considered fluid. The velocity of sound in a fluid is highly influenced by the temperature and pressure conditions encountered by the fluid.

$$\text{Mach} = \frac{V}{a} \tag{3.12}$$

Depending on the value of this number, the state and the regime of the flow changes. Table 3.1 shows the different existing types of regimes for a flow, depending on its Mach number.

Regime name	Mach number value	Regime description
Incompressible subsonic	$M < 0.3$	The considered flow is incompressible
Compressible	$M > 0.3$	The considered flow is compressible and it can be modeled with an ideal gas law

Table 3.1. Regimes of a flow for different Mach numbers

Looking at Table 3.1, the first existing regime is the incompressible subsonic regime which is encountered if the Mach number is inferior to 0.3. In this configuration, the flow’s velocity is not great enough to start compressing the flow’s particles. Incompressible hypothesis can be used for constitutive equations.

The second existing regime, the compressible subsonic regime, occurs when the Mach number’s value is between 0.3 and 0.8. At this regime, the fluid’s velocity is high enough for compressing flow’s particles. This compressible fluid’s behavior can be described by a perfect gas law.

In our work, we tried to always verify that the Mach number is below $M < 0.3$ because the equations and numerical models used for describing the flow’s behavior only modeled incompressible fluids. No compressible fluid model was implemented in this numerical solution.

3.3.3 Boundary Layer

For air or water flows with a high Reynolds number passing around an object, the flow can be divided in three regions: (1) An unperturbed area where the streamlines remain parallel, (2) A thin viscous area on the surface of the object immersed in a flow (see Figure 3.12) where the viscous forces act as depicted in the subsection A.2.1, and (3) a region behind the object, where the fluid’s pressure and velocity are low.

This thin area depicted in (2) is called a boundary layer, a region where the shear forces have a high impact on the flow. The unperturbed region of the flow (1) is called "the external flow", it is considered as being inviscid because the shear stress effect on the flow becomes negligible. The region behind the object (3) is called "the wake". It is a region that appears when the boundary layer detaches from the immersed object leading to low pressure and low velocity (see Figure 3.12). Hence, the limit that separates the two regions starts where the shear stress effect on the flow becomes negligible. In practical terms, this occurs when the x component of the velocity of the flow in the boundary layer U has a value close to 99 percent of the x component of the velocity of the external flow U_∞ (see Equation 3.13). On Figure 3.12, this limit is the black line between region (1) and region (2).

$$U(\eta(y) = \delta) = 0.99U_\infty \tag{3.13}$$

In Equation 3.13, δ represents the thickness of the boundary layer, and η represents

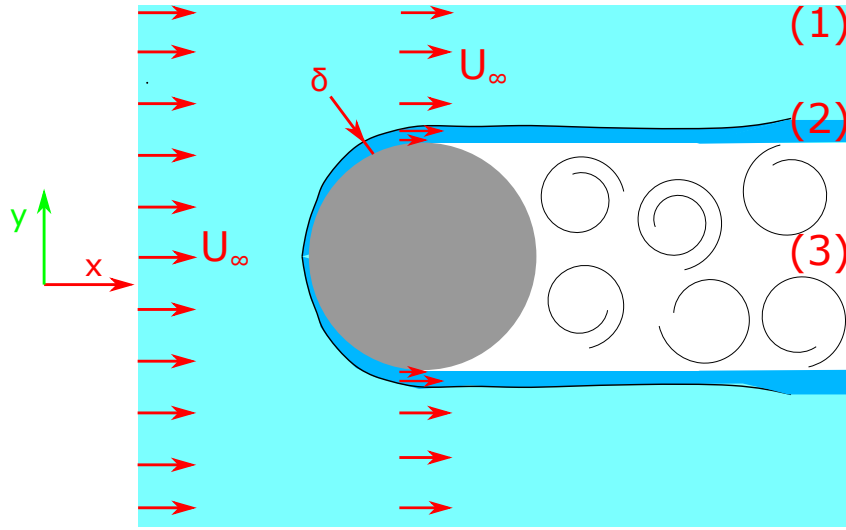


Figure 3.12. Three existing areas of the flow (1) Inviscid external flow (2) Viscous boundary Layer (3) Low pressure wake

the immersed object's curvilinear height coordinate from the object's surface. This curvilinear height coordinate is dependent on the global object's height coordinate y .

In addition to this limit, there is another object with which the boundary layer has a border: it is the immersed object itself. The flow particles passing on a solid's object surface stick to this surface. For fluid particles, it implies that their velocity is null at the object's surface. Equation 3.14 formulates this observation mathematically. Note that at $\eta(y) = 0$, a considered point is located on the object's surface.

$$U(\eta(y) = 0) = 0 \quad (3.14)$$

As Figure 3.12 seems to illustrate, the boundary layer thickness δ tends to grow along the object. Indeed, the Reynolds number, the velocity and the pressure tends to change along the boundary layer. The Reynolds number for a boundary layer is estimated by Equation 3.15. Where s is the curvilinear position on the surface of the immersed object.

$$Re = \frac{U_\infty s}{\nu} \quad (3.15)$$

Equation 3.15 shows that the boundary layer's Reynolds number increases along the object's curvilinear length. Thus, it means that the inertial forces and energy increase

with length inside the boundary layer. This implies that the velocity increases within the boundary layer. Indeed, the shear stress increases linearly with the shear rate, which is a sum of velocity gradients. Hence, if the velocity inside the boundary layer increases alongside the object, so does the shear rate and the shear stress. This increase in shear stress implies a thickening of the boundary layer, as the flow gains kinetic energy.

The increase in velocity along the object’s surface leads to an another important observation for 2D flow problems: the x component of velocity u (direction x is considered to be alongside the surface of the immersed object) is way greater than the y component of velocity v (direction normal to the object’s surface). Thus, the pressure gradient depends directly on the velocity compounds u and v (see Equation 3.16).

$$\begin{aligned} -\frac{\partial P}{\partial x} &= A(t, x, y)u \\ -\frac{\partial P}{\partial y} &= B(t, x, y)v \end{aligned} \quad (3.16)$$

In Equation 3.16, $A(t, x, y)$ and $B(t, x, y)$ are complex gradient operator. Using the hypothesis that $u \gg v$ on this equation leads to Equation 3.17.

$$\begin{aligned} -\frac{\partial P}{\partial x} &\gg -\frac{\partial P}{\partial y} \\ -\frac{\partial P}{\partial y} &\approx 0 \end{aligned} \quad (3.17)$$

This hypothesis is true for most types of flows (laminar, turbulent, supersonic...), only flows that have a Mach number superior or equal to 20 do not respect this hypothesis [29]. Nonetheless, these types of flows are way out of the scope of our work where Mach number never exceed 0.3.

Having said that, if the velocity is high enough and if the object is long enough, Equation 3.15 implies also that the boundary layer can pass from a laminar state to a transition state and then to a turbulent state on the surface of the immersed object. This is indeed the case, at the front edges of the object, the boundary layer is always laminar. But after some time the boundary layer becomes turbulent (see Figure 3.13). The transition state, being highly complex, is out of the scope of this work.

Having two different flow states means that the equations governing the boundary layer’s behavior also change. Indeed in laminar boundary layers, the inertial energy of the boundary layer is low. Thus, the particles velocity inside the boundary layer is low which leads to have laminar streamlines that remain parallel to the object’s surfaces. Hence, having parallel streamlines implies that the exchange of inertia and momentum between

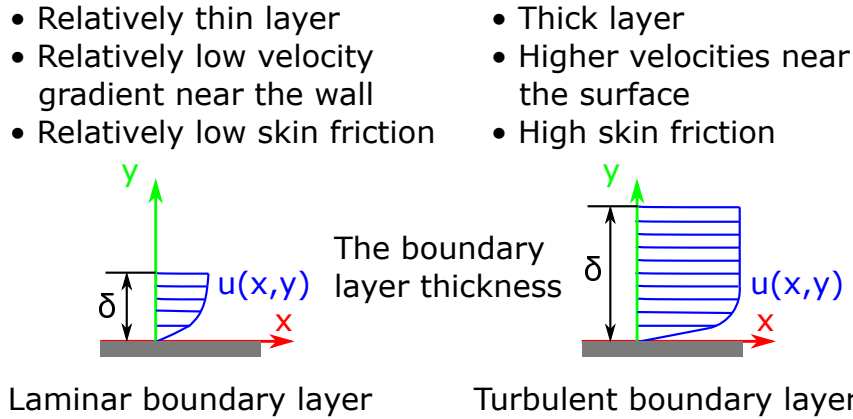


Figure 3.13. Laminar and turbulent boundary layer

the different streamlines composing the boundary layer is made on a microscopic level.

The low inertial energy of laminar streamlines and the microscopic momentum exchange between streamlines for laminar boundary layers make the development of constitutive equations governing the behavior of laminar boundary layers possible. This constitutive equation is given in Equation 3.18. This last equation will not be thoroughly explained and discussed, as it is not used later on. It is just provided for the reader to know the equation's main form. We will advise the reader to go and check reference [29] for more details.

The equation will not be detailed here for many reasons. First of all, in this work, we will be focused on studying a turbulent hydrofoil fluid flow with numerical methods. Thus, explaining this equation thoroughly will be out of the scope of this work. Secondly, the derivation and explanation of this equation is very challenging, hence the only thing to remember from this equation is the possibility to find a governing equation for laminar boundary layers. For solving Equation 3.18, one must find the f' value, representing the relative velocity of a streamline in a boundary layer $f' = \frac{U}{U_\infty}$. The 'prime' signs in the equation are derivatives with regard to $\eta(y)$.

$$\begin{aligned}
 f f'' + f''' + [1 - (f')^2] \beta &= 0 \\
 f' &= \frac{U}{U_\infty}
 \end{aligned}
 \tag{3.18}$$

On the contrary of laminar boundary layers, turbulent boundary layers have high inertial energy. Hence, the particles inside this boundary layer have a very high velocity. The

inertial energy in this kind of state is so great that the particles do not form streamlines anymore, but move frenetically up and down in the boundary layer. With the particles having that kind of behavior, the momentum exchange is not microscopic anymore, as it was in the laminar boundary layer. Right now, it is macroscopic: the particles move from the top to the bottom of the boundary layer.

Having said that, in the turbulent case, there is currently no governing equation that has been found for accurately describing the flow's behavior. Indeed, the turbulence understanding is still incomplete and is a current very active research topic [277], [278]. Nevertheless, some attempts have been tried for being able to find equations that fit the macroscopic velocity variation in the boundary for some particular basic cases.

One of the basic cases studied for better understanding turbulent boundary layers is a flow over a flat plate. Even in this case no exact solution exists. Nonetheless, some attempts have been made for finding mathematical models that fit more or less precisely the empirical results obtained on the turbulent flat plate boundary layer flow.

Ludwig Prandtl, the engineer and scientist that theorised and discovered the boundary layers, made an hypothesis for the boundary layer's flow very near to the wall: in this region, the viscous shear forces outperform inertial forces and creates a laminar sub-layer. He deduced that the velocity in this region depends on three parameters: the wall shear stress, the fluid's physical properties and the distance y from the wall. **In turbulent flows, one does not use pure velocities anymore but uses mean time-averaged velocities \bar{u} instead.** The reason for that is linked to the lack of knowledge in modeling the turbulence's behavior.

Hence, if the flow's profile is linear near the wall, \bar{u} is proportional to y . The shear stress expression for a Newtonian fluid must still be true (see Equation 3.19). In this expression τ_w is called the wall shear stress, it physically represents the shear forces applying just above the surface of the object called a "wall" here.

$$\tau_w = \mu \left(\frac{\partial \bar{u}}{\partial y} \right)_{y \rightarrow 0} = \mu \frac{\bar{u}}{y} \quad (3.19)$$

Despite the fact that it has been observed for a flat plate, this laminar sub-region

exists in all the different types of boundary layers that can be encountered and in general turbulent flows. Thus, in an attempt of generalising the results and observations made here for other kinds of problems, all datas and variables have been adimensionalised. For instance, the velocity is expressed as the variable u^+ , called "the wall velocity" and defined by Equation 3.20.

$$u^+ = \frac{\bar{u}}{u^*} \quad (3.20)$$

In Equation 3.20, u^* represents the "wall-friction velocity". Physically, it represents the velocity that is infinitesimally above the wall, at a distance $y = 0^+$ from the wall. It's value is defined by dimensional analysis with Equation 3.21.

$$u^* = \sqrt{\frac{\tau_w}{\rho}} \quad (3.21)$$

The distance from the wall y^+ expressed in non-dimensional "wall units" is given by Equation 3.22.

$$y^+ = \frac{yu^*}{\nu} \quad (3.22)$$

In Equation 3.22, ν represents the fluid's kinematic viscosity. By looking at this equation more carefully, it can be seen that the non-dimensional distance has the form of the Reynolds number. If u^+ of Equation 3.20 and y^+ of Equation 3.22 are replaced in Equation 3.23.

$$\tau_w = \mu \frac{u^+ u^*}{(y^+ \nu) / u^*} = \left(\frac{u^+}{y^+} \right) \rho u^{*2} \quad (3.23)$$

Now, if the definition of wall-friction velocity (see Equation 3.21) is introduced into Equation 3.23. It is obvious that:

$$u^+ = y^+ \quad (3.24)$$

The model described in Equation 3.24 is known as the "linear sublayer law". The laminar sublayer, where the velocities are small and where the viscous forces dominate the flow, lies under a y^+ value of 5. This means that the viscous sublayer law described in Equation 3.24 is true up to a y^+ value of 5, *i.e.* the viscous sublayer law is true until the inertial forces of the boundary layer reach a value 5 times superior to the viscous forces

(the y^+ having an expression similar to the Reynolds number). The y^+ can go up to 10, if there is a 10 percent error tolerance on the velocity precision.

Beyond this laminar region, there are other sub regions that exists. The viscous sub-layer, a region where the viscous forces dominate the flow, is composed of the linear laminar layer seen just before and located at a y^+ interval of 0 and 5 and the "buffer layer", a region located between a y^+ location of 5 and 50. In the buffer layer region, the flow becomes so complex that there is currently no model that describes this region accurately.

Above a y^+ value of 50, there are two other regions composing the "Defect-law region": the Log-law region and the Outer region. In those regions, Theodore von Kármán, a hungarian physicist, showed that the velocity magnitude did not directly depend on the viscosity anymore, but it depended directly on the wall shear stress and the distance y over which this effect has diffused. Having said that, von Kármán showed that there is a logarithmic relation between the velocity and the distance from the wall. Equation 3.25 depicts this mathematical relation. In this equation, κ is called the von Kármán constant, this constant physically represents the wall shear stress diffusion in the upper layers of the boundary layer. It is because of this mathematical fitting law that the "log law region" was named this way. This fitting law remains true up to a y^+ value of 200.

$$\begin{aligned} u^+ &= \frac{1}{\kappa} \ln y^+ + B \\ \kappa &\approx 0.4 - 0.41 \\ B &\approx 5.0 - 5.5 \end{aligned} \tag{3.25}$$

The last region is called the outer region, which is the thickest one in the boundary layer, it represents 80 to 90 percent of the overall boundary layer size and starts at a value of y^+ of 200. In the outer region, another nameless fitting law was discovered (see Equation 3.26). In this equation, u_∞^+ represents the dimensionless free stream velocity $u_\infty^+ = \frac{U_\infty}{u^*}$ and δ is the boundary layer height.

$$\begin{aligned} u_\infty^+ - u^+ &= -\frac{1}{\kappa} \ln \frac{y}{\delta} + A \\ \kappa &\approx 0.4 - 0.41 \\ A &\approx 2.35 \end{aligned} \tag{3.26}$$

Those semi-empirical fitting equations are very important for turbulence modeling. Even though they were developed for flat plates, it is widely used in simulation softwares

and numerical analyses for estimating the physical quantities in the boundary layer of complex objects - *e.g.* cylinders, airfoils, aircrafts... Figure 3.14 resumes all the regions encountered so far and shows their various locations.

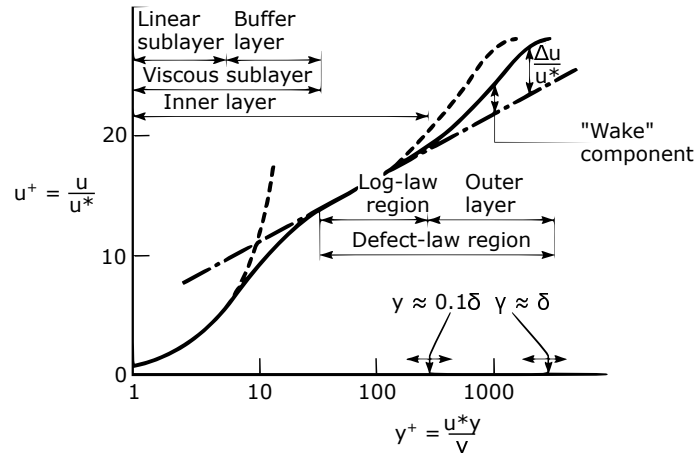


Figure 3.14. Turbulent boundary layer regions, graph taken from [29]

To summarise everything that has been said in this section, a boundary layer is defined as being the region that separates the external flow from the object's surfaces. This region is considered to have high viscous effects compared to the external flow, however these viscous effects decrease alongside the object's curvilinear length in the profit of inertial forces. Indeed, if the object is long enough, the boundary layer passes through three different states: the laminar, the transition and the turbulent state. The laminar boundary layer behavior is depictable with analytic constitutive equations on the contrary of transition and turbulent state.

Despite the absence of constitutive models, semi-empirical mathematical laws have been developed by dividing the turbulent boundary layer into several regions. A region called the viscous sub-layer, very close to the object's surface, where the viscous forces are so high that the flow is in laminar state.

Very close to the wall, the dimensionless velocity rises linearly with the dimensionless height from the wall. Above the viscous layer, the Defect-law region is not influenced directly by the viscous forces, but by the diffusion of the shear stress near the surface in those upper regions of the boundary layer. Here, the dimensionless velocity evolves in a logarithmic trend with the dimensionless height of the boundary layer. Figure 3.15

illustrates the evolution of the boundary layer with regard to curvilinear length of the surface.

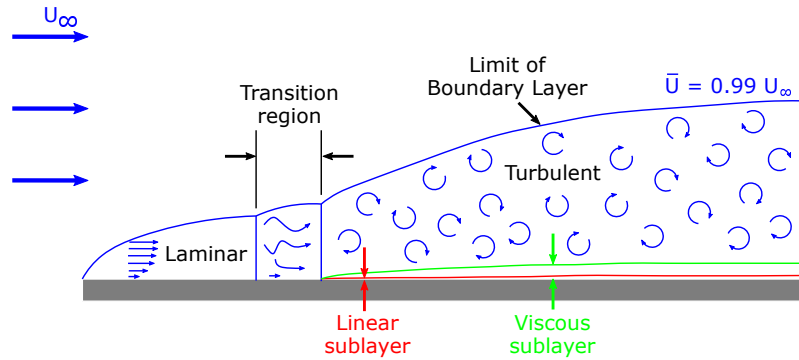


Figure 3.15. Summary of a boundary layer properties and states

3.3.4 Aero- and hydrodynamic coefficients

When an aero- or hydrodynamic object is subjected to a fluid flow, there are hydrodynamic forces that apply on its surface with the form of hydrodynamic pressure (see Figure 3.16). The main forces resulting from the pressure forces on this object are lift and drag.

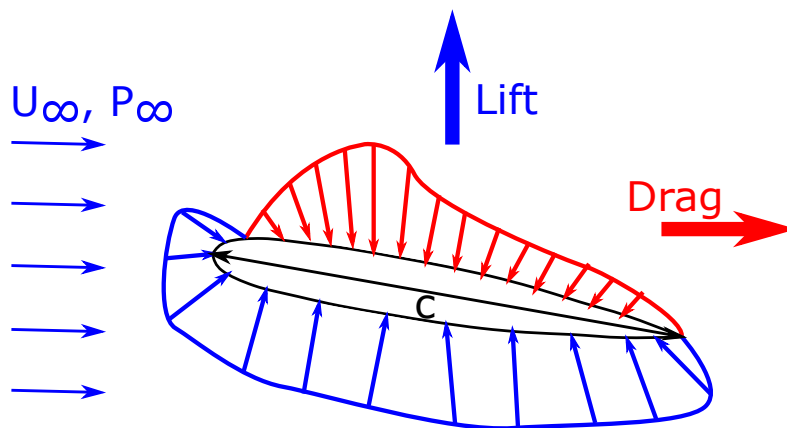


Figure 3.16. Hydrodynamic pressure forces on the hydrofoil

The lift force is defined as the force that is perpendicular to the oncoming flow direction. Whereas, the drag force is the force that opposes to the object's motion in the surrounding fluid. As it can be seen on Figure 3.16, these forces depend on the pressure forces that act on the object and the viscous friction forces made by the flow on the object's surface. The drag force depends strongly on the viscous friction forces for high velocities.

As suggested in the previous Sections, the pressure forces in a fluid flow strongly depend on the fluid flow's properties (density, viscosity, velocity...) and the object's geometry (shape, length, width...).

Thus, if someone would like to compare the best geometrical shapes, and shapes only, for some targeted force, (*e.g.* shapes that generate highest lifts, shapes that generate highest drag, best lift/drag ratio...) how should he/she proceed ? Indeed, because of the numerous parameters affecting pressure forces applied to an object in a flow, how is it possible to isolate the shape only ? The answer to this problem is the same as the one implemented for the Reynolds number's issues: non-dimensionalisation of forces.

All these forces depend on the pressure field around the object, and this pressure field is strongly dependent on the geometry, the fluid's velocity and the fluid's density. Hence, even for pressure, there is a need of isolating the effect of geometry only and not the other parameters. The solution to do that for pressure, is to remove the hydrostatic pressure component of the total pressure expression, and divide the total amount of pressure around a body by the initial dynamic pressure of the fluid (see Equation 3.27).

$$C_p^i = \frac{P_i - P_\infty}{\frac{1}{2}\rho U_\infty^2} \quad (3.27)$$

In Equation 3.27, C_p^i represents the non-dimensional pressure coefficient at a given location i , P_i is the pressure value of a given location, P_∞ represents the hydrostatic pressure value of the fluid flow far from the object, ρ stands for density and U_∞ is the flow's velocity far from the object.

This pressure coefficient gives insight on how the pressure in the flow is affected by the object's geometry. The pressure coefficient C_p^i can have negative, positive or null values.

- A negative value of C_p^i means that the local pressure near this region of the object is lower than the reference pressure P_∞ (in a majority of cases, for aeronautics problems, the reference pressure is the atmospheric pressure $P_{atm} = 1.10^5 Pa$). It is said that these regions are "low" or "under-pressured" regions of the flow.
- On the contrary, a positive value of C_p^i means that the local pressure near this region of the object is higher than the reference pressure. It is said that these regions are "over-pressured" regions of the flow.
- Finally, a null value of C_p^i means that the local pressure near this region of the object is equal to the reference pressure. For these types of regions there is no specific name attributed.

The product $\frac{1}{2}\rho U_\infty^2$ states as the dynamic pressure term, it represents the dynamic pressure embodied by the flow. Despite being negative, null or positive, the pressure coefficient C_p^i can have values inferior, equal or superior to 1. Depending on the absolute value exhibited by this coefficient, this gives information about the flow's velocity status.

- An absolute value of C_p^i inferior to 1 means that the local velocity in the considered region of the object is lower than the reference velocity U_∞ (in a majority of cases, the reference velocity is the velocity far from the considered object).
- On the contrary, an absolute value of C_p^i superior to 1 means that the local velocity in the considered region of the object is higher than the reference velocity.
- Finally, an absolute value of C_p^i equal to one means that the local velocity near this region of the object is equal to the reference velocity. This type of region is called a "stagnation point".

An additional interesting property from the formulation of pressure coefficient C_p^i in Equation 3.27 is that no quantity related to the object's dimension is included (length, radius, width...). This implies that the values of pressure coefficients obtained for a smaller scale object are the same for bigger size objects. Thus the pressure coefficients values obtained for the 1/10th scale model of an aircraft is the same as the full scale aircraft.

Now, for the lift and drag forces that are related to pressure forces, the logic is the same for non-dimensionalising them. However, on the contrary of pressure, the forces have a direct dependance on the scale of the objects that must be taken into account in the non-dimensional equations. To be more precise, the lift and drag forces have a direct dependence with the surface of contact of the considered object. Having said that, the non dimensional lift coefficient C_L and drag coefficient C_D are defined by Equation 3.28.

$$\begin{aligned} C_L &= \frac{F_{Lift}}{\frac{1}{2}\rho U_\infty^2 S} \\ C_D &= \frac{F_{Drag}}{\frac{1}{2}\rho U_\infty^2 S} \end{aligned} \tag{3.28}$$

In Equation 3.28, F_{Lift} and F_{Drag} are respectively the total lift force and the total drag force that applies on the object. S is the surface where the lift and pressure forces apply. For the case of a 2D profile with an infinite span, the surface can be replaced by the characteristic length of the object (*e.g.* the chord length c for an air- or hydrofoil represented on Figure 3.16). Equation 3.29 represents the lift and drag coefficients for a

2D hydrofoil.

$$C_L = \frac{F_{Lift}}{\frac{1}{2}\rho U_\infty^2 c \times 1m} \quad (3.29)$$

$$C_D = \frac{F_{Drag}}{\frac{1}{2}\rho U_\infty^2 c \times 1m}$$

In Equations 3.28 and 3.29, there is still a link to be made between the lift forces and the drag forces and the pressure forces applying to an immersed object (see Equation 3.27). For being able to do that, the external forces applying to the object must be listed. Equation 3.30 lists all forces applied from the fluid to the immersed object.

$$\begin{aligned} \sum F_{Fluid \rightarrow Object} &= F_{Pressure} + F_{Friction drag} \\ &= F_{Lift} + F_{Drag pressure} + F_{Friction drag} \end{aligned} \quad (3.30)$$

It can be seen that the pressure forces can be divided in two categories: lift forces and drag forces. Lift forces are composed of the pressure forces components that are perpendicular to the flow motion, whereas drag forces are composed of the pressure forces components that are parallel to the flow motion. In addition to these, there are also the viscous friction forces that result from the flow's movement next to the surface of the object. Figure 3.17 illustrates how the forces act on the immersed object.

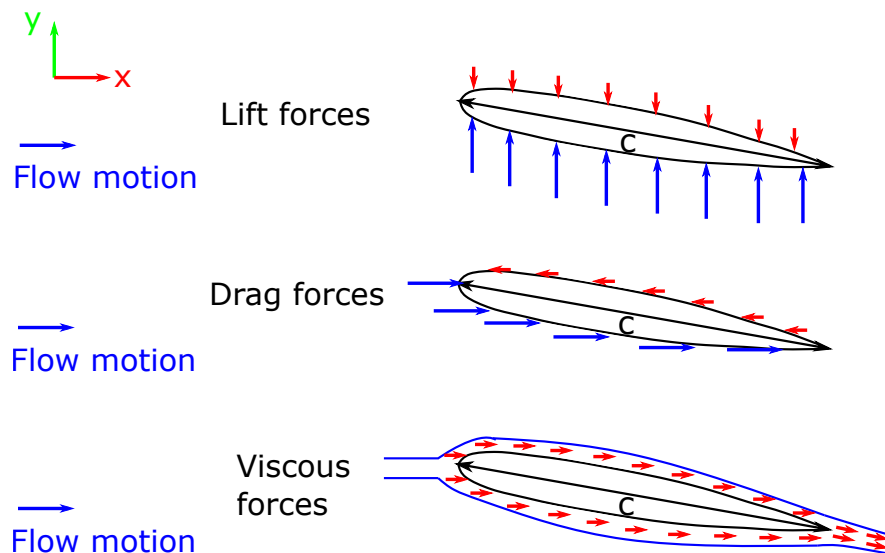


Figure 3.17. Fluid forces action on the immersed object

Now that the fluid forces exerted on the object have been explicitated, each force will be

isolated and its expression will be sought after. The lift forces are the first to be concerned, these ones are composed of the pressure forces components that are normal to the flow motion, thus these forces can be formulated by Equation 3.31. Considering Figure 3.17, the direction normal to the flow motion is considered as being the vector \bar{y} , \bar{n}_S being the surface normal vector and S being the exterior surface of the object.

$$F_{Lift} = \int_S (P(S) - P_\infty) \cdot \bar{n}_S \cdot \bar{y} \cdot dS \quad (3.31)$$

Now that the expression of the lift forces have been expressed, if Equation 3.31 is introduced into Equation 3.28, the expression of the lift Coefficient is given in Equation 3.32.

$$C_L = \frac{1}{\frac{1}{2}\rho U_\infty^2 S} \int_S (P(S) - P_\infty) \cdot \bar{n}_S \cdot \bar{y} \cdot dS = \frac{1}{S} \int_S C_p(S) \cdot \bar{n}_S \cdot \bar{y} \cdot dS \quad (3.32)$$

If the considered problem is 2 dimensional (*i.e.* the object’s span is infinite), Equation 3.32 can be rewritten as Equation 3.33 with c being the object’s length (*i.e.* c is used for an hydrofoil chord).

$$C_L = \frac{1}{c} \int_x C_p(x) \cdot \bar{n}_S \cdot \bar{y} \cdot dx \quad (3.33)$$

Reciprocally, for the drag forces coming from the fluid’s pressure on the object can be expressed in a similar form (see Equation 3.34). Here, the only thing that changes is the components of the pressure forces that are taken, which are taken in the \bar{x} direction.

$$C_{Dp} = \frac{1}{c} \int_x C_p(x) \cdot \bar{n}_S \cdot \bar{x} \cdot dx \quad (3.34)$$

The last forces that need to be expressed are the friction viscous forces that oppose to the object’s movement. The viscous frictions occurs very near the wall, inside the boundary layer of the object. Thus, the viscous forces can be expressed as the surface integral of the product of the local wall shear stress τ_w (see section A.2.7 for more details) and the object’s local surface dS (see Equation 3.35).

$$F_{Viscous} = \int_S \tau_w(S) \cdot \bar{n}_S \cdot \bar{x} \cdot dS \quad (3.35)$$

Dividing these forces by the dynamic forces expression $\frac{1}{2}\rho U_\infty^2 S$, it gives the expression of the viscous friction forces non-dimensional coefficient, the skin-friction coefficient (see Equation 3.36). With $c_f(S)$ being the local skin friction coefficient.

$$C_f = \frac{1}{\frac{1}{2}\rho U_\infty^2 S} \int_S \tau_w(S) \cdot \bar{n}_S \cdot \bar{x} \cdot dS = \frac{1}{S} \int_S c_f(S) \cdot \bar{n}_S \cdot \bar{x} \cdot dS \quad (3.36)$$

As for the other coefficients, in a 2D problem, Equation 3.36 can be rewritten as Equation 3.37.

$$C_f = \frac{1}{c} \int_x c_f(x) \cdot \bar{n}_S \cdot \bar{x} \cdot dx \quad (3.37)$$

Adding Equation 3.34 and 3.37 gives the final expression of the total drag coefficient 3.38.

$$C_D = C_{Dp} + C_f = \frac{1}{c} \int_x (C_P(x) + c_f(x)) \cdot \bar{n}_S \cdot \bar{x} \cdot dx \quad (3.38)$$

3.3.5 Incompressible turbulent flow governing equations

When the Reynolds number turns out to be big and the flow becomes turbulent, the velocity profile measured empirically starts to have a rather chaotic behavior (see Figure 3.18). Pressure and velocity being coupled, the pressure profile also displays such a behavior. This type of velocity profile is currently non-solvable numerically or theoretically.

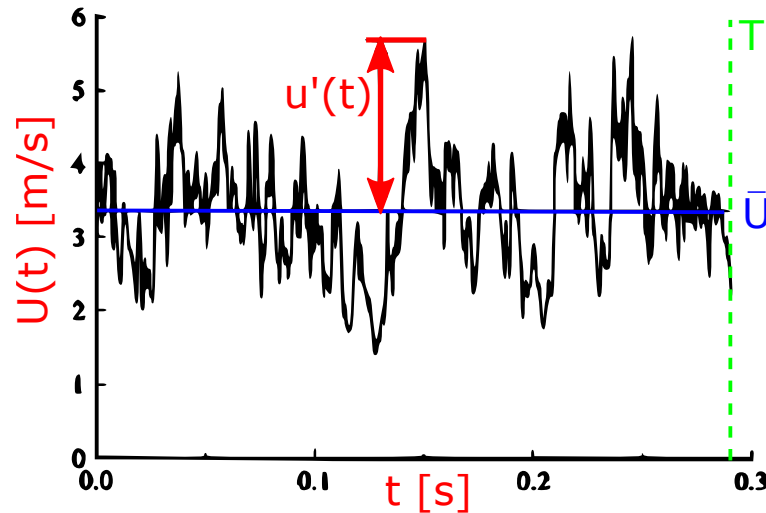


Figure 3.18. Example of a velocity profile in a turbulent flow [29]

As engineers, being able to predict these kind of profiles precisely is not interesting for our application (simulating the water flow around a turbulent hydrofoil): only the mean

velocity matters. Hence, Osborne Reynolds has developed an idea in 1895, time averaging the velocity profile of turbulent flows. Equation 3.39 shows the time averaging formula.

$$\bar{V}_i = \frac{1}{T} \int_0^T v_i(t) dt \quad (3.39)$$

In this equation, \bar{V}_i represents the mean velocity vector, T is the averaging period and $v_i(t)$ is the fluctuating velocity profile. On Figure 3.18, $U(t)$ represents the turbulent fluctuating velocity and \bar{U} is the mean velocity profile. Having said that, the fluctuating velocity equation can be formulated by Equation 3.40.

$$v_i(t) = \bar{V}_i + v'_i(t) \quad (3.40)$$

In Equation 3.40, the $v'_i(t)$ term represents the fluctuations in velocity due to turbulence in the flow. By time averaging these fluctuations, it can be found that its final value is 0 (see Equation 3.41). For this equation to be true, the period T must be taken so that T is much greater than the fluctuation period (*e.g.* in Figure 3.18, the period T is equal to 0.3 s which includes hundreds of fluctuations).

$$\overline{v'_i(t)} = \frac{1}{T} \int_0^T v_i(t) - \bar{V}_i dt = \bar{V}_i - \bar{V}_i = 0 \quad (3.41)$$

Nonetheless, one must be careful, the time averaging of the product of fluctuating terms is not equal to zero (see Equation 3.42). The principle of time-averaging quantities is to eliminate those unknown fluctuations, thus having expressions in fluid dynamics constitutive equations similar to the ones time-averaged in Equation 3.42 would be though. Indeed, there would be no analytical or numerical ways to estimate this term in a direct approach.

$$\overline{v'_i(t)^2} = \frac{1}{T} \int_0^T v'_i(t)^2 dt \neq 0 \quad (3.42)$$

As implied earlier, the Reynolds time-averaging is also true for pressure values (see Equation 3.43).

$$\begin{cases} \bar{P} = \frac{1}{T} \int_0^T p(t) dt \\ p(t) = \bar{P} + p'(t) \\ \overline{p'(t)} = \frac{1}{T} \int_0^T p(t) - \bar{P} dt = \bar{P} - \bar{P} = 0 \end{cases} \quad (3.43)$$

The two main sets of equations used for the modeling of incompressible water flows, the Navier-Stokes Equations (NSE) and the Poisson's Pressure Equation (PPE), are time-averaged through the Reynolds time-averaging procedure. Equation 3.44 gives respectively the Reynolds Averaged Navier-Stokes equations (RANS) and the Reynolds Averaged Poisson's Pressure Equation (RAPPE). In this equation, \bar{P}_k is the sum of the mean fluid pressure \bar{P} and the isotropic Reynolds stress $\bar{P}_k = \bar{P} + \frac{2}{3}\rho k$ where k is the turbulence kinetic energy $k = \frac{1}{2}\overline{v'_i v'_i}$ and ν_t is the turbulent viscosity of the turbulent flow.

$$\begin{array}{c}
 \text{RANS} \\
 \bar{V}_j \frac{\partial \bar{V}_i}{\partial x_j} = -\frac{1}{\rho} \frac{\partial \bar{P}_k}{\partial x_i} + \frac{\partial}{\partial x_j} \left((\nu_t + \nu) \left(\frac{\partial \bar{V}_i}{\partial x_j} + \frac{\partial \bar{V}_j}{\partial x_i} \right) \right) \\
 \text{RAPPE} \\
 \frac{1}{\rho} \frac{\partial^2 \bar{P}_k}{\partial x_i^2} = -\frac{\partial \bar{V}_j}{\partial x_i} \frac{\partial \bar{V}_i}{\partial x_j} + \frac{\partial^2}{\partial x_j \partial x_i} \left(\nu_t \left(\frac{\partial \bar{V}_i}{\partial x_j} + \frac{\partial \bar{V}_j}{\partial x_i} \right) \right)
 \end{array} \tag{3.44}$$

In addition to the classic unknowns, the velocity field \bar{V}_i and the pressure field \bar{P}_k , the turbulent viscosity ν_t must also be determined. To do that, turbulence models are used in complement to this set of equations to determine this turbulent viscosity. The turbulence model used in this study is known as the Spalart-Allmaras model [279]. Appendix A details this turbulence model and details the comparative simulations realised with NASA's NACA0012 airfoil simulations [214] for validating the use of this turbulence model.

3.4 Materials and Methods

3.4.1 Initial flow conditions

Before starting to develop the numerical fluid model of our hydrofoil, it is very important to clearly identify the conditions to which the flow will be subjugated (velocity, hydrofoil size, Reynolds number of the flow...). The first thing to identify is the flow's velocity range that can be attained by a foiling vehicle (sailing boat, motorised boat, surf...) that is equipped with hydrofoils. In our work, we are especially interested in the velocity ranges that can be attained while the boat is foiling (when the boat's hull is widely above the water's surface while moving). To do that, it can be interesting to look at the scientific literature and the commercial products speed that are available.

In the scientific literature, Graf *et al* have tried to optimise some sailing parameters for

being able to reach the maximum’s velocity attainable for an Olympic sailing boat while foiling over water [28]. In their predictions, the maximum speed that the sailing boat could attain while foiling was comprised between 8 and 9.5 m/s for true wind speeds ranged between 5 and 9 m/s [28]. Nonetheless, the highest measured velocity for the sailing boat while foiling was 7 m/s for a true wind velocity of 7 m/s [28]. In the work of Hagemeister *et al* [27], they tried to predict the velocity of foiling sailing catamarans used for America’s Cup. In these studies, Hagemeister *et al* predicted that the boat’s foiling velocity was ranged from 12 m/s up to 25 m/s [27]. In the commercial area, electric motorised foiling surfs have been developed [280], the maximum velocity attainable is approximately 9 m/s. However, the surf can start foiling at a speed lower than this one, even though the speed is not specified in the video. Other small sailing boats, called Moths, have speed ranged between 5 m/s and 10 m/s [281]. Hence the range of speed that can be targeted in our work would be between 5 m/s and 20 m/s.

Now that the velocity range has been fixed, we must determine the size of the hydrofoil that will be underwater. In their work, Hagemeister *et al* stated that the hydrofoil’s chord length varied depending on the region and the type of foil considered [27]. The hydrofoil’s length is ranged for 0.30 meters for the smallest and 0.80 meters for the longest one [27].

So with these data, and by knowing the fact that water’s kinematic viscosity value is $\nu = 1.10^{-6}$, the Reynolds number range of functionality can be calculated for an hydrofoil. The Reynolds number ranges from 1.5×10^6 to 16×10^6 , which makes the water flow around the airfoil strongly turbulent. Moreover, knowing that the speed of sound in water is approximately 1480 m/s in water, this leads to have a Mach number with a value extremely close to zero. Hence, this water flow is incompressible. All these criteria are summed up in Table 3.2.

The very last requirement needed, that is not present in the Table, is the obligation to **avoid cavitation around hydrofoil**.

3.4.2 Hydrofoil selection and fluid flow’s boundary conditions

In the studies where passive morphing is investigated, the airfoil Eppler 420 is used [47], [69], [76]. The reason behind this choice is **the location of the center of pressure**, which is located in the trailing edge of the airfoil. Hence, when the airfoil is clamped in a cantilever configuration and submitted to an airflow, the trailing edge region is the one to deform.

Hydrofoil properties	Range values
Fluid name and properties	Water $\rho = 1000 \text{ kg/m}^3$ $\mu = 1.10^{-3} \text{ Pa.s}$
Mach number	Mach ≈ 0 Incompressible fluid
Hydrofoil dimensions	min = 0.3 m max = 0.8 m
Flow speed	min = 5 m/s max = 20 m/s
Reynolds number	min = 1 500 000 max = 16 000 000

Table 3.2. Boat's hydrofoil flow properties

These studies are the reference studies of this chapter, which results need to be replicated with our cellular morphing hydrofoil concept. Thus, **the Eppler 420 hydrofoil is chosen for this study**. Now, the waterflow velocity and the hydrofoil's size have to be defined. In Table 3.2, a list of requirements was established.

In addition to these requirements, cavitation must be avoided in the numerical model and the hydrofoil size must be printable on the Anisoprint printer's plate. The plate's size is 29.7cm \times 42cm. The printer was changed from the original Ultimaker used for manufacturing the samples of Chapter 2 to an Anisoprint because of its ability to 3D-print continuous fibers reinforced thermo-plastics [170]. Even though only 3D-printable polymers will be considered for this study, carbon or glass fibers composites might be useful for later designs.

In § 1.2.2 of Chapter 1, it has been shown that for cavitation to occur, the local pressure P_i has to be lower than the vapor pressure $P_v \approx 2000 \text{ Pa}$. Thus, around the Eppler 420 hydrofoil, Equation 3.45 must be respected with P_i^{min} being the minimal pressure around the hydrofoil.

$$P_i^{min} > P_v \quad (3.45)$$

Equation 3.46 gives the maximal velocity for which this condition is respected, with P_0 being the reference pressure, C_p^{min} being the minimum pressure coefficient around the hydrofoil and ρ being the water's density. Arithmetically, P_0 is considered to be the

atmospheric pressure $P_{atm} = 1.10^5 Pa$, $C_p^{min} = -1.8$ and $\rho = 1000 kg.m^{-3}$. By changing all those values in Equation 3.46, the minimal fluid velocity for avoiding cavitation is $v_{max} = 10.4 m.s^{-1}$.

$$v_{max} < \sqrt{\frac{2.(P_0 - P_v)}{|C_p^{min}|.\rho}} \quad (3.46)$$

Table 3.3 shows the different values of the hydrofoil’s geometric properties and the flow’s parameters. With a chord length of 43 cm, the hydrofoil can be printed in the diagonal of the Anisoprint’s plate which is 51 cm long. Here the flow velocity was chosen to be 7 m.s⁻¹ to be far enough from the cavitating velocity and ensure the absence of cavitation around the hydrofoil. These conditions are within the ranges fixed in Table 3.2.

Hydrofoil and flow properties	values
Fluid name and properties	Water $\rho = 1000 kg/m^3$ $\mu = 1.10^{-3} Pa.s$
Mach number	Mach ≈ 0 Incompressible fluid
Hydrofoil chord length	0.43 m
Flow velocity	7 m/s
Reynolds number	3 000 000

Table 3.3. Hydrofoil dimensions and water flow parameters

3.4.3 Fluid-structure interaction model development: the fluid model

In Table 3.3, it can be seen that the Reynolds number is close to 3 million indicating that the flow is **turbulent** around the Eppler 420 hydrofoil. Thus, the modeling techniques developed on Abaqus CFD in Appendix A can be reused here.

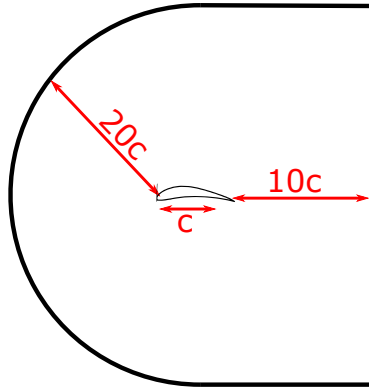
Table 3.4 show the simulation parameters used for simulating the water flow around the Eppler 420 hydrofoil depicted in Table 3.3.

The conclusions of chapter A pointed out that the simulation time was far too long to be used for a FSI approach. Thus, the model was changed for having a fluid simulation

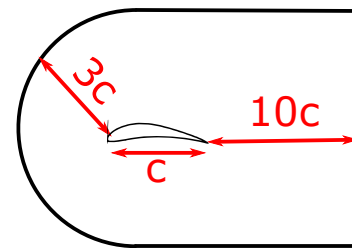
Water flow properties	values
Fluid name and properties	Water $\rho = 1000 \text{ kg/m}^3$ $\mu = 1.00^{-3} \text{ Pa.s}$
Mach number	Mach ≈ 0 Incompressible fluid
Hydrofoil dimensions	0.43 m
Flow speed	7 m/s
Reynolds number	3 million
Angle of attack	2°
Turbulence model used	Spalart-Allmaras
y^+ value	62.5 log-law region
Simulation time T	0.0015 s

Table 3.4. *Eppler 420 flow boundary conditions*

time close to 5 min. Two parameters were changed for reducing the simulation time: firstly, the total fluid simulated time was passed from $T = 0.33 \text{ s}$ to $T = 1.5 \times 10^{-3} \text{ s}$ (see Table 3.4), then the size of the front semi-circle of the domain was reduced to three times the size of the chord (see Figure 3.19). The angle of attack of the hydrofoil was set to $\alpha = 2^\circ$ because it was the angle of attack used for all passive morphing studies using the Eppler 420 profile [47], [69], [76].



(a) Numerical model geometry for the Eppler 420 modelisation in chapter A



(b) Numerical model geometry for the Eppler 420 modelisation for the FSI

Figure 3.19. *Eppler 420 numerical domain sizes from chapter A and for the FSI*

Figure 3.20 shows the boundary conditions applied to the current fluid domain for simulating the water flow.

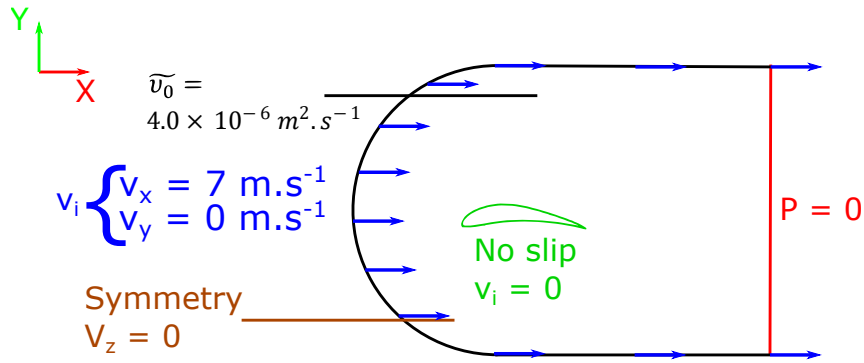


Figure 3.20. Fluid model’s boundary conditions

For meshing this model, a partition needs to be made and meshing gradients must be applied on the partitioning edges. The meshing gradient and the partition of the domain is shown in Figure 3.21, the gradient starts from a mesh size of 0.36 m at the external boundaries to a mesh size of $2.27 \cdot 10^{-4}$ m near the hydrofoil edges. The meshing size around the hydrofoil was obtained through the method depicted in § A.5.2 of Chapter A. The hydrofoil contour size was set to 8 times the height of the hydrofoil mesh ($2.27 \cdot 10^{-4}$ m); *i.e.* 1.82×10^{-3} m.

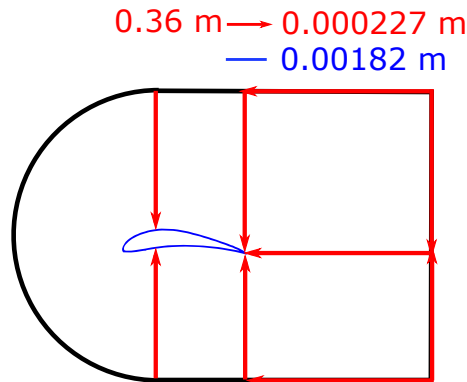


Figure 3.21. Numerical model’s partition and mesh gradient sizes

Figure 3.22 shows the final meshed model, where, the total number of elements is 15 888. The elements used are 3D hexahedral 8 nodes linear bricks.

By strongly reducing the domain’s size and the simulated time, the results displayed by this simulation will inevitably be less close to reality. Thus, the aim of this study is more focused on the methodology for achieving a controllable passive morphing hydrofoil rather than the raw results data obtained by it. If a super-calculator or a CFD technique

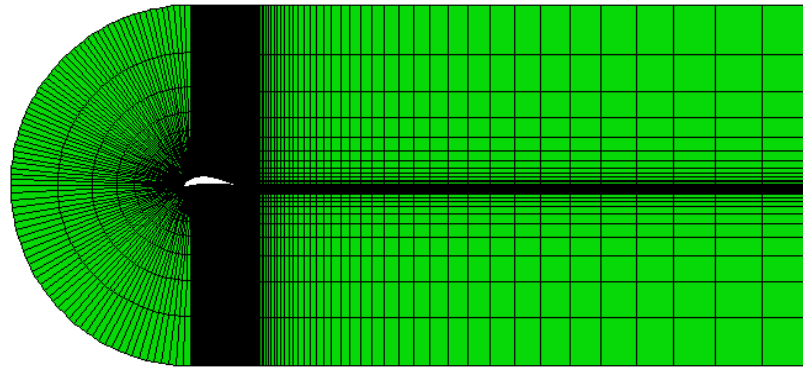


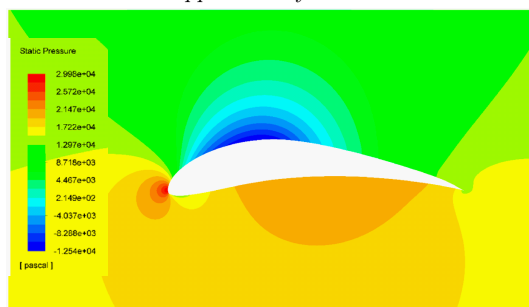
Figure 3.22. FSI Eppler 420 meshed model

that accelerates the simulation time is used, bigger scaled Fluid domains and longer simulation time could be used.

However, despite showing non-accurate data, the pressure field displayed by this FSI fluid model is expected to be close to the pressure distribution of the complete model. On Figure 3.23, it can be seen that the pressure distribution for the simplified FSI model is close to the pressure distribution obtained by Aguilar *et al* [282].



(a) Pressure isovalues around the Eppler 420 hydrofoil obtained with the fluid FSI model



(b) Pressure isovalues around the Eppler 420 hydrofoil from Aguilar *et al* [282]

Figure 3.23. Eppler 420 numerical domain sizes from chapter A and for the FSI

3.4.4 Fluid-structure interaction model development: the solid model

The cellular morphing hydrofoil is constituted of two different parts: a skin and a cellular core. As concluded in Chapter 2, the skin and the cellular core will be modeled with continuous materials. The hydrofoil’s core being a homogeneous equivalent material of a cellular structure. In order to use this configuration, the scale difference in the skin’s principle and the core’s rigidity coefficients must be at least of 100 times (see § 2.4.2 in Chapter 2).

Figure 3.24 shows the hydrofoil configuration. The skin is modeled as an isotropic material with two elastic coefficients: the Young’s modulus and the Poisson’s ratio. The skin is expected to be a 3D-printable polymer, thus the value of the Young’s modulus is expected to be between a few hundreds of MPa to 3000 MPa (corresponds to the most rigid 3D-printable polymer). Moreover, it has been chosen as isotropic, because there is currently no information about the anisotropic coefficients of the skin if it is 3D-printed. Thus, keeping an isotropic skin remains the simplest solution. The core is modeled as an anisotropic elastic material with nine coefficients of elasticity. The homogeneous anisotropic core is a representation of a polymeric cellular material, thus its rigidities values fluctuate between few MPa to one hundred of MPa at max. The leading-edge of the hydrofoil is pinned for the trailing-edge to move under the hydrodynamic loading. The hydrodynamic loads are then applied to the hydrofoil’s upper and lower surface.

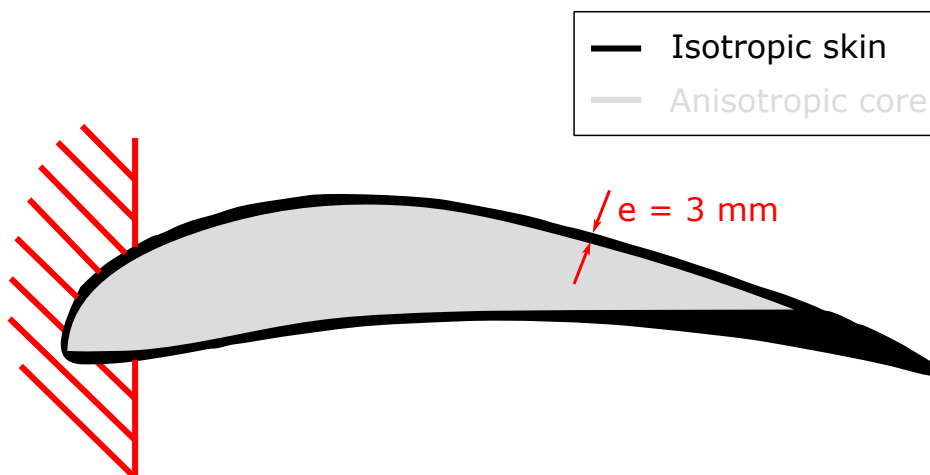


Figure 3.24. Solid hydrofoil model’s configuration

The solid model's units are not in $N.mm^{-1}$ but in $N.m^{-1}$. This unit system has been chosen, because the fluid model is based on $N.m^{-1}$, hence for avoiding unit mismatching the fluid model's unit system is conserved. The model's mesh was generated with 3D quadratic finite elements with full integration. A quadratic mesh was selected instead of a linear mesh for being able to precisely model the bending deformations. 1729 elements were used in total to mesh this model.

3.4.5 Fluid-structure interaction model development: spatial and temporal interfacing

The model's temporal interfacing was conducted by dissociating the solid's simulated time and the fluid's simulated time in an **explicit synchronised offsetted scheme** (see § 3.1). The fluid's model pressure forces are modeled and then sent after 0.0015 s of simulated time, the reaction displacements are then estimated by the solid solver and these displacements are then sent back to the fluid model.

For transmitting the pressure forces from the fluid model to the solid model, a spatial interface is used. Indeed, the airfoil's wall boundary in the fluid model is composed of almost 1300 nodes whereas the solid model's hydrofoil boundaries are composed of approximately 750. In order to transmit the pressure to the solid model, a **spatial interface** is used.

This spatial interface consists in grouping the 1300 values of pressures into **pressure regions**. For applying specific pressure values on an area on a solid model in Abaqus, **the mesh maximal size needs to be at the size of the pressure region considered**. Thus, if no interface is used, the 1300 nodes values will be considered as pressure regions, inducing that the solid model must have 1300 elements which will slow the simulation down in a non-negligible way.

Hence, the different pressure nodes of the 1300 nodes on the boundaries are grouped in **pressure regions** where a mean pressure value \bar{P} is applied on the solid's surface. In a pressure region, the pressure values are located within a range of $\bar{P} \pm 10\%$. Algorithm 3 depicts the procedure of how a pressure region is generated. In this algorithm, the Eppler 420 profile is divided into a *superior edge* and an *inferior edge*. The procedure depicted

in Algorithm 3 is done separately for the superior and the inferior edges. The continuity between the pressure regions is ensured by setting the end point of a pressure region as the starting point of another pressure region.

Algorithm 3 Pressure region algorithm

Require: $X_{s_{start}} = X_{s_0}$ ▷ Initialise the starting pressure region’s coordinate
Require: $X_{s_{end}} = X_{s_0}$ ▷ Initialise the ending pressure region’s coordinate
Require: $\bar{P} \leftarrow P_0$
1: **for** $i \leftarrow 1:n$ **do** ▷ n is the number of nodes on the superior or the inferior hydrofoil edge
2: **if** $|\bar{P} - P_i| > 0.1 \times \bar{P}$ **then**
3: Store the actual start and end pressure region points and the \bar{P} value
4: $X_{start} = X_{end}$
5: nbPoints = 0 ▷ number of points in the pressure region
6: PressureSum = 0 ▷ sum of pressure values in the pressure region
7: **end if**
8: nbPoints += 1
9: PressureSum += P_i
10: $\bar{P} = \text{PressureSum}/\text{nbPoints}$
11: $X_{end} = X_i$
12: **end for**

Figure 3.25 shows the different pressure regions on the Eppler 420 faces obtained with Algorithm 3.

A spatial interfacing is also used for transmitting the structure’s deformed shape to the fluid model. Indeed, the solid meshing being highly refined, the 750 nodes that underwent a displacement are available for representing the hydrofoil’s geometric shape. This number of points being large and highly time-consuming for drawing the hydrofoil in a CAD software, a point number diminution is needed.

Algorithm 4 shows how this displacement interfacing is realised for Eppler 420 profile. Once again here, the hydrofoil is separated into 2 edges: a superior edge and an inferior edge. The reduction of the number of points begins after a value of 0.015% of the chord’s length, because a lot of points is needed for precisely representing the Eppler 420 hydrofoil’s leading edge.

After this chord’s value, one out of eight nodes are stored into the coordinate file that will be used later for building the hydrofoil’s shape in the fluid domain. An exception is

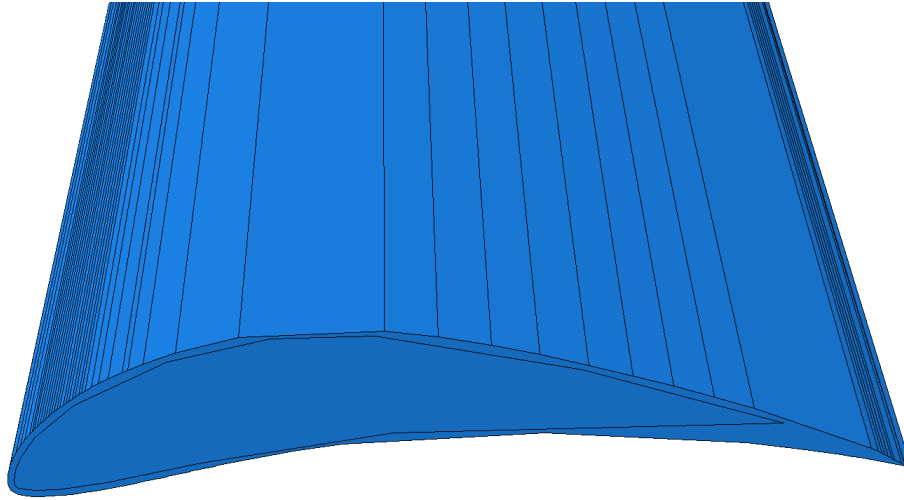


Figure 3.25. Pressure regions obtained for around the hydrofoil

made for the final trailing edge node of the superior and inferior edges of the hydrofoil, this one is always stored because it is common to both edges. With this procedure, the number of points is reduced down to 100 points instead of 750.

Algorithm 4 Hydrofoil points reduction algorithm

- 1: **for** $i \leftarrow 1:n$ **do** $\triangleright n$ is the number of nodes on the superior or the inferior hydrofoil edge
 - 2: **if** x coordinate $< 0.015 \cdot \text{chord length}$ **then**
 - 3: Store the points coordinate into a data structure
 - 4: **else**
 - 5: Store the points coordinate once every 8 rows
 - 6: **end if**
 - 7: **end for**
 - 8: Store the points into a new file
-

3.4.6 Fluid-structure interaction program operation

Now that all the building blocks of the Fluid-Structure Interaction program have been presented, this section aims to present how the program operates. On the contrary of regular Fluid-Structure Interaction programs that have a temporal stopping criteria; *i.e.* the program is stopped when the simulated time is attained by the program, the FSI program developed in this thesis stops when the passive hydrofoil stops moving.

Algorithm 5 presents the operation of the FSI program. This algorithm is mainly a loop that finishes running only until the trailing edge tip of the hydrofoil displacement becomes small compared to the total trailing edge displacement; *i.e.* the displacement of the final iteration is smaller than 10 % of the total value.

Algorithm 5 Hydrofoil points reduction algorithm

Require: $i \leftarrow 1$ ▷ Number of FSI iterations

- 1: **while** $U_{last}^{tip}/U_{tot}^{tip} > 0.1$ **do** ▷ Stopping criteria = the last displacement value of the trailing Edge tip is inferior to 10 % of the total tip’s displacement
- 2: **Fluid model** generation with latest hydrofoil geometric shape
- 3: **Fluid model:** flow around hydrofoil simulated
- 4: **Spatial interface:** Extraction of pressure values and pressure regions generation
- 5: **Solid model** generation and pressure regions application
- 6: **if** $i = 1$ **then** ▷ First iteration
- 7: **Solid model:** Hydrofoil’s displacement simulated
- 8: **else** ▷ Other iterations
- 9: **Solid model:** Previous iteration’s solid model’s residual stress mapped on the new one
- 10: **Solid model:** Hydrofoil’s displacement simulated
- 11: **end if**
- 12: **Solid model:** Store the current trailing edge tip displacements and update the total tip displacement
- 13: **Spatial interface:** Deformed hydrofoil’s contour transferred to the fluid model
- 14: **end while**

For operating, firstly, the fluid model is built with the latest version of the Eppler 420 profile; *i.e.* the original undeformed profile if it is the first iteration and the lastly deformed one otherwise. After building the fluid model, the flow simulation is ran. The pressure values obtained with this model are then transmitted, with the spatial interface, towards the solid model.

Afterwards, the solid model is generated with the different pressure regions. However, the next step depends on the iteration numbers. If, it is the first iteration, the simulation is ran directly after building the model. Else, if the number of iterations is superior to one, the previous iteration’s solid residual stress is mapped on the current solid model before running the new simulation. This is done in order to take the elastic spring-back effect of the hydrofoil’s deformations.

After the simulation is finished, the displacement of the trailing edge tip is stored and

the total displacement is updated. Finally, the spatial interface is used to transfer the deformed hydrofoil's contour to the fluid model and the whole procedure is repeated until the stopping criteria is met.

Figure 3.26 summarizes the operation of the Fluid-Structure Interaction algorithm.

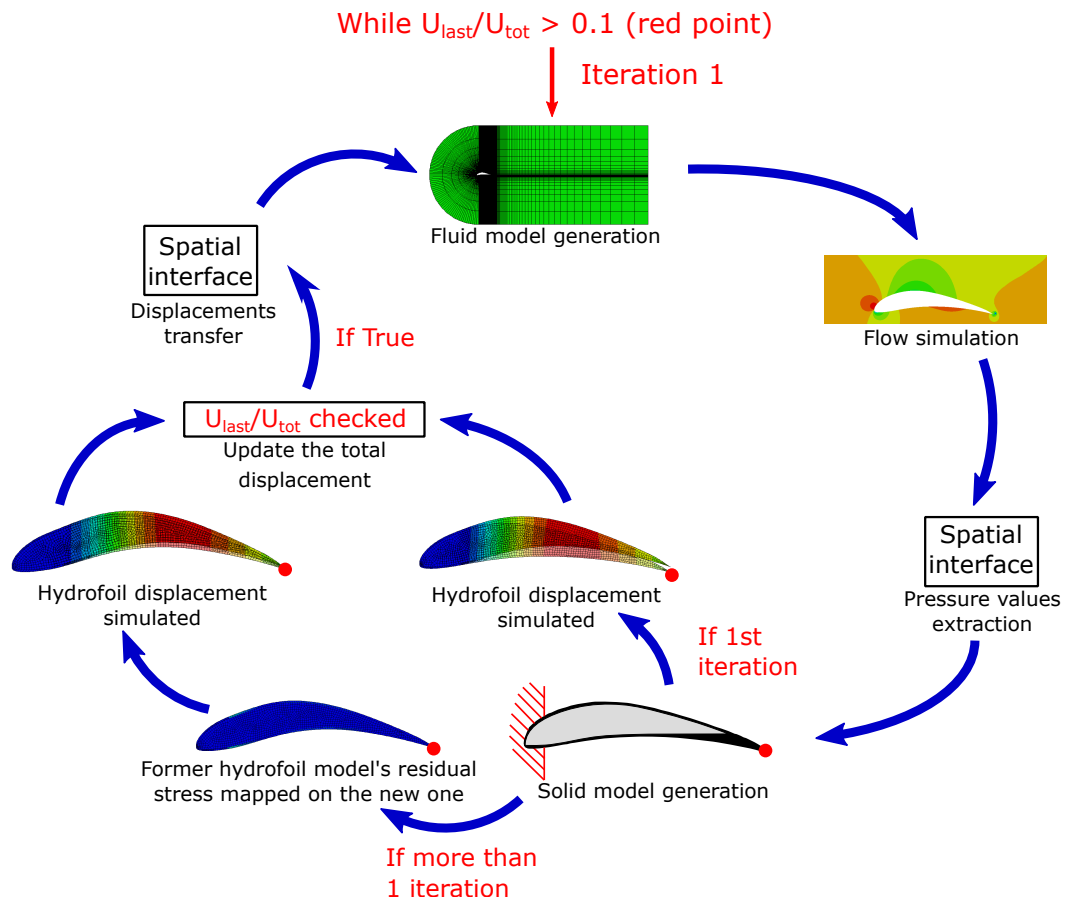


Figure 3.26. FSI operation schematic

3.4.7 Sensitive core elastic coefficient identification protocol

Now that the FSI algorithm has been presented, a focus needs to be made on the solid's model components, namely the hydrofoil's skin and the hydrofoil's core, elastic coefficients need to be set to the skin and the core. Then with a parametric optimisation program the continuous anisotropic core's properties will be approximated with a double-arrow cellular material previously presented in Section 2.2.5.

However, before doing that, it must be noted that optimising a cellular structure for exactly fitting 9 coefficients of elasticity is a complex task. Thus, for simplifying the optimisation problem, the elastic coefficients of the core having an actual effect on the hydrofoil flexural properties must be identified.

In order to do that, a numerical experiment is set up where the skin and the core of the hydrofoil are submitted to the hydrodynamic load described in § 3.4.3. Specific values have been given to the hydrofoil’s skin and core, these are presented in Table 3.5 and Table 3.6 respectively. In the latter Table ‘M’ stands as ‘Millions’ for making the Table more comprehensive.

Young’s modulus	Poisson’s ratio
(Pa)	(-)
1 900 000 000	0.37

Table 3.5. *Elastic properties of the hydrofoil’s skin*

E_{11}	E_{22}	E_{33}	ν_{12}	ν_{13}	ν_{23}	G_{12}	G_{13}	G_{23}
(Pa)	(Pa)	(Pa)	(-)	(-)	(-)	(Pa)	(Pa)	(Pa)
72.5 M	73.5 M	1 310 M	0	0	0	10 M	215 M	215 M

Table 3.6. *Elastic properties of the hydrofoil’s anisotropic core*

The elastic coefficients provided in Table 3.5 correspond to the isotropic CPE polymer used for 3D printing structures in Chapter 2. The elastic coefficients used in Table 3.6 are based on the swastika pattern’s homogenised elastic coefficients seen in Chapter 2. The swastika pattern’s homogenised coefficients were chosen here, because each coefficient can undergo strong individual variations while respecting the material stability requirements (see Equation 3.47).

$$\left\{ \begin{array}{l} E_{11}, E_{22}, E_{33}, G_{12}, G_{13}, G_{23} > 0 \\ |\nu_{12}| < \left(\frac{E_{11}}{E_{22}}\right)^{1/2} \\ |\nu_{13}| < \left(\frac{E_{11}}{E_{33}}\right)^{1/2} \\ |\nu_{23}| < \left(\frac{E_{22}}{E_{33}}\right)^{1/2} \\ 1 - \nu_{12}\nu_{21} - \nu_{23}\nu_{32} - \nu_{31}\nu_{13} - 2\nu_{21}\nu_{32}\nu_{13} > 0 \end{array} \right. \quad (3.47)$$

For other pattern's homogenised elastic coefficients, the testing of certain coefficients would need to readjust the other coefficients values. The new elastic rigidity coefficients of Table 3.6 were set higher than those of Chapter 3.6 for ensuring no hydroelastic instabilities.

A FSI simulation is ran with these coefficients in the same configuration as described in § 3.4.4 and the total hydrofoil tip displacement; *i.e.* the red point's displacement in Figure 3.27 is measured at the end of the simulation. The anisotropic core's properties depicted in Table 3.6 and its associated displacement value of the morphing hydrofoil depicted in Figure 3.27 are considered as the **initial configuration** to which other configurations with different coefficients of elasticity will be compared to.

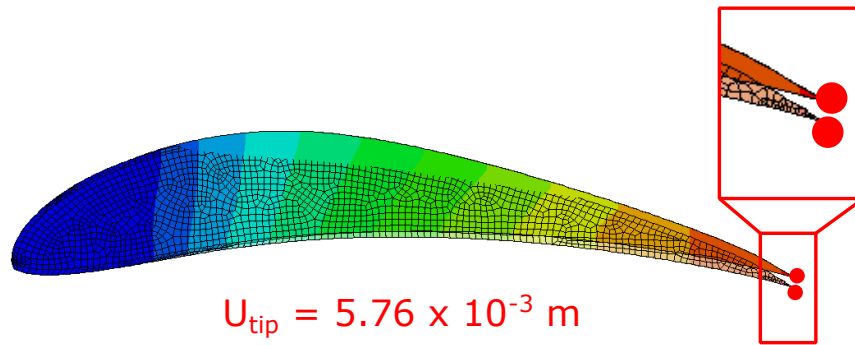


Figure 3.27. Displacement of the initial configuration of the sensitivity test

For testing the sensitivity of the final hydrofoil's tip displacement with regard to the different elastic coefficients of the core, each elastic coefficient will be individually increased or decreased and the relative difference of tip displacements between the different configurations will be calculated with Equation 3.48. In this Equation, U_{tested} is the hydrofoil's final displacement of a configuration where one elastic coefficient is tested and

U_{init} is the displacement of the initial configuration tested above.

$$r = \frac{U_{tested} - U_{init}}{U_{init}} \quad (3.48)$$

For increasing or decreasing each elastic coefficient, two different methods will be used for two groups of coefficients: the elastic tensile and shear rigidities and the Poisson’s ratios. For the elastic rigidities, the coefficient of interest is divided by 10 and multiplied by 10. An example is provided in Table 3.7 with the coefficient E_{11} . Such extreme decreases and increases are made, because of the morphing concept chosen here, the skin’s rigidity should be the main parameter tailoring the hydrofoil’s behavior. Thus, such extreme variations are required for observing some differences on the trailing edge displacements.

Configuration	E_{11} (Pa)	E_{22} (Pa)	E_{33} (Pa)	ν_{12} (-)	ν_{13} (-)	ν_{23} (-)	G_{12} (Pa)	G_{13} (Pa)	G_{23} (Pa)
Initial	72.5 M	73.5 M	1 310 M	0	0	0	10 M	215 M	215 M
Divided by 10	7.25 M	73.5 M	1 310 M	0	0	0	10 M	215 M	215 M
Multiplied by 10	725 M	73.5 M	1 310 M	0	0	0	10 M	215 M	215 M

Table 3.7. An example of rigidity testing with the E_{11} coefficient

For the Poisson’s ratios, because of their null values, they are submitted to an increase of 0.2 and a decrease of 0.2. Table 3.8 shows an example with the coefficient ν_{12} .

Configuration	E_{11} (Pa)	E_{22} (Pa)	E_{33} (Pa)	ν_{12} (-)	ν_{13} (-)	ν_{23} (-)	G_{12} (Pa)	G_{13} (Pa)	G_{23} (Pa)
Initial	72.5 M	73.5 M	1 310 M	0	0	0	10 M	215 M	215 M
0.2 decrease	72.5 M	73.5 M	1 310 M	-0.2	0	0	10 M	215 M	215 M
0.2 increase	725 M	73.5 M	1 310 M	0.2	0	0	10 M	215 M	215 M

Table 3.8. An example of Poisson’s ratio testing with the ν_{12} coefficient

Out of the 9 elastic coefficients, 8 will be tested. The Poisson’s ratio ν_{13} won’t be tested, because for this morphing concept, it is expected to be null. Indeed, a non-null ν_{13} Poisson’s ratio would induce a torsion of the structure that is not wanted.

3.4.8 Tailorability tests of the morphing hydrofoil

The aim of this section is to determine the tailorability range, *i.e.* the relative trailing edge displacement (see Equation 3.50), of the current hydrofoil morphing concept. In order to do that, the mechanical properties of the core will be fixed to specific elastic coefficients and the skin rigidity's mechanical properties are then tailored. The fixed anisotropic core's elastic coefficients values are given in Table 3.9.

E_{11}	E_{22}	E_{33}	ν_{12}	ν_{13}	ν_{23}	G_{12}	G_{13}	G_{23}
(Pa)	(Pa)	(Pa)	(-)	(-)	(-)	(Pa)	(Pa)	(Pa)
7 M	7 M	152 M	-0.5	0	0	15 M	24 M	24 M

Table 3.9. Elastic properties of the hydrofoil's anisotropic core

The coefficients shown in Table 3.9 are purposely low for two reasons: firstly, in order to maximize the tailorability range, the core's rigidity needs to be the lowest possible, and the second reason is to ensure that the core main elastic rigidities are always at least 10 times lower than the skin's elastic rigidity for having a behaviour similar to a sandwich composite (see Chapter 2). This coefficient distribution was chosen to be close to the values of the elastic coefficients of a homogenised double-arrow pattern.

The skin's rigidity is tailored in an interval given in Equation 3.49. The lower and upper bounds values correspond to the minimum and maximum rigidity of 3D printable polymers. The lower bound of 200 M Pa corresponds to the rigidity of a compliant Polyethylene, whereas the upper bound of 3000 M Pa corresponds to the rigidity of a PEEK polymer. For all the skin rigidities included in this interval, a corresponding 3D-printable thermoplastic polymer can be found. This latter requirement ensures the manufacturability of the skin.

$$E_{skin} \in [200 \text{ M Pa}, 3000 \text{ M Pa}] \quad (3.49)$$

The reason for modifying the skin's mechanical properties instead of the core's is linked to the hydrofoil's operation mode. Indeed, the hydrofoil operates as a sandwich composite and the sandwich composite's bending stiffness is theoretically more affected by the skin's mechanical properties variations than the core's mechanical properties variations [283].

In this interval, the evolution of the tailorability in function of the skin rigidity values will be displayed. If, the tailorability ranges of the three reference concepts are matched, namely Heo’s [76], Bornengo’s [47] and Spadoni’s [284] concepts, a 3D-printable polymer will be associated with their tailorability values. Finally, the evolution of the lift/drag ratio C_L/C_D in function of the hydrofoil’s tailorability will be displayed in order to see the impact of the hydrofoil’s deformations on the hydrodynamic properties of the hydrofoil. Equation 3.50 shows how the tailorability is calculated. The tailorability of a concept is defined as the ratio between U_{tip} , the tip total displacement, seen in § 3.4.7 and the chord length $chord$ given in Eq. 3.50.

$$Tailorability = \frac{U_{tip}}{chord} \quad (3.50)$$

3.4.9 Parametric optimisation algorithm of the double arrow architecture

The aim of this section is to present and develop an algorithm able to optimise the geometric features of an architected material’s pattern for approaching its homogenised mechanical properties to the anisotropic mechanical properties of the homogeneous core. The selected architected material here is the double-arrow shape investigated in chapter 2. This pattern was selected for its high shear rigidity/relative density ratio, thus its homogenised coefficients could match a large interval of values.

Figure 3.28 show the double arrow pattern’s geometric features to optimize: the double arrow’s width L , the inner inner angle θ , the outer angle α and the cell wall thickness t . The cell’s height H can be determined with the other parameters.

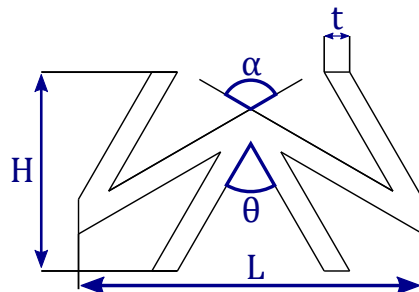


Figure 3.28. Geometric parameters defining a Double-arrow unit cell

The intervals of optimisation of each parameters are given in Equation 3.51. The value of the hydrofoil's maximal height corresponds to the maximal height attainable in the hydrofoil's thickness direction. This value is dependent on the type of hydrofoil used in the simulation model, here with the Eppler 420 profile, the hydrofoil's maximal height corresponds to $h_{max} = \text{chord} \times 0.14$.

$$\left\{ \begin{array}{l} \mathbf{L} \in \left[\frac{\text{Hydrofoil max height}}{15} \text{ mm}; \frac{\text{Hydrofoil max height}}{5} \text{ mm} \right] \\ \mathbf{t} \in [0.5 \text{ mm}; 4 \text{ mm}] \\ \boldsymbol{\alpha} \in [95^\circ; 160^\circ] \\ \boldsymbol{\theta} \in [5^\circ; 80^\circ] \end{array} \right. \quad (3.51)$$

Thus, in our case, the precise values are $\mathbf{L} \in [4 \text{ mm}; 12.4 \text{ mm}]$. The lower boundary value was set to be very low, in order to broaden the research domain as much as possible. Indeed, null values cannot be explicitly specified in the interval for avoiding geometry generation problems in the algorithm. Because of some constraints, that will be detailed later, the width value \mathbf{L} cannot reach the lower boundary.

Because of geometry generation issues in the Abaqus code, the width \mathbf{L} has been selected instead of the cell's height \mathbf{H} as the cell's size parameter. In Chapter 2, it has been shown that the cell size has not a tremendous impact on the bending stiffness of a cellular bending structure. Thus, it should be only ensured that the cell's height is not superior to the hydrofoil's height. Hence, as an almost square Representative Volume Element (RVE) is expected, the cell's width is set to be lower than one fifth of the hydrofoil's height to ensure to have a cell size that is not too large.

In addition to these intervals, optimisation constraints were added to this optimisation for avoiding geometry generation problems. Equation 3.52 shows the different optimisation constraints used for generating the geometry. the two first constraints on \mathbf{t} and the $\boldsymbol{\theta}/\boldsymbol{\alpha}$ ratio consist in avoiding self-intersection between the different struts composing the double-arrow.

$$t < \frac{L}{8} \quad \text{AND} \quad \frac{\theta}{\alpha} < 0.5 \quad \text{AND} \quad \frac{\rho^*}{\rho_s} < 0.3 \quad \text{AND} \quad H < \frac{\text{Hydrofoil height}}{5} \quad (3.52)$$

The two other constraints affect the relative density $\frac{\rho^*}{\rho_s}$ and the hydrofoil’s height H . To calculate these values, the set of equations of Equation 2.27 are used. These sets of equations are given back in Equation 3.53.

$$\begin{aligned}
 H_1 &= \frac{L}{4\sin\left(\frac{\theta}{2}\right)} \\
 H_2 &= \frac{L}{2\sin\left(\frac{\alpha}{2}\right)} \\
 H &= 2H_1\cos\left(\frac{\theta}{2}\right) - H_2\cos\left(\frac{\alpha}{2}\right) \\
 \frac{\rho^*}{\rho_s} &= \frac{4H_1t + 2H_2t}{H.L}
 \end{aligned} \tag{3.53}$$

The constraint on the relative density aims to avoid to exceed the limit relative density of 0.3, beyond which the cellular material do not behave as a compliant cellular material anymore [108]. The constraint on the height H is needed to be sure that the cell size is not too long compared to the hydrofoil’s core height.

The interval values of both angles α and θ are set as large as possible. If their values exceed the lower or the upper boundaries of the interval, the geometry cannot be generated.

The lower interval value of the wall thickness t corresponds to the minimum thickness of a polymeric 3D printed layer. However, the upper boundary value was set as big as possible in order to not avoid any possible solution.

The link between the pattern’s geometric values and its homogenised mechanical properties is complex and the amount of combination needed is too important to just try them all out and see which ones provide the closest mechanical properties to the homogeneous core. Thus, a parametric optimisation algorithm based on the meta-heuristic optimisation algorithm PSO is used for finding the geometric features values leading to the best homogenised mechanical properties. The PSO algorithm used was found on [259] and adapted to the problem.

Before developing the algorithm, one must define precisely the objective function tar-

geted. In this case, the objective function can be defined as having homogenised double-arrow elastic coefficients as close as the homogeneous core's coefficients presented in Table 3.9 of § 3.4.8.

The results of the experiment presented in § 3.4.7 that will be presented in § 3.5 demonstrate that only three coefficients E_{11} , E_{22} and G_{12} out of the original nine have an impact on the bending properties of the hydrofoil. Hence, only those three coefficients will be approximated. Thus, the optimisation vector X is composed of three coefficients and its form is given in Equation 3.54.

$$X = \begin{pmatrix} E_{11} \\ E_{22} \\ G_{12} \end{pmatrix} \quad (3.54)$$

To do that, the objective function is formulated in Equation 3.55. The objective function corresponds to the norm of the error vector between the homogenised coefficients E_{11} , E_{22} and G_{12} and the targeted elastic coefficients E_{11}^{Tar} , E_{22}^{Tar} and G_{12}^{Tar} corresponding to the homogeneous core depicted in Table 3.9 of § 3.4.8.

$$f(X) = \left\| \begin{pmatrix} \frac{E_{11} - E_{11}^{Tar}}{E_{11}^{Tar}} \\ \frac{E_{22} - E_{22}^{Tar}}{E_{22}^{Tar}} \\ \frac{G_{12} - G_{12}^{Tar}}{G_{12}^{Tar}} \end{pmatrix} \right\| \quad (3.55)$$

Algorithm 6 shows the pseudo-code used for this optimisation. This algorithm is very close to the PSO algorithm depicted in Algorithm 2 and presented in § 3.2.2. The difference lies from lines 5 to 13, where the objective function is calculated for all particles and the stopping criteria has to be detailed.

Algorithm 6 Particle Swarm Optimisation

```

1: N = Particles number
2: D = number of dimensions
3: while Number of max iterations not attained AND Speed low than minimal step do
4:   for i=1,N do
5:     if the geometry can be generated then
6:       Generate and homogenise the double-arrow pattern
7:       calculate the objective function  $f(X_i)$ 
8:     else
9:        $f(X_i) = 1000000$  ▷ Large fitness value for non-convergence
10:    end if
11:  end for
12:  for i=1,N do
13:    if  $f(X_i) > f(P_i)$  then
14:      for d=1,D do
15:         $p_{id} = k_{id}$  ▷  $p_{id}$  is the best individual fitness so far
16:      end for
17:    end if
18:  end for
19:   $g = i$ 
20:  for All the neighboring particles of  $i$  do
21:    if  $f(P_j) > f(P_g)$  then
22:       $g = j$  ▷  $g$  is the best individual of the neighborhood
23:    end if
24:  end for
25:  for d=1,D do
26:    Updating speeds and positions with Equation 3.56
27:  end for
28: end while

```

The Equation used at line 26 of Algorithm 6 is reminded in Equation 3.56.

$$\begin{cases} V_i^k = \underbrace{\omega \times V_i^k}_{\text{Inertia}} + \underbrace{c_1 \times rand_1 \times (P_{i,best}^k - X_i^{k-1})}_{\text{Particle's best position memory}} + \underbrace{c_2 \times rand_2 \times (G_{i,best}^k - X_i^{k-1})}_{\text{Best position in the neighborhood}} \\ X_i^k = X_i^{k-1} + V_i^k \end{cases} \quad (3.56)$$

Two stopping criteria are used in this algorithm, the first one is when the maximum number of iterations is reached. In this algorithm, the maximal number of iterations has been set to $MI = 100$. The other stopping criterion is when the speed do not excess the minimal speed. At the beginning of the simulation, a minimum step of $MS = 1.10^{-3}$ is set, when the value of the speed of all the particles is inferior to this value, it means that global minimum of that function is found.

From line 4 to 10, the fitness is calculated for all the different particles. To do that, for each particle, the algorithm checks whether the geometry can be generated and if the constraints linked to the geometry are fulfilled. Two generative constraints are set: the first one checks that the wall thickness $t < L/8$ and that the angle ratio $\alpha/\theta < 0.5$. These parameters have been determined empirically on a parameterized CAD model on Abaqus. These conditions have to be checked before the constraint, otherwise the program crashes during operation. If the generative constraints are not met a large fitness value of 1000000 is attributed to the concerned particle.

The different parameters used for this simulation are given in Equation 3.57:

$$\begin{cases} \omega = 0.8 \\ N = 20 \\ c_1 = 0.5 \\ c_2 = 0.5 \\ \text{Maximum iterations} = 100 \\ \text{Minimum steps} = 1.10^{-3} \end{cases} \quad (3.57)$$

Figure 3.29 summarises the operation of the algorithm operation.

Once the optimised geometric parameters and the optimised elastic properties E_{11} , E_{22} and E_{33} are obtained with the optimisation algorithm, the resulting homogenised elastic properties will be introduced in the hydrofoil's homogeneous core (see Figure 3.30).

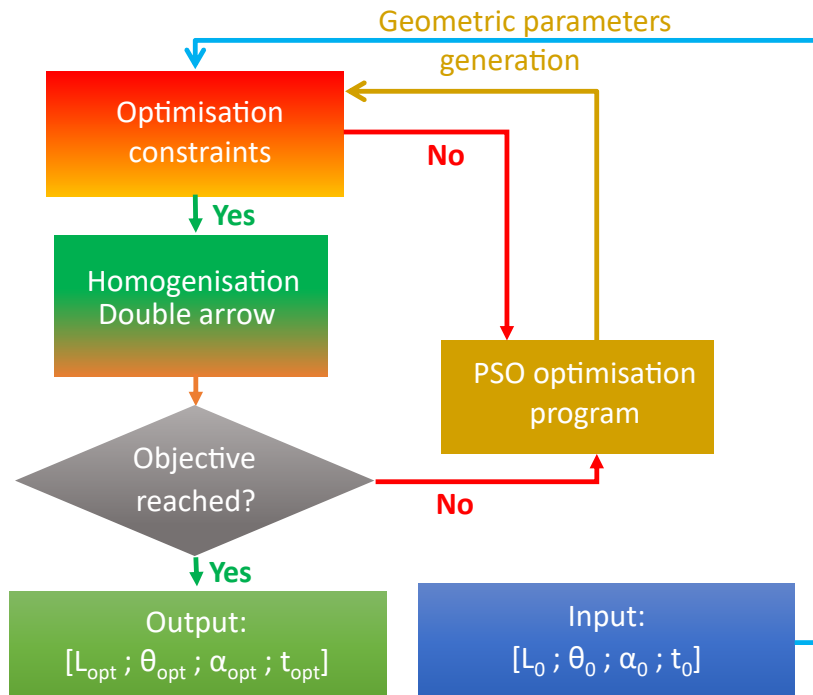


Figure 3.29. Parametric optimisation algorithm

The FSI computations depicted in § 3.4.8 are ran another time with the double-arrow’s optimised homogeneous elastic properties used in the anisotropic core. The results will then be compared to the ones obtained with the protocol of § 3.4.8.

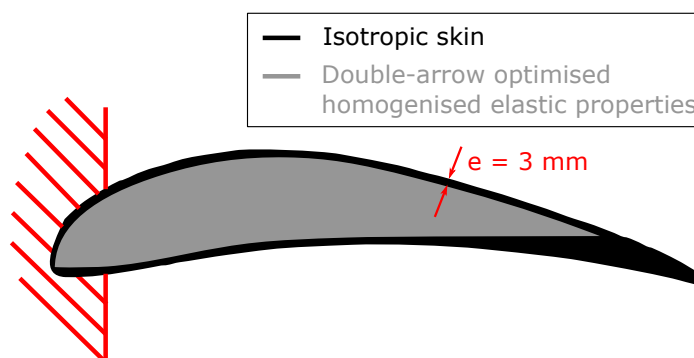


Figure 3.30. FSI solid configuration with double-arrow optimised homogenised elastic coefficients used in the anisotropic core

3.5 Results

3.5.1 Sensitive elastic coefficient identification

Figure 3.31 shows the relative difference in tip displacements for increased and decreased elastic coefficients compared to the original configuration. On this Figure, it can be clearly seen that out of the nine coefficients, only 3 coefficients have a clear impact on the hydrofoil passive bending : E_{11} , E_{22} and G_{12} . The hydrofoil bending stiffness is governed by these 3 coefficients. Thus, in real life, a material having similar E_{11} , E_{22} and G_{12} as the anisotropic continuous core can be used for targeting the same bending properties.

Hence, concerning the parametric optimisation algorithm, only approaching E_{11} , E_{22} and G_{12} with the homogenised elastic coefficients of the double arrow pattern is sufficient for obtaining similar bending properties for the hydrofoil with a cellular core.

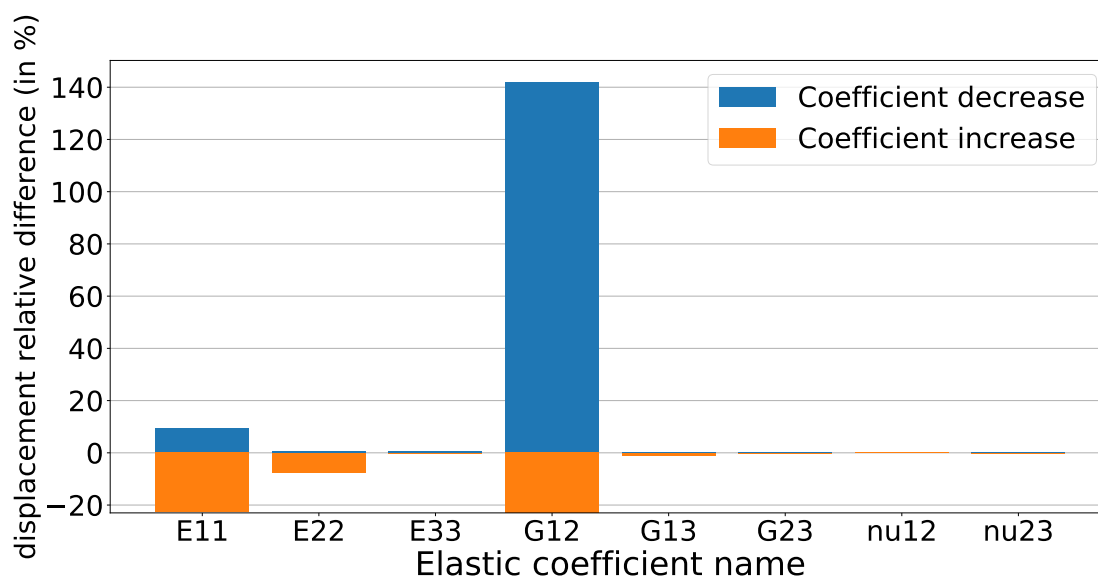


Figure 3.31. Relative difference in hydrofoil tip displacement between a modified configuration and the original one

3.5.2 Tailorability tests of the morphing hydrofoil

Figure 3.32 shows the evolution of the tailorability as a function of the skin's stiffness. On this figure, it can be seen that the tailorability decreases in a linear trend with regard

to skin’s rigidity value. These results are in good agreement with Spadoni’s study that also observed numerically a decrease of the profile’s decambering with the increase of skin’s rigidity [96].

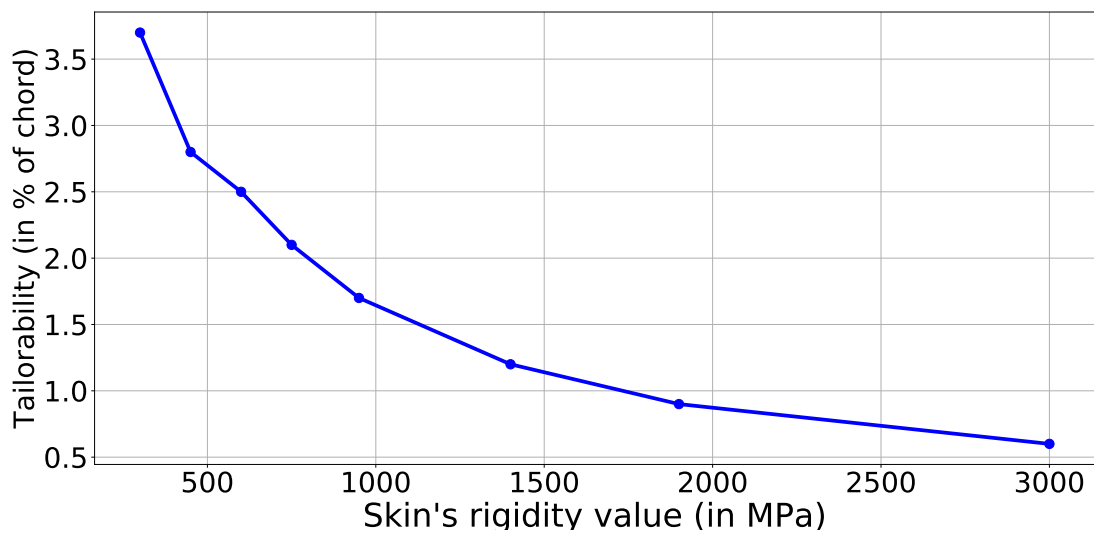


Figure 3.32. Evolution of the tailorability in function of the skin’s rigidity

Table 3.10 shows the tailorability ranges obtained with 3 different skin configurations compared to the tailorability range of the reference concepts found in the literature. It can be seen that, the new passive hydrofoil morphing concept is able to attain the same operation ranges as most of the different concepts encountered in the literature with 3D printable polymer skins ensuring their manufacturability. Only Heo’s concept cannot be attained with 3D printable polymers, the underlying reasons will be discussed in the next Section. One must also be careful to not attain skin rigidity values that are too low. For example here, with a Skin rigidity of 200 MPa, an aeroelastic instability occurs and the algorithm never converges.

Skin type	PEEK	PP	PE (high)	PE (low)
$E_{skin}(Pa)$	3 000 M	950 M	400 M	200 M
Tailorability range Δ (in % of chord)	0.6	1.7	3.0	No convergence
Tailorability range Δ of the literature (in % of chord)	0.4 Heo [76]	1.6 Bornengo [47]	3.2 Spadoni [69]	(-)

Table 3.10. The tailorability ranges obtained with the different skin rigidity configurations associated to 3D printable polymers and the different tailorability ranges found in the literature

Figure 3.33 shows the evolution of the lift/drag ratio C_L/C_D and the tailorability ranges. It can be seen that, the lift/drag ratio increases linearly with the tailorability. These results are in good accordance with the morphing literature that predicts a lift/drag ratio increase with 2D morphing [9], [82], as seen in Chapter 1. These results also fulfill the objective set at the beginning of the study: being able to deform the hydrofoil, when the boat starts foiling, for reducing the drag intensity and having an energy efficient flight.

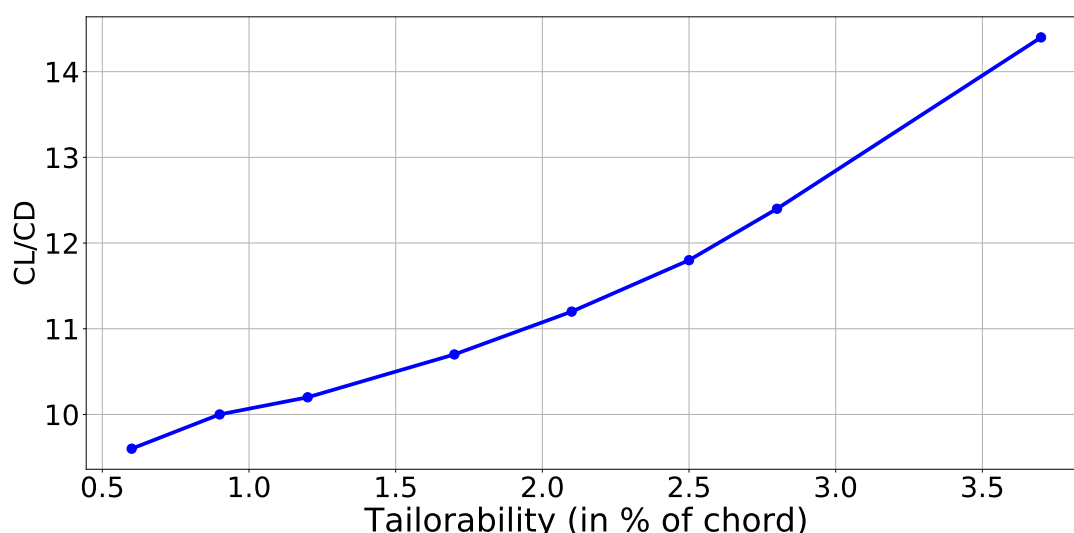


Figure 3.33. Evolution of the Lift/Drag ratio in function of the hydrofoil's tailorability

3.5.3 Parametric optimisation algorithm of the double arrow architecture

Figure 3.34 depicts the geometry of the optimised double-arrow pattern and Table 3.11 details the values of the different optimised patterns.

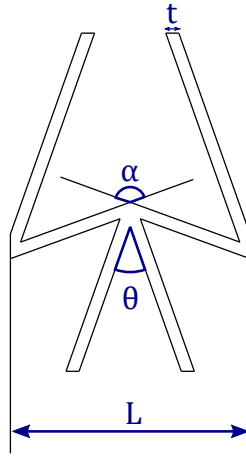


Figure 3.34. Optimised geometric pattern

Parameter	L	t	α	θ
name	(mm)	(mm)	($^{\circ}$)	($^{\circ}$)
Value	9.7	0.5	140	39

Table 3.11. Double-arrow geometric parameters optimised values

Figure 3.35 shows the convergence curves of 3 different optimisation algorithm’s computations. All three computations outputted the same optimised geometric parameters that are given in Table 3.11. The minimum fitness value of the three computations converged towards 0.088. All the computations fully converged after approximately 40 iterations.

Table 3.12 shows the corresponding homogenised elastic coefficients of the optimised double-arrow, which parameters are given in Table 3.11. On this Table, it can be seen that the E_{11} , E_{22} and G_{12} coefficients are very close to the anisotropic core’s elastic values demonstrating that the optimisation algorithm developed here works well.

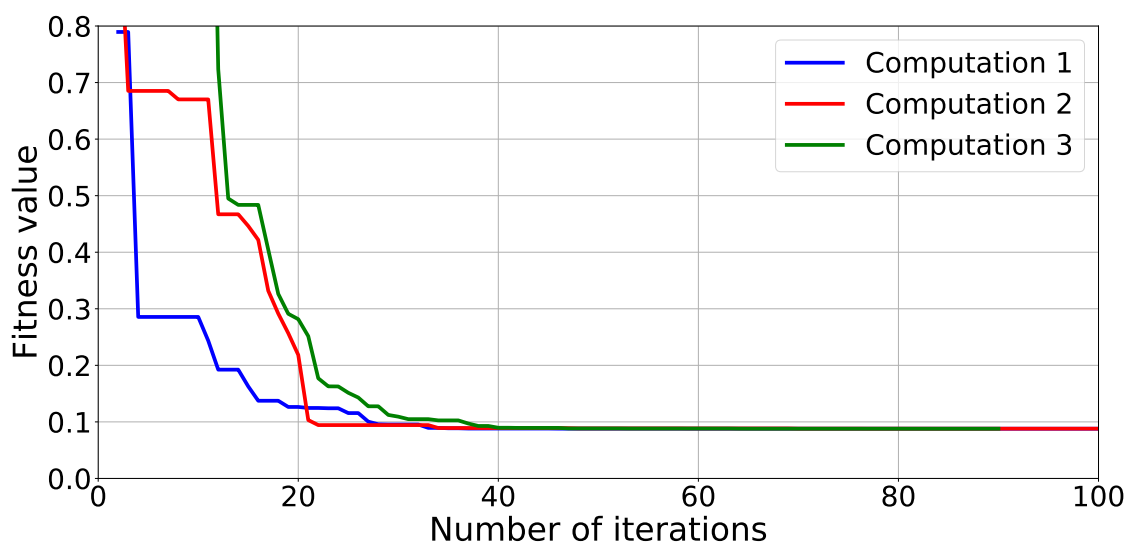


Figure 3.35. Evolution of the tailorability in function of the skin's rigidity

Material type	E_{11} (Pa)	E_{22} (Pa)	E_{33} (Pa)	ν_{12} (-)	ν_{13} (-)	ν_{23} (-)	G_{12} (Pa)	G_{13} (Pa)	G_{23} (Pa)
Anisotropic core	7 M	7 M	152 M	-0.5	0	0	15 M	24 M	24 M
Homogenised Double-arrow	6.9 M	7.1 M	153 M	-0.89	0	0	16.3 M	23.6 M	28.3 M

Table 3.12. Comparison between the original anisotropic core and the double-arrow's homogenised optimum elastic properties

Figure 3.36 compares the morphing hydrofoil's tailorability obtained with the original anisotropic core and with the double-arrow optimised homonogenised elastic properties. These results show that the approach chosen in this thesis can reliably tailor a cellular hydrofoil's passive deformation by optimising the geometric parameters of the cellular pattern while ensuring the manufacturability of the structure.

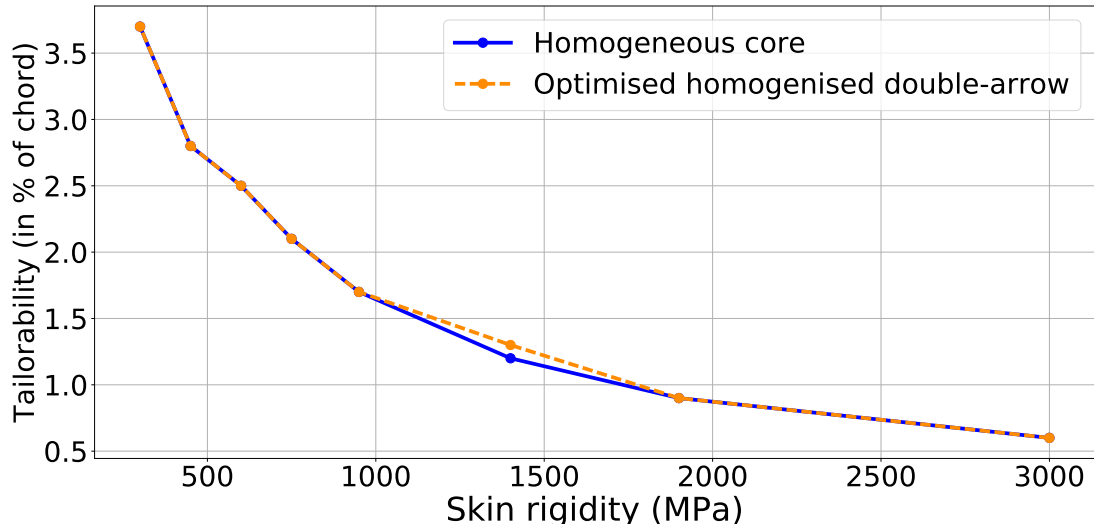


Figure 3.36. Tailorability comparison between the homogeneous elastic core elastic coefficients values and the optimised homogenised elastic coefficients in function of the skin’s rigidity

3.6 Discussions

3.6.1 Sensitive elastic coefficient identification

In the results displayed in § 3.5.1, one can note that the in-plane Poisson’s ratio ν_{12} of the continuous material does not play any significant role in the decambering control of the hydrofoil. This observation goes against most of the literature that states that the Poisson’s ratio ν_{12} is linked to the shear modulus G_{12} , a coefficient that strongly governs the hydrofoil bending behaviour [47], [115], [285]. However, as shown in § 2.3 of Chapter 2, one has to verify first that the material is transversely isotropic. Indeed, a direct relation between auxeticity and shear rigidity is only true for isotropic or transversely isotropic materials [286].

Furthermore, the results of § 3.5.1 show that the shear coefficient G_{12} is the elastic coefficient that has the largest impact on the bending properties of the hydrofoil. This result is in good concordance with what has been found in Chapter 2, in a sandwich composite mode, the shear rigidity coefficient G_{12} is the elastic coefficient of the core that governs the bending properties of the structure. This result is a concordant element evidencing that the core behaves in shear mode and that the conclusions drawn in chapter 2 are

applicable to this current morphing hydrofoil.

On Figure 3.31, it can be seen that the largest displacement differences between configurations is obtained when the shear coefficient G_{12} is divided by 10. Indeed, when G_{12} is divided by 10, the divided configuration's displacement is 143 % more important than the original configuration, whereas when the coefficient's value is multiplied by 10 the multiplied configuration's displacement is approximately 20 % lower than the original coefficient.

This relative difference value can also be obtained by multiplying E_{11} by 10. This difference can be explained by the fact that the hydrofoil becomes so rigid, when E_{11} and G_{12} are multiplied by 10, that the displacements are almost null. Thus, the elastic coefficients used on the original configurations are too high. The elastic coefficients E_{11} , E_{22} and G_{12} need to be set as low as possible, while trying to avoid hydroelastic instabilities.

3.6.2 Tailorability tests of the morphing hydrofoil

The results observed in Table 3.10 show that, at best, the tailorability of the present morphing hydrofoil concept is midly more effective than the morphing concept developed by Spadoni *et al*, 3.7 % for our concept and 3.2% for their concept [69]. However, it is important to note that the dynamic forces with which a tailorability of 3.7 % was reached are almost twice more important than the ones modeled in the studies of Heo and Spadoni [76], [284]. Equation 3.58 shows the dynamic pressures estimation around the morphing hydrofoil of this study and the morphing airfoils investigated by Heo and Spadoni (see § 3.3.4 for more details).

$$\begin{cases} P_{dyn}^{hydrofoil} = \frac{1}{2}\rho_{water}U_{\infty}^2 = \frac{1}{2} \times 1000 \times 7^2 = 24\,500 \text{ Pa} \\ P_{dyn}^{airfoil} = \frac{1}{2}\rho_{air}U_{\infty}^2 = \frac{1}{2} \times 1.2 \times (0.45 \times 343)^2 = 14\,300 \text{ Pa} \end{cases} \quad (3.58)$$

This observation implies that the concept developed in this study is far more stiffer than the ones developed by Spadoni [76], [284]. The hydroelastic instability that appeared for a skin rigidity of 200 MPa implies that this increase of stiffness is necessary for morphing hydrofoils applications. Indeed, Table 3.4.2 of § 3.4.2 indicates that the flow velocity regime, and thus the dynamic pressure intensity, is in the lower part of the velocity interval that a sailing boat can reach. Hence, a stiffening is necessary for avoiding such

instabilities at higher velocities.

This large difference of dynamic pressures also explains why it is not possible to attain Heo’s tailorability value [76] with the concept developed in this thesis. The forces are too important to be able to ensure such small deformations with polymeric materials.

The other observable results of Table 3.10 showed that, by tailoring the elastic properties of the skin with existing polymers, one can attain the scale of tailorability of all the different morphing concepts. Hence, these results show that the bending stiffness of the morphing concept developed in this thesis can be tuned from a stiff configuration [76] to a more compliant one [96] according to the needs. This tailorability was attained while ensuring the manufacturability of the morphing hydrofoil. This was not possible in the concepts previously encountered that were either compliant [47], [284] or stiff [76].

This approach of adjusting the hydrofoil’s skin rigidity is also novel compared to what has been investigated in the literature so far. All the morphing concepts focused on tailoring the pattern’s geometry [76] or the geometric parameters of a given pattern [69], [284]. Moreover, the insurance of the skins and the core’s printability adds a new novelty compared to the literature. Considering the double arrow-pattern, new simulations are carried out to check whether the pattern’s geometric parameters have an equal or a greater importance on the structure’s bending properties than the skin’s rigidity.

To do that, new FSI simulations are carried out with 3 different double-arrow homogenised elastic coefficients configurations, corresponding to 3 different sets of parameters, with a skin rigidity corresponding to a high PE ($E = 300 \text{ MPa}$). These new elastic coefficients configurations are presented in Table 3.13. The first one is the original one depicted in § 3.4.8, this configuration has the lowest elastic coefficients and it is considered as a compliant configuration. The second one is the double-arrow configuration investigated in Chapter 2, here, the main double-arrow’s homogenised elastic coefficients are two times more rigid than the first compliant configuration.

Configuration	E_{11} (Pa)	E_{22} (Pa)	E_{33} (Pa)	ν_{12} (-)	ν_{13} (-)	ν_{23} (-)	G_{12} (Pa)	G_{13} (Pa)	G_{23} (Pa)
Original	7.1 M	6.9 M	152 M	-0.88	0	0	16.3 M	23.6 M	28.3 M
Chapter 2	17.4 M	12.3 M	152 M	-0.99	0	0	33.6 M	24 M	24 M
Rigid	56 M	45 M	2618 M	-0.99	0	0	172 M	429 M	429 M

Table 3.13. Elastic properties of homogenised double anisotropic core

For the last configuration, geometric parameters values have been selected to have 7 times more rigid homogenised elastic coefficients than the original one. This configuration is obtained by homogenising the geometric parameters depicted in Table 3.14 with a bulk material rigidity of $E = 10000 \text{ MPa}$.

Parameter name	L (mm)	t (mm)	α ($^\circ$)	θ ($^\circ$)	E (Pa)
Value	9.7	0.5	140	39	10000 M

Table 3.14. Rigid configuration of the double-arrow pattern's geometric and material's parameters values

The tailorability results found for these three configurations are showed in Table 3.15. In this Table, it can be seen that, the tailorability range of the most rigid configuration is 20 % lower than the original configuration, while its elastic rigidities are 7 times higher than the original ones. Whereas, on Table 3.10, it can be seen that, by dividing the skin rigidity by 4, the morphing hydrofoil's tailorability is multiplied by 4.

Configuration	Original	Chapter 2	rigid
Tailorability range Δ (in % of chord)	3.6	3.5	3.0

Table 3.15. The tailorability ranges obtained with different double-arrow homogenised elastic coefficients

This can be explained by the fact that, in general, sandwich composites rigidity depends on the skin's rigidity, the core's size and mass repartition [283]. Because the core

size is constant and the mass repartition is fixed with the double-arrow shape, only the skin’s rigidity can be tuned to modify considerably the hydrofoil’s bending stiffness. Thus, for morphing hydrofoils based on the sandwich composite modes of operation, **tailoring the skin’s rigidity directly is more efficient than tailoring the pattern’s geometric parameters.**

The latter conclusion must also take into account the fact that the skin’s rigidity value order must be always 10 times superior to the core’s elastic rigidities for keeping a sandwich composite behaviour mode [286]. In this thesis, this condition has been taken into account, indeed Figure 3.32 shows that the tailorability is inversely proportional to the skin’s rigidity.

Equation 3.59 gives the exact relation between the deflection δ and the beam’s Young modulus E of a cantilever sandwich composite bending problem. This equation is constituted of two members: one that represents the deflection due to skin’s rigidity and the other one represents the deflection due to core’s shear rigidity, with F being the applied force, L being the length of the beam, I being the second moment of area, G being the shear modulus and \bar{A} being the specific area of the core. In this equation, all the terms are constant except the skin’s rigidity E . Thus, in Equation 3.59, only the *skin rigidity deflection* term changes with the variation of the skin’s rigidity.

$$\delta = \underbrace{\frac{FL^3}{3EI}}_{\text{skin rigidity deflection}} + \underbrace{\frac{FL}{4G\bar{A}}}_{\text{core's deflection}} \quad (3.59)$$

The evolution of the hydrofoil’s tailorability and the beam’s skin rigidity observed on Figure 3.32 is in a good concordance with the inverse proportional relation of the beam’s deflection δ and the skin’s rigidity E observed in Equation 3.59. The results observed in Table 3.15 and Figure 3.32 and discussed earlier also tend towards the conclusion that the morphing hydrofoil behaves like a sandwich composite. Hence, the morphing hydrofoil problem can be assimilated to a cantilever sandwich bending problem with a complex geometry.

Indeed, in § 2.4.2 of Chapter 2, it has been shown that when the skin’s rigidity becomes too soft, its rigidity variations do not impact the bending properties of the structure anymore. Hence, having a skin that still impacts the bending behavior of the hydrofoil is an

additional hint that it operates in a sandwich composite mode.

Figure 3.33 depicts the evolution of the lift/drag ratio with the hydrofoil's tailorability. On this Figure, it can be seen that the lift/drag ratio evolves linearly with the hydrofoil's trailing edge displacement. A linear regression gives a slope value of 1.47, an intercept of 8.44 and an r value of 0.97.

This evolution seems to be consistent with the fact that the lift/drag ratio evolves linearly with the angle of attack, when the value of the latter remains small [287]. Indeed, changing the hydrofoil's cambering is an indirect way of changing the angle of attack [33] (see § 1.1.2 of Chapter 1 for more details). However, while decambering, it could be interesting to see how the lift coefficient C_L and the drag coefficient C_D evolves with the tailorability: is it the lift coefficient C_L that decreases and makes the ratio decrease? Or is it the drag coefficient C_D ? Or maybe it is both?

Figure 3.37 shows the evolution of the lift and drag coefficients as function of the tailorability. On this Figure, it can be seen that the drag coefficient C_D and the lift coefficient C_L both decrease with the increase of tailorability. However, the lift coefficient decreases much faster than the drag coefficient. Thus, during operation, one should ensure that enough lift force is generated by the hydrofoil for keeping the boat at the water's surface.

3.6.3 Parametric optimisation algorithm of the double arrow architecture

The results obtained in Table 3.12 show that the optimisation algorithm developed in § 3.4.9 is able to optimise the different geometric parameters of the double-arrow pattern in order for its homogenised elastic coefficients to attain accurately the targeted values of a given homogenised equivalent material's elastic coefficients.

The results obtained in Figure 3.36 also highlighted that the use of the double-arrow optimised homogenised elastic coefficients displayed the same tailorability capabilities as when the continuous elastic core's coefficients are used. Nonetheless, despite this good operation, the targeted continuous core's elastic coefficients E_{11}^{Tar} , E_{22}^{Tar} and G_{12}^{Tar} were

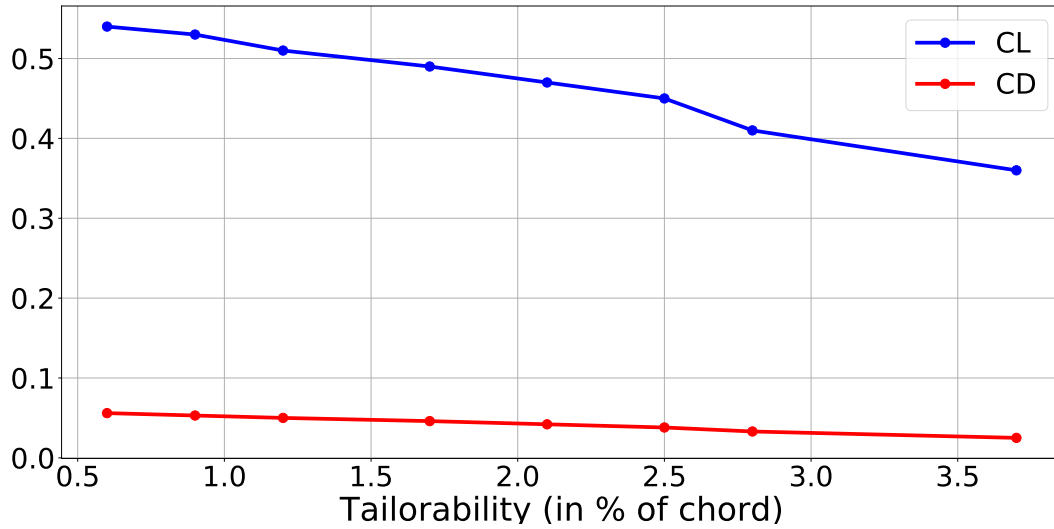


Figure 3.37. Evolution of the lift coefficient C_L and the drag coefficient C_D in function of the hydrofoil’s tailorability

purposely chosen to ensure a possible convergence, would it be possible to have such a good targeted elastic coefficients approximation using the double-arrow pattern with more random coefficients?

For answering that question, new optimisation computations were carried out with new coefficients. Table 3.16 shows the new targeted coefficients used for testing the parametric optimisation algorithm. In this case, E_{11}^{Tar} and E_{22}^{Tar} were not changed compared to the previous run, only the G_{12} was changed and set equal to the two other coefficients.

Coefficient	E_{11}^{Tar}	E_{22}^{Tar}	G_{12}^{Tar}
Value (in MPa)	7	7	7

Table 3.16. New targeted elastic coefficient values for testing the parametric optimisation algorithm

Table 3.17 shows the comparison between the targeted elastic coefficients and the double arrow’s optimised homogenised elastic coefficients. Figure 3.38 shows the convergence of the optimisation computations. The computation converges towards a fitness value of 0.966. By looking at the fitness value of Figure 3.38 and the coefficient comparison in Table 3.17, it can be seen that the coefficients that are obtained are dramatically different

from the targeted values. These results show the limit of the current optimisation method, not all the targeted elastic coefficients are targetable with the double-arrow pattern.

Coefficient	E_{11}^{Tar}	E_{22}^{Tar}	G_{12}^{Tar}
Target values (in MPa)	7	7	7
Optimisation values 1 (in MPa)	1	7.3	10
Optimisation values 2 & 3 (in MPa)	1	6.5	13.4

Table 3.17. New targeted elastic coefficient values for testing the parametric optimisation algorithm

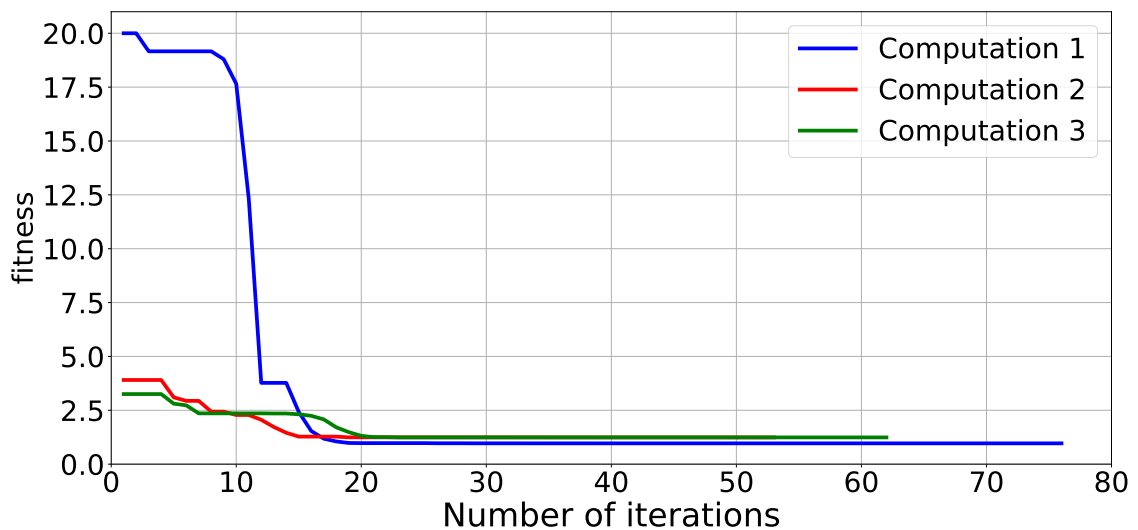


Figure 3.38. Convergence curve of the optimisation computation

Multiple studies have shown that the elastic rigidity values that an architected pattern can have is limited by the symmetries induced by its geometry [288]–[290]. Thus, for being able to target a large scope of elastic coefficients, multiple strategies can be investigated. One strategy would be to compile different patterns in a library with different patterns with different symmetries for different coefficients, for instance for cases where $E_{11} \cong E_{22}$, transverse isotropic patterns can be used such as the hexachiral pattern or

the regular hexagon [95], [108] or some pattern that exhibits 90° symmetries where the shear modulus is not connected to the latter coefficients values [289]. If one coefficient is superior to the other, *e.g.* $E_{11} > E_{22}$, a pattern that presents a strong directionality such as the reentrant pattern can be used.

This solution would allow to enlarge the number of elastic coefficients that could be targeted, nevertheless it might not be exhaustive. For those reasons, a new type of optimisation, **topology optimisation**, is currently deeply researched in the literature [291]–[293]. Topology optimisation can be defined as the optimisation of the repartition of matter in a given space that must respect constraints in order to match some objective function [292]. Being able to tailor the matter distribution for an RVE would allow to tailor its homogenised coefficients and make them match precisely any targeted coefficients.

3.7 Summary

In this chapter, in order to fulfill the objectives set at the beginning of this thesis; *i.e.* **design a 3D-printable hydrofoil that can control its passive deformation and improve its hydrodynamic properties**; a Fluid-Structure Interaction program and a parametric optimisation program were developed. The FSI program aimed at modeling the interaction between the turbulent fluid-flow and the solid hydrofoil in order to investigate the hydrofoil’s tailorability and its impact on the properties. The hydrofoil was modeled in a sandwich composite mode, a rigid skin 10 times stiffer than the core. The core is modeled with a homogeneous elastic anisotropic material. The FSI showed that the most influential core’s coefficients governing the hydrofoil’s bending properties were the in-plane shear rigidity coefficient G_{12} and the in-plane tensile coefficients E_{11} and E_{22} . Only these three coefficients need to be matched, for a real material to replace the homogeneous one. Out of these coefficients, G_{12} is the most influential one, confirming that the hydrofoil’s behavior is similar to a sandwich composite.

In this mode, the FSI has shown that the skin’s rigidity influences dramatically more the tailorability of the hydrofoil than the core’s elastic rigidities. Thus, the core was set as compliant as possible for maximising the hydrofoil’s tailorability. The skin’s rigidity was tailored from 200 MPa to 3000 MPa and the tailorability of the hydrofoil was then measured. These values of rigidities correspond to the rigidity of the softer and the most

rigid 3D-printable existing polymers. Results demonstrated that most of the previously encountered morphing concepts were attainable with 3D-printable polymer skin's. Only Heo's rigid concept was not attainable due to hydrodynamic forces that were too important. The trailing-edge tailoring of the hydrofoil improved the lift/drag ratio by strongly decreasing the lift's value. Thus, for a foiling boat application, this parameter must be taken into account for ensuring enough lift generation.

For replacing the homogeneous equivalent core by a manufacturable cellular material, a parametric optimisation algorithm was developed. This algorithm's objective function is to optimise the geometric parameters of a double-arrow pattern in order to match the G_{12} , E_{11} and E_{22} values of the continuous core. Manufacturability constraints were implemented in the algorithm for ensuring that the final output of the program is 3D-printable. The optimisation program managed to find optimum values for the initial values of the elastic core. Nevertheless, for the constraints set to the double-arrow pattern, the number of optimisable elastic coefficients is limited. To enlarge this scope, other strategies based on the parametric optimisation of different patterns or on topology optimisation could provide deeper insights.

CONCLUSION AND OUTLOOKS

Conclusion

In this thesis multiple objectives were set in the introductory section, a global objective and smaller subsidiaries objectives:

- The global objective of this thesis was to design and develop a passive adaptive foil concept that could be manufactured and whose deformations could be controlled,
- The first subsidiary objective was to get a state of the art of the existing technologies and identify one that might be interesting to develop,
- The second subsidiary objective was to identify a manufacturing process that is suitable for fabricating the morphing hydrofoil and study the impact of the manufacturing process on the morphing hydrofoil's elastic properties,
- The third subsidiary objective was to deeply investigate the morphing operation mechanism of the morphing technology selected and identify the different parameters tailoring its behaviour,
- The final subsidiary objective was to model numerically the morphing hydrofoil in a turbulent water flow and optimise the different governing parameters to be able to control the hydrofoil's deflection. The manufacturing constraints are integrated into the optimisation for ensuring the fabrication of the prototype.

The objective behind being able to control the hydrofoil's deflections is the possibility to tailor the hydrofoil's hydrodynamic properties. Indeed, 3 navigation modes were identified where different hydrodynamic properties are needed:

- The first one corresponds to the moments before the boat takes off, the hydrofoil must provide a high lift force for lifting the boat's hull over the surface. Hydrofoil morphing is not expected here, the hydrofoil is already designed for generating high lift,

-
- The second one corresponds to the moment when the boat's hull is above the water's surface. At this time, the hydrofoil's shape must favor the best lift/drag ratio for keeping the flight stable and energy efficient. This is at this time that the morphing is expected to happen,
 - The last navigation mode corresponds to the landing, for this mode the hydrofoil is expected to produce a high lift for landing the boat's hull smoothly. At this stage, the morphing mechanism is expected to stop operating.

All these objectives were fulfilled in this thesis work. In the first chapter, the 2D morphing cellular airfoil concept, developed by Bornengo [47], was selected to be investigated deeper. This morphing concept is constituted of an architected cellular core and a surrounding skin. The major reason for selecting this application is its ability to adapt the air-or-hydrofoil's camber passively and autonomously, with the architected core acting as the camber control device. This passive operation implies an absence of electronic or mechanic actuation systems, that are highly prone to maintenance, and present major issues for already existing morphing devices.

In order to manufacture this structure containing architected materials, additive manufacturing has been identified as the process family that present the most promising characteristics. Indeed, this family of processes have been developed for manufacturing complex geometric shapes, especially the 3D-printing polymer Fused Filament Fabrication (FFF) process. This process consists in extruding a heated polymer from a nozzle that deposit the hot filament on a heated plate in order to build the final part layer per layer. The interest of using this process particularly, instead of any other process, is firstly its ability to build a given part in a relatively acceptable time. Secondly, the bulk materials used, polymers, are cheap materials that are perfect for developing prototypes. Finally, the 3D printing of continuous fiber composites is being currently developed on FFF. The parts manufactured with this process exhibit similar mechanical properties as metallic 3D printed parts. Thus, the methods used in this thesis for manufacturing a polymeric hydrofoil can be later reused for a composite hydrofoil that has better mechanical properties.

Yet, using this process for manufacturing the hydrofoil impacts its bulk material's mechanical properties. Indeed, the use of the FFF process induces the presence of anisotropy and porosity that transforms the bulk polymer material's properties. These changes of

properties also impact the global structural behaviour and properties.

For being able to take into account these changes of properties numerically and to predict the behaviour of the structure, a methodology has been developed through an experimental and numerical multi-scale analysis. This study has demonstrated that characterising the anisotropic mechanical properties of the 3D-printed bulk material, setting local material orientations in a numerical structural model and associating the local orientation of the model to the experimental anisotropic elastic coefficients is sufficient for being able to reliably correlate the numerical structure's elastic behaviour with the experimental structure's elastic behaviour.

The multi-scale analysis used earlier did not only target to take into account reliably the changes of the bulk material's mechanical properties and to predict the behaviour of a 3D-printed structure. Its original aim was to investigate the morphing mechanism of the cellular hydrofoil and identify key parameters governing the airfoil's bending properties. With the use of representative cellular semi-structures (cellular beam), the theory of homogenisation and the characterisation of the 3D-printed bulk material, a key parameter governing the bending behavior was identified: the structure's skin rigidity.

Indeed, two different modes of behaviour can be identified with different skin rigidities. If the skin is considered rigid; *i.e.* its rigidity scale order is at least 10 times superior to the core's elastic rigidity values; the morphing structure behaves as a sandwich composite. The cellular core of the hydrofoil is submitted uniformly in shear, with the rigid skins concentrating the bending moment. The rigid skin opposes to the bending deformation and stiffens the structure. The core's shear rigidity is the other parameter tailoring the bending behavior of the structure. Because of the uniform shear loading, the cellular core's unit cell size has a negligible impact on the bending properties of the structure, compared to the skin's rigidity and the core's shear rigidity. Furthermore, thanks to the uniform shear loading of the core, the bending behavior of the structure can reliably be modeled numerically by replacing the cellular core with a Homogeneous Equivalent Material (HEM) having the homogenised elastic properties of the cellular pattern. Replacing the cellular core by the HEM fastens the structure's bending deformation simulation.

Now, if the skin is considered soft; *i.e.* its rigidity scale order is at least 10 times inferior to the core's elastic rigidity values; the morphing structure behaves in a more complex way. The core is submitted to a non-uniform complex loading, where the dominant deformation mode is the tensile/compressive mode. This behaviour originates from

a too soft skin that does not concentrate the bending moment anymore and transmits them directly to the core. Indeed, the rigidity variations of the skin do not modify the bending stiffness of the structure anymore, in this behavioural mode. In this configuration, the superior and inferior regions of the core are tensile/compressive dominated and the center of the cellular core is loaded in shear. In this mode, the unit cell size has a strong influence on the bending properties, increasing the number of cells in the direction of the beam's width dramatically increases the bending stiffness of the beam. This dependence is so important, that in this bending mode, the cell size is the most important parameter tailoring the beam's bending behaviour. Because of this dependence, the beam's core can not be modeled numerically with a HEM having the homogenised elastic properties of the cellular pattern. Indeed, the cell size dependence cannot be reliably modeled with continuous homogeneous materials.

After identifying the various parameters governing the beam bending properties and the different modes of behaviour of a morphing structure, a Fluid-Structure Interaction (FSI) numerical simulation between the cellular morphing hydrofoil and a turbulent waterflow was numerically modeled. The turbulent fluid model was developed on a hybrid finite-element and finite volume CFD code using the Reynolds Averaged Navier-Stokes (RANS) method with the Spalart-Allmaras turbulence model. The solid hydrofoil model was modeled with a rigid skin and a homogeneous anisotropic elastic core. Because of the use of the homogeneous material as the hydrofoil's core, the solid hydrofoil is expected to operate in a sandwich composite operation mode. This operation mode was favored over the soft skin mode, because of the reduction of the calculation time induced by the use of a homogeneous core instead of a cellular core.

In order to be able to predict and control the hydrofoil's deflections under a hydrodynamic loading, the anisotropic core properties were fixed and the skin's rigidity values were taken in an interval between 200 MPa and 3000 MPa. This interval corresponds to the rigidity interval of 3D-printable thermoplastic polymers. Then, the tailorability of the hydrofoil is simulated by changing the skin's rigidity value in the previous interval.

The results demonstrated that the tailorability values obtained with this new morphing hydrofoil concept was able to match or outperform almost all the different cellular airfoil morphing concepts encountered earlier in the literature. These results were obtained with a hydrodynamic pressure that was two times superior to the aerodynamic pressure of the concepts studied in the literature. The latter point justifies the use of the sandwich

composite concept for hydrofoil morphing application, the additional stiffness provided by the rigid skin prevents the apparition of hydro-elastic instabilities due to too important hydrodynamic loads. When the skin rigidity becomes close to 200 MPa, these instabilities start appearing

With these tailorability increase, the lift/drag ratio can be improved up to 50 % of its original value. These results fulfill the objective of the morphing mechanism: improving the lift/drag ratio of the hydrofoil. However, this reduction is obtained with a very high lift reduction. Thus, one must take this into account and verify that enough lift is still produced to lift the boat's hull above the water's surface.

To finish with, for ensuring the manufacturability of the hydrofoil, an existing cellular material that matches the anisotropic core's elastic properties must be identified. In order to do that, a parametric optimisation algorithm has been developed. This parametric optimisation algorithm optimises the geometric parameters of a cellular pattern; in this thesis a double-arrow pattern was selected; for making its homogenised elastic coefficients match with the core's elastic coefficients. In this thesis, this algorithm demonstrated that this method was effective, optimised solutions existed and had the same performance once integrated into the hydrofoil's core. Nevertheless, the scope of the core's elastic coefficient that can be matched with optimisation is limited. It can only be done with few selected coefficients. Improving the operability scope of this algorithm can be considered as a perspective.

Outlooks

As said in the former paragraph, the first identifiable perspective is the improvement of the parametric optimisation algorithm. For improving it, the parametric optimisation of a given pattern can be replaced by a topology optimisation algorithm. This topology optimisation algorithm can optimise the material repartition inside a periodic pattern for being able to match any core elastic coefficient.

Other aspects regarding the hydrofoil's operation can be researched, such as the prediction of plasticity. Indeed, for operating efficiently, the hydrofoil must always remain in the elastic regime for being able to recover totally the hydrofoil's deformation when the boat's hull is landing. In this thesis, only the elastic regime of the hydrofoil has been

studied, no plasticity modeling has been made. Being able to predict the apparition of plasticity can be important to see whether the hydrofoil can undergo the higher level of tailorability numerically predicted without plastifying. In the literature, the effective tailorability of some passive cellular airfoil morphing concepts was reduced after taking plasticity into account [69]. For the concept developed in this thesis, the plasticity is likely to appear in the skin where the majority of loads is concentrated.

An other aspect of the structure needs to be studied, it is its performance in fatigue. Most of the racing sailboats are expected to travel through all the oceans of the world during almost half a year. Thus, seeking the performance in fatigue of the morphing hydrofoil can be interesting to see how much cycles the hydrofoil can undergo with the hydrodynamic loading, without plastifying or failing.

Yet, all these perspectives, despite being important, are still long term perspectives. The most immediate perspective is the actual possibility of manufacturing a prototype that can be tested for verifying the operation of the solution practically. A polymeric prototype can be manufacture and tested in a water tunnel to see if the sturcture deforms under the hydrodynamic loads.

After validating the experimental operability of the concept with a polymeric prototype, continuous carbon fiber prototypes can be 3D-printed and tested in the conditions of a racing sail boat at full speed.

All these objectives pretend to reach one objective, having a wide mainstream implementation of passive morphing hydrofoils on boats.

NUMERICAL MODELING OF A TURBULENT WATER FLOW AROUND A HYDROFOIL

This chapter's objectives are to select the hydrofoil shape that will be used for the optimisation and to generate numerically the dynamic loading around the hydrofoil. To achieve these objectives, we need to use Fluid dynamics and *Computational Fluid Dynamics* (CFD). In the following sections, these two domains will be presented and numerical models and methodologies will be developed for simulating the waterflow around a hydrofoil.

A.1 General overview

Fluid dynamics is a discipline in fluid mechanics that studies the properties of a fluid in motion, also known as a flow, around a particular object. In physics, a fluid is defined as an object that cannot resist shearing stress [274]. In other words, it means that as long as a shear stress is applied on a fluid, the fluid keeps on moving.

CFD is a branch of fluid dynamics that uses numerical analysis and data structures to analyse and solve problems that involve fluid flows. Thus, before being focused on CFD, the physical objects, the physical properties and the governing equations of fluid dynamics need to be presented.

The physical objects called fluids are liquids (water, oil, honey...) and gases (air, methane, helium). The property differentiating those two objects is the compressibility. Gases are compressible, whereas liquids are not. In fluid flows, the compressible or incompressible nature of a fluid can lead to major distinctions in behavior, when the flow encounters an object. Thus, one must be able to quickly assess whether the fluid is compressible or not. For a compressible fluid, such as air, very complex phenomena known as shock waves can occur, when the flow reaches very high velocities. The physics governing shock waves are based on the compressibility of a fluid. Those extreme conditions are

usually met around an airplane's wing or a rocket engine [294], [295]. For incompressible fluid flows, other unique physical phenomena occur as for instance cavitation in water flows. An efficient way to verify a fluid's compressibility is by checking its isothermal compressibility factor noted κ_T for English speakers and χ_T for French speakers. In the rest of this paper, this coefficient will be noted down as κ_T . The expression of this coefficient is given in Eq. A.1 where V is the volume of fluid and P the pressure of the fluid.

$$\kappa_T = -\frac{1}{V} \left(\frac{\partial V}{\partial P} \right)_T \quad (\text{A.1})$$

For a fluid to be considered as incompressible, the isothermal compressibility factor must be equal to zero. Now that we know that fluids are defined as objects that can be set in motion through the application of a shear stress, one can address the following question: How is it possible to link the flow state (velocity, pressure, temperature...) with the intensity of the shear stress applied? And what other parameters influence the flow state? These questions, which are highly complex and are currently deeply studied in literature, will be addressed in the following paragraph, where the different physical parameters and non-dimensional numbers that give explanation keys to these questions will be presented.

A.2 Key physical properties, concepts and dimensionless numbers

In fluid dynamics, being able to understand the behavior of a flow around an object means being able to define the following quantities in the whole considered fluid field: the flow velocity, the flow pressure and the flow temperature. The variation of these quantities are highly dependent on several physical parameters and inner flow properties. The most important ones to consider are the following: the viscosity, the density, the Reynolds number and the Mach number. Depending on the considered problem, other dimensionless numbers can be used.

A.2.1 Viscosity

In the General overview section A.1, the following question has been raised: How is it possible to link the flow state (velocity, pressure, temperature...) with the intensity of

the shear stress applied ? This questioning can be partially answered with the concept of fluid viscosity. For fully understanding this concept, the shear stress must be clearly defined in this section. In solid mechanics, the aim of studying static deformable solids is to link the stress field to the strain field of that object, through elasticity tensors and/or constitutive models. Here, the idea is similar in fluid dynamics, however because the fluid is unable to statically deform to burden the shear stress, using the concept of strain is impossible in this case. Instead, the stress field is linked with the shear rate of the fluid. To illustrate this concept, a flow between two parallel plates distant from a height of h (measured in meters), where one plate is moving at velocity v (measured in meters per seconds) and the other one remains stationary is considered (see Figure A.1). This flow is known in the literature as the Couette flow and it is the most simple example where the shear rate is observable [296].

By looking more carefully to Figure A.1, it can be seen that there is a constant gradient of velocity between the upper plate P_1 and the lower plate P_2 . This gradient of velocity can be explained by viscosity, viscous fluid particles tend to stick to solid surfaces (*e.g.* water on wet human hand). Thus, by sticking to a solid, the fluid gains the solid's velocity: the fluid particles stucked on the plate P_1 have a velocity of v and those stucked on the plate P_2 have a velocity of 0. Now, if the non-sticked fluid layer just beneath the plate P_1 are considered, its constitutive particles will now start to move, because the particles stucked to P_1 will transmit their kinetic energy to them. However, because the fluid is viscous, the fluid particles are sticky. So a part of that kinetic energy will be lost through particle-particle friction, resulting in a lower velocity for that layer. By going lower and lower in the fluid particle layers, their velocity will decrease through the same mechanism until reaching a velocity of 0 where fluid particles are stucked to P_2 . In the considered problem, the evolution of velocity is linear, but in more complicated flows the fluid interlayer might be more complicated and result in non-linear relationships.

If the previous explanations are translated into equations, the fluid's velocity can be expressed with Equation A.2:

$$v(y) = Cy \tag{A.2}$$

Where C is a constant velocity gradient. This constant is what we call the shear rate of the fluid. physically, this quantity tend to describe how the velocity of one fluid layer

is influenced by its surrounding layers. It is dimensionally defined as the relation between a characteristic velocity and a characteristic length. By combining Equation A.2 with the fact that $v(y = h) = v$ and $v(y = 0) = 0$. The shear rate of the Couette flow is defined with Equation A.3. where $\dot{\gamma}$ is the shear rate (measured in per seconds).

$$\dot{\gamma} = \frac{v}{h} \quad (\text{A.3})$$

In this simple case, the shear rate was a constant. However, in other cases (*e.g.* a pipe flow), its expression might be more complex: the shear rate can be directionally dependent ($\dot{\gamma} = \dot{\gamma}(x, y)$). Thus a more general relation is needed. Instinctively, it can be presupposed that the shear rate relation, describing fluid interlayer influence on each other, will involve velocity gradients with partial derivatives. Moreover, the shear rate field is linked with the shear stress field, hence the final shear rate relation must be a tensorial Equation. To finish with, its final form must be similar to the solid strain tensor, due to its link to shear stresses. The general relation of the shear flow rate is given by Equation A.4.

$$\dot{\gamma}_{ij} = \frac{\partial v_i}{\partial x_j} + \frac{\partial v_j}{\partial x_i} \quad (\text{A.4})$$

By looking at Equation A.4, it can be seen that its form is similar to the strain tensor in solid mechanics (*i.e.* the sum of a gradient and its transposed form), as predicted. Furthermore, the use of partial derivatives on velocities describes perfectly the complex fluid interlayer interactions.

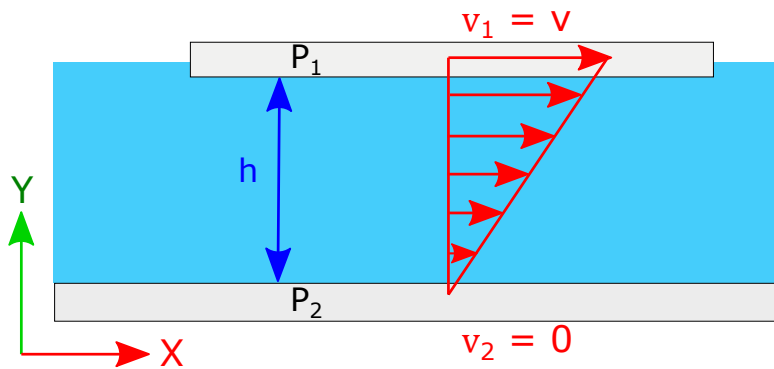


Figure A.1. Planar Couette flow

As said earlier, the shear stress field τ_{ij} and the shear rate $\dot{\gamma}_{ij}$ are linked by a physical quantity. This quantity is called viscosity and is noted η in Equation A.5.

$$\tau_{ij} = \eta \dot{\gamma}_{ij} \quad (\text{A.5})$$

Depending on the type of fluid considered, the values and types of η are numerous. It can be either be a combination of constants or a combination of various complex physical parameters. The different categories of viscous fluids are depicted in Figure A.2.

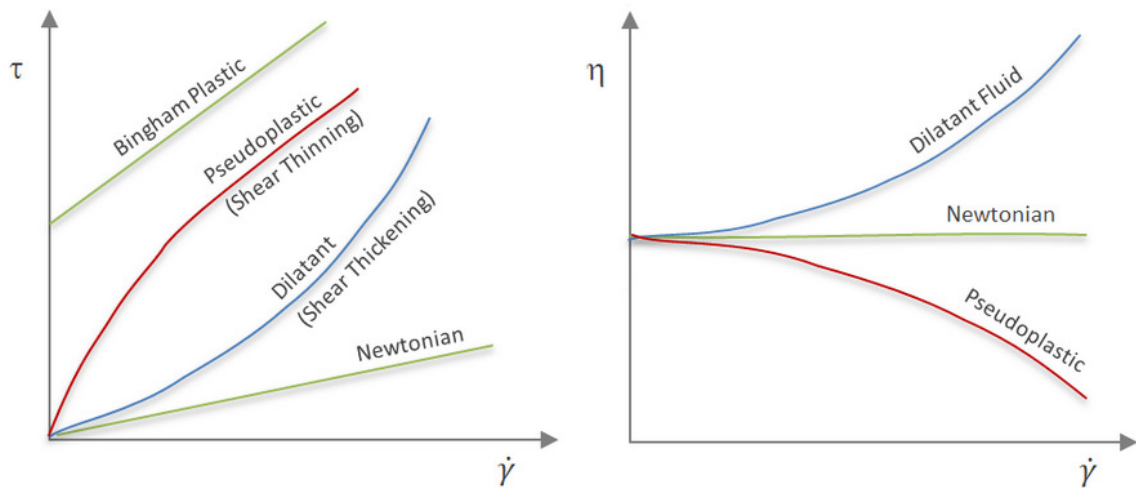


Figure A.2. The different types of existing fluids¹

From Figure A.2, it can be seen that three main types of fluids exist in nature: The Newtonian fluids, the dilatant shear thickening fluids and the pseudoplastic shear thinning fluids. Pseudoplastic fluids have a non-linear viscosity that decreases over time, which leads the stress to grow slower and slower with the rise of shear rate. Whipped cream or modern paints are examples of fluids that exhibit a shear thinning behaviour. On the contrary of those fluids, dilatant fluids have a viscosity that rises with the growth of shear rate. This rise in viscosity leads to a growth of shear stress with shear rate. Corn starch is a good example of dilatant fluids existing in nature. To finish with, newtonian fluids are fluids whose viscosity remains constant with the growth of shear rate. This constant viscosity leads to a linear behaviour between stress and shear rate. Common fluids, like water and air have a Newtonian fluid behaviour. For the range of flows investigated here, we essentially dealt with water and air which are Newtonian fluids.

The relation between shear stress and shear rate for Newtonian fluids is given by the Equation A.6. In this Equation, μ is called the dynamic viscosity expressed in Pa.s, μ' is

1. Image found on [297]

called the volumic viscosity also expressed in Pa.s and δ_{ij} is the Kronecker's symbol for identity tensor.

$$\tau_{ij} = \mu \dot{\gamma}_{ij} + \mu' \frac{\partial v_i}{\partial x_i} \delta_{ij} \quad (\text{A.6})$$

The dynamic viscosity is physically measurable with rheometers. This is generally this viscosity that comes into peoples mind when nothing is precised on the nature of viscosity. This viscosity is highly sensitive to temperature. The volumic viscosity is in nature very similar to the previous one, nevertheless its value changes depending on the hypothesis on the flow. If the fluid is incompressible, its value is equal to zero. In the compressible case, the Stokes' hypothesis is used for determining its value [298]. Stokes' hypothesis is described in Equation A.7.

$$\mu' + \frac{2}{3}\mu = 0 \quad (\text{A.7})$$

In the rest of this work, the considered fluids will mostly be incompressible, thus μ' will be considered as zero.

Having set these models, it can be interesting to use all the previous equations to determine the shear stress field and shear rate field of water in the Couette's flow problem and see if the final results are similar with what has been found at Equation A.3 (see Figure A.1). The fluid considered in this problem is water and the velocity v has only an x component: $v(y) = [v(y) \ 0]^T$.

In the first place, the shear rate of the flow must be calculated with Equation A.4. The result is given at Equation A.8.

$$\dot{\gamma}_{ij} = \begin{bmatrix} 0 & \frac{dv}{dy} \\ \frac{dv}{dy} & 0 \end{bmatrix} \quad (\text{A.8})$$

In Equation A.4, because the velocity is only in function of y full derivatives can be used instead of partial derivatives. Now by using Equations A.5 and A.7, the shear stress field in the Couette's flow can be expressed in Equation A.9

$$\tau_{ij} = \begin{bmatrix} 0 & \mu_{water} \frac{dv}{dy} \\ \mu_{water} \frac{dv}{dy} & 0 \end{bmatrix} \quad (\text{A.9})$$

Now knowing the stress field and the shear rate field, these theoretical results can be compared to the mean ones expressed in A.3. The shear stress vector τ_i in the y direction

(normal direction) is given by Equation A.10.

$$\tau_i = \tau_{ij}n_j = \begin{bmatrix} 0 & \mu_{water} \frac{dv}{dy} \\ \mu_{water} \frac{dv}{dy} & 0 \end{bmatrix} \begin{bmatrix} 0 \\ 1 \end{bmatrix} = \begin{bmatrix} \mu_{water} \frac{dv}{dy} \\ 0 \end{bmatrix} \quad (\text{A.10})$$

So, if the quantity $v(y)$ is replaced by the quantities encountered in Figure A.1 and depicted in Equation A.11.

$$v(y) = \frac{v}{h}y \quad (\text{A.11})$$

Equations A.12 and A.13 become:

$$\hat{\gamma}_{ij} = \begin{bmatrix} 0 & \frac{v}{h} \\ \frac{v}{h} & 0 \end{bmatrix} \quad (\text{A.12})$$

$$\tau_{ij} = \begin{bmatrix} 0 & \mu_{water} \frac{v}{h} \\ \mu_{water} \frac{v}{h} & 0 \end{bmatrix} \quad (\text{A.13})$$

The final tensors are symmetric and are totally consistent with what has been found in Equation A.3. This is a proof that general Equations A.4, A.5 and A.7 are relevant to describe the fluid's behavior. Now that the viscosity has been thoroughly described, the use in fluid mechanics of an another fundamental quantity will be introduced: the density.

A.2.2 Conservation of mass: mass density and Reference Fluid Volume Element (RFVE)

In fluid dynamics, the mass density expressed in kg per cubic meters, is a fundamental quantity that is used in every constitutive equation of a fluid to describe its state. At first sight, it might look surprising, because generally in physics the mass is encountered at the place of density (*e.g.* Newton's second law of motion, Gravitation equation, Coulomb's law...). So, why is the mass density preferred over the mass to describe a fluid's behavior ?

For answering that question, the concept of Reference Fluid Volume Element (RFVE) must be introduced. In highly complex problems, such as pipe network flows, setting the flow's constitutive equations and finding the pressures, velocities and densities of the flow in the full domain is impossible. Thus, the considered flow domain can be divided in small volumes where the constitutive equations can be applied and where it is easier to find

the fundamental physical quantities of the flow. This volume is called a Reference Fluid Volume Element (RFVE), it is generally represented by an infinitesimally small cube of fluid. Figure A.3 gives an illustration of what this volume looks like for compressible fluids.

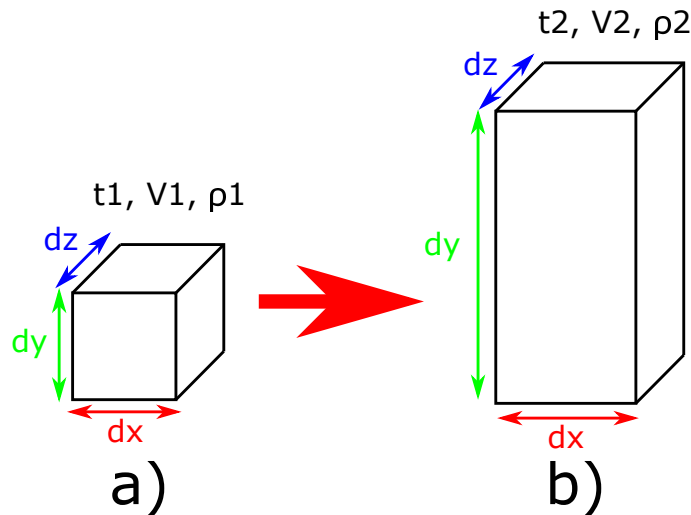


Figure A.3. Reference Fluid Volume elements in two different flow configurations for compressible fluids

For incompressible fluids, the volume of the RFVE remains constant and does not change its shape (see Figure A.3). As depicted in Figure A.3, compressible fluid's RVFE changes its shape with respect to time. Having said that, this Reference Volume must respect one constitutive law of physics which is the conservation of mass (see Equation A.14).

$$\frac{dm}{dt} = 0 \quad (\text{A.14})$$

This Equation states that the mass of the volume must remain constant with respect to the change of time. Thus, if the volume of the Reference Element taken can change with time, it means that for having a mass that remains constant the density of the fluid must also change. So, studying the behaviour of the fluid by using its mass in these equations means dealing with two intrinsic physical quantities that changes with time: density and volume. To avoid that, fluid mechanics decided to manipulate only density. By doing so, they only deal with one variable physical quantity instead of two. Equation A.14 will be rewritten accordingly with density and volume in section A.3.1.

A.2.3 Reynolds number

In fluid dynamics, the fluid's motion can be categorised in two types of flow: laminar flow and turbulent flow. The fluid's motion state depends on the kinetic energy of the considered flow. When the kinetic energy is low, the flow particles follow rectilinear streamlines in the flow and the general state of the flow is non-chaotic. This state is called the laminar state (see Figure A.4 on the bottom). When the kinetic energy of the flow is high, the momentum accumulated by the particles becomes too high to follow rectilinear streamlines. So the particles start swirling and the motion of the fluid becomes chaotic and non-deterministic. This state of flow is called a turbulent state (see Figure A.4 on the top). One third state exists, which is called transient. This state is only observable when a flow passes from a laminar to a turbulent state.

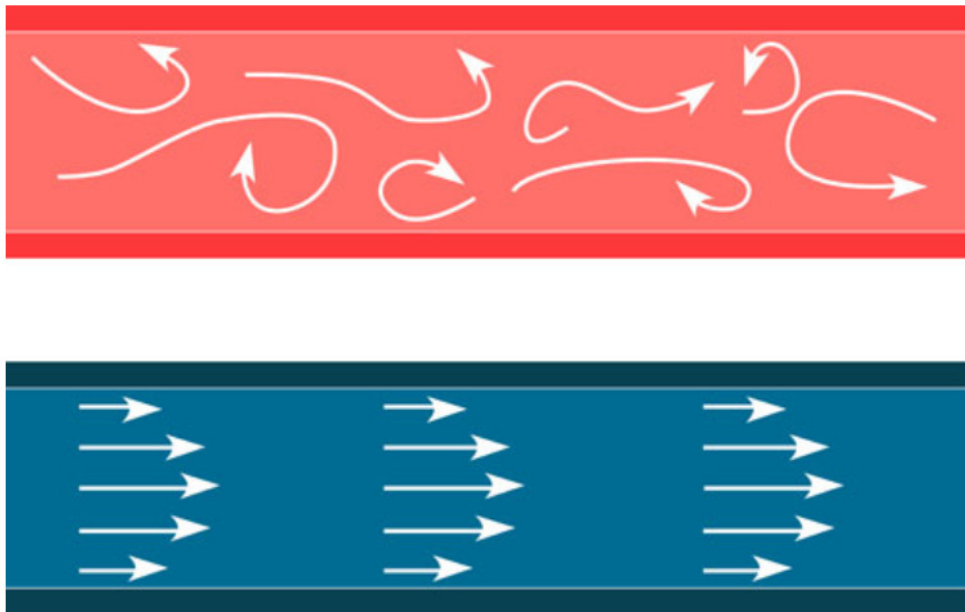


Figure A.4. *Turbulent flow (on the top) and laminar flow (on the bottom)*

Now that these states are identified, how is it possible to determine qualitatively the state of the flow? The answer to this question is by using a fundamental number of fluid dynamics: the Reynolds number. The Reynolds number was named after Osborne Reynolds, who evidenced in 1883 that a flow has 3 different states: laminar, transition from laminar to turbulent (transient) and turbulent state. He is also the one who publicised the use of this number. This number's most common expression is given in Equation A.15. With Re being the Reynolds number, ρ being the fluid's density, V being the fluid's

velocity, D being a characteristic length and μ being the dynamic viscosity.

$$Re = \frac{\rho V D}{\mu} \quad (\text{A.15})$$

The expression of the Reynolds number given in Equation A.15 is very interesting. The numerator of this number is the product of the momentum of the fluid ρV and the characteristic length D . This characteristic length will change depending on the object and problem considered. For instance, the characteristic length considered for a flow inside a pipe will be its diameter D instead of its length L (see Figure A.5 a)). Whereas, for an airfoil, the characteristic length considered will be its chord c instead of its thickness d (see Figure A.5 b)). By looking at Figure A.5 a), it can be seen that alongside the pipe's length L the velocity profile does not change. However alongside the diameter D of the pipe, the velocity profile changes depending on the distance the particle of fluid is from the rims of the pipe. Thus, it is the diameter of the pipe that has to be considered as the reference length governing the flow's motion, not the length of the pipe. On the contrary, airfoil flows do not change because of airfoil's thickness (see Figure A.5 b)). The state of the flow changes depending on the position considered alongside the airfoil's chord c . Hence, the length of the airfoil c will be preferred for being used as a reference length. In the Reynolds number's expression, this quantity is used for describing "the quantity of fluid that must be set in motion". The bigger this length is, the more energy the fluid needs for getting in motion and the unsteadier the flow would be.

The product of the momentum and the reference length are considered as being a representation of the "inertial forces of the fluid" in the Reynolds number. Indeed, the higher this numerator is, the higher inertial energy the flow has. On the contrary, the denominator is composed of the dynamic viscosity μ only (see Equation A.15). This denominator is representing the viscous forces occurring inside the flow as depicted in the paragraph dedicated to viscosity. These forces tend to reduce the inertial velocity inside the flow and makes it steadier. Physically speaking, the Reynolds number is a ratio between the inertial forces and the viscous forces (see Equation A.16).

$$Re = \frac{\text{inertial forces}}{\text{viscous forces}} \quad (\text{A.16})$$

When this ratio is far less than 1. It means that the viscous forces dominate the flow's behavior. This flow is called the Stokes flow and it has already been widely studied for flows around spheres [272], [273]. When the value of the Reynolds number is far greater

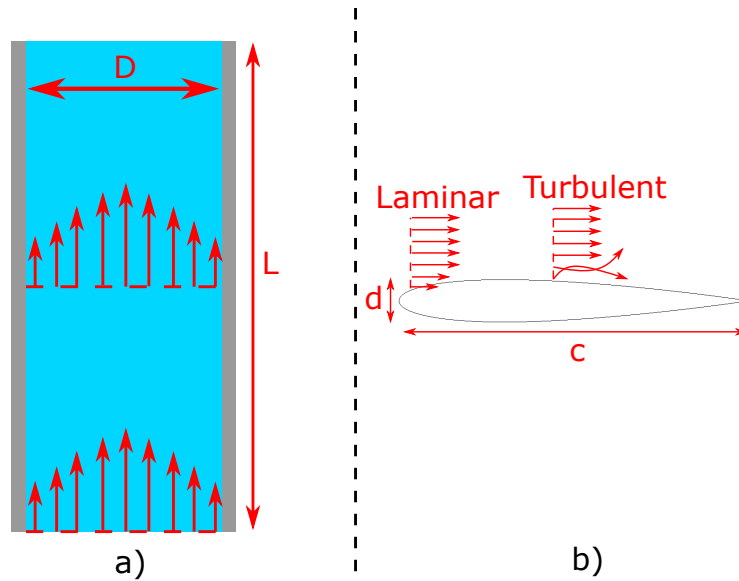


Figure A.5. *Differents object characteristic length for a) a pipe flow b) an airfoil flow*

than 1 (which happens quite often in nature), the inertial forces dominate the flow. Depending on the value of this number, the state of the flow can be either a laminar flow, a transient flow or a turbulent flow. When the Reynolds number is below a certain limit, the flow has a low inertial energy which is observable as a laminar flow behavior (see Figure A.4). This limit changes depending on the considered problem, for instance for pipe flows the Reynolds number limit value of a laminar flow is 2000, for an opened channel flow passing over a flat plate the limit value of the Reynolds number is $5 \cdot 10^5$ [274] and for flows passing over airfoils, the laminar limit depend on the type of the considered airfoil. This limit value varied from $3.5 \cdot 10^4$ to $1 \cdot 10^5$ [275]. However, if the limit is unknown, the laminar transition point taken will taken at $Re = 5 \cdot 10^5$, the laminar limit value for a flat plate.

Beyond this limit value, there is an interval where the flow has a complex behavior for which turbulences and small vortices start appearing in the flow. Moreover, the speed and the pressure in the flow starts to be erratic. It is the transient flow status. As for the laminar limit, this interval changes depending on the problem considered. For pipe flows, this interval is between a Reynolds number of 2300 and 4000 and for a flat plate, this interval is between $5 \cdot 10^5$ and $1 \cdot 10^6$ [274].

If the Reynolds number is greater than the upper boundary of the interval, the inertial

forces of the flow are so important that an infinite number of chaotic vortices are present inside the flow, the speed and the pressure of the flow become chaotic and brutally oscillate non-periodically. This state is called the turbulent state of the flow (see Figure A.4).

Besides being able to predict the state of a given flow and qualitatively estimating the inertial forces present in it, the Reynolds number is also very popular because of its ability to link geometric and kinetic quantities of two different scaled flows. Figure A.6 shows a motorised boats models, one is a full scale model with a length L_1 that moves at a velocity v_1 . The other model is a small scale model with a length L_2 that moves at a velocity v_2 . A motorised boat is usually 8m long ($L_1 = 8$ m) and moves at a velocity of 8.2 m/s ($v_1 = 8.2$ m/s).

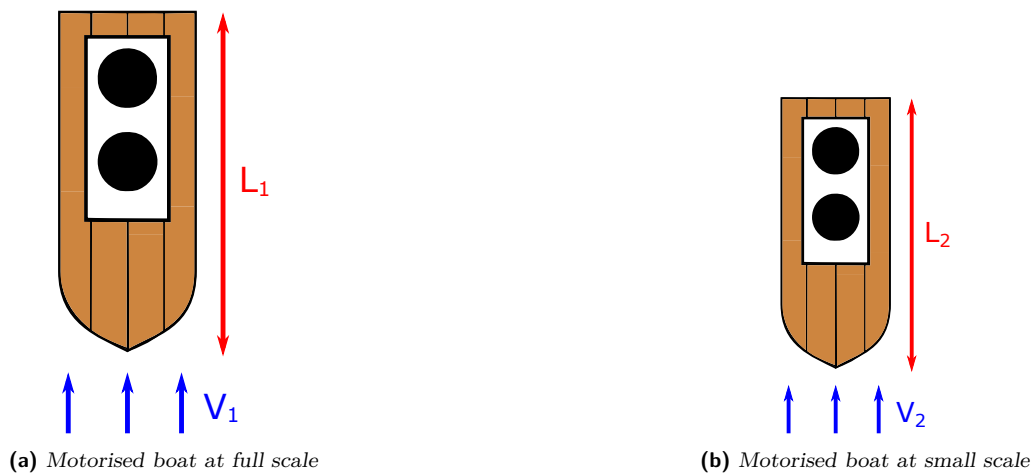


Figure A.6. Motorised boat at full scale and at reduced scale

Before manufacturing the boat, a smaller scale prototype is tested on water. This smaller scale prototype is designer at the 1/4th scale of the full boat. This small scale boat will be tested in a water tunnel, *i.e.* large tubes where water is expelled at controlled high velocities for testing boats in cruising conditions. According to the Vaschy-Buckingham similitude principle, the small and the bigger scale problems can be put in the same conditions of navigation. However, because of the difference of scale size, the speed must be modified accordingly to have a flow that is in the same state for the full scale and small scale model.

As explained earlier, the Reynolds number is a mean of qualitatively estimating the

inertial forces inside a flow for a given fluid dynamics problem. So for two problems, that have the same boundary conditions but where only the scale of the considered objects change; Having a similar Reynolds for the two problems means that the state of the flow, and thus its inertial energy, are the same for the both considered problems. So, it said that the two problems are in a dynamic similarity. Equation A.17 shows the dynamic similarity between the full scale boat 1 and the small scale boat 2.

$$\begin{aligned}
 Re_1 &= Re_2 \\
 \frac{\rho V_1 L_1}{\mu} &= \frac{\rho V_2 L_2}{\mu}
 \end{aligned}
 \tag{A.17}$$

The dynamic similarity is not only used for boats, but also for aircrafts and other complex industrial systems [276]. Nevertheless, as implied previously by studying the Reynolds number, the dynamic similarity of different scales depend strongly on the problem considered. Thus, having only a similar Reynolds number is not enough, for some problems, to have a dynamic similarity. For instance for problems where the flow velocity is close enough or superior to the speed of sound, the Mach number must also be checked to be sure that the flow is in the same conditions on the scaling model and in reality.

The Mach number will be later introduced in § A.2.5. For the problems encountered in this work, checking the Reynolds number and the Mach number similarity is sufficient for having a dynamic similarity.

A.2.4 Kinematic viscosity

In the Reynolds number equation depicted in Equation A.15, the physical quantities V , the velocity and D , the characteristic length are characteristics that are proper to the flow, regardless of the type of the fluid described. On the contrary of these quantities, the density ρ and the dynamic viscosity μ are not properties of the flow, but of the fluid. That is why, usually, researchers in fluid dynamics prefer to write the Reynolds number expression in an alternative way (see Equation A.18).

$$Re = \frac{VD}{\nu}
 \tag{A.18}$$

With ν being the kinematic viscosity, and it is defined by Equation A.19. With μ being

the dynamic viscosity and ρ being the fluid's density.

$$\nu = \frac{\mu}{\rho} \quad (\text{A.19})$$

In this new form, the kinematic viscosity represents the capacity of a given fluid to go into motion. Hence, this quantity represents the amount of energy to provide for transforming a static fluid into a flow. Moreover, the viscosity and the density of a fluid are temperature and pressure dependant. So, for variational studies, having the Reynolds number equation written in the form seen in Equation A.15 obliges the studies to take into account the variation of two parameters instead of one in the form of Equation A.18.

A.2.5 Mach number

As said in the paragraph devoted to the Reynolds number, many dimensionless numbers can be used for describing and comparing the states of different flows submitted to different conditions. They are also used to scale up or down fluid flow problems by having similar dimensionless numbers. The Mach number is one of these dimensionless numbers.

The Mach number compares the velocity of a flow to the speed of sound in this fluid. Its expression is given in Equation A.20. With V being the velocity of the flow and a being the velocity of sound in the considered fluid. The velocity of sound in a fluid is highly influenced by the temperature and pressure conditions encountered by the fluid.

$$\text{Mach} = \frac{V}{a} \quad (\text{A.20})$$

Depending on the value of this number, the state and the regime of the flow changes. Table A.1 shows the different existing types of regimes for a flow, depending on its Mach number.

Looking at Table A.1, the first existing regime is the incompressible subsonic regime which is encountered if the Mach number is inferior to 0.3. In this configuration, the flow's velocity is not great enough to start compressing the flow's particles. Incompressible hypothesis can be used for constitutive equations.

The second existing regime, the compressible subsonic regime, occurs when the Mach number's value is between 0.3 and 0.8. At this regime, the fluid's velocity is high enough for compressing flow's particles. This compressible fluid's behaviour can be described by

Regime name	Mach number value	Regime description
Incompressible subsonic	$M < 0.3$	The considered flow is incompressible
Compressible subsonic	$0.3 < M < 0.8$	The considered flow is compressible and it can be modeled with an ideal gas law
Transonic	$0.8 < M < 1.2$	The flow's velocity is high enough for the apparition of the first shock waves, but these are located on the backside of the object inside the flow
Supersonic	$1.2 < M < 5$	The flow's velocity is greater than the speed of sound in this media, which leads to the appearance of shock waves in the front of this object
Hypersonic	$M > 5$	The flow's velocity is so great that the fluid's friction starts to heat the object's surface, which changes many physical laws governing the flow

Table A.1. Regimes of a flow for different Mach numbers

a perfect gas law.

The transonic regime can be observed for Mach numbers reaching values between 0.8 and 1.2. At these velocities, the changes in pressure and temperature in the flow around the object leads to local regions where the speed of the fluid exceeds the speed of sound. By reaching the speed of sound, the fluid particles become so compressed that brutal changes in temperature and pressure happen inside the fluid. These brutal changes lead to the appearance of two regions: one where the flow's physical properties (pressure, temperature and velocity) are low and a region where the physical properties are high. The border between these regions is called a shockwave (see Figure A.7). This border is a region where the flow velocity has compressed the particles so much, that the compressed fluid becomes a physical wall that brutally collide with the upcoming particles. This compressed air region acts like a discontinuity in the flow, the supersonic upcoming flow separates after this shockwave.

The supersonic regime is encountered for Mach numbers values between 1.2 and 5. For such high Mach numbers, the fluid particles are compressed up to a point of forming shockwaves before encountering the object. These shockwaves are what people call "the

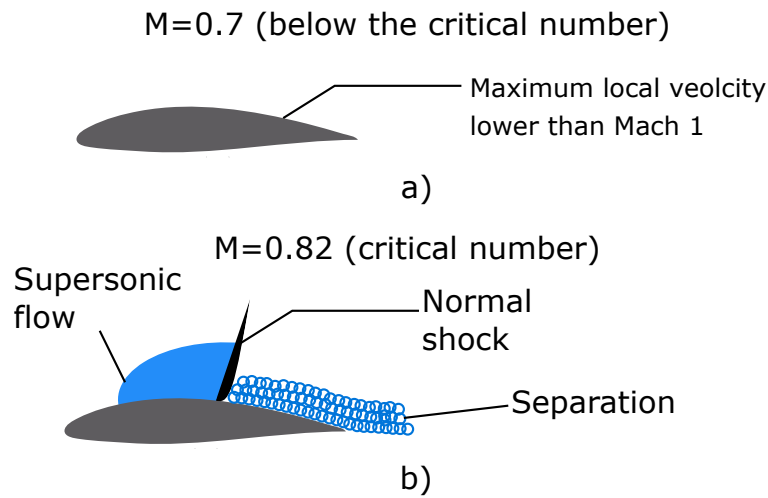


Figure A.7. Visualisation of two different Mach regimes: a) Subsonic b) Transonic

sound wall". They are the reason why condensate water appears around fighter jets when they approach the speed of sound and the "sonic boom" that can be heard when the fighter jet crossed the speed of sound corresponds to the moment when the jet crosses this wall of particles.

The hypersonic regime can be observed for Mach numbers greater than 5. In this regime, the flow velocity is so important that the fluid friction over the surface starts degrading the surfaces of the object. Moreover, the compressible fluid cannot be described by a perfect gas law anymore, other models need to be used for describing the fluid's behavior.

In our work, we tried to always verify that the Mach number is below to $M < 0.3$ because the equations and numerical models used for describing the flow's behavior only modeled incompressible fluids. No compressible fluid model was implemented in this numerical solution.

A.2.6 Lagrangian and Eulerian descriptions

Once again, if fluid dynamics are compared to solid mechanics, the ways of describing the evolution in time of a system's physical quantities are substantially different. Two major ways of tracking their evolution lie in two systemic descriptions: the Lagrangian description and the Eulerian description. Solid mechanics mostly use the Lagrangian description to depict the evolution of a physical system (at the exception of some solid

mechanics subfields, (such as finite transformations) and Fluid mechanics mostly use the Eulerian description to keep a track of a system's evolution. Figure A.8 will be used for explaining the way these two description operate.

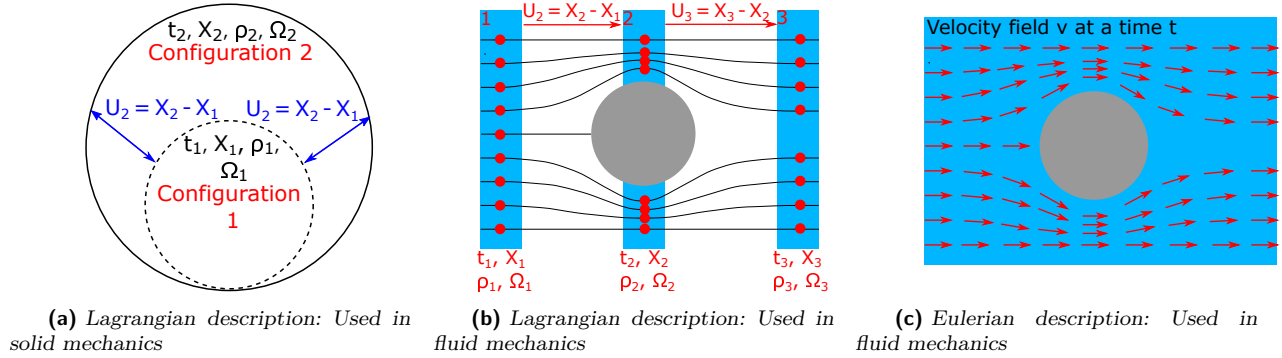


Figure A.8. Description of two possible physical descriptions: Lagrangian and Eulerian

In solid mechanics, usually for estimating the time variations of a physical quantity, an initial configuration is selected at a reference time. Figure A.8a shows an example of an inflating sphere. This system's name is configuration 1. Configuration 1 is composed of all the points present on the sphere. In this system, t_1 is the reference time, X_1 is the system's reference position, ρ_1 is the initial density of the system and Ω_1 is the system's reference volume.

After charging the system with loads, the system starts to change with respect to time. For observing these changes, the system needs to be observed at a time t_2 . This new configuration has the name configuration 2 on Figure A.8. For calculating the evolution of a physical quantity of the system (*e.g.* the density), the difference between the final configuration (configuration 2) and the initial configuration (configuration 1) needs to be made with regard to the time. Equation A.21 depicts the variation of density with time from the case in Figure A.8a.

$$\frac{\delta\rho(X_i, t)}{\partial t} = \text{Final configuration} - \text{Initial configuration} = \frac{\rho_2(X_i, t) - \rho_1(X_i, t)}{t_2 - t_1} \quad (\text{A.21})$$

The description depicted until now is the Lagrangian description. The principle of this description is following the system's deformation and evolution from a starting point up to a final point.

Figure A.8b, shows the Lagrangian description for studying a 2D flow around a cylinder. On this Figure, the studied system is represented by the blue square that represents a volume of fluid. In this volume, some fluid particles have been highlighted in red. The behavior of these particles will be tracked with the displacement of the volume. For the initial configuration denoted by the number 1 in the blue volume of Figure A.8b, it can be seen that the selected particles belong to parallel streamlines that seem to share the same velocities independently from the particles position.

The configuration number 2 of Figure A.8b has been now displaced by a value U_2 . At this displaced configuration, the volume has been split in two because of the cylinder's presence. This split in volume has changed the particles trajectories, *i.e.* their velocities also (see Figure A.8b). In this new configuration, the physical properties, like velocity or pressure, are dependent on the distance of the particle with the cylinder surface. However, the lower and upper volumes have a symmetrical behavior due to the symmetrical geometry of the cylinder.

For the last configuration, configuration number 3 of Figure A.8b, the volume of fluid displaced from a displacement value U_3 and is now far behind the cylinder. At this configuration, the particle's trajectory is rectilinear again. These are the same as the ones seen in configuration 1, the cylinder has no more effect on the flow and the fluid flow turned back as it was before encountering the obstacle.

As it has been described just above, the configuration 3 of Figure A.21 has the same physical properties as configuration 1. Far from the objects, the flow's streamlines are parallel and have a rectilinear trajectory. Thus, those regions of the model do not need to be simulated because their behavior is simple and easily predictable. The real deal comes for estimating flow's physical properties around objects, that are the interesting regions. So with the Lagrangian description, the fluid volume needs to be reseted to its original position (position 1 for Figure A.8b) for being able to describe the fluid's properties effectively. As exposed here, this type of description is not very effective for describing the flow's property around an object: calculation time is lost on positions where the flow's description is easy to predict. Moreover, using the Lagrangian configuration is not effective for describing non-stationary flows. Indeed, the control volume is only able to describe

the flow's properties for one particular position at one particular time. However, for accurately describing a non-stationary flow's properties, for a given position the flow's properties must be known for all step of time. For these reasons, the Lagrangian description is not an accurate way of describing a flow's behavior in fluid dynamics.

The other way found by physicists for describing effectively a flow's behavior is the Eulerian configuration (see Figure A.8c). The Eulerian description consists in "taking photos" of a particular flow volume (also called a flow domain) at a given time and then estimating the flow's properties (velocity, pressure, density...) for all the points of the fluid domain at this time. This picture of the volume is called a "control volume", it is static and it only captures the fluid flow that is inside it at a given time t . Usually, this control volume is selected in a way that the solid object is included in this volume domain (see Figure A.8c). However, one new problem arises with this new configuration: the fluid properties variations are no more predictable with Equation A.21 because there is only one configuration here (no more initial and final configuration).

These physical properties variations can be estimated through the variation of other variables on which the considered physical property depends. Usually, the flow's physical properties depend on time, noted down by t and the spatial position in the control volume noted down by the vector X_i . With this being said, let us try to express the variation of density $\rho(X_i, t)$ with regard to time with the Eulerian description. Equation A.22 gives the differentiation of the density.

$$d\rho(X_i, t) = \frac{\partial \rho}{\partial t} dt + \frac{\partial \rho}{\partial X_i} dX_i \quad (\text{A.22})$$

Now for finding back the time derivative of density with respect to time, Equation A.22 has to be divided by dt . Equation A.23 shows the final result.

$$\frac{d\rho(X_i, t)}{dt} = \frac{\partial \rho}{\partial t} + \frac{\partial \rho}{\partial X_i} \frac{dX_i}{dt} \quad (\text{A.23})$$

Equation A.23 can be more simplified: the term $\frac{dX_i}{dt}$ represents the variation of the position of a fluid particle inside the volume with respect to time, this term represents in fact the velocity of that particle. It will be denoted by v . The term $\frac{\partial \rho}{\partial X_i}$ represents the variation of density with respect to its spatial position, this term is in fact the spatial gradient of the density. By rearranging the considered terms of Equation A.23, Equation

A.24 can be found.

$$\frac{d\rho(X_i, t)}{dt} = \frac{\partial\rho}{\partial t} + \frac{\partial\rho}{\partial X_i}v_i \quad (\text{A.24})$$

Equation A.24 is called the "material derivative" of the density, this type of Equation is used for describing the variation with respect to time of any physical quantity inside the control volume used in the Eulerian description. Equation A.25 gives the general form of the material derivative for any physical quantity (*e.g.* velocity, pressure, density...) inside the fluid, with a being the considered quantity.

$$\frac{da(X_i, t)}{dt} = \frac{\partial a}{\partial t} + v_i \left(\frac{\partial}{\partial X_i} \right) a \quad (\text{A.25})$$

Having said that, in the following sections of this paper, fluid models and fluid-structure interaction models will be presented. All the models that will be exposed in the fluid sections are presented in an Eulerian description, whereas the solid models that will be exposed are presented in a Lagrangian description. All the different quantities estimated in these models will be calculated accordingly with the corresponding time variational models presented for each description.

A.2.7 Boundary Layer

For air or water flows with a high Reynolds number passing around an object, the flow can be divided in three regions: (1) An unperturbed area where the streamlines remain parallel (*i.e.* the regions in front of and behind the cylinder in Figure A.8b) (2) A thin viscous area on the surface of the object immersed in a flow (see Figure A.9) where the viscous forces act as depicted in the subsection A.2.1 (3) a region behind the object, where the fluid's pressure and velocity are low.

This thin area depicted in (2) is called a boundary layer, a region where the shear forces have a high impact on the flow. The unperturbed region of the flow (1) is called "the external flow", it is considered as being inviscid because the shear stress effect on the flow becomes negligible. The region behind the object (3) is called "the wake". It is a region that appears when the boundary layer detaches from the immersed object leading to low pressure and low velocity (see Figure A.9). Hence, the limit that separates the two regions starts where the shear stress effect on the flow becomes negligible. In practical terms, this occurs when the x component of the velocity of the flow in the boundary layer

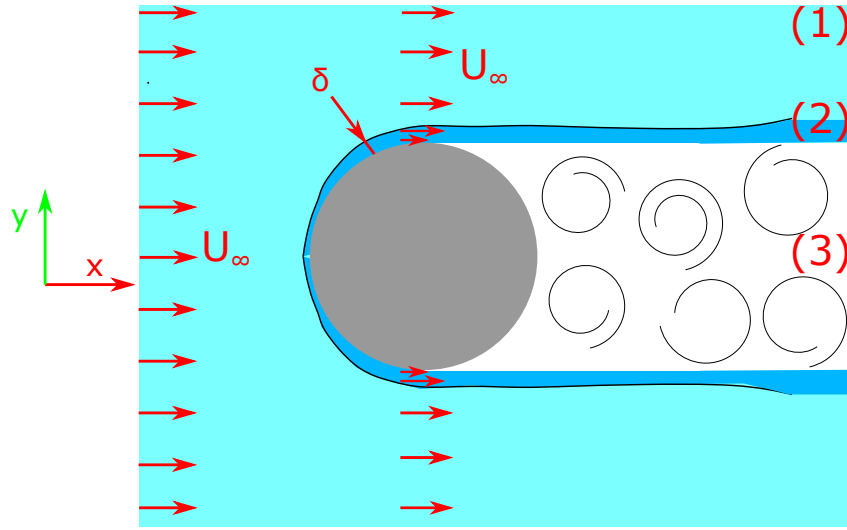


Figure A.9. Three existing areas of the flow (1) Inviscid external flow (2) Viscous boundary Layer (3) Low pressure wake

U has a value close to 99 percent of the x component of the velocity of the external flow U_∞ (see Equation A.26). On Figure A.9, this limit is the black line between region (1) and region (2).

$$U(\eta(y) = \delta) = 0.99U_\infty \quad (\text{A.26})$$

In Equation A.26, δ represents the thickness of the boundary layer, and η represents the immersed object's curvilinear height coordinate from the object's surface. This curvilinear height coordinate is dependent on the global object's height coordinate y .

In addition to this limit, there is another object with which the boundary layer has a border: it is the immersed object itself. As stated in Section A.2.1, flow particles passing on a solid's object surface stick to this surface. For fluid particles, it implies that their velocity is null at the object's surface. Equation A.27 formulates this observation mathematically. Note that at $\eta(y) = 0$, a considered point is located on the object's surface.

$$U(\eta(y) = 0) = 0 \quad (\text{A.27})$$

As Figure A.9 seems to illustrate, the boundary layer thickness δ tends to grow along the object. Indeed, the Reynolds number, the velocity and the pressure tends to change

along the boundary layer. The Reynolds number for a boundary layer is estimated by Equation A.28. Where s is the curvilinear position on the surface of the immersed object.

$$Re = \frac{U_{\infty}s}{\nu} \quad (\text{A.28})$$

Equation A.28 shows that the boundary layer's Reynolds number increases along the object's curvilinear length. Thus, it means that the inertial forces and energy increase with length inside the boundary layer. This implies that the velocity increases within the boundary layer. In section A.2.1, it has been showed that the shear stress increases linearly with the shear rate, which is a sum of velocity gradients. Hence, if the velocity inside the boundary layer increases alongside the object, so does the shear rate and the shear stress. This increase in shear stress implies a thickening of the boundary layer, as the flow gains kinetic energy.

The increase in velocity along the object's surface leads to an another important observations for 2D flow problems: the X component of velocity u (direction X is considered to be alongside the surface of the immersed object) is way greater than the Y component of velocity v (direction normal to the object's surface). Using this hypothesis in the constitutive momentum equation for fluids (*i.e.* Equation A.69, paragraph A.6), it can be shown that the pressure gradient depends directly on the velocity compounds u and v (see Equation A.29).

$$\begin{aligned} -\frac{\partial P}{\partial x} &= A(t, x, y)u \\ -\frac{\partial P}{\partial y} &= B(t, x, y)v \end{aligned} \quad (\text{A.29})$$

In Equation A.29, $A(t, x, y)$ and $B(t, x, y)$ are complex gradient operator. Using the hypothesis that $u \gg v$ on this equation leads to Equation A.30.

$$\begin{aligned} -\frac{\partial P}{\partial x} &\gg -\frac{\partial P}{\partial y} \\ -\frac{\partial P}{\partial y} &\approx 0 \end{aligned} \quad (\text{A.30})$$

This hypothesis is true for most types of flows (laminar, turbulent, supersonic...), only flows that have a Mach number superior or equal to 20 do not respect this hypothesis [29]. Nonetheless, these types of flows are way out of the scope of our work where Mach number never exceeds 0.3.

Having said that, if the velocity is high enough and if the object is long enough, Equation A.28 implies also that the boundary layer can pass from a laminar state to

a transition state and then to a turbulent state on the surface of the immersed object. This is indeed the case, at the front edges of the object, the boundary layer is always laminar. But after some time the boundary layer becomes turbulent (see Figure A.10). The transition state, being highly complex, is out of the scope of our manuscript.

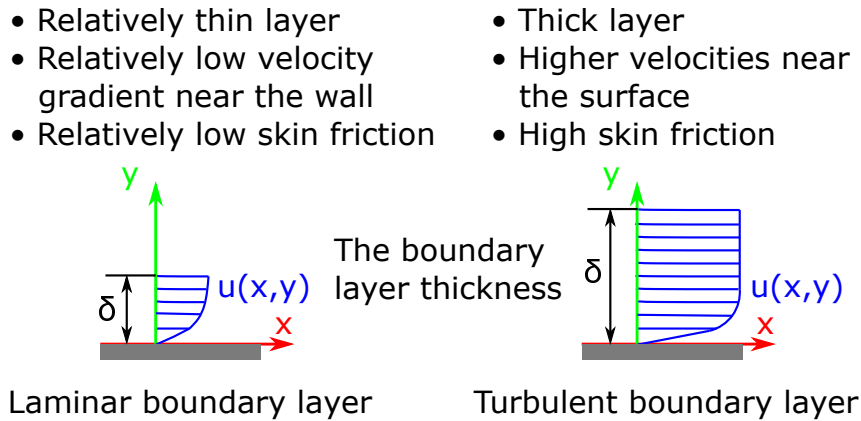


Figure A.10. *Laminar and turbulent boundary layer*

Having two different flow states means that the equations governing the boundary layer's behavior also change. Indeed in laminar boundary layers, the inertial energy of the boundary layer is low. Thus, the particles velocity inside the boundary layer is low which leads to have laminar streamlines that remain parallel to the object's surfaces. Hence, having parallel streamlines implies that the exchange of inertia and momentum between the different streamlines composing the boundary layer is made on a microscopic level as depicted in section A.2.1.

The low inertial energy of laminar streamlines and the microscopic momentum exchange between streamlines for laminar boundary layers make the development of constitutive equations governing the behavior of laminar boundary layers possible. This constitutive equation is given in Equation A.31. This last equation will not be thoroughly explained and discussed, as it is not used later on. It is just provided for the reader to know the equation's main form. We will advise the reader to go and check Reference [29] for more details.

The equation will not be detailed here for many reasons. First of all, in this work, we will be focused on studying a turbulent hydrofoil fluid flow with numerical methods. Thus, explaining this equation thoroughly will be out of the scope of this work. Secondly,

the derivation and explanation of this equation is very challenging, hence the only thing to remember from this equation is the possibility to find a governing equation for laminar boundary layers. For solving Equation A.31, one must find the f' value, representing the relative velocity of a streamline in a boundary layer $f' = \frac{U}{U_\infty}$. The 'prime' signs in the equation are derivatives with regard to $\eta(y)$.

$$\begin{aligned} f f'' + f''' + [1 - (f')^2] \beta &= 0 \\ f' &= \frac{U}{U_\infty} \end{aligned} \tag{A.31}$$

On the contrary of laminar boundary layers, turbulent boundary layers have high inertial energy. Hence, the particles inside this boundary layer have a very high velocity. The inertial energy in this kind of state is so great that the particles do not form streamlines anymore, but move frenetically up and down in the boundary layer. With the particles having that kind of behavior, the momentum exchange is not microscopic anymore, as it was in the laminar boundary layer. Right now, it is macroscopic: the particles move from the top to the bottom of the boundary layer.

Having said that, in the turbulent case, there is currently no governing equations that has been found for accurately describing the flow's behavior. Indeed, the turbulence understanding is still incomplete and is a current very active research topic [277], [278]. Nevertheless, some attempts have been tried for being able to find equations that fits the macroscopic velocity variation in the boundary for some particular basic cases.

One of the basic cases studied for better understanding turbulent boundary layers is a flow over a flat plate. Even in this case no exact solution exists. Nonetheless, some attempts have been made for finding mathematical models that fit more or less precisely the empirical results obtained on the turbulent flat plate boundary layer flow.

Ludwig Prandtl, the engineer and scientist that theorised and discovered the boundary layers, made an hypothesis for the boundary layer's flow very near to the wall: in this region, the viscous shear forces outperform inertial forces and creates a laminar sub-layer. He deduced that the velocity in this region depends on three parameters: the wall shear stress, the fluid's physical properties and the distance y from the wall. **In turbulent flows, one does not use pure velocities anymore but uses mean time-averaged velocities \bar{u} instead.** The reason behind this will be explained in Section A.4, however

it is linked to the lack of knowledge in Turbulence's behavior.

Hence, if the flow's profile is linear near the wall, \bar{u} is proportional to y . The shear stress expression for a Newtonian fluid must still be true (see Equation A.32). In this expression τ_w is called the wall shear stress, it physically represents the shear forces applying just above the surface of the object called a "wall" here.

$$\tau_w = \mu \left(\frac{\partial \bar{u}}{\partial y} \right)_{y \rightarrow 0} = \mu \frac{\bar{u}}{y} \quad (\text{A.32})$$

Despite the fact, that it has been observed for a flat plate, this laminar sub-region exists in all the different types of boundary layers that can be encountered and in general turbulent flows. Thus, in an attempt of generalising the results and observations made here for other kinds of problems, all datas and variables have been adimensionalised. For instance, the velocity is expressed as the variable u^+ , called "the wall velocity" and defined by Equation A.33.

$$u^+ = \frac{\bar{u}}{u^*} \quad (\text{A.33})$$

In Equation A.33, u^* represents the "wall-friction velocity". Physically, it represents the velocity that is infinitesimally above the wall, at a distance $y = 0^+$ from the wall. It's value is defined by dimensional analysis with Equation A.34.

$$u^* = \sqrt{\frac{\tau_w}{\rho}} \quad (\text{A.34})$$

The distance from the wall y^+ expressed in non-dimensional "wall units" is given by Equation A.35.

$$y^+ = \frac{y u^*}{\nu} \quad (\text{A.35})$$

In Equation A.35, ν represents the fluid's kinematic viscosity. By looking at this equation more carefully, it can be seen that the non-dimensional distance has the form of the Reynolds number. If u^+ of Equation A.33 and y^+ of Equation A.35 are replaced in Equation A.36.

$$\tau_w = \mu \frac{u^+ u^*}{(y^+ \nu) / u^*} = \left(\frac{u^+}{y^+} \right) \rho u^{*2} \quad (\text{A.36})$$

Now, if the definition of wall-friction velocity (see Equation A.34) is introduced into Equation A.36. It is obvious that:

$$u^+ = y^+ \quad (\text{A.37})$$

The model described in Equation A.37 is known as the "linear sublayer law". The laminar sublayer, where the velocities are small and where the viscous forces dominate the flow, lies under a y^+ value of 5. This means that the viscous sublayer law described in Equation A.37 is true up to a y^+ value of 5, *i.e.* the viscous sublayer law is true until the inertial forces of the boundary layer reach a value 5 times superior to the viscous forces (the y^+ having an expression similar to the Reynolds number). The y^+ can go up to 10, if there is a 10 percent error tolerance on the velocity precision.

Beyond this laminar region, there are other sub regions that exists. The viscous sublayer, a region where the viscous forces dominate the flow, is composed of the linear laminar layer seen just before and located at a y^+ interval of 0 and 5 and the "buffer layer" a region located between a y^+ location of 5 and 50. In the buffer layer region, the flow becomes so complex that there is currently no model that describes this region accurately.

Above a y^+ value of 50, there are two other regions composing the "Defect-law region": the Log-law region and the Outer region. In those regions, Theodore von Kármán, a hungarian physicist, showed that the velocity magnitude did not directly depend on the viscosity anymore, but it depended directly on the wall shear stress and the distance y over which this effect has diffused. Having said that, von Kármán showed that there is a logarithmic relation between the velocity and the distance from the wall. Equation A.38 depicts this mathematical relation. In this equation, κ is called the von Kármán constant, this constant physically represents the wall shear stress diffusion in the upper layers of the boundary layer. It is because of this mathematical fitting law that the "log law region" was named this way. This fitting law remains true up to a y^+ value of 200.

$$\begin{aligned} u^+ &= \frac{1}{\kappa} \ln y^+ + B \\ \kappa &\approx 0.4 - 0.41 \\ B &\approx 5.0 - 5.5 \end{aligned} \quad (\text{A.38})$$

The last region is called the outer region, this region is the thickest one in the boundary layer, it represents 80 to 90 percent of the overall boundary layer size and starts at a value

of y^+ of 200. In the outer region, another nameless fitting law was discovered (see Equation A.39). In this equation, u_∞^+ represents the dimensionless free stream velocity $u_\infty^+ = \frac{U_\infty}{u^*}$ and δ is the boundary layer height.

$$\begin{aligned} u_\infty^+ - u^+ &= -\frac{1}{\kappa} \ln \frac{y}{\delta} + A \\ \kappa &\approx 0.4 - 0.41 \\ A &\approx 2.35 \end{aligned} \tag{A.39}$$

Those semi-empirical fitting equations are very important for turbulence modeling. Even though they were developed for flat plates, it is widely used in simulation software and numerical analyses for estimating the physical quantities in the boundary layer of complex objects - *e.g.* cylinders, airfoils, aircrafts... - (see section A.4.1). Figure A.11 resumes all the regions encountered so far and shows their various locations.

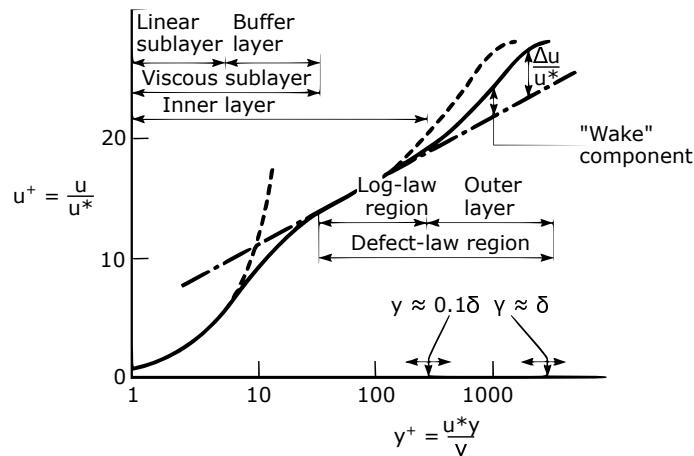


Figure A.11. Turbulent boundary layer regions, graph taken from [29]

To summarise everything that has been said in this section, a boundary layer is defined as being the region that separates the external flow from the object's surfaces. This region is considered to have high viscous effects compared to the external flow, however these viscous effects decrease alongside the object's curvilinear length in the profit of inertial forces. Indeed, if the object is long enough, the boundary layer passes through three different states: the laminar, the transition and the turbulent state. The laminar boundary layer behavior is depictable with analytic constitutive equations on the contrary of transition and turbulent state.

Despite the absence of constitutive models, semi-empirical mathematical laws have

been developed by dividing the turbulent boundary layer into several regions. A region called the viscous sub-layer very close to the object's surface, where the viscous forces are so high that the flow is in laminar state.

Very close to the wall, the dimensionless velocity rises linearly with the dimensionless height from the wall. Above the viscous layer, the Defect-law region is not influenced directly by the viscous forces, but by the diffusion of the shear stress near the surface in those upper regions of the boundary layer. Here, the dimensionless velocity evolves in a logarithmic trend with the dimensionless height of the boundary layer. Figure A.12 illustrates the evolution of the boundary layer with regard to curvilinear length of the surface.

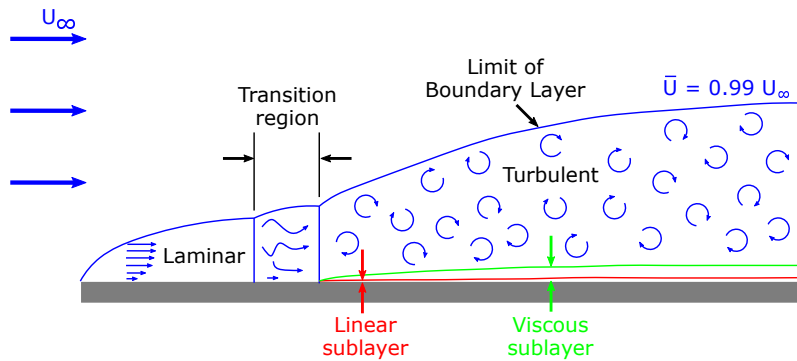


Figure A.12. Summary of a boundary layer properties and states

A.2.8 Aero- and hydrodynamic coefficients

When an aero- or hydrodynamic object is subjected to a fluid flow, there are hydrodynamic forces that apply on its surface with the form of hydrodynamic pressure (see Figure A.13). The main forces resulting from the pressure forces on this object are lift and drag.

The lift force is defined as the force that is perpendicular to the oncoming flow direction. Whereas, the drag force is the force that opposes to the object's motion in the surrounding fluid. As it can be seen on Figure A.13, these forces depend on the pressure forces that act on the object and the viscous friction forces made by the flow on the object's surface. The drag force depends strongly on the viscous friction forces for high velocities. As suggested in the previous sections, the pressure forces in a fluid flow strongly depend on the fluid flow's properties (density, viscosity, velocity...) and the object's geometry (shape, length, width...).

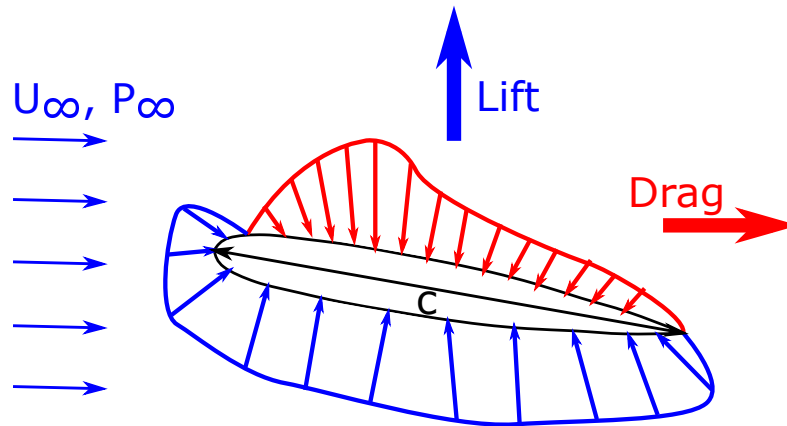


Figure A.13. Hydrodynamic pressure forces on the hydrofoil

Thus, if someone would like to compare the best geometrical shapes, and shapes only, for some targeted force, (*e.g.* shapes that generates highest lifts, shapes that generates highest drag, best lift/drag ratio...) how should he proceed ? Indeed, because of the numerous parameters affecting pressure forces applied to an object in a flow, how is it possible to isolate the shape only ? The answer to this problem is the same as the one implemented for the Reynolds number's issues: non-dimensionalisation of forces.

All these forces depend on the pressure field around the object, and this pressure field is strongly dependent on the geometry, the fluid's velocity and the fluid's density. Hence, even for pressure, there is a need of isolating the effect of geometry only and not the other parameters. The solution to do that for pressure, is to remove the hydrostatic pressure component of the total pressure expression, and divide the total amount of pressure around a body by the initial dynamic pressure of the fluid (see Equation A.40).

$$C_p^i = \frac{P_i - P_\infty}{\frac{1}{2}\rho U_\infty^2} \quad (\text{A.40})$$

In Equation A.40, C_p^i represents the non-dimensional pressure coefficient at a given location, P_i is the pressure value of a given location, P_∞ represents the hydrostatic pressure value of the fluid flow far from the object, ρ stands for density and U_∞ is the flow's velocity far from the object.

This pressure coefficient gives insight on how the pressure in the flow is affected by the object's geometry. The pressure coefficient C_p^i can have negative, positive or null values.

- A negative value of C_p^i means that the local pressure near this region of the object is lower than the reference pressure P_∞ (in a majority of cases, for aeronautics

problems, the reference pressure is the atmospheric pressure $P_{atm} = 1.10^5 Pa$). It is said that these regions are "low" or "under-pressured" regions of the flow.

- On the contrary, a negative value of C_p^i means that the local pressure near this region of the object is higher than the reference pressure. It is said that these regions are "over-pressured" regions of the flow.
- Finally, a null value of C_p^i means that the local pressure near this region of the object is equal to the reference pressure. For these types of regions there is no specific name attributed.

The product $\frac{1}{2}\rho U_\infty^2$ states as the dynamic pressure term, it represents the dynamic pressure embodied by the flow. Despite being negative, null or positive, the pressure coefficient C_p^i can have values inferior, equal or superior to 1. Depending on the absolute value exhibited by this coefficient, this gives information about the flow's velocity status.

- An absolute value of C_p^i inferior to 1 means that the local velocity in the considered region of the object is lower than the reference velocity U_∞ (in a majority of cases, the reference velocity is the velocity far from the considered object).
- On the contrary, an absolute value of C_p^i superior to 1 means that the local velocity in the considered region of the object is higher than the reference velocity.
- Finally, an absolute value of C_p^i equal to one means that the local velocity near this region of the object is equal to the reference velocity. This type of region is called a "stagnation point".

An additional interesting properties from the formulation of pressure coefficient C_p^i in Equation A.40 is that no quantity related to the object's dimension is included (length, radius, width...). This imply that the values of pressure coefficients obtained for a smaller scale object are the same for bigger size objects. Thus the pressure coefficients values obtained for the 1/10th scale model of an aircraft is the same as the full scale aircraft.

Now, for the lift and drag forces that are related to pressure forces, the logic is the same for non-dimensionalising them. However, on the contrary of pressure, the forces have a direct dependance on the scale of the objects that must be taken into account in the non-dimensional equations. To be more precise, the lift and drag forces have a direct dependence with the surface of contact of the considered object. Having said that, the non dimensional lift coefficient C_L and drag coefficient C_D are defined by Equation A.41.

$$\begin{aligned}
C_L &= \frac{F_{Lift}}{\frac{1}{2}\rho U_\infty^2 S} \\
C_D &= \frac{F_{Drag}}{\frac{1}{2}\rho U_\infty^2 S}
\end{aligned}
\tag{A.41}$$

In Equation A.41, F_{Lift} and F_{Drag} are respectively the total lift force and the total drag force that applies on the object. S is the surface where the lift and pressure forces apply. For the case of a 2D profile with an infinite span, the surface can be replaced by the characteristic length of the object (*e.g.* the chord length c for an air- or hydrofoil represented on Figure A.13). Equation A.42 represents the lift and drag coefficients for a 2D hydrofoil.

$$\begin{aligned}
C_L &= \frac{F_{Lift}}{\frac{1}{2}\rho U_\infty^2 c \times 1\text{m}} \\
C_D &= \frac{F_{Drag}}{\frac{1}{2}\rho U_\infty^2 c \times 1\text{m}}
\end{aligned}
\tag{A.42}$$

In Equations A.41 and A.42, there is still a link to be made between the lift forces and the drag forces and the pressure forces applying to an immersed object (see Equation A.40). For being able to do that, the external forces applying to the object must be listed. Equation A.43 lists all forces applied from the fluid to the immersed object.

$$\begin{aligned}
\sum F_{Fluid \rightarrow Object} &= F_{Pressure} + F_{Friction\ drag} \\
&= F_{Lift} + F_{Drag\ pressure} + F_{Friction\ drag}
\end{aligned}
\tag{A.43}$$

It can be seen that the pressure forces can be divided in two categories: lift forces and drag forces. Lift forces are composed of the pressure forces components that are perpendicular to the flow motion, whereas drag forces are composed of the pressure forces components that are parallel to the flow motion. In addition to these, there are also the viscous friction forces that result from the flow's movement next to the surface of the object. Figure A.14 illustrates how the forces act on the immersed object.

Now that the fluid forces exerted on the object have been explicated, each force will be isolated and its expression will be sought after. The lift forces are the first to be concerned, these ones are composed of the pressure forces components that are normal to the flow motion, thus these forces can be formulated by Equation A.44. Considering Figure A.14,

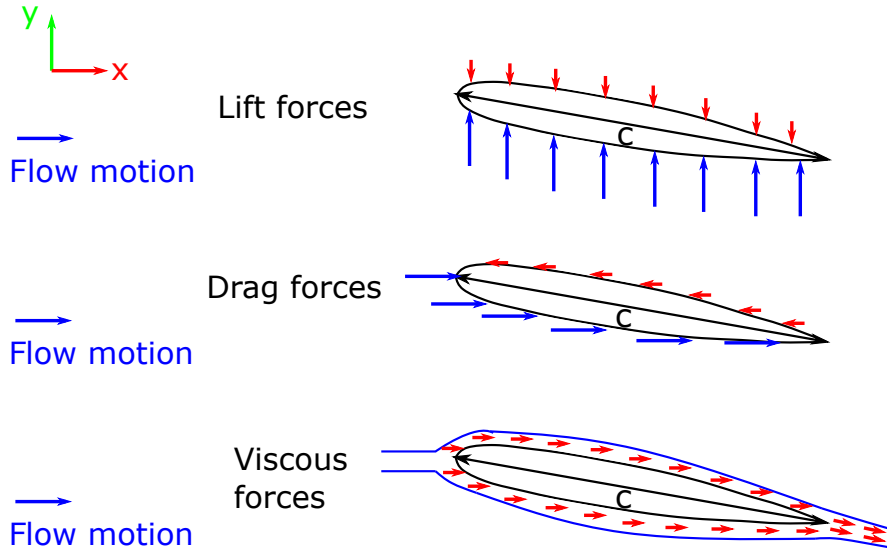


Figure A.14. Fluid forces action on the immersed object

the direction normal to the flow motion is considered as being the vector \bar{y} , \bar{n}_S being the surface normal vector and S being the exterior surface of the object.

$$F_{Lift} = \int_S (P(S) - P_\infty) \cdot \bar{n}_S \cdot \bar{y} \cdot dS \quad (\text{A.44})$$

Now that the expression of the lift forces have been expressed, if Equation A.44 is introduced into Equation A.41, the expression of the lift Coefficient is given in Equation A.45.

$$C_L = \frac{1}{\frac{1}{2}\rho U_\infty^2 S} \int_S (P(S) - P_\infty) \cdot \bar{n}_S \cdot \bar{y} \cdot dS = \frac{1}{S} \int_S C_p(S) \cdot \bar{n}_S \cdot \bar{y} \cdot dS \quad (\text{A.45})$$

If the considered problem is 2 dimensional (*i.e.* the object's span is infinite), Equation A.45 can be rewritten as Equation A.46 with c being the object's length (*i.e.* c is used for an hydrofoil chord).

$$C_L = \frac{1}{c} \int_x C_p(x) \cdot \bar{n}_S \cdot \bar{y} \cdot dx \quad (\text{A.46})$$

Reciprocally, for the drag forces coming from the fluid's pressure on the object can be expressed in a similar form (see Equation A.47). Here, the only thing that changes is the components of the pressure forces that are taken, these are taken in the \bar{x} direction.

$$C_{Dp} = \frac{1}{c} \int_x C_p(x) \cdot \bar{n}_S \cdot \bar{x} \cdot dx \quad (\text{A.47})$$

The last forces that need to be expressed are the friction viscous forces that opposes to the object's movement. The viscous frictions occurs very near the wall, inside the boundary layer of the object. Thus, the viscous forces can be expressed as the surface integral of the product of the local wall shear stress τ_w (see section A.2.7 for more details) and the object's local surface dS (see Equation A.48).

$$F_{Viscous} = \int_S \tau_w(S) \cdot \bar{n}_S \cdot \bar{x} \cdot dS \quad (\text{A.48})$$

Dividing these forces by the dynamic forces expression $\frac{1}{2}\rho U_\infty^2 S$, it gives the expression of the viscous friction forces non-dimensional coefficient, the skin-friction coefficient (see Equation A.49). With $c_f(S)$ being the local skin friction coefficient.

$$C_f = \frac{1}{\frac{1}{2}\rho U_\infty^2 S} \int_S \tau_w(S) \cdot \bar{n}_S \cdot \bar{x} \cdot dS = \frac{1}{S} \int_S c_f(S) \cdot \bar{n}_S \cdot \bar{x} \cdot dS \quad (\text{A.49})$$

As for the other coefficients, in a 2D problem, Equation A.49 can be rewritten as Equation A.50.

$$C_f = \frac{1}{c} \int_x c_f(x) \cdot \bar{n}_S \cdot \bar{x} \cdot dx \quad (\text{A.50})$$

Adding Equation A.47 and A.50 gives the final expression of the total drag coefficient A.51.

$$C_D = C_{Dp} + C_f = \frac{1}{c} \int_x (C_P(x) + c_f(x)) \cdot \bar{n}_S \cdot \bar{x} \cdot dx \quad (\text{A.51})$$

A.3 Fluid dynamics governing equations

For any scientific discipline, solving a given problem consists in finding all the unknown variables and unknown fields by solving their governing equations. In fluid dynamics, there are 6 unknowns variables and fields to be found: the pressure field P , the 3 components of the velocity field $v(v_x, v_y, v_z)$, the density field ρ and the temperature field T . Thus, for solving fluid dynamics problems 6 different equations are needed for finding those fields. Generally these equations are derived by adapting three laws of physics that govern the behavior of all objects found in nature: the governing of mass, Newton's second law and the laws of thermodynamics (1st and 2nd law of thermodynamics). In the next paragraphs the governing equations of fluid dynamics will be derived from these physical laws.

A.3.1 Continuity equation

This first equation is derived from the principle of the conservation of mass. This principle states that, for a given system, the total mass should always remain constant in this system. No variation of mass through time should be observed in this system. Equation A.52 translates this principle into an equation.

$$\frac{dm}{dt} = 0 \quad (\text{A.52})$$

The considered system of study will be a Reference Fluid Volume Element (RFVE) where a flow passes through its faces (see Figure A.15). In Figure A.15, $d\Omega_e$ represents the infinitesimal volume value of the RFVE, $d\Gamma_e$ represents the infinitesimal surface value of the faces of the RFVE and v represents the velocity of the flow passing through the RFVE faces. This system will be studied in the Eulerian description, where the RFVE is used as the control volume.

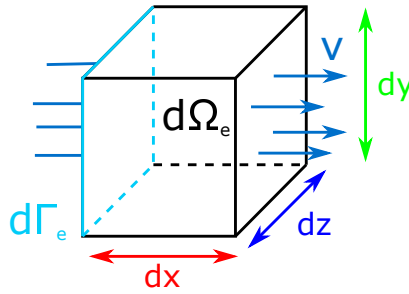


Figure A.15. Reference fluid volume element studied for the conservation of mass

Three physical actions have an action on the RVFE's mass in this problem: the density variations inside the RVFE, the massic flow of fluid entering the RVFE and the massic flow of fluid going out of the volume. With respect to conservation of mass, all these quantities must be equal to zero. The equilibrium of these mass actions is depicted in Equation A.53.

$$\underbrace{\int_{\Omega_e} \frac{d\rho_e}{dt} d\Omega_e}_{\text{Density variations}} + \underbrace{(\rho_e \Gamma_e v)_{out}}_{\text{Massic outflow}} - \underbrace{(\rho_e \Gamma_e v)_{in}}_{\text{Massic inflow}} = 0 \quad (\text{A.53})$$

By choosing a very small size of RVFE, the term devoted to density variations can be simplified into a differential term (see Equation A.54).

$$\int_{\Omega_e} \frac{d\rho_e}{dt} d\Omega_e = \frac{d\rho_e}{dt} dx dy dz \quad (\text{A.54})$$

The mass inflow term of Equation A.53 remains the same and is presented in Equation A.55.

$$(\rho_e \Gamma_e v)_{in} = \rho_e \Gamma_e v \quad (\text{A.55})$$

The mass outflow term of Equation A.53 undergoes some changes, in the RVFE all properties are considered to be uniformly varying functions of time and position. Thus, mass outflow could have slightly changed on the opposite face of the inflow. if the inflow mass is known $Q_{in} = \rho v$, the variations of the mass outflow can be quantified as $Q_{out} = \rho v + \frac{\partial v}{\partial x} dx$. Equation A.56 shows the expression of the massic outflow term.

$$(\rho_e \Gamma_e v)_{out} = \rho_e \Gamma_e \left(v + \frac{\partial v}{\partial x} dx \right) \quad (\text{A.56})$$

Now, if all these terms are put back into Equation A.53, its final form would become Equation A.57. This final form is the form of the conservation of mass for one directional fluid flows.

$$\frac{d\rho_e}{dt} + \rho_e \frac{\partial v}{\partial x} = 0 \quad (\text{A.57})$$

In a similar manner, if the derivation is expanded for a 3 directional flow problem, Equation A.58 is obtained. This final form of the 3D mass conservation equation is also known as the **continuity equation**.

$$\frac{d\rho_e}{dt} + \rho_e \frac{\partial v_i}{\partial x_i} = 0 \quad (\text{A.58})$$

For incompressible fluids, the density is considered constant. Hence, the general form of the continuity equation for incompressible fluids is given in Equation A.59.

$$\frac{\partial v_i}{\partial x_i} = 0 \quad (\text{A.59})$$

In CFD, some numerical methods use this equation for finding the velocity and pressure unknowns for incompressible flows [299], [300]. In the rest of the manuscript, the fluid flow problems encountered are mostly incompressible, thus the considered continuity equation for these problems will be Equation A.59.

A.3.2 Navier-Stokes equations: the transport of momentum

In fluid mechanics, the Navier-Stokes equations are the most fundamental equations used for describing fluid flow motions. These equations are derived from the Newton's second law. This law states that the sum of the external forces applied on a closed system are equal to the product of the mass of this system and its acceleration. The general form of Newton's second law is given in Equation A.60. With F_i^{ext} being the external forces applied to the fluid, m being the mass of fluid and a_i being the acceleration of the fluid.

$$\sum F_i^{ext} = ma_i \quad (\text{A.60})$$

As clarified earlier, in § A.2.2, the use of density in the fluid's motion equations is more relevant than the use of mass. Thus, the forces that will be expressed later on are forces per volume unit. Moreover, the definition of the acceleration is the time derivative of the velocity of the fluid. Having said that, Equation A.60 becomes Equation A.61. **In this new Equation, all the forces expressed are dimensionally homogeneous to a force per unit volume (N/m^3).**

$$\sum F_i^{ext} = \rho \frac{dv_i}{dt} \quad (\text{A.61})$$

Now for continuing the derivation of the Navier-Stokes equations, Equation A.61 will be applied on a system similar to the one shown in Figure A.15. This system is composed of a RVFE with fluid flows passing through all its faces. Figure A.16 sums up the overall external forces applying to the RVFE. All the possible forces applicable to a fluid are at the number of three: the pressure forces, the body (gravitational) forces and the viscous forces. If Equation A.61 is changed accordingly to those forces, Equation A.62 is obtained.

$$F_i^{Pressure} + F_i^{Body} + F_i^{Shear} = \rho \frac{dv_i}{dt} \quad (\text{A.62})$$

The final form of the equations describing the different forces are given in Equation A.63. These are derived in a similar method as continuity equation was derived in § A.3.1, by summing the actions of the forces on the different faces of the RVFE. In these equations, P_i is the pressure field, f_i is the gravitational acceleration vector, η is the viscosity of the fluid and v_i is the velocity of the fluid. For more details about the derivation of these forms, see the following Reference [274].

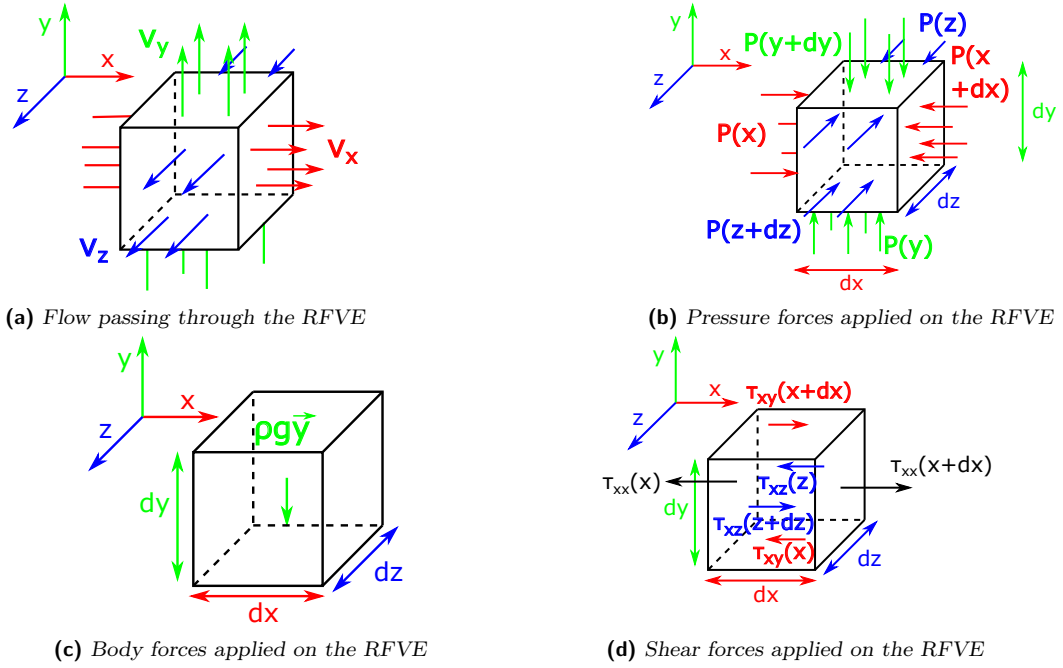


Figure A.16. External forces applied to the RVFE

$$\begin{aligned}
 F_i^{Pressure} &= -\frac{\partial P_i}{\partial x_i} \\
 F_i^{Body} &= \rho f_i \\
 F_i^{shear} &= \frac{\partial}{\partial x_j} \left(\eta \left(\frac{\partial v_i}{\partial x_j} + \frac{\partial v_j}{\partial x_i} \right) \right)
 \end{aligned}
 \tag{A.63}$$

Now that all forces have been mathematically fully defined, the inertial term of Equation A.62 $\rho \frac{dv_i}{dt}$ has to be finally developed. This term describes mathematically the motion of the flow in the control volume (see Figure A.16a). The Eulerian description's material derivative from Equation A.25 of § A.2.6 is used for this term (see Paragraph "Lagrangian and Eulerian description" from Section A.2). The final form of the inertial term is given in Equation A.64.

$$\rho \frac{dv_i}{dt} = \rho \frac{\partial v_i}{\partial t} + \rho v_j \left(\frac{\partial v_i}{\partial x_j} \right)
 \tag{A.64}$$

Now if all the forces terms calculated so far are brought back into Equation A.62, it gives the general form of flow motion Equations also known as Navier's Equation. Navier's

Equation is depicted in Equation A.65.

$$\rho \frac{\partial v_i}{\partial t} + \rho v_j \left(\frac{\partial v_i}{\partial x_j} \right) = -\frac{\partial P}{\partial x_i} + \rho f_i + \frac{\partial}{\partial x_j} \left(\eta \left(\frac{\partial v_i}{\partial x_j} + \frac{\partial v_j}{\partial x_i} \right) \right) \quad (\text{A.65})$$

At the time of the mathematician and engineer who found this equation, Henri Navier, it was hard to use this equation for studying fluids. Indeed, the general viscosity term η was not well known for fluids, even the most common ones as water or air which made the equation not usable.

To expand the term η , the investigated fluid's type must be identified (cf § A.2.1). The fluids studied in this thesis are Newtonian fluids. Hence, the general expression of the viscous stresses for Newtonian fluids is reminded in Equation A.66.

$$\begin{cases} \mu' + \frac{2}{3}\mu = 0 \\ \tau_{ij} = \mu \dot{\gamma}_{ij} + \mu' \frac{\partial v_k}{\partial x_k} \delta_{ij} \\ \dot{\gamma}_{ij} = \frac{\partial v_i}{\partial x_j} + \frac{\partial v_j}{\partial x_i} \end{cases} \quad (\text{A.66})$$

By changing the viscous term with the general form of Newtonian fluid's shear stress and by injecting Stokes hypothesis, the regular Navier-Stokes final form equation for Newtonian compressible fluids is obtained in Equation A.67.

$$\rho \frac{\partial v_i}{\partial t} + \rho v_j \left(\frac{\partial v_i}{\partial x_j} \right) = -\frac{\partial P}{\partial x_i} + \rho f_i + \mu \frac{\partial^2 v_i}{\partial x_j^2} + \frac{1}{3}\mu \frac{\partial}{\partial x_j} \left(\frac{\partial v_i}{\partial x_j} \right) \quad (\text{A.67})$$

This last Equation is the one governing the motion of all compressible Newtonian fluids. Now, if the considered fluid is incompressible, the continuity equation ensures a divergence free velocity field (*i.e.* $\frac{\partial v_i}{\partial x_i} = 0$). This transforms Equation A.67 into Equation A.68 that governs the motion of incompressible Newtonian fluids.

$$\rho \frac{\partial v_i}{\partial t} + \rho v_j \left(\frac{\partial v_i}{\partial x_j} \right) = -\frac{\partial P}{\partial x_i} + \rho f_i + \mu \frac{\partial^2 v_i}{\partial x_j^2} \quad (\text{A.68})$$

Depending on the type of problem considered, the equation can be further simplified. For a turbulent water flow around a hydrofoil, the gravitational body forces are negligible, thus the Navier-Stokes equation can be simplified in Equation A.69.

$$\rho \frac{\partial v_i}{\partial t} + \rho v_j \left(\frac{\partial v_i}{\partial x_j} \right) = - \frac{\partial P}{\partial x_i} + \mu \frac{\partial^2 v_i}{\partial x_j^2} \quad (\text{A.69})$$

A.3.3 The energy equation

With the continuity equation and the Navier-Stokes equations, there are now four scalar equations that can determine four of the six unknown variables. The continuity equation can be used for determining the velocity components or the fluid's pressure, and with the Navier-Stokes equations the velocity compounds can be found. However, there is currently no equation for thermal dependent flows. Hence, for developing a new equation, the first law of thermodynamics will be used. Indeed, this law describes the evolution of a system where its energy exchange, and thus temperature variations occur.

The first law of thermodynamics states that for an isolated system, its energy state remains constant. The energy inside the system cannot be created, nor destroyed, it can only be transformed. Equation A.70 shows the mathematical expression of this first law. dE represents the change of internal energy in the system, δQ denotes the quantity of energy given to the system as heat and δW is the energy given or ejected by the system as thermodynamic work.

$$dE = \delta Q - \delta W \quad (\text{A.70})$$

Thus, if a fluid flow system is considered, the different types of internal energies (dE) composing the system are the following : (1) the kinetic energy of the system k_e , (2) its potential energy p_e and (3) all other energies u_e . Thus Equation A.70 can be rewritten in the following form (see Equation A.71) for a fluid flow system:

$$de = dk_e + dp_e + du_e = \delta q - \delta w \quad (\text{A.71})$$

Here all the precedent physical quantities dE , Q and W are written in lower cases in Equation A.70, because those quantities are expressed as energy per unit mass of fluid. Now for estimating the variation of energy in an RFVE per unit time, Equation A.70 is written in its rate form in Equation A.72.

$$\rho \frac{dk_e}{dt} + \rho \frac{dp_e}{dt} + \rho \frac{du_e}{dt} = \rho \dot{q} - \rho \dot{w} \quad (\text{A.72})$$

As it was done for the previous equations, each term has to be expanded for finding the final form of the first principle of thermodynamics applied to fluids dynamics. Equation A.73 shows the final form of the different terms involved in the equation. The first term represents the work done by the RVFE, without taking into account the body force, the main work change produced by the RVFE comes from pressure and viscous forces. In this term, μ is the fluid's viscosity, P is the pressure, v_i is the velocity field and γ_{ij} is the shear rate.

The second term represents the heat change, this heat change is mostly done between the fluid and the solid through surfaces contact, thus the Fourier's law of conduction is used for the RVFE. In this expression, k is the thermal conductivity coefficient and T is the fluid's temperature. The third term corresponds to the potential energy changes, *i.e.* gravity. The potential is obtained by multiplying the body force vector f_i by the velocity field v_i .

The fourth term corresponds to the internal energy of the system and it is obtained by adding the specific enthalpy of the RVFE h and the ratio between the pressure P and the density ρ . The last term corresponds to the kinetic energy and its expression corresponds to the half of the square of the velocity.

$$\left\{ \begin{array}{l} -\rho\dot{w} = 2\mu \left[\left(\frac{\partial v_i}{\partial x_i} \right)^2 \right] - P \left(\frac{\partial v_i}{\partial x_i} \right) - \frac{2}{3}\mu \left[\frac{\partial v_i}{\partial x_i} \right]^2 + \mu \left[\left(\frac{\partial v_i}{\partial x_j} + \frac{\partial v_j}{\partial x_i} \right)^2 \right] \\ \quad + v_i \frac{\partial \left(-P - \frac{2}{3}\mu \frac{\partial v_i}{\partial x_i} \right)}{\partial x_i} + v_j \left(\frac{\partial \mu \gamma_{ij}}{\partial x_i} \right) + v_i \left(\frac{\partial \mu \gamma_{ij}}{\partial x_j} \right) \\ \rho\dot{q} = \frac{\partial}{\partial x_i} \left(k \frac{\partial T}{\partial x_i} \right) \\ \rho \frac{dp_e}{dt} = -\rho v_i f_i \\ u_e = h + \frac{P}{\rho} \\ k_e = \frac{v_i^2}{2} \end{array} \right. \quad (\text{A.73})$$

By introducing the terms of Equation A.73 into Equation A.72, the final Energy equation is obtained in Equation A.74. For looking at the derivation for this Equation we

refer to reference [29].

$$\begin{aligned} \rho \frac{dh}{dt} - \frac{dp}{dt} &= \frac{\partial}{\partial x_j} \left(k \frac{\partial T}{\partial x_j} \right) + \phi \\ \phi &= -\frac{2}{3}\mu \left(\frac{\partial v_i}{\partial x_i} \right)^2 + 2\mu \left(\frac{\partial v_i}{\partial x_i} \right)^2 + \mu \left(\frac{\partial v_i}{\partial x_j} \right)^2 + \mu \left[\left(\frac{\partial v_i}{\partial x_j} + \frac{\partial v_j}{\partial x_i} \right)^2 \right] \end{aligned} \quad (\text{A.74})$$

In fluid dynamics, the energy equation is used for keeping a track of the evolution of the temperature in the flow.

The problems treated in this paper are considered to be isothermic. Thus, the energy equation won't be used for the numerical models needed for solving these problems.

With this thermal equation, there is now 5 equations in our equations library: the continuity equation, the Navier-Stokes equations and the energy equation. These libraries of equations are used for finding five variables, the three velocity vector components, the pressure and the temperature. But what about the density ? It is also a variable. For density variations, other sets of constitutive equations are used but these belong more to the field of thermodynamics rather than fluid dynamics. These equations usually describe the evolution of the fluid's density with respect to pressure or temperature [301]. This equation cancels our reference library, the equation library has as much equations as unknowns : six equations for six unknowns.

A.3.4 Poisson's pressure equation

As said in the upper paragraphs, the problems encountered in this manuscript will be isothermal and incompressible fluid flow problems. Thus, only two sets of equations will be relevant here: the continuity equation and the Navier-Stokes equations. The continuity equation imposes a divergence free velocity (*i.e.* $\frac{\partial v_i}{\partial x_i} = 0$) to the incompressible flow. Then, only the Navier-stokes equations remain for determining the velocity components and the pressure components.

Nevertheless, it is difficult to couple velocity and pressure from these equations only. Indeed, the Navier-Stokes equations do not provide any boundary conditions for the pressure. For overcoming this difficulty, an another equation with pressure boundary conditions is sought. To find this new equation, the divergence of incompressible Navier-Stokes

(see Equation A.68) are taken. Equation A.75 depicts the result of the divergence of Equation A.68.

$$\rho \frac{\partial}{\partial t} \frac{\partial v_i}{\partial x_i} + \rho \frac{\partial}{\partial x_i} \left(v_j \left(\frac{\partial v_i}{\partial x_j} \right) \right) = -\frac{\partial^2 P}{\partial x_i^2} + \rho \frac{\partial f_i}{\partial x_i} + \mu \frac{\partial}{\partial x_i} \frac{\partial^2 v_i}{\partial x_j^2} \quad (\text{A.75})$$

Now considering the continuity equation (*i.e.* divergence free velocity $\frac{\partial v_i}{\partial x_i} = 0$), Equation A.68 is simplified to come to the Poisson's pressure equation (see Equation A.76).

$$\frac{\partial^2 P}{\partial x_i^2} = -\rho \frac{\partial v_j}{\partial x_i} \frac{\partial v_i}{\partial x_j} \quad (\text{A.76})$$

Usually for incompressible flows, the Poisson's pressure equation, replaces the continuity equation for solving fluid flow problems. This equation gives boundary conditions to the pressure term, furthermore it respects the divergence free conditions.

A.4 Fluid dynamics closure equations

In section A.3, all the equations governing the motion of fluids flow were introduced. However, one of the equations, the Navier-Stokes equations, is not analytically solvable until today's day for turbulent inviscid flows. Indeed, the advective term $\rho v_j \left(\frac{\partial v_i}{\partial x_j} \right)$ from Equation A.69 is the one causing the turbulences. This term is highly non-linear and gives many difficulties to theoretical and numerical mathematicians for solving this equation. Indeed, the velocity and pressure profiles observed in a turbulent flow have a chaotic behavior and are toughly usable in an analytical or a numerical method to solve these equations. Thus, additional equations and hypothesis had to be used for finding solutions for these equations: these conditions and equations are called the closure equations.

A.4.1 Turbulence modeling approaches

Current approaches for turbulence modeling are included in one of these three groups: Direct Numerical Simulations (DNS), Large-Eddy Simulations (LES) and Reynolds-averaged Navier-Stokes (RANS) [29], [302], [303].

The Direct Numerical Simulation (DNS) methods consists in solving numerically the turbulent Navier-Stokes equations (Equation A.69) without any turbulence models or time averaging of the Navier-Stokes equations. To be able to do this, all different scales of a turbulent flow must be directly solved: the viscous sublayer, the log-law region, the outer

region... (see section A.2.7) and the interscale turbulence diffusion must be well simulated.

In order to numerically solve all these scales, the meshing of the control volume of the fluid flow problem must be highly refined. Bertin *et al* [29] estimate that the grid size N is proportional to $Re_x^{9/4}$, with x being the streamwise length of the object. In 2021, Yang and Griffin [304] estimated that the number of grids needed for spatial and time discretisation to solve directly Equation A.69 is proportional respectively to $Re_x^{2.05}$ and to $Re_x^{2.91}$.

In the types of problems studied in our work, water flows over hydrofoils, the Reynolds number can go up to 3 millions or 6 millions. For these kind of problems, the number of points needed for using a Direct Numerical Simulation (DNS) would be located between $2 \cdot 10^{13}$ and $7 \cdot 10^{18}$ if Yang and Griffin [304] calculations are used.

These values of grids imply that the time needed for solving such problems is extremely long. In fact, those methods can be used only for low Reynolds numbers. A fact already confirmed by Moin and Mahesh [305] in 1998 that saw these kinds of simulations more as a tool for continuing to explore Turbulence reasearch on various problems (*e.g.* aeroacoustics) rather than using it for engineering problems. Spalart *et al.* [302] estimated that DNS computations for full aircrafts at flight number would not be possible before 2080, if the computer speed simulation growth kept on. All these informations tend to show that using this approach for morphing hydrofoil flow problems would not be suitable.

The second type of approaches, the Large Eddy Simulation (LES) turbulence simulation technique do not try to deal directly with Navier-Stokes equations anymore. In fact, in these approaches, the smaller turbulence scales are neglected (the most time consuming ones to solve numerically). To do that, a low-pass filtering function is used for suppressing the effect of smaller scales eddies (an another name of turbulences). This low-pass filtering acts on a spatial and temporal dimensions of the problem. Equation A.77 shows the filtering operation. With G being the filtering function, $*$ being the convolution operator and (X, t) being respectively the variables representing space and time.

$$\overline{v_i(X, t)} = G * v_i = \int_{-\infty}^{\infty} \int_{-\infty}^{\infty} v_i(r, \tau) G(X - r, t - \tau) d\tau dr \quad (\text{A.77})$$

Depending on the type of flow encountered, different filtering functions exist. Nonetheless, all of them define a minimal spatial scale Δ and a minimal temporal scale τ_c as

variables. The filtering function eliminates all eddies which spatial scale is inferior to Δ or which temporal scale is inferior to τ_c . The "Box filter" is given as an example in Equation A.78.

$$G(x - r) = \begin{cases} \frac{1}{\Delta}, & \text{if } |x - r| \leq \frac{\Delta}{2} \\ 0, & \text{otherwise} \end{cases} \quad (\text{A.78})$$

Equation A.77 enables the smoothing of velocity and pressure behavior (see Figure A.17), nonetheless they remain unsteady and large eddies can be accurately simulated with this method. Compared to DNS, the LES computational time has been reduced that allows to simulate higher Reynolds numbers with this method. Moreover, this method precisely captures eddies compared to the RANS method that will be presented later [306].

However, despite those improvements, the computational time needed for computing this approach for engineering problems remain to big. Indeed, Spalart *et al.* [302] have calculated that for an airfoil with a fully turbulent boundary layer and a Reynolds number of 6.5×10^6 , a number of 5 million time steps would be needed, which will result in 10^{20} simulation operations. The reason for having such a big number lies in the difficulty to formulate inlet boundary conditions [307]. As Tabor *et al.* [307] said the final results of a LES simulation change consequently with the precision of these inlet boundary conditions. The inlet flow must include a random number generation at each step of time that must "look" like turbulence and be easy to specify. This is this parameter especially that needs high computational power and is time consuming.

Targeting a simulation of a turbulent waterflow over an hydrofoil and in a further step trying to couple this fluid simulation with a deformable solid numerical model, this type of approach would not be adapted for our case.

The final types of existing approaches is the Reynolds Averaged Navier-Stokes (RANS) approach. The aim of this approach here is to come back to a configuration that is known and easier to solve. In laminar stationary viscous flows, at one particular point, the velocity remains constant with respect to time and in these kind of cases analytic governing equations and numerical results can be found (see section A.2.7). To come back to this kind of problems, the turbulent velocity is time-averaged over a fixed period T (see Figure

A.17). The time-averaging approach will be detailed in the following sections.

This approach simplifies the problems: All the quantity that were time dependent become constant. Nonetheless, despite time-averaging all quantities and the Navier-Stokes equations some quantity remain analytically and numerically non-solvable (see section A.4.3). Thus additional equations have to be added to successfully determine those quantities. The different RANS modeling techniques are identified by the number of side equations used for calculating the unknown terms: Zero-equation models, equation models or two equation models.

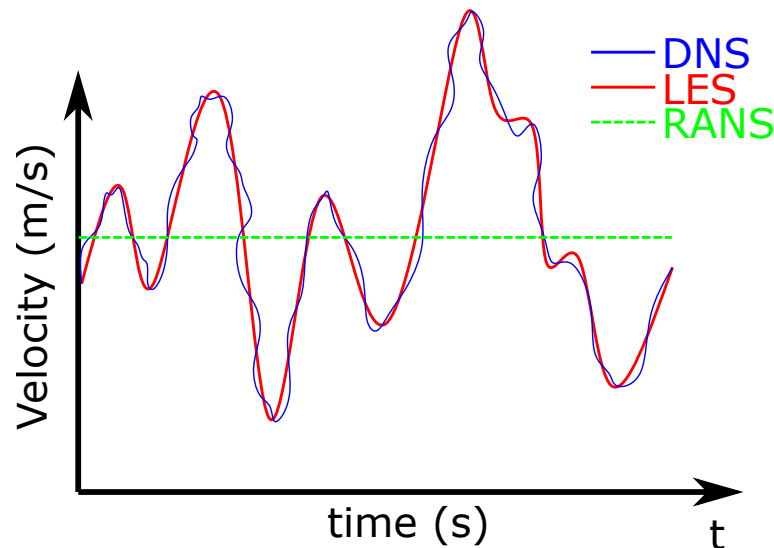


Figure A.17. Summary of the different turbulence modelisation approaches

Having said that, on the contrary of DNS and LES, RANS approaches are computationally efficient and are adapted to uses for industrial applications. Moreover, RANS approaches can model most of the scales on the contrary of LES. Nonetheless, time-averaging has a major flaw compared to DNS and LES approaches: the precision of RANS results is way less performant than the other approaches (see Figure A.18). Indeed, in RANS simulation and only time-averaged isovalues are displayed, the flow is not time dependent anymore. This leads to neglecting phenomena as turbulence diffusion that are highly time dependent.

Despite those flaws, the RANS approaches have been chosen in order to model our

turbulent flow over a passive morphing hydrofoil. For our work purpose, that are calculating the hydrodynamic coefficients C_L and C_D and determining the pressure forces around the hydrofoil, having mean pressure and velocity values are enough for being able to do a proper fluid-structure interaction. Using LES or DNS would enable us to model the diffusion of the flow around the morphing hydrofoil precisely and get velocity and pressure fields with high precision. However, the computational time devoted to that would also dramatically increase. As it will be shown later, the computational time is already highly problematic for the fluid-structure interaction part. Thus, making it increase would be non-desirable for our applications.

Hence, the RANS approach is chosen here to model turbulent flows. This approach will be detailed in the following sections.

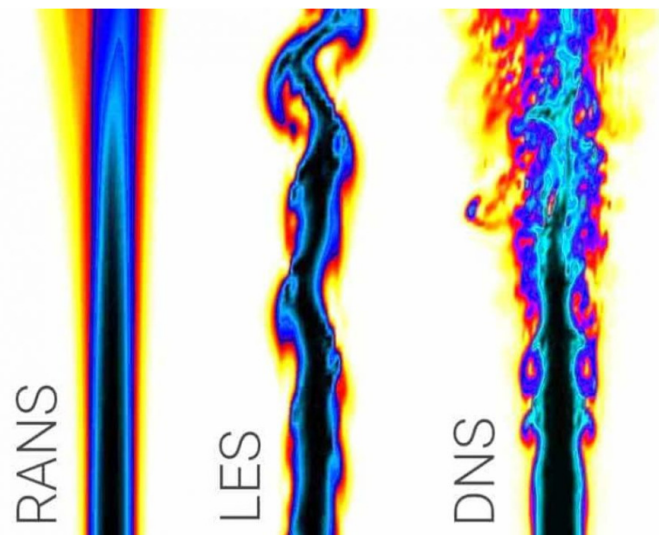


Figure A.18. *Simulation of a turbulent jet by RANS, LES and DNS techniques [308]*

A.4.2 Reynolds time-averaging concept

As said in the paragraph above, the advective term of Navier-Stokes equations (see Equation A.69) is a very difficult mathematical term to estimate. For low Reynolds flows, this term is estimable with numerical methods [300]. However, when the Reynolds number turns out to be big and the flow becomes turbulent, the velocity profile measured in empirically starts to have a rather chaotic behavior (see Figure A.19). Pressure and velocity being coupled, the pressure profile also displays such a behavior. This type of

velocity profile is currently non-solvable numerically or theoretically with Equation A.69 only.

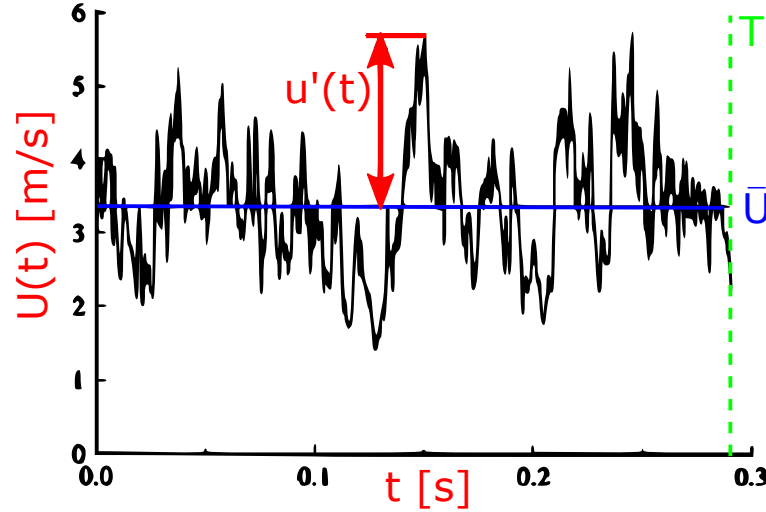


Figure A.19. Example of a velocity profile in a turbulent flow [29]

As engineers, being able to predict these kind of profiles precisely is not interesting for our application (simulating the water flow around a turbulent hydrofoil): only the mean velocity matters. Hence, Osborne Reynolds has developed an idea in 1895, time averaging the velocity profile of turbulent flows. Equation A.79 shows the time averaging formula.

$$\bar{V}_i = \frac{1}{T} \int_0^T v_i(t) dt \quad (\text{A.79})$$

In this equation, \bar{V}_i represents the mean velocity vector, T is the averaging period and $v_i(t)$ is the fluctuating velocity profile. On Figure A.19, $U(t)$ represents the turbulent fluctuating velocity and \bar{U} is the mean velocity profile. Having said that, the fluctuating velocity equation can be formulated by Equation A.80.

$$v_i(t) = \bar{V}_i + v'_i(t) \quad (\text{A.80})$$

In Equation A.80, the $v'_i(t)$ term represents the fluctuations in velocity due to turbulence in the flow. By time averaging these fluctuations, it can be found that its final value is 0 (see Equation A.81). For this equation to be true, the period T must be taken so that T is much greater than the fluctuation period (*e.g.* in Figure A.19, the period T is equal to 0.3 s which includes hundreds of fluctuations).

$$\overline{v'_i(t)} = \frac{1}{T} \int_0^T v_i(t) - \bar{V}_i dt = \bar{V}_i - \bar{V}_i = 0 \quad (\text{A.81})$$

Nonetheless, one must be careful, the time averaging of the product of fluctuating terms is not equal to zero (see Equation A.82). The principle of time-averaging quantities is to eliminate those unknown fluctuations, thus having expressions in fluid dynamics constitutive equations similar to the ones time-averaged in Equation A.82 would be though. Indeed, there would be no analytical or numerical ways to estimate this term in a direct approach.

$$\overline{v'_i(t)^2} = \frac{1}{T} \int_0^T v'_i(t)^2 dt \neq 0 \quad (\text{A.82})$$

As implied earlier, the Reynolds time-averaging is also true for pressure values (see Equation A.83).

$$\begin{cases} \bar{P} = \frac{1}{T} \int_0^T p(t) dt \\ p(t) = \bar{P} + p'(t) \\ \overline{p'(t)} = \frac{1}{T} \int_0^T v(t) - \bar{P} dt = \bar{P} - \bar{P} = 0 \end{cases} \quad (\text{A.83})$$

A.4.3 Reynolds averaged Navier-Stokes (RANS) approach: time averaging governing equations

Now that the Reynold's averaging method has been presented, it can be applied to the continuity equation (see Equation A.59), the Navier-Stokes equations (see Equation A.69) and the Pressure Poisson's Equation (see Equation A.76). Equation A.84 shows the Reynolds averaging of continuity equation.

$$\begin{aligned} \frac{\partial \bar{V}_i}{\partial t} &= 0 \\ \frac{\partial \overline{v'_i(t)}}{\partial t} &= 0 \end{aligned} \quad (\text{A.84})$$

Now that the continuity equation has been time averaged, it is the turn of the Navier-Stokes equations to be transformed (Equation A.69). Equation A.85 shows the final result after many adjustments that are detailed in [29].

$$\boxed{\rho \bar{V}_j \frac{\partial \bar{V}_i}{\partial x_j} = -\frac{\partial \bar{P}}{\partial x_i} + \mu \frac{\partial}{\partial x_j} \left(\frac{\partial \bar{V}_i}{\partial x_j} + \frac{\partial \bar{V}_j}{\partial x_i} \right) - \rho \frac{\overline{\partial v'_i v'_j(t)}}{\partial x_j}} \quad (\text{A.85})$$

The final form obtained in Equation A.85 is called Reynolds Averaged Navier-Stokes (RANS). The last remaining equation to time average is the Pressure Poisson's Equation. The expression of the time averaged Poisson's Pressure Equation is given in Equation A.86. The method for deriving the final form is very similar to the method depicted in [29] for deriving the RANS equations.

$$\frac{\partial^2 \bar{P}}{\partial x_i^2} = -\rho \frac{\partial \bar{V}_j}{\partial x_i} \frac{\partial \bar{V}_i}{\partial x_j} - \rho \frac{\partial^2 \overline{v'_i v'_j(t)}}{\partial x_j \partial x_i} \quad (\text{A.86})$$

In these new forms, all the terms of Equation A.85 and Equation A.86 can be calculated numerically in a direct way, except the terms $-\rho \frac{\partial \overline{v'_i v'_j(t)}}{\partial x_j}$ and $-\rho \frac{\partial^2 \overline{v'_i v'_j(t)}}{\partial x_j \partial x_i}$ for RANS and averaged Poisson's Pressure Equation respectively. These terms are very problematic, because they are composed of the product of velocity fluctuations. There are no hypothesis in the time-averaging theory describing the evolution of fluctuations. There are currently no ways known for directly estimating those terms numerically.

However, if a dimensional analysis is done on the term $\overline{\rho v'_i v'_j(t)}$, it can be found that it is expressed in $kg.m^{-1}.s^{-1}$. These units are actually homogenous to... a stress ! So this unknown term actually is identified as the turbulent shear stress and is known as the Reynold's stress in the literature. Knowing that, Equation A.87 and A.88 are written in a different way.

$$\rho \bar{V}_j \frac{\partial \bar{V}_i}{\partial x_j} = -\frac{\partial \bar{P}}{\partial x_i} + \frac{\partial}{\partial x_j} \left(\mu \left(\frac{\partial \bar{V}_i}{\partial x_j} + \frac{\partial \bar{V}_j}{\partial x_i} \right) - \overline{\rho v'_i v'_j(t)} \right) \quad (\text{A.87})$$

Because the analytical form of the Reynolds shear stress is not known, many methods were developed for estimating this term in fluid flows. This problem is known as the "closure problem" for turbulent flows, hence those solutions are also known as "solution for closure".

$$\frac{\partial^2 \bar{P}}{\partial x_i^2} = -\rho \frac{\partial \bar{V}_j}{\partial x_i} \frac{\partial \bar{V}_i}{\partial x_j} + \frac{\partial^2}{\partial x_j \partial x_i} \left(-\overline{\rho v'_i v'_j(t)} \right) \quad (\text{A.88})$$

A.4.4 Turbulence closure equations

The aim of turbulence closures models or procedures are to be able to estimate effectively the Reynolds stress tensor $-\overline{\rho v'_i v'_j(t)}$. For doing that, many models assume that the Reynolds stress tensor is proportional to the mean stress tensor (see Equation A.89). This assumption is known as the Boussinesq eddy-viscosity approximation, introduced in the late nineteenth century. In Equation A.89, The parameter μ_t is known as the turbulent eddy viscosity. This term becomes the new unknown to determine. In this Equation, the term $\frac{2}{3}\rho k\delta_{ij}$ represents the spherical part of the Reynolds stress tensor. The term k represents the turbulence kinetic energy, the value of this turbulent kinetic energy is $k = \frac{1}{2}\overline{v'_i v'_i}$ (see Equation A.95).

$$\begin{aligned} -\overline{\rho v'_i v'_j(t)} &\equiv \tau_{ij}^{Reynolds} \\ -\overline{\rho v'_i v'_j(t)} &= \mu_t \left(\frac{\partial \bar{V}_i}{\partial x_j} + \frac{\partial \bar{V}_j}{\partial x_i} \right) - \frac{2}{3}\rho k\delta_{ij} \quad (\text{Boussinesq approximation}) \end{aligned} \quad (\text{A.89})$$

Applying the Boussinesq eddy-viscosity approximation on Equations A.87 and A.88 leads to having a new form for these equations (see Equation A.90 and A.91). In these new equations, the pressure \bar{P}_k is the sum of the fluid pressure \bar{P} and the isotropic Reynolds stress $\bar{P}_k = \bar{P} + \frac{2}{3}\rho k$.

$$\bar{V}_j \frac{\partial \bar{V}_i}{\partial x_j} = -\frac{1}{\rho} \frac{\partial \bar{P}_k}{\partial x_i} + \frac{\partial}{\partial x_j} \left(\nu_{eff} \left(\frac{\partial \bar{V}_i}{\partial x_j} + \frac{\partial \bar{V}_j}{\partial x_i} \right) \right) \quad (\text{A.90})$$

$$\frac{1}{\rho} \frac{\partial^2 \bar{P}_k}{\partial x_i^2} = -\frac{\partial \bar{V}_j}{\partial x_i} \frac{\partial \bar{V}_i}{\partial x_j} + \frac{\partial^2}{\partial x_j \partial x_i} \left(\nu_t \left(\frac{\partial \bar{V}_i}{\partial x_j} + \frac{\partial \bar{V}_j}{\partial x_i} \right) \right) \quad (\text{A.91})$$

In Equation A.90, the ν_{eff} is the effective kinematic viscosity of the flow. It is composed of the regular kinematic viscosity and of the turbulent eddy kinematic viscosity (see Equation A.92). Something interesting can be highlighted in this formula: the effective and the eddy viscosity are position and time dependent, whereas the kinematic viscosity is not. This difference can be explained by the fact that the regular kinematic viscosity is an intrinsic fluid property, whereas the turbulent viscosity is a flow property. If a fluid flow is considered where all the conditions are similar to the original flow (Reynolds number, Mach number...), but the fluid changes, the turbulent viscosity would remain the same. Thus, if the flow depends directly on time and position in the boundary layer, so does

the turbulent viscosity. And because the effective viscosity is composed of the turbulent viscosity, it automatically becomes dependent on space and time.

$$\nu_{eff}(X, t) = \nu + \nu_t(X, t) \quad (\text{A.92})$$

The closure procedures objective is to find a way to determine the turbulent eddy viscosity ν_t , for doing that each method is identified as the number of additional partial differential equations that are used: zero-equation, one-equation or two equation models being the most popular ones.

Algebraic models

The zero equation models are known as algebraic turbulence models. For high scale simulations, like full aircraft configurations, these algebraic turbulence models are the most popular solution due to their simplicity [309]. They are mostly used for simple problems where the local production of turbulence is balanced with the local dissipation of turbulence. One of the most popular solution used for solving boundary layer problems is the mixing length concept.

This concept was proposed by Prandtl, and found an empirical relation for estimating the kinematic eddy viscosity in a boundary layer. This empirical relation is depicted in Equation A.93. l_{mix} is the mixing length, physically it represents the maximal size eddies can get at a particular region of the flow. \bar{U} is the x-component mean velocity in the boundary layer.

$$\nu_t(X, t) = l_{mix}^2 \left| \frac{\partial \bar{U}}{\partial y} \right| \quad (\text{A.93})$$

The mixing length parameter l_{mix} in the equation cannot be analytically or numerically found, it can only be found through experiments and its value is strongly dependent on the state of the flow. That makes the mixing length model a semi-empirical model.

As seen in section A.2.7, the boundary layer is made up of composite regions and layers where different physical mechanisms and quantities control the turbulence. This mixing length formulation does not take into account those composite layers, as l_{mix} is constant. It doesn't also take into account the numerous interactions between those layers. Multiple models have been developed for describing the turbulence behavior in these

different layers. The Van-Driest model, for example takes into account the effect of viscosity on the mixing length at the viscous sub-layer [309]. Many others empirical models exist for describing the turbulent eddy viscosity in the outer region (*e.g.* Baldwin-Lomax model [309]) or in the inner regions of the boundary layer but for different Mach numbers (Subsonic flows, transonic flows, hypersonic flows...).

This multiplicity of empirical models and their lack of generality for estimating the mixing length leads to various problems. The first one is the precision of the values obtained for the turbulent boundary layer. Indeed, the models are calibrated with a set of assumptions that apply only to particular types of flows (*e.g.* one model, the Baldwin-Lomax model, is calibrated for transonic flows only. For hypersonic flows, the results obtained with this model lacks of precision). Though, for many engineering applications, these algebraic models provide reasonable turbulent viscosity and shear stress results [29].

Nonetheless, the second big problem encountered with having a lot of models for limited range of applications is the difficulty to apply these solutions to the problems. Despite the fact that these models are computationally simple to implement, in a single flow problem different types of turbulent flows can be encountered (*e.g.* the inner region of a boundary layer is not modeled the same way as the outer region). Hence, multiple algebraic models for mixing length calculations must be applied for each region of the flow [309].

The last big problem encountered by those models is the conceptual description of turbulence. Here with the algebraic models, the turbulences are described as static quantities. However, the eddies diffuses through the whole flow and have a convective motion in the flow that influences all the different composite layers of the turbulent boundary layer. The expression of diffusion and convection is absent in algebraic descriptions.

For our turbulent hydrofoil flow problem, this kind of approach would have been interesting despite the complications linked to the empirical estimation of the mixing length. Nevertheless, because of our lack of expertise and experience in all the different algebraic models used for determining the different mixing lengths in the boundary layer and the time that would have been needed for having deep knowledge in all the different models, the algebraic solutions have not been selected.

One equation models

In order to formulate the diffusion of turbulence inside the flow and having a more global expression for the eddy kinematic viscosity ν_t , a new approach has been sought by engineers and researchers. In 1942, an other equation for expressing the eddy kinematic viscosity has been found through dimensional analysis (see Equation A.94). This new expression's name is the Prandtl-Kolmogorov formula [310].

$$\nu_t = C_\mu k^{\frac{1}{2}} l \quad (\text{A.94})$$

In Equation A.94, l defines the turbulence length scale. Contrary to the mixing length l_{mix} , the length scale represents the actual eddies size and not just the largest ones. The variable k is known as the turbulence kinetic energy and is defined by Equation A.95 and C_μ is a constant also called a "closure coefficient" [310].

$$k = \frac{1}{2} \overline{v'_i v'_i} \quad (\text{A.95})$$

With this new expression of the eddy viscosity, there is a new variable that needs to be found. This variable is the turbulence energy k . Thus, for finding it, there is a need to have a new partial derivative constitutive equation for the turbulence energy k . In order to find it, the different physical processes in charge for producing turbulence must be listed (look at [310] for more details):

- **The convection \mathbf{C}** inside the flow that helps the turbulence to travel in the entire boundary layer flow.
- **The production \mathbf{P}** is the rate at which the kinetic energy of the mean flow (noted by \bar{V}_i) is transferred to the turbulence (noted by v'_i)
- **The dissipation \mathbf{E}** is the rate at which turbulence kinetic energy is converted into thermal internal energy
- **The molecular diffusion ∇T** is the diffusion of the turbulence energy caused by the fluid's natural molecular transport process
- **The turbulent transport T** is the rate at which turbulence energy is transported through the fluid by turbulent fluctuations
- **The Pressure diffusion ∇P** represents the turbulence transport resulting from correlation of pressure and velocity fluctuations

All those physical processes are considered to compensate each other, having said that, Equation A.96 can be written down. This equation is called the "turbulence energy

equation" [310]. This equation is on the basis of all the further turbulence governing equations models, only the considered quantity and the derivatives expressions change.

$$C - P + E - \nabla T - T - \nabla P = 0 \quad (\text{A.96})$$

Each physical term is then formulated through dimensional analysis in the turbulent flow (see [309] for more information). Equation A.97 shows the final form of the partial differential equation governing the behavior of the turbulence kinetic energy.

$$\underbrace{\frac{\partial k}{\partial t} + \bar{V}_i \frac{\partial k}{\partial x_j}}_{\text{Convection}} = \underbrace{\frac{1}{\rho} \tau_{ij} \frac{\partial \bar{V}_i}{\partial x_j}}_{\text{Production}} - \underbrace{\epsilon}_{\text{Dissipation}} + \underbrace{\frac{\partial}{\partial x_j} \left((\nu + \nu_t / \sigma_k) \frac{\partial k}{\partial x_j} \right)}_{\text{Molecular diffusion + Turbulent transport + Pressure diffusion}} \quad (\text{A.97})$$

In Equation A.97, τ_{ij} is the Reynolds stress tensor (see Equation A.89), ϵ is the dissipation per unit mass which expression is detailed in Equation A.98 and σ_k is an another "closure constant". Having said that, in the current situation, Equation A.97 cannot be solved, the quantities ϵ and ν_t have yet to be expressed more explicitly.

$$\epsilon = \nu \overline{\frac{\partial v'_i}{\partial x_j} \frac{\partial v'_i}{\partial x_j}} \quad (\text{A.98})$$

In 1935, Taylor showed through a dimensional analysis that the dissipation rate is proportional to the turbulence length scale and the turbulence kinetic energy (see Equation A.99).

$$\epsilon = C_D \frac{k^{\frac{3}{2}}}{l} \quad (\text{A.99})$$

For the turbulent kinematic viscosity ν_t , by using Equation A.94 and assuming that the constant C_μ is equal to one, the final version of the turbulence kinetic energy equation can be found (see Equation A.100).

$$\frac{\partial k}{\partial t} + \bar{V}_i \frac{\partial k}{\partial x_j} = \frac{1}{\rho} \tau_{ij} \frac{\partial \bar{V}_i}{\partial x_j} - C_D \frac{k^{\frac{3}{2}}}{l} + \frac{\partial}{\partial x_j} \left((\nu + k^{\frac{1}{2}} l / \sigma_k) \frac{\partial k}{\partial x_j} \right) \quad (\text{A.100})$$

The set of Equations A.94 and A.100 are known as the One-Equation Models for determining the turbulent viscosity. The main transport equation for turbulence kinetic energy is numerically solvable if the length scale l and the closure coefficients σ_k and C_D are provided. These closure coefficients were estimated to be equal to $\sigma_k = 1$ and C_μ

being between 0.07 and 0.09 [311], [312]. The last closure variable l was estimated with distribution models for estimating the turbulence length scales [313], [314].

Decades later, new models have been developed that are not based on the Turbulence energy equation directly (Equation A.97), nonetheless they are still based on the primitive turbulence equilibrium equation (see Equation A.96). The most popular models, still used nowadays, are the Baldwin-Barth model [315] and the Spalart-Allmaras model [279]. These new equations avoid the need of having algebraic length scales models for solving the partial differential equation, they are self-sufficient.

The Baldwin-Barth model is derived from the two differential equations model $k-\epsilon$. On the contrary of the previously studied one equation models, the principle variable to find with this new differential equation is not the turbulence kinetic energy k anymore, but the turbulence Reynolds number $R_T = \frac{k^2}{\nu \epsilon}$. The definition of the eddy viscosity ν_t do not change from Equation A.94. The constants of this new model have then been set empirically in order for it to describe as close as possible the behavior of the different turbulent regions and the skin friction on a flat plate. Baldwin and Barth then tested their new model on a Transonic Viscous RAE 2822 airfoil in the following conditions : $M_\infty = 0.75$ and an angle of attack of $\alpha = 2.72^\circ$. Their model showed a very good agreement with the different experiments conducted [315].

The Spalart-Allmaras one equation model, is different from the other equations depicted earlier. Spalart *et al.* developed a one differential equation model where the variable to find is the turbulent eddy viscosity ν_t itself, no intermediate variables are needed [279]. Moreover, the model handles dissipation of turbulence with an other way compared to the previous model. The dissipative term is now called *Destruction*, it just takes into account the friction of the eddies with the wall. Equation A.99 is not considered true anymore. For more details, the full derivation of the set of Equations is detailed in the Appendix section A. Equation A.101 shows the new turbulence equilibrium for Spalart-Allmaras model.

$$C - P + D - \nabla T - T - \nabla P = 0 \tag{A.101}$$

The different terms of this differential equation have been found by Spalart *et al* through a dimensional analysis and through an iterative process. In different set of flows

starting from the most simple ones and going towards the most complicated ones, each term of the equation is identified and the coefficients are set to respect the Galilean invariance (*i.e.* must be independent from the referential frame chosen) and to match the empirical results measured in a flat plate turbulent boundary layer. The final form of the Spalart-Allmaras model's set of Equations is given below, see the Appendix section A.1 for more details on the derivation.

Spalart-Allmaras

Kinematic Eddy Viscosity

$$\nu_t = \tilde{\nu} f_{v1} \quad (\text{A.102})$$

Eddy Viscosity Equation

$$\frac{\partial \nu_t}{\partial t} + \bar{V}_i \frac{\partial \nu_t}{\partial x_i} = c_{b1} \tilde{S} \tilde{\nu} + \frac{1}{\sigma} \left[\frac{\partial}{\partial x_i} \left((\nu + \tilde{\nu}) \frac{\partial \tilde{\nu}}{\partial x_i} \right) + c_{b2} \left(\frac{\partial \tilde{\nu}}{\partial x_i} \right)^2 \right] - c_{w1} f_w \left(\frac{\tilde{\nu}}{d} \right)^2 \quad (\text{A.103})$$

Closure coefficients

$$\begin{aligned} c_{b1} &= 0.1355, & c_{b2} &= 0.622, & c_{v1} &= 7.1, & \sigma &= 2/3 \\ c_{w1} &= \frac{c_{b1}}{\kappa^2} + \frac{1+c_{b2}}{\sigma}, & c_{w2} &= 0.3, & c_{w3} &= 2, & \kappa &= 0.41 \end{aligned} \quad (\text{A.104})$$

Auxiliary Relations

$$\begin{aligned} f_{v1} &= \frac{\chi^3}{\chi^3 + c_{v1}^3}, & f_{v2} &= 1 - \frac{\chi}{1 + \chi f_{v1}}, & f_w(r) &= g \left[\frac{1+c_{w3}^6}{g^6+c_{w3}^6} \right]^{1/6}, \\ \chi &= \frac{\tilde{\nu}}{\nu}, & g &= r + c_{w2}(r^6 - r), & r &= \frac{\nu_t}{S \kappa^2 d^2} \\ \tilde{S} &= S + \frac{\tilde{\nu}}{\kappa^2 d^2} f_{v2}, & S &= \sqrt{2 \Omega_{ij} \Omega_{ij}}, & \Omega_{ij} &= \frac{1}{2} \left(\frac{\partial \bar{V}_i}{\partial x_j} - \frac{\partial \bar{V}_j}{\partial x_i} \right) \end{aligned} \quad (\text{A.105})$$

Compared to algebraic models, the gain obtained by the last versions of one-equation model is important. First of all, the implementation of one differential equation models is way more straight forward than it used to be with algebraic models. Indeed, the differential equation used for estimating the eddy viscosity gives more freedom to the user to apply it on a wide range of flows. Then, these equations showed very promising results, especially for the modeling of boundary-layer flows around turbulent airfoils. Finally, one-equation model are not limited to boundary layer flows anymore, it gives now pretty decent results

for a majority of free shear flows. Despite being less precise than algebraic models for simple flows like the Samuel-Joubert flow.

On the other hand, these models are far from being universal models. As seen before, they either still use some algebraic models for being solved or some coefficients and expressions are based on empirical laws or results, such as the Baldwin-Barth model and the Spalart-Allmaras model. For totally removing those algebraic model's presence, two equations models are investigated to try to define a second partial derivative equation for determining the dissipation's value without going for empirical models or dimensional analysis.

Two equations models

The two equations models of turbulence are the ones that are right now the most widely used in turbulence research and applications. These models provide computational solutions to the turbulence kinetic energy k and the length scale l linked to the dissipation ϵ . Thus, these models are complete, there is no need of prior knowledge in the turbulence structure of the considered problem. The only thing to provide for solving those two models equations are the initial turbulence kinetic energy k and the initial dissipation rate ϵ or ω (depending on the model used) of the free stream flow. As shown earlier, there is multiple ways of determining the length scale l or the dissipation ϵ in an equivalent manner: with algebraic models, empirical models or through dimensional analysis. In 1942, Kolmogorov [316] was the first to propose to add a supplementary differential equation for finding these physical quantities. To do that he introduced a new variable, the specific dissipation rate per unit volume ω that links the turbulence energy, the turbulence length scale, the dissipation rate and the turbulent viscosity together (see Equation A.106). These relations were built through a dimensional analysis.

$$\nu_t \sim k/\omega, \quad l \sim k^{1/2}/\omega, \quad \epsilon \sim \omega k \quad (\text{A.106})$$

In the mean time, Chou [317] proposed to add a partial differential equation for finding ϵ directly. He also proposed the following dimensional relations for linking ν_t , l and ϵ (see Equation A.107). As the $k - \omega$ base relations, these relations were built through dimensional analysis.

$$\nu_t \sim k^2/\epsilon, \quad l \sim k^{3/2}/\epsilon \quad (\text{A.107})$$

Kolmogorov works will inspire Wilcox [318] in his work for developing the $k - \omega$ turbulence model and the work of Chou has served as basis for developing the $k - \epsilon$ turbulence model by Launder *et al* [319]. These two models are the most widely used ones in turbulence related problems in industrial and academic fields.

$k - \omega$ and $k - \epsilon$ models are presented in Equation A.108 and A.109, the details leading to those equations are given in Appendix A.2 and A.3.

k-omega (k - ω)

$$\left\{ \begin{array}{l} \frac{\partial k}{\partial t} + \bar{V}_i \frac{\partial k}{\partial x_j} = \frac{1}{\rho} \tau_{ij} \frac{\partial \bar{V}_i}{\partial x_j} - \beta^* k \omega + \frac{\partial}{\partial x_j} \left((\nu + \sigma^* \nu_t) \frac{\partial k}{\partial x_j} \right) \\ \frac{\partial \omega}{\partial t} + \bar{V}_i \frac{\partial \omega}{\partial x_j} = \frac{1}{\rho} \alpha \frac{\omega}{k} \tau_{ij} \frac{\partial \bar{V}_i}{\partial x_j} - \beta \omega^2 + \frac{\partial}{\partial x_j} \left((\nu + \sigma \nu_t) \frac{\partial \omega}{\partial x_j} \right) \\ \alpha = 5/9, \quad \beta = 3/40, \quad \beta^* = 9/100, \quad \sigma = 1/2, \quad \sigma^* = 1/2 \end{array} \right. \quad (\text{A.108})$$

k-epsilon (k - ϵ)

$$\left\{ \begin{array}{l} \frac{\partial k}{\partial t} + \bar{V}_i \frac{\partial k}{\partial x_j} = \frac{1}{\rho} \tau_{ij} \frac{\partial \bar{V}_i}{\partial x_j} - \epsilon + \frac{\partial}{\partial x_j} \left((\nu + \nu_t / \sigma_k) \frac{\partial k}{\partial x_j} \right) \\ \frac{\partial \epsilon}{\partial t} + \bar{V}_i \frac{\partial \epsilon}{\partial x_j} = \frac{1}{\rho} C_{\epsilon 1} \frac{\epsilon}{k} \tau_{ij} \frac{\partial \bar{V}_i}{\partial x_j} - C_{\epsilon 2} \frac{\epsilon^2}{k} + \frac{\partial}{\partial x_j} \left((\nu + \nu_t / \sigma_\epsilon) \frac{\partial \epsilon}{\partial x_j} \right) \\ C_{\epsilon 1} = 1.44, \quad C_{\epsilon 2} = 1.92, \quad C_\mu = 0.09, \quad \sigma_k = 1.0, \quad \sigma_\epsilon = 1.3 \end{array} \right. \quad (\text{A.109})$$

These two models give good relations to free shear flows and wakes. Nonetheless, major drawbacks are to be pointed out, none of these models have a near wall treatment for viscous sublayers of boundary layers. There is no modelisation of the alteration of the turbulence length scales in viscous layers like what has been done for the Spalart-Allmaras model or the Van-Driest model. Thus, when using these equations on numerical models, the mesh should be refined enough to well discretise the viscous sublayer (mesh size must be at a size $y^+ < 1$), furthermore the final results observed in the boundary layer are highly sensitive to the values of k and ω of the free stream. Consequently, for being able to handle these effects, near wall treatments were set up which lead to alternative models for the $k - \omega$ model: Shear-Stress Transport (SST) $k - \omega$ model [320] or modified $k - \omega$ model [310].

For the $k - \epsilon$ model, a damping function f_μ was added to the equation defining turbulent viscosity (see Equation A.110). This damping function's aim is to model the fluid's viscous effect on turbulence. To model these viscous effects, supplementary terms are added to Equation A.109. The value of the function f_μ and the value of the additional terms vary with the type of models used for modeling viscous effects [321]–[323]. Other solutions, common for both models, consist in using algebraic equations when the mesh stops at the log-law layer. These are called wall functions and reduce model's sensitivity to mesh refinement.

$$\nu_t = C_\mu f_\mu k^2 / \epsilon \quad (\text{A.110})$$

The algebraic models used consist in the log-law region velocity equation detailed in section A.2.7 (see Equation A.38) for estimating the friction velocity u^* and the gradient inside the viscous sublayer. This technique allows to close the two differential equations while having a mesh that stops in the log-law region. In the literature, this kind of approach is called as a **High Reynolds Number (HRN) treatment**, whereas the solution where the mesh is highly refined and damping functions are used is called the **Low Reynolds Number (LRN) treatment**.

To conclude, the main advantage earned with two equations models compared to the previous turbulence modeling technique is the gain in generality with those techniques. As said earlier, these equations are complete and do not require any prior knowledge on the flow to obtain results. Thus, for many practical cases reliable predictions can be obtained with those models. Having two equations for modeling turbulence also leads to take into account a greater number of quantities and mechanisms influencing the turbulence production, diffusion or dissipation leading to more precise results. However, in some complex flows like flows around wind turbine airfoils, this leads to some physical inconsistencies which do not happen with the $k - \omega$ SST model [324]. Despite these major advantages, two-equations models also suffer from major drawbacks, the major issues encountered by these models is their convergence rate. Because of the lack of terms handling the viscous sublayer and their strong non-linearity, the convergence of those models are strongly dependent on the free stream's initial turbulence kinetic energy and dissipation rate values and mesh refinement. Moreover, despite their great improvements, two-equations models

still cannot model some turbulent flow cases like jet flows for instance.

Conclusion

My personal opinion as the author of this manuscript on the accuracy and efficiency of these different turbulence models is that as long as we lack a strong and general definition of turbulence, those models will remain imprecise and flawed to some extent. Indeed, the only definition we have of turbulence is a chaotic fluctuation noted v'_i that oscillate around the mean velocity field \bar{V}_i . No information is known about this oscillation: no time period, no knowledge on the movement of particles at the molecular level, a little knowledge on the scale of turbulence... Thus, without a clear definition of turbulence, the best thing that can be done is trying to approach empirical observations of turbulence in various flow environments with different turbulence models. As seen earlier, in each turbulence model construction, there is a portion of it that is calibrated with empirical data observed in some particular cases (*e.g.* closure coefficients for Spalart-Allmaras, $k - \omega$ or $k - \epsilon$ models are calibrated for log regions of free shear flows and flat-plate boundary layers). Moreover, those models rely very much on dimensional analysis that approximate turbulence well, but do not unveil any feature of the underlying physics behind turbulence phenomena. That is why, the best thing to do is to use turbulence models that are well fitted for some kind of application.

Hence, for our application the software Abaqus v.6-14 is used for developing numerical models and solving these equations. On this version of the software, two turbulence models were implemented: the Spalart-Allmaras model and the $k - \epsilon$ model. By looking at many studies that comparatively tested turbulence models for airfoil problems. These studies showed that for simulating the airfoil flow, the Spalart-Allmaras model and the SST $k - \omega$ model were the ones that gave the most precise results [324], [325]. Moreover, these papers have put forward the robustness of the Spalart-Allmaras model that converges to a result pretty fast. The inlet boundary condition required for the Spalart-Allmaras model is only an initial turbulent viscosity ν_t^0 which value is approximately equal to 3 or 5 times the molecular viscosity $\nu_t^0 = (3 - 5)\nu$ [326]. For comparison, the $k - \epsilon$ model is less robust, it is highly dependent on the inlet boundary conditions of the free stream k and ϵ . Thus for all these reasons, the Spalart-Allmaras model is chosen for our future works.

A.5 Methodology for numerical model development: validation test

Now that all the theoretical bases were set, it is time to start the development of a numerical model for simulating a water flow around a hydrofoil. Developing such a model is a complicated task that needs to be carried out in multiple steps. In a first step, there is a need of defining precisely the flow conditions to be simulated. In a second step, there is a need of defining how the hydrofoil fluid domain should be modeled. In a third step, discussions should be carried out on the different boundary conditions to use in the model. And finally, after simulating the flow, comparing the results obtained with our numerical model with a reference model.

A.5.1 Initial flow conditions

Before starting to develop the numerical model, it is very important to clearly identify the conditions to which the flow will be subjugated (velocity, hydrofoil size, Reynolds number of the flow...). The first thing to identify is the flow's velocity range that can be attained by a foiling vehicle (sailing boat, motorised boat, surf...) that is equipped with hydrofoils. In our work, we are especially interested in the velocity ranges that can be attained while the boat is foiling (when the boat's hull is widely above the water's surface while moving). To do that, it can be interesting to look at the scientific literature and the commercial products speed that are available.

In the scientific literature, Graf *et al* have tried to optimise some sailing parameters for being able to reach the maximum's velocity attainable for an Olympic sailing boat while foiling over water [28]. In their predictions, the maximum speed that the sailing boat could attain while foiling was comprised between 8 and 9.5 m/s for true wind speeds ranged between 5 and 9 m/s [28]. Nonetheless, the highest measured velocity for the sailing boat while foiling was 7 m/s for a true wind velocity of 7 m/s [28]. In the work of Hagemeister *et al* [27], they tried to predict the velocity of foiling sailing catamarans used for America's Cup. In these studies, Hagemeister *et al* predicted that the boat's foiling velocity was ranged from 12 m/s up to 25 m/s [27]. In the commercial area, electric motorised foiling surfs have been developed [280], the maximum velocity attainable is approximately 9 m/s. However, the surf can start foiling at a speed lower than this one, even though the speed is not specified in the video. Other small sailing boats, called Moths have speed ranged

between 5 m/s and 10 m/s [281]. Hence the range of speed that can be targeted in our work would be between 5 m/s and 20 m/s.

Now that the velocity range has been fixed, we must determine the size of the hydrofoil that will be underwater. In their work, Hagemeister *et al* stated that the hydrofoil's chord length varied depending on the region and the type of foil considered [27]. The hydrofoil's length is ranged for 0.30 meters for the smallest and 0.80 meters for the longest one [27].

So with these data, and by knowing the fact that water's kinematic viscosity value is $\nu = 1.10^{-6}$, the Reynolds number range of functionality can be calculated for an hydrofoil. The Reynolds number ranges from 1500000 to 16000000, which makes the water flow around the airfoil strongly turbulent. Moreover, knowing that the speed of sound in water is approximately 1480 m/s in water, this leads to have a Mach number with a value extremely close to zero. Hence, this water flow is incompressible. All these criteria are summed up in Table A.2.

Hydrofoil properties	Range values
Fluid name and properties	Water $\rho = 1000 \text{ kg/m}^3$ $\mu = 1.10^{-3} \text{ Pa.s}$
Mach number	Mach ≈ 0 Incompressible fluid
Hydrofoil dimensions	min = 0.3 m max = 0.8 m
Flow speed	min = 5 m/s max = 20 m/s
Reynolds number	min = 1 500 000 max = 16 000 000

Table A.2. Boat's hydrofoil flow properties

The very last requirement needed, that is not present in the Table, is the obligation to **avoid cavitation around hydrofoil**.

A.5.2 Material and methods

In the introduction, it has been shown that turbulence models reliance is limited if the results obtained with those are not compared to experimental data. Thus, for assessing of the efficiency of the Spalart-Allmaras model, it is necessary to compare it to

experimental data or reliable numerical data. Fortunately, the NASA tested and developed a numerical modeling of the NACA0012 tested with 4 different simulation codes and compared to experimental data [214]. The flow conditions simulated in NASA's work is given in Table A.3. Logically, because the fluid properties changed, the dimensions and velocities encountered in this problem are way higher than the ones encountered in Table A.2. However, the Reynolds number and the Mach number requirements are met if the values from Table A.3 are in the same range as Table A.2. Consequently, this implies that the flow conditions developed here can be reused in future models. Thus, as a first model, the numerical model will be developed with these data.

Airfoil flow properties	values
Fluid name and properties	Air $\rho = 1.2 \text{ kg/m}^3$ $\mu = 1.85^{-5} \text{ Pa.s}$
Mach number	Mach = 0.15 < 0.3 Incompressible fluid
Airfoil dimensions	1.82 m
Flow speed	51.6 m/s
Reynolds number	6 millions
Angle of attack	0°
Turbulence model used	Spalart-Allmaras

Table A.3. NASA's airfoil simulations input data [214]

The model used by the NASA for modeling the turbulent flow around an airfoil is the C shaped domain (see Figure A.20a). These domains are regularly used for modeling airfoil or hydrofoil turbulent flows [327]–[329]. Their popularity lies in many reasons: this domain is good for having a structured mesh that matches the leading-edge curvature which helps with flow separation, it helps controlling the mesh wall size for good results and finally gives better convergence for airfoils flows. The size of this model is given in Figure A.20a. This model is approximately 910 m × 910 m big for an airfoil of size $c = 1.82$ m. The domain needs to be large enough for avoiding fluid's recirculation or modification because of the control volume's borders. The **Farfield** needs to be far enough. Nonetheless, this domain is so large that the numerical simulation of this model needs a supercalculator to have the results in a reasonable amount of time. This type of domain is used to have differences that are inferior to 1 % from reality. However, for our model, such a precision is not needed. A model of size 11 m × 18 m is more than enough for having differences in

a 5 % range in a respectable amount of time (see Figure A.20b).



Figure A.20. *C-type models for airfoils*

Now that the model has been defined, it is time to define the boundary conditions of this flow. The boundary conditions of this control volume are given in Figure A.21. First, the velocity values of the free stream must be defined here corresponding to the front, the top and the bottom of this control volume. The flow's velocity vector has a non-zero value of 51.6 m/s only in the x direction. Then, on the surface of the airfoil, a non-slip condition is specified. This non-slip boundary conditions is used for specifying that a solid boundary is here and that at this location $||v_i|| = 0$. The surface on the back of the control volume is used for specifying the relative pressure of the free stream. The relative pressure is defined as the difference between the measured pressure $P(\bar{X})$ and the hydrostatic pressure P_{atm} : $P_{rel}(\bar{X}) = P(\bar{X}) - P_{atm}$ with an atmospheric pressure value of $P_{atm} = 1.10^5 Pa$. To finish with, two final boundary conditions are added to the model: a 2D flow boundary condition is specified, the z velocity component is 0 everywhere in the model and an initial value for the turbulent viscosity $\tilde{\nu}_0$ is initialised. This initial value is equal to 5 times the kinematic viscosity of air $\tilde{\nu}_0 = 7.5.10^{-6} m^2.s^{-1}$ as advised in the Abaqus documentation [326].

To finish with, the model has to be meshed for being able to solve the equations. In Abaqus v6-14, the fluid's constitutive equations are the RANS equation (Equation A.87) and the time averaged Poisson's equation (Equation A.88). Numerically, those equations are solved differently: the RANS equation is solved with a finite volume numerical technique, and the time averaged Poisson's equation is solved with a finite Element technique. Here, both methods won't be thoroughly developed, the reader can check the following references for further information for finite volume numerical technique [330]. The reader must just know that, the main difference between the both methods lies in the location where the exact solution of the partial differential equation is estimated: for the finite

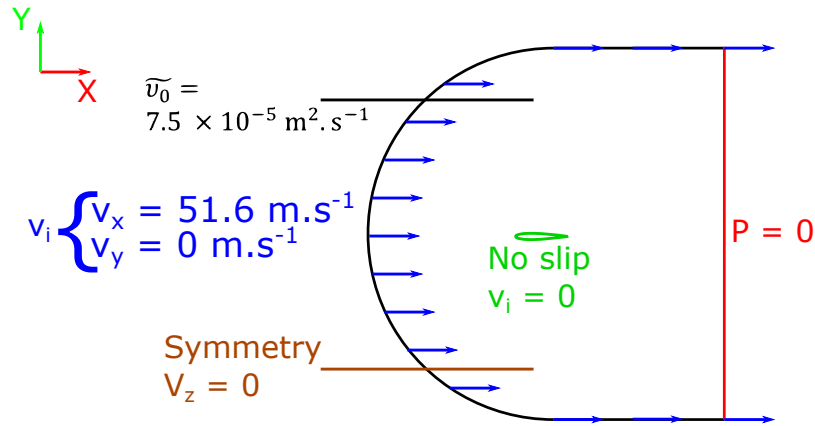


Figure A.21. Airfoil fluid model's boundary conditions

volume method, it is in the center of the finite volume element and for the finite element method it is at the nodes of the finite element. For meshing this model, 3D hexahedral 8 nodes linear bricks are used. Linear elements are sufficient for solving these CFD problems with the finite volume and elements method.

For estimating well the pressure field and the velocity field, the most important part to mesh finely is the boundary layer of the airfoil. As seen in paragraph A.2.7, the boundary layer is constituted of different composite regions: the viscous region, the log region and the outer region. These regions must be meshed as precisely as possible for having the most precise results. This implies that the mesh's size near the airfoil's wall must be inferior or equal to the dimensionless height $y^+ = 1$ for covering all these regions (See section A.2.7 for more details). for converting the dimensionless boundary layer height y^+ into an absolute height y , *i.e.* the mesh's size, Equation A.111 needs to be used (equation already depicted in Section A.2.7, Equation A.35).

$$y^+ = \frac{yu^*}{\nu} \quad (\text{A.111})$$

In this Equation, the wall velocity u^* is not known for the NASA flow problem around the NACA0012 airfoil. This makes it currently not usable for estimating the mesh's size. Thus, u^* must be estimated through an empirical approach. The empirical method used was found on the internet site *CFD online* [331]. For estimating the mesh size, firstly, the skin friction coefficient must be empirically estimated. Then, the wall shear stress needs to be calculated with this skin friction coefficient. With the wall shear stress, an estimation for the friction velocity u^* can be found. And finally, the mesh size can be estimated for

a desired y^+ .

For estimating the skin friction over the airfoil, the Schlichting formula was used (see Equation A.112). This Equation is used for estimating the turbulent skin-friction coefficient for a turbulent flow passing over a flat plate which has a Reynolds number inferior to 10^9 [332]. By using the Reynolds number at the end of the airfoil $Re_c = 6.10^6$ in Equation A.112, the empirical value of the skin friction coefficient can be estimated as $C_f = 2.79 \times 10^{-3}$.

$$C_f = [2 \log_{10}(Re_x) - 0.65]^{-2.3} \quad (\text{A.112})$$

With an estimated value of the skin friction coefficient, it is now possible to estimate the wall shear stress τ_w with Equation A.113 (see Section A.2.8 Equation A.49 for more details). With this Equation, the wall shear stress is estimated to be $\tau_w = 4.46 Pa$.

$$\tau_w = \frac{1}{2} C_f \rho U_\infty^2 \quad (\text{A.113})$$

Finally, with Equation A.114 it is possible to find the estimation of the wall-friction velocity u^* (see Section A.2.7 Equation A.34 for more details). Its estimated value is $u^* = 1.93 m.s^{-1}$.

$$u^* = \sqrt{\frac{\tau_w}{\rho}} \quad (\text{A.114})$$

For being able to reach the region with a $y^+ = 1$, the mesh's size y would have to be $y = 7.78 \times 10^{-6} m$ if Equation A.111 is used. Unfortunately, with the technique used for meshing the model was not able to generate a mesh that is so low. This technique was able to mesh low enough to attain the log region with $y^+ = 64$ corresponding to a meshing size of $y = 5.10^{-4} m$. Reminding the reader that, the exact velocity of a finite volume element is computed in the center of this volume. The center, being at a value $y^+ = 32 > 30$, the finite volume element is in the log region.

Comparing this mesh height size of $y = 5.10^{-4} m$ to the control volume's total surface of $11 \times 18 m^2$, there is quite a scaling problem for the control volume meshing. One has to pass from a meshing scale of 1 m for the farfield meshing to a meshing scale of $1.10^{-4} m$ for the airfoil's walls. This represents a scale factor of $10^4 m$. This difference in scale is a big issue not encountered so far in the solid mechanics part. For solving this issue, the

C-shape control volume is perfect: it is possible to easily partition the control volume for imposing a meshing gradient while keeping simple geometric parts to be meshed (see Figure A.22). The front leading edge domain of the control volume is composed of two semi-circles and the back trailing edge domain of the control volume is composed of two rectangles (see Figure A.22). These simple geometric shapes assure a structured mesh in the whole domain. Along the partition lines, a gradient of size is imposed: near the outer edges of the control volume, the mesh's height is 1 m and near the airfoil the mesh's height is 0.0005 m. To assure such extreme gradients, the automatic meshing procedure of Abaqus is used. The airfoil's boundaries mesh is 0.0015 m wide (see Figure A.22), it is the minimum that was affordable by the automatic Abaqus meshing software. For lower values, the algorithm was not able to generate the gradient mesh. Nonetheless, having a mesh size of 0.0005 m \times 0.0015 m at the airfoil's boundaries is a decent size and aspect ratio (equal to 3) that guarantees precise results and a good convergence. The mesh's out-of-plane depth value is 0.910 m and only one row of element is present in the model's depth direction.

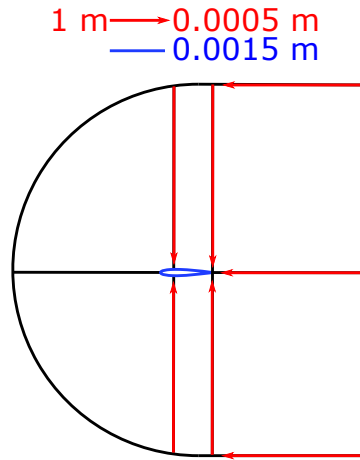


Figure A.22. Numerical model's partition and mesh gradient size

The total number of elements used in the model is 297 432, Figure A.23 shows the final numerical model's shape.

The results that need to be extracted from these models for comparing our model to the NASA model are the pressure coefficient C_p , the lift coefficient C_L and the drag coefficient C_D . These coefficients are not computed by Abaqus and need to be calculated on our own. The Equations for calculating these coefficients are given in Section A.2.8, respectively Equation A.40, A.46 and A.51. However, most of these equations are integral equations

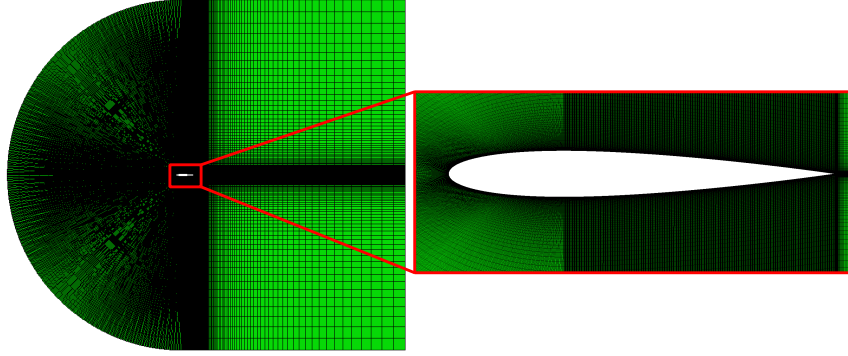


Figure A.23. NACA0012 C type model meshed

or are spatially dependent equations. Hence, these equations need to be reformulated for them to match the finite element model developed here. The C_p Equation adapted for airfoils is given in Equation A.115. In this Equation, P_i represents the pressure at a considered node on the airfoil's wall.

$$C_p^i = \frac{P_i - P_\infty}{\frac{1}{2}\rho U_\infty^2} \quad (\text{A.115})$$

The C_L equation is an integral equation, consequently there is a need to transform Equation A.46, a continuous sum in space, into a new Equation that would be discrete in space as the finite elements are. Equation A.116 depicts the new discrete lift coefficient equation. In this Equation, $c_{airfoil}$ represents the chord of the airfoil, C_{p_i} represents the pressure coefficient at a considered node on the airfoil's wall, \bar{n}_{c_i} represents the vector normal to the edge of a considered element that is in contact with the airfoil's wall and finally dc_i is the length of the edge of a considered element that is in contact with the airfoil's wall.

$$C_L \approx \frac{1}{c_{airfoil}} \sum_{i=1}^{n_c} C_{p_i} \cdot \bar{n}_{c_i} \cdot \bar{y} \cdot dc_i \quad (\text{A.116})$$

For the drag coefficient C_D integral Equation, the same approach is done. Equation A.117 is the discrete equation for calculating C_D in the numerical model. In this equation, $c_{airfoil}$ represents the chord of the airfoil, $C_{p(i,j)}$ represents the pressure coefficient at a considered node on the airfoil's wall, $\bar{n}_{c(i,j)}$ represents the vector normal to the edge of a considered element that is in contact with the airfoil's wall, $dc_{(i,j)}$ is the length of the edge of a considered element that is in contact with the airfoil's wall and $c_{f(i,j+1)}$ represents the local skin friction coefficient of the upper nodes of a considered element in contact with

the airfoil's wall. The latter information is not given by Abaqus directly, an additional step is needed for estimating it.

$$C_D \approx \frac{1}{C_{airfoil}} \sum_{i=1}^{n_c} (C_{Pi} + c_{f(i,j+1)}) \cdot \bar{n}_{ci} \cdot \bar{x} \cdot dc_i \quad (\text{A.117})$$

For determining the local friction coefficient $c_{f(i,j+1)}$, according to Equations A.113 and A.114 the wall shear stress τ_w and the friction velocity u^* . Here, the "law of the wall" will be needed once again to determine u^* . The mesh size being in the log region, Equation A.38 holds for the elements at the airfoil's walls (the ones of interest here). So, if this Equation is reformulated into Equation A.118 for having u^* as the main variable. In this equation, u_i is the streamwise velocity at a given node.

$$\begin{cases} u_i^* \ln \left(\frac{y_i u_i^*}{\nu} \right) + B \kappa u_i^* - \kappa u_i = 0 \\ \kappa = 0.41 \\ B = 5.0 \end{cases} \quad (\text{A.118})$$

Unfortunately, this equation is not solvable in a straightforward method, that is why a dichotomy algorithm was used for finding the value of u_i^* . After determining the friction velocity at a particular node, the wall shear stress at this node τ_{wi} can be estimated with Equation A.119.

$$\tau_{wi} = (u_i^*)^2 \rho \quad (\text{A.119})$$

And with Equation A.120 and the local wall shear stress value obtained at one particular node, the local skin friction coefficient $c_{f(i,j+1)}$ can be estimated and the total drag over the airfoil can finally be calculated with Equation A.117.

$$c_{f(i,j+1)} = \frac{\tau_{wi}}{\frac{1}{2} \rho U_\infty^2} \quad (\text{A.120})$$

A.5.3 Results and discussion

Figure A.24 displays the pressure isovalues (see Figure A.24a) and velocity isovalues (see Figure A.24b) obtained with the numerical model formerly described. On these figures, it can clearly be seen that because of the symmetric geometry, the pressure and the velocity gradients are also symmetric. Seeing that the angle of attack of the hydrofoil is 0 deg, matching this with the previous observation leads to have a lift coefficient value that

must be close to zero. Moreover, it can be seen on Figure A.24b that the boundary layer remains well attached to the hydrofoil up to the trailing edge, thus the drag coefficient is mostly composed of skin friction and not the pressure drag.

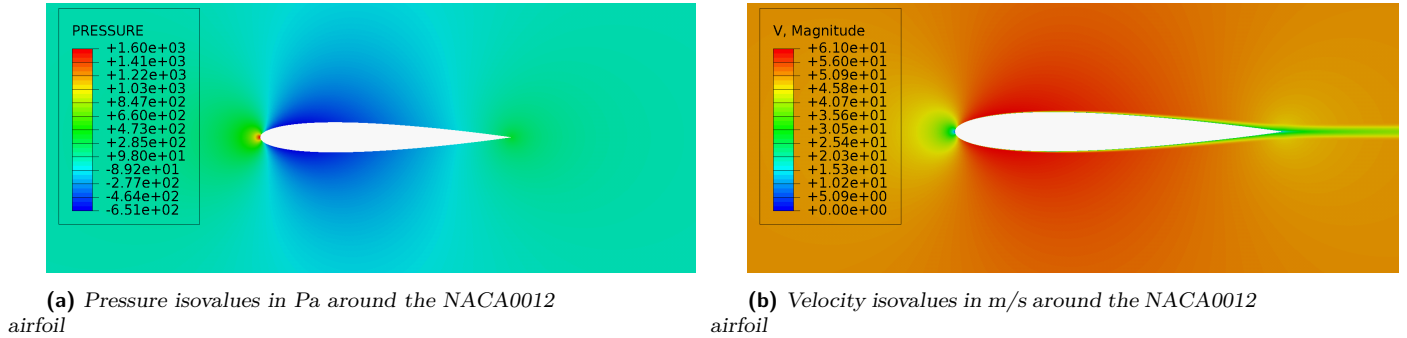


Figure A.24. NACA0012 pressure and velocity profiles

Figure A.25 shows the pressure coefficient C_p distribution along the NACA0012 airfoil for the numerical model we developed with Abaqus, the numerical model used by the NASA CFL3D and experimental values obtained by NASA scientists Ladson *et al.* It can be seen on this Figure that the values predicted by our Abaqus model matches perfectly with the NASA CFL3D numerical model. And both models match very closely the experimental pressure coefficients distribution of Ladson *et al.* The differences between numerical and experimental data might come from a combination of two factors, first of all the measurement of pressure values for turbulent boundary layers can be very though and the values can vary from their initial theoretical values, and on a second hand, Section A.4 has showed that turbulence modeling is quite approximative, especially the RANS approach, so this might also play a role in the difference observed. Nonetheless, our numerical model matches NASA's results quite decently, this is a first sign showing up that the Spalart-Allmaras model is reliable for modeling a turbulent flow over an airfoil. it also shows that our approach for using numerical model is reliable.

Table A.4 displays the comparison between the lift and drag coefficients obtained with our numerical model developed on Abaqus and the numerical model developed by the NASA. On this Table, it can be seen that the Lift coefficient and Drag coefficient values are very close and no significative difference can be observed. Nonetheless, for the drag coefficient, there is a small difference of 1.8% and it can be interesting to see the origin of this difference. To do that, the drag coefficient can be split in two components, the pressure drag component and the skin friction drag.

Table A.5 shows the pressure and friction drag percentage part of the total drag

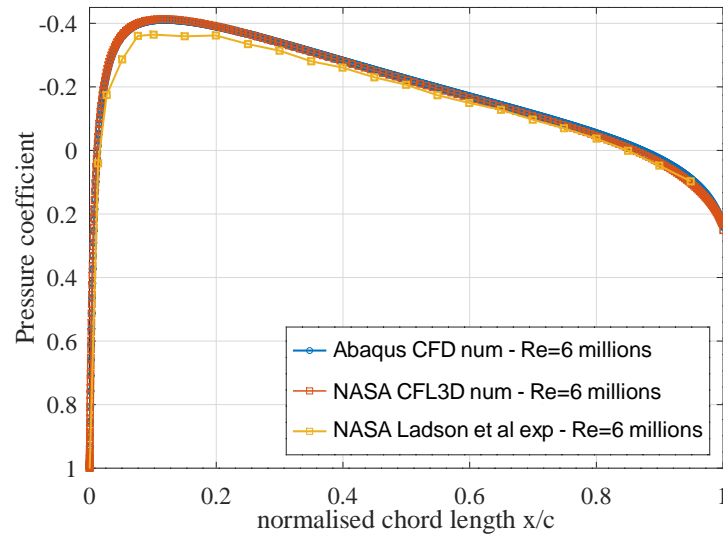


Figure A.25. Pressure coefficients distribution along the NACA0012 airfoil

Aerodynamic coefficient	NASA CFL3D value	Abaqus value	difference (in %)
Lift coefficient C_L	Approx 0	-3.43×10^{-17}	0
Drag coefficient C_D	0.00819	0.00804	1.83%

Table A.4. Lift and drag coefficients comparison with the NASA

coefficient obtained with the numerical model on Abaqus. The skin friction mechanism is the one dominating the total drag. To model this mechanism well, the mesh must refine closely the airfoil's walls. However, in our numerical model the mesh goes down to the log region and not to the viscous sublayer. The small difference might come from the skin friction coefficient distribution.

Drag coefficient component	value	percentage of total drag (in %)
Pressure drag coefficient C_{Dp}	0.00135	17%
Skin friction coefficient C_f	0.00668	83%

Table A.5. Pressure and skin friction components of the final drag coefficients

Figure A.26 displays the local skin friction coefficient distribution along the NACA0012 airfoil used for the calculation of the global skin friction coefficient. On this figure, it can be seen that there is a small overestimation of the skin friction very near the leading edge

of the airfoil. Then along the airfoil, the skin-friction coefficient becomes pretty close to the one estimated by the NASA again.

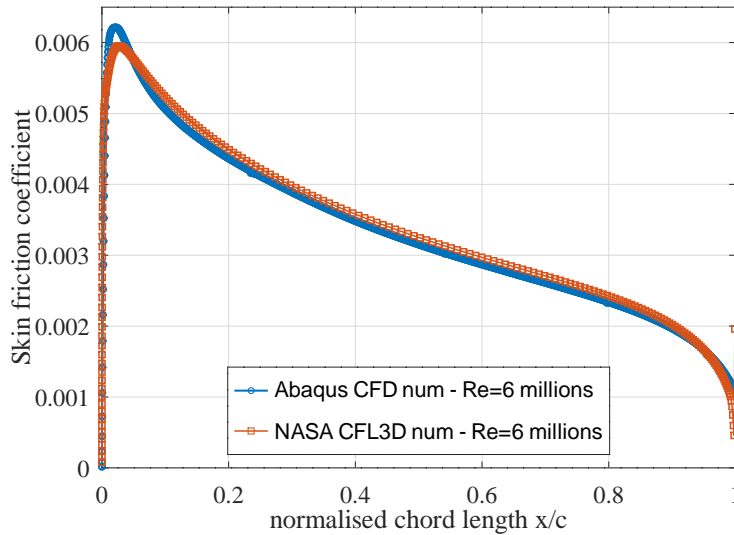


Figure A.26. Simulated local skin friction coefficient distribution along the NACA0012 airfoil

Saravia, in a master thesis work of 2014, used the same approach depicted here to model the turbulent NACA0012 airfoil proposed by the NASA: meshing down to log-law layer and then using walls of the law for determining the skin friction for finally comparing the to highly meshed results ($y^+ < 1$) [333]. The only difference in this work from this study and NASA’s work is the use of the $k - \omega$ SST model as a turbulence modeling strategy instead of the Spalart-Allmaras model. At different y^+ values of the log regions, Saravia showed that the skin-friction part of the drag coefficient is ranging from a lower value of 0.00665 up to 0.00745. The value found from our model lies in this interval and is very close to the lower boundary. In this work, Saravia also did the same comparison comparison for the pressure drag coefficient C_{Dp} . He showed that for this coefficient, being in the log-layer or the viscous sublayer do not change the results so much, they are located in a interval between 0.0012 and 0.0014. The pressure coefficient obtained with Abaqus is located in this interval.

Thus, these results prove that the Spalart-Allmaras turbulence model is reliable for modeling turbulent flows around airfoils. Not only the turbulence model, these results

imply that the method chosen to develop the numerical model, to mesh the numerical model and to post-treat the results obtained with it are also highly reliable. The only weakness that can be witnessed for this model is the time needed for obtaining fully converged results. For the NACA0012 Abaqus numerical model, the time needed for having fully converged results is 3 hours and 40 minutes. This is far too long, especially if these results need to be reused for a fluid-structure interaction problem. In addition to this problem, our method showed a reliable answer only for a symmetric airfoil at an angle of attack of 0 deg without the presence of wake or strong adverse pressure gradients. For non-symmetric cambered airfoils or hydrofoils, the ones for interest for morphing, the performance of this methodology developed here was not yet tested. In the following section, the very same methodology will be applied for a cambered hydrofoil: the Eppler420 hydrofoil.

A.6 Methodology for numerical model development: cambered hydrofoil test

The Eppler420 airfoil is a highly cambered airfoil profile that was already used in numerous passive morphing studies and applications [47], [69], [207]. This airfoil was selected in these applications, because its cambered profile enhances the pressure gradient between the lower and the upper surface which helps its deformation. Moreover, the more an aerodynamic profile is cambered, the more its pressure center point will move towards the leading-edge resulting in leading edge deformation if the pressure forces are sufficient. The Eppler 420 profile is a perfect candidate for morphing study and for testing the methodology developed in § A.5. Fortunately, a study was conducted by Aguilar *et al* [282] where a turbulent water flow around an Eppler420 hydrofoil was modeled. The objective of this section will be to compare the results obtained by a numerical model developed on Abaqus with the numerical results obtained in Aguilar *et al*'s study.

A.6.1 Material and Methods

As it was the case for the previous model, the initial conditions simulated in the work of Aguilar *et al*. is given in Table A.6. If these values are compared with the values of Table A.2, it can be seen that the velocity simulated here is in the range of the velocity that foiling boats can undergo. However, the hydrofoil's chord has half the value of the

smallest encountered foils, which has an impact on the Reynolds Number. The Reynolds number of the flow studied in this configuration is a little bit out of the interval where foiling boats perform. Nonetheless, it is very close to the lower boundary of the Reynolds number interval $Re = 1500000$ that is not very different from a Reynolds number value of $Re = 1000000$, indeed in both cases the flow is turbulent. The turbulence model used here the $k - \omega$ SST model is different from the Spalart-Allmaras model used previously, but considering some papers the results obtained with both of the models are very similar [324], [325]. Hence, this case study can be considered as being representative to conditions of foiling boats. In terms of software, Aguilar *et al* used Ansys Fluent 19 R1 and the model here is developed on Abaqus CFD.

Airfoil flow properties	values
Fluid name and properties	Water $\rho = 1000 \text{ kg/m}^3$ $\mu = 1.00^{-3} \text{ Pa.s}$
Mach number	Mach ≈ 0 Incompressible fluid
Airfoil dimensions	0.177 m
Flow speed	5.52 m/s
Reynolds number	1 million
Angle of attack	3°
Turbulence model used	$k - \omega$ SST

Table A.6. Eppler 420 flow boundary conditions

The domain used by Aguilar *et al* is also a C-shaped domain that has the following dimensions: 10 chords upstream (1.77 m) and 20 chords downstream (3.54 m) (see Figure A.27). The exact same model was developed on Abaqus.

Figure A.28 shows the boundary conditions used for the Eppler 420 numerical modeling. On this model the boundary conditions are very similar to the ones displayed for the NACA0012 at Figure A.21, the only difference lies in the velocity x value that was changed to 5.52 m.s^{-1} . The initial turbulent viscosity was set to $\tilde{\nu}_0 = 4.0 \times 10^{-6} \text{ m}^2.\text{s}^{-1}$, which is four times the flow's kinematic viscosity.

For determining the mesh, the same method as the one depicted in Section A.5.2 was used. The changes that were made in the formulas concerned the kinematic viscosity of the fluid $\nu_{water} = 1.10^{-6}$, the y^+ that was sized down to $y^+ = 45$ and the plate Reynolds number in the Schlichting Equation that passed to $Re = 1000000$. All these changes

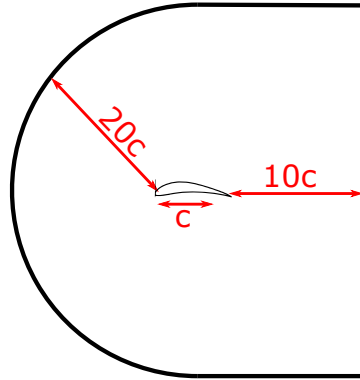


Figure A.27. Numerical model geometry for the Eppler 420 modelisation

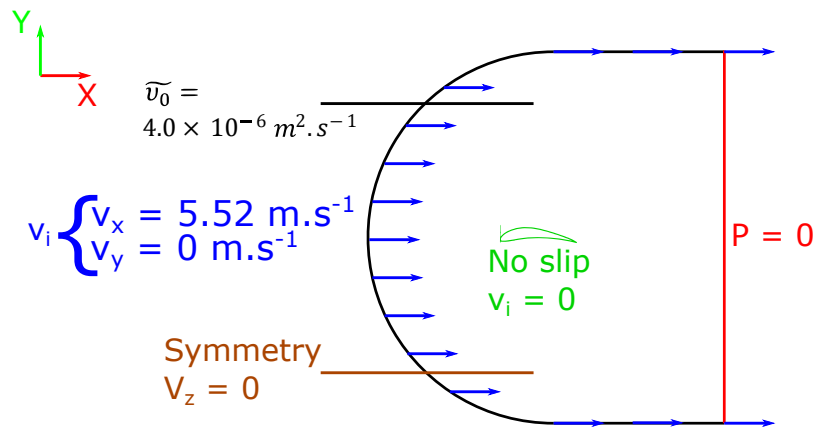


Figure A.28. Boundary conditions used for the Eppler 420 numerical model

lead to a minimum mesh size of $1.63 \times 10^{-4} m$, with this mesh the log region was clearly targeted again. However, here it is important to note that Aguilar *et al* highlighted the fact that the mesh needed to go down to $y^+ = 0.1431$ to start having reliable results [282]. Unfortunately, this region of the boundary layer was not accessible with the default Abaqus meshing system. As it was the case for the NACA0012 airfoil, a mesh gradient was imposed on the domain, this mesh gradient had a max size of $0.1 m$ for the external boundaries of the model and a minimum height of $1.63 \times 10^{-4} m$ for the hydrofoil walls (see Figure A.29). The same mesh size of $1.63 \times 10^{-4} m$ was used for the hydrofoil's wall leading to meshes with an aspect ratio of 1 in the plane. The out of plane depth of the elements is $4.4 \times 10^{-3} m$ long. This value in depth has been selected to ensure that one row of elements is present in the model's depth.

Figure A.30 shows the fully meshed Eppler 420 numerical model meshed on Abaqus. The total number of elements of the model is 303 744.

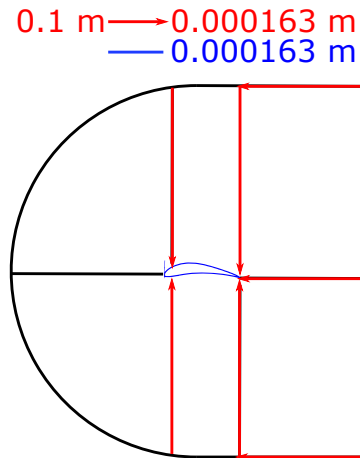


Figure A.29. *Eppler 420 numerical model's partition and mesh gradient size*

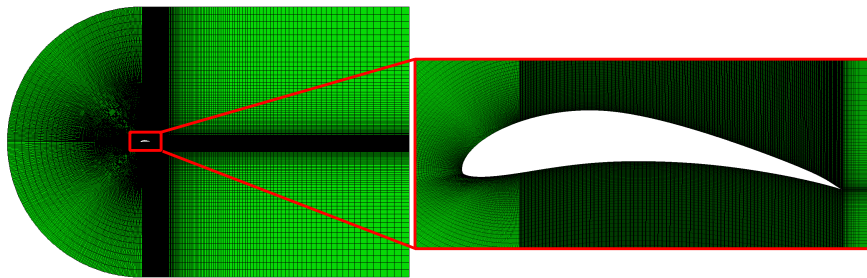


Figure A.30. *Eppler 420 C type model meshed*

For this model, the results to be extracted remain the pressure coefficients C_p , the lift coefficient C_L and the drag coefficient C_D . All the formulas to compute them are the same as the one depicted at the end of Section A.5.2.

A.6.2 Results and discussion

Figure A.31 and Figure A.32 show pressure and velocity isovalues comparison between the results obtained by Aguilar *et al* [282] and the ones obtained on Abaqus. By comparing Figure A.31a and Figure A.31b, globally the isovalues are very similar to each other, there is a global minimum of pressure where the curvature is maximum. There is also an over pressure at most of the lower side of the hydrofoil, and the stagnation pressure is present at the leading edge of the hydrofoil. However, despite these similarities, there are major differences between the two models. Indeed, in the results obtained with Abaqus, there are two regions of strong underpressure that are not present in Aguilar *et al*'s model. Under the leading edge and at the trailing edge of Figure A.31a there are zones that are

strongly green colored/lightly blue colored indicating strong depression zones that are not present on Figure A.31b.

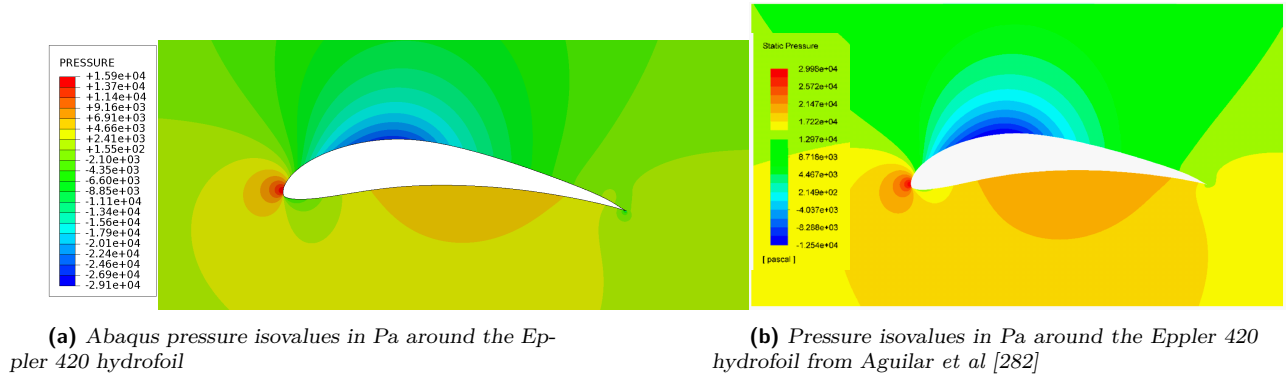


Figure A.31. Eppler 420 pressure and velocity profiles

These depression zones have also an impact on the hydrofoil velocities. If Figure A.32a and Figure A.32b are compared, they are exactly the same: the overpressure and depression zones are located in similar zones, the maximum and minimum velocity scales simulated are the same. However, at the same positions that depression regions were observed, there are reductions of the flow velocity near these regions.

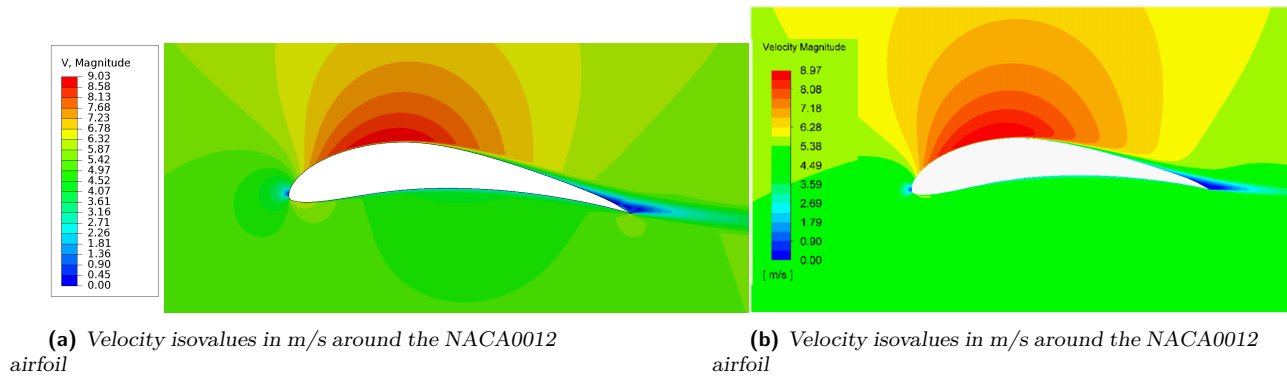


Figure A.32. Eppler 420 pressure and velocity profiles

If the C_p values distribution is observed on Figure A.33, it can be seen that the regions where the depression zones were observed the C_p distribution curves obtained from Abaqus (blue curve) drops sharply whereas the C_p distribution curves obtained by Aguilar *et al* do not change so much (red curve). Despite these changes, the global shape of the curves remain similar. Yet a general difference of values between the two curves can be observed, the curves follow each other in a parallel way. The hypothesis explaining these changes might come from the mesh refinement difference of the two models.

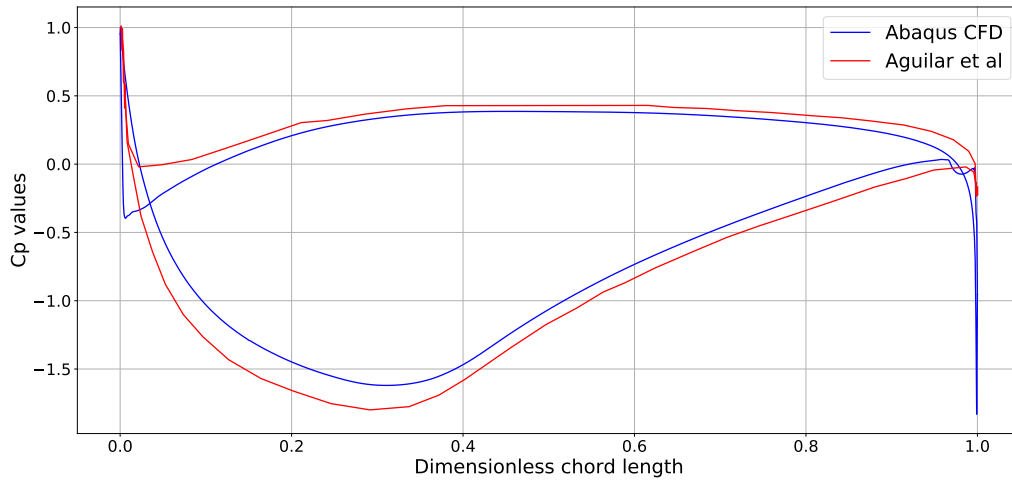


Figure A.33. Eppler 420 pressure coefficient distribution comparison around the hydrofoil

Coming back to the depression zones, these ones also strongly affect the lift and drag coefficients. On Table A.7, the global difference observed between the lift and drag coefficients obtained with Abaqus and by Aguilar *et al* are in the range of 20%. Without these strong depressions, there would be less difference between coefficients. Having said that, a question can be addressed: What is the origins these depression in these regions of the hydrofoil?

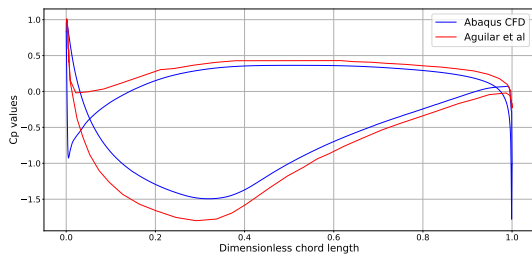
Aerodynamic coefficient	Aguilar <i>et al</i> [282]	Abaqus value	difference (in %)
Lift coefficient C_L	1.25	1.04	17%
Pressure drag coefficient C_{Dp}	0.0209	0.0251	20%

Table A.7. Eppler 420 lift and drag coefficients comparison between Aguilar [282] and Abaqus-CFD for $t=0.33s$

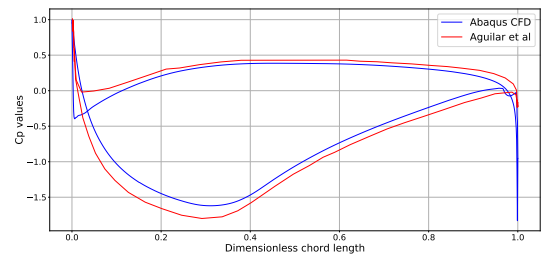
For the depression zone located at the trailing edge of the hydrofoil, this one is due to the difference of turbulence models used. Indeed, Reggio *et al* observed similar differences while testing different turbulence models (Spalart-Allmaras, $k - \omega$ SST, $k - \epsilon$ RNG and RSM turbulence models) for a NACA 63-415 airfoil [324]. The author supposed that this difference came from the fact that the Spalart-Allmaras model's destructive term is fully based on the wall's distance, the dissipation as a quantity does not explicitly exist in the model. Whereas, the $k - \omega$ SST model handles the dissipation best with a partial

differential equation for handling the specific dissipation rate ω .

Figure A.34 shows the pressure coefficient C_p distribution along the Eppler 420 airfoil at two different simulated time: the first one represents the C_p distribution at a simulated time of $t = 0.086 s$ and the second one represents it at a simulated time of $t = 0.33 s$. The main difference that can be observed between the two models is the intensity of the depression zone near the leading edge. At a simulated time of $t = 0.086 s$, the C_p reached a value near to -1.0 in this region, whereas at a simulated time of $t = 0.33 s$, this peak was lower than -0.5 . These C_p values imply that the simulation is not fully converged. Other things tend to imply this, the upper surface C_p distribution modeled with Abaqus (blue curve tending to negative values of C_p) has almost reached the upper surface C_p distribution modeled by Aguilar *et al* (red curve tending to negative values of C_p) at a time of $t = 0.33 s$. Note down that, despite the difference of time, the trailing edge values of pressure coefficient did not change at all.



(a) Eppler 420 pressure coefficient distribution for a simulation time of $t=0.086s$



(b) Eppler 420 pressure coefficient distribution for a simulation time of $t=0.39s$

Figure A.34. Eppler 420 Abaqus modeling at two different times

Figure A.35 shows the evolution of the pressure coefficient in the depression region. This figure shows that while the simulation was progressing, the pressure coefficient was rising. At a simulated time of approximately $t = 0.23 s$, the pressure coefficient/time relationship started to evolve quasi linearly. Thank to a linear regression, the fitting relation between the pressure coefficient and the time was $y = 0.68x - 0.60$. If the convergence time did not change anymore, the value simulated in this region by Aguilar *et al* (*i.e.* $C_p = 0$) would have been attained at a simulation time of $t = 0.88 s$. Consequently, the reasons why the values compared to Aguilar *et al* were so different are because not fully converged results were compared to fully converged ones.

Unfortunately, the Eppler 420 modeling displayed above are the best results that were

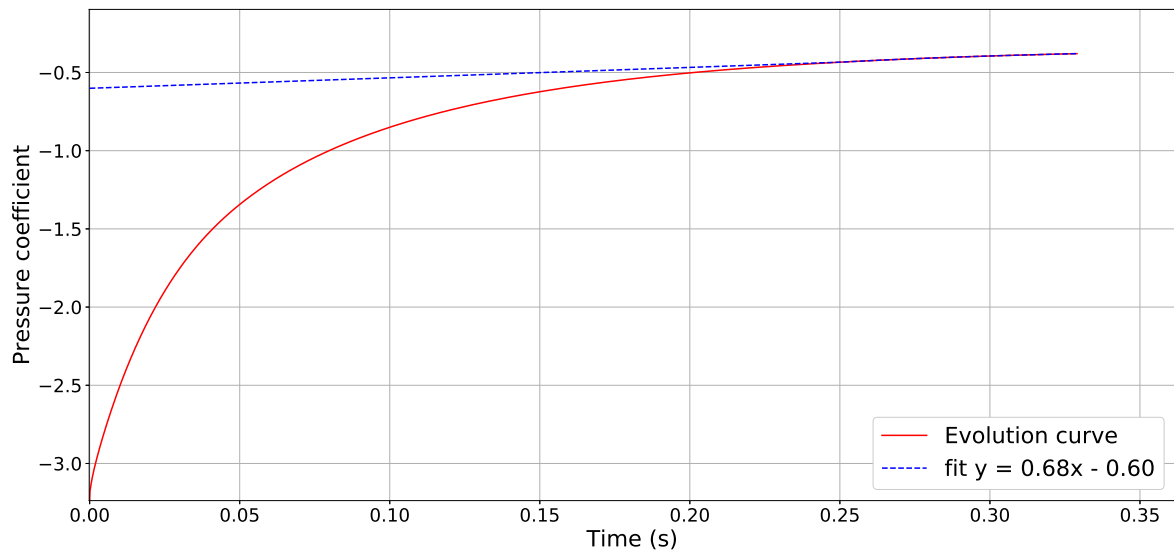


Figure A.35. *Eppler 420 pressure coefficient evolution in the leading edge depression in function of simulated time*

attainable with the current model design. Indeed, the simulation stopped after too many divergences of the time averaged Poisson Pressure Equation, the biggest divergence problem encountered with turbulent flows on Abaqus. To fix those problems, the solution might be to mesh down to $y^+ = 0.1431$ as suggested by Aguilar *et al* [282]. However, this would bring another issue, the explosion of the simulation time. With a mesh reaching $y^+ = 45$, 10 days were necessary to have the simulation converge to these results before diverging ! This case shows the limits of the modeling strategy chosen: not precise enough to have "true" pressure values and far too time consuming to use fully converged simulations to model a turbulent water flow for a fluid-structure interaction purpose.

A.7 Summary

In this chapter, we built a methodology to generate numerical models for being able to model turbulent water flows around hydrofoils of foiling boats. This model's purpose is to be reused for building a fluid-structure optimisation program later. In the numerical model development strategy, the use of the Spalart-Allmaras turbulent model needed to be confirmed as being a reliable model for predicting a turbulent's flow behavior for aerodynamic profiles. For that purpose, the model was compared to a NASA's NACA0012

airfoil numerical simulation that matched pretty well foiling boat's conditions, that were compared to experimental results and that also used the Spalart-Allmaras model. The pressure coefficient distribution, the lift coefficient prediction and the drag coefficient prediction given by the Abaqus CFD model were almost the same as the one found by the NASA, numerically and experimentally, this confirmed the relevance of choosing the Spalart-Allmaras turbulence model for modeling a turbulent water flow. It also showed that very precise results could be found with a boundary layer meshed down to the log law region, without having the need to mesh the viscous region.

After validating the turbulence model, it was the occasion to test the modeling strategy for hydrofoils that were already used for morphing purpose, the Eppler 420 profile. The methodology developed earlier was used again for the Eppler 420 hydrofoil. The flow conditions were set considering a research work done by Aguilar *et al* [282] that modeled numerically a turbulent water flow over an Eppler 420 hydrofoil with conditions close to a foiling boat's conditions. This time the pressure coefficient distribution and the lift and drag predictions were different from Aguilar *et al*'s results. The main reasons explaining this is the difference of turbulence models used and the non-total convergence of our numerical model. This comparison showed the limits in precision of our numerical modeling strategy for turbulent water flows and in time that can be afforded for simulating this flow: 10 days of simulation were necessary to obtain these results.

Nonetheless, despite not being accurate in results displayed, the modeling strategy developed in this chapter always showed reliable pressure distribution around the Eppler 420 airfoil. Thus, for the fluid-structure optimisation program using the numerical model we developed would give a first idea of the pressure to which the hydrofoil would be submitted. The pressure computed by our model would be qualitatively correct, but not quantitatively. Consequently, if a fluid-structure optimisation program is developed on the basis of that model, the results it would provide would remain true for these qualitative pressures. And one day, if methods are found to have more reliable pressure outputs in a short amount of time, this turbulent flow modeling technique can be upgraded or replaced in the fluid-structure optimisation program while having a global reliable method. Moreover, this model is currently the only option we have for determining dynamically a pressure field for a morphing hydrofoil. For that reason, this modeling strategy will be reused in the next chapter for the development the fluid-structure optimisation.

APPENDIX

A.1 Appendix One: Spalart-Allmaras one equation model details

The first types of turbulent flows that are considered for developing a turbulence model are the free shear flows. The free shear flow category represents all the types of viscous flows that are not attached to any solid wall or boundaries, for instance wakes behind an airfoil, buoyant jet from an erupting volcano or the jet of air coming out of one's mouth after exhalation are types of free shear flows. In these types of flows, the turbulence is globally homogeneous, different scales of turbulence can cohabit in the same region on the contrary of boundary layer flows. Because of the lack of solid boundaries, many physical terms from Equation A.101 can be neglected. The dissipation of turbulence E (also called "destruction term" by Spalart *et al*) is not effective because of the absence of wall that implies the absence of friction, as much as the molecular diffusion ∇T that becomes negligible with the absence of molecular friction. So Equation A.101 can be simplified as following for free shear flows (see Equation A.1).

$$C = P + T + \nabla P \quad (\text{A.1})$$

In Equation A.1, the convection C , the production P , the turbulence transport T and the pressure diffusion ∇P are the main physical quantities influencing the turbulence behavior. The convective term of this equation can naturally be described by $\frac{D\nu_t}{Dt}$, by using the eulerian particular derivative to expand this term, the new equation becomes $\frac{D\nu_t}{Dt} \equiv \frac{\partial \nu_t}{\partial t} + \bar{V}_i \frac{\partial \nu_t}{\partial x_i}$.

The production was defined as the rate at which the kinetic energy of the mean flow is transferred to the turbulence field. Quite logically, Spalart *et al* wanted to use the term $\frac{\partial \bar{V}_i}{\partial x_j}$ as it was used in all other turbulence models and represents the mean flow rate.

Nonetheless, many requirements have to be met in order to integrate it into the model. First of all, since that variable ν_t is a scalar, a scalar norm of this tensor that will be noted by the term S must be used to have a final scalar equation. The final expression of the production term would be in the form $P \equiv c_{b1}S\nu_t$, a term that fits the dimension of $\frac{D\nu_t}{Dt}$. c_{b1} is a constant where the subscript b stands for "basic". The second requirement that needs to be met by the norm S is that it must provide the Galilean invariance. The perfect candidate selected by Spalart *et al* was the vorticity $S = \sqrt{2\Omega_{ij}\Omega_{ij}}$ where $\Omega_{ij} = \frac{1}{2} \left(\frac{\partial \bar{V}_i}{\partial x_j} - \frac{\partial \bar{V}_j}{\partial x_i} \right)$.

The turbulence Transport T and the pressure diffusion ∇P are usually expressed together in a single term that has the following form $\frac{\partial}{\partial x_i} \left(\frac{\nu_t}{\sigma} \frac{\nu_t}{\partial x_i} \right)$. This form has been chosen in many models because its form conserves the integral of ν_t (*i.e.* the expression of ν_t is similar to a potential), nevertheless Spalart *et al* do not see any good reason why this integral should be conserved. They then developed a term $\frac{1}{\sigma} \left[\frac{\partial}{\partial x_i} \left(\nu_t \frac{\partial \nu_t}{\partial x_i} \right) + c_{b2} \left(\frac{\partial \nu_t}{\partial x_i} \right)^2 \right]$ that is non-conservative for ν_t but that is for $\nu_t^{1+c_{b2}}$. More details and information are provided in [279] for explaining thoroughly why this second term has been adopted.

The different constants c_{b1} , c_{b2} and σ were fixed by calibrating the model (see Equation A.2) by requiring correct levels of shear stress in two dimensional mixing layers and wakes. The values found are $\sigma = 2/3$, $c_{b1} = 0.1355$ and $c_{b2} = 0.622$.

$$\frac{D\nu_t}{Dt} = c_{b1}S\nu_t + \frac{1}{\sigma} \left[\frac{\partial}{\partial x_i} \left(\nu_t \frac{\partial \nu_t}{\partial x_i} \right) + c_{b2} \left(\frac{\partial \nu_t}{\partial x_i} \right)^2 \right] \quad (\text{A.2})$$

Now that the model has been calibrated for free shear flows, Spalart *et al* expanded the model for boundary layer flows. They first focused on the Near-wall Regions where the Reynolds number is high (log-law region and outer region of the boundary layer). In this configuration, because of the presence of the wall, the dissipation mechanism E has now to be taken into account. The sum of physical processes influencing the turbulence is now depicted in Equation A.3.

$$C = P + T + \nabla P - E \quad (\text{A.3})$$

In this new equation, only the dissipation term (also called "destruction" in [279]) has to be expanded through a dimensional analysis. To find a suitable term, a list of

requirements that the term must ensure is listed. First of all, the effect of dissipation is inversely proportional to the distance d of a region in the flow from the wall. The closer it is to the wall, the more turbulence energy dissipates into thermal energy. Secondly, far enough from the wall the dissipation is not effective anymore, so for $d \rightarrow \infty$ the term should be zero. Finally, empirically this term has a non-linear behavior. Spalart *et al* expressed the dissipation in the following form $E = c_{w1}(\nu_t/d)^2$. Here, the subscript w stands for "wall" in the coefficient c_{w1} . Replacing all the physical quantities by their expression in Equation A.3 gives a new form to the Spalart-Allmaras one equation model (see Equation A.4).

$$\frac{D\nu_t}{Dt} = c_{b1}S\nu_t + \frac{1}{\sigma} \left[\frac{\partial}{\partial x_i} \left(\nu_t \frac{\partial \nu_t}{\partial x_i} \right) + c_{b2} \left(\frac{\partial \nu_t}{\partial x_i} \right)^2 \right] - c_{w1} \left(\frac{\nu_t}{d} \right)^2 \quad (\text{A.4})$$

In this new Equation, the constant c_{w1} is still unknown and must be clarified. To find the value of c_{w1} , the log-law region would be of interest. Empirically, in this region the productive, the diffusive and the dissipative terms are in equilibrium. This leads to the absence of convection in this region, *i.e.* $\frac{D\nu_t}{Dt} = 0$. In a classical log-law layer, by taking the expression of the streamwise velocity depicted in Equation A.38 of the paragraph A.2.7, the rotational norm in the log-law is $S = u^*/(\kappa.d)$ and $\nu_t = u^*\kappa d$ with u^* being the friction velocity at the wall (see Section A.2.7). By injecting all these information in Equation A.4 and solving it, the final expression of the constant is $c_{w1} = c_{b1}/\kappa^2 + (1 + c_{b2})/\sigma$. Spalart *et al* have tested the model given in Equation A.4 on a flat-plate boundary layer. This model predicted accurately the behavior of its log-law layer.

Nevertheless, the skin-friction coefficient obtained with this model was too low. The explanation for this is because the dissipative term do not reduce fast enough in the outer region of the boundary layer. To address this problem, the destructive term is multiplied by a non-dimensional function f_w that helps this term decreasing fast enough. Thus, the Spalart-Allmaras model equation is changed (see Equation A.5).

$$\frac{D\nu_t}{Dt} = c_{b1}S\nu_t + \frac{1}{\sigma} \left[\frac{\partial}{\partial x_i} \left(\nu_t \frac{\partial \nu_t}{\partial x_i} \right) + c_{b2} \left(\frac{\partial \nu_t}{\partial x_i} \right)^2 \right] - c_{w1}f_w \left(\frac{\nu_t}{d} \right)^2 \quad (\text{A.5})$$

The requirements set for this function is that its value must be equal to 1 when the log-law layer is reached, this function must affect the destructive term only when the outer-layer is reached, with this model the results obtained in the log-law region is accurate. To

develop this function, the authors inspired themselves from the existing algebraic models with the mixing length concept. They defined the mixing length as being $l \equiv \sqrt{\nu_t/S}$, then they formulated a non-dimensional argument r representing the non-dimensional mixing length (see Equation A.6). Both r and f_w are equal to 1 in the log layer and both decrease in the outer layer.

$$r \equiv \left(\frac{l}{\kappa d} \right) = \frac{\nu_t}{S \kappa^2 d^2} \quad (\text{A.6})$$

A satisfactory function f_w was developed by Spalart *et al* (see Equation A.7). At r equal 1, f_w is also equal to 1 and when r decreases, f_w decreases also. In this Equation, the step from g to f_w is just a limiter for avoiding large values of f_w . The values of the different constants c_{w2} and c_{w3} were set by Spalart *et al* so that the skin friction coefficient predicted by the model matches the skin friction coefficient of a turbulent flat-plate boundary layer.

$$f_w(r) = g \left[\frac{1 + c_{w3}^6}{g^6 + c_{w3}^6} \right]^{1/6}, \quad g = r + c_{w2}(r^6 - r) \quad (\text{A.7})$$

Now that the high Reynolds regions of a boundary layer have been investigated, the low Reynolds number regions (*i.e.* the buffer layer and the viscous sublayer) remain for investigation. As said earlier, in the algebraic models, near the wall the viscous forces are so strong that the fluid becomes laminar again. These viscous forces influence the eddies size which become smaller than the eddies of the more turbulent regions. In these configurations, the viscous molecular diffusion mechanism becomes highly influential on the turbulence transport in the boundary layer. However, on the contrary of other one equation models, Spalart *et al* did not only add a new term in the equation. He added viscous functions for modeling the impact of molecular diffusion on the eddy viscosity ν_t . Taking into account the molecular diffusion, The final global equation summing the different turbulence processes is given in Equation A.8

$$C = P + T + \nabla P + \nabla T, \quad \nu_t = \nabla T(\tilde{\nu}) \quad (\text{A.8})$$

So Spalart *et al* decided to add a new variable $\tilde{\nu}$ that represents the eddy viscosity in the turbulent regions of the turbulent boundary layer. From the log-law layer up to the outer layer, the value of the turbulent viscosity is $\nu_t = \kappa d u^*$, it is only in the viscous laminar parts of the turbulent boundary layer that this relation is not true anymore.

Thus, in this case, the way chosen for modeling the evolution of the turbulent viscosity in the laminar viscous layers is similar to what have been done for the previous dissipation term: using damping functions on the turbulent eddy viscosity $\tilde{\nu}$ in order to find the true eddy viscosity ν_t . Equation A.9 is used for modeling this behavior. In this equation, the subscript v stands for "viscous".

$$\tilde{\nu} = \kappa du^*, \quad \nu_t = \tilde{\nu} f_{v1} \quad (\text{A.9})$$

The reason why the molecular diffusive term is written that way is because Equation A.5 is already set to give very precise values for high Reynolds regions of the turbulent boundary layers. The global equation must not change, only the effect of viscosity must be modeled by this viscous function. Equation A.5 is used for calculating $\tilde{\nu}$, the eddy viscosity in turbulent layers and then, with the damping function, this term is corrected for being coherent with the empirical results observed in the viscous sublayer.

As the previous wall function, this new function must fulfill two requirements: it must be non-dimensional and it must be equal to 1 when coming in the log-law layer. For formulating this function, Spalart *et al* inspired themselves from an another work that formulated this function, see [279] directly for more details. Equation A.10 shows how the damping function is implemented. In this equation, the value of c_{v1} is set to 7.1 and χ represents the dimensionless eddies size in the viscous layers.

$$\chi \equiv \frac{\tilde{\nu}}{\nu}, \quad f_{v1} = \frac{\chi^3}{\chi^3 + c_{v1}^3} \quad (\text{A.10})$$

This function here models the impact of viscosity on turbulence when the region is close to the wall. Spalart acknowledged that having a function based on the Van-Driest model would be equivalent to this current function. Now Equation A.5 can be transformed into a new equation with $\tilde{\nu}$ as the center variable (see Equation A.11).

$$\frac{D\tilde{\nu}}{Dt} = c_{b1}\tilde{S}\tilde{\nu} + \frac{1}{\sigma} \left[\frac{\partial}{\partial x_i} \left((\nu + \tilde{\nu}) \frac{\partial \tilde{\nu}}{\partial x_i} \right) + c_{b2} \left(\frac{\partial \tilde{\nu}}{\partial x_i} \right)^2 \right] - c_{w1} f_w \left(\frac{\tilde{\nu}}{d} \right)^2 \quad (\text{A.11})$$

In addition of changing variables, the rotational norm \tilde{S} replaces now the former norm S . This new norm is constructed in a way that \tilde{S} maintain its log-law region behavior from the wall to the outer layer so that $\tilde{\nu}$ can maintain its log-law behavior. This change of norm is given by Equation A.12. This change of norm also impacts other quantities

developed before in order for them to keep the value they have in the log-law layer, *e.g.* r that is now defined as $r \equiv \frac{\tilde{\nu}}{\tilde{S}\kappa^2 d^2}$.

$$\tilde{S} \equiv S + \frac{\tilde{\nu}}{\kappa^2 d^2} f_{v2}, \quad f_{v2} = 1 - \frac{\chi}{1 + \chi f_{v1}} \quad (\text{A.12})$$

Furthermore, a diffusion term ν has been added with respect to the boundary condition that $\tilde{\nu} = 0$. This term has been placed in the equation so that it has a negligible impact in the log-law layer, $\tilde{\nu}$ evolving linearly, with high values its Laplacian would be negligible. Equation A.11 yields equilibrium $\frac{D\tilde{\nu}}{Dt} = 0$ from $d=0$ to the outer layer of the boundary layer. Thus, this version of the differential equation is the final one. Equation A.13, A.14, A.15 and A.16 sums up all the equations and constants used for this final version of the model.

Kinematic Eddy Viscosity

$$\nu_t = \tilde{\nu} f_{v1} \quad (\text{A.13})$$

Eddy Viscosity Equation

$$\frac{\partial \nu_t}{\partial t} + \bar{V}_i \frac{\partial \nu_t}{\partial x_i} = c_{b1} \tilde{S} \tilde{\nu} + \frac{1}{\sigma} \left[\frac{\partial}{\partial x_i} \left((\nu + \tilde{\nu}) \frac{\partial \tilde{\nu}}{\partial x_i} \right) + c_{b2} \left(\frac{\partial \tilde{\nu}}{\partial x_i} \right)^2 \right] - c_{w1} f_w \left(\frac{\tilde{\nu}}{d} \right)^2 \quad (\text{A.14})$$

Closure coefficients

$$\begin{aligned} c_{b1} &= 0.1355, & c_{b2} &= 0.622, & c_{v1} &= 7.1, & \sigma &= 2/3 \\ c_{w1} &= \frac{c_{b1}}{\kappa^2} + \frac{1+c_{b2}}{\sigma}, & c_{w2} &= 0.3, & c_{w3} &= 2, & \kappa &= 0.41 \end{aligned} \quad (\text{A.15})$$

Auxiliary Relations

$$\begin{aligned} f_{v1} &= \frac{\chi^3}{\chi^3 + c_{v1}^3}, & f_{v2} &= 1 - \frac{\chi}{1 + \chi f_{v1}}, & f_w(r) &= g \left[\frac{1 + c_{w3}^6}{g^6 + c_{w3}^6} \right]^{1/6}, \\ \chi &= \frac{\tilde{\nu}}{\nu}, & g &= r + c_{w2}(r^6 - r), & r &= \frac{\nu_t}{\tilde{S}\kappa^2 d^2} \\ \tilde{S} &= S + \frac{\tilde{\nu}}{\kappa^2 d^2} f_{v2}, & S &= \sqrt{2\Omega_{ij}\Omega_{ij}}, & \Omega_{ij} &= \frac{1}{2} \left(\frac{\partial \bar{V}_i}{\partial x_j} - \frac{\partial \bar{V}_j}{\partial x_i} \right) \end{aligned} \quad (\text{A.16})$$

Spalart *et al* tested then their models on various types of experimental flows. This model predicted in a reliable way a great number of flows. The results for flow cases where the pressure gradient was very strong, like airfoil flows, were the most reliable and highly precise.

A.2 Appendix two: k-omega turbulence model

For building the $k - \omega$ model, Wilcox *et al* [318] used the dimensional relations in Equation A.106 are used for building the relations that will be needed for building the main relations used for approximating the eddy viscosity ν_t . These relations are presented in Equation A.17. With β^* being a constant.

$$\nu_t = k/\omega, \quad l = k^{1/2}/\omega, \quad \epsilon = \beta^* \omega k \quad (\text{A.17})$$

The definition of these new equations allows Wilcox *et al* to change the original turbulence energy transport equation (see Equation A.97) into a new one. Equation A.18 shows the turbulence kinetic transport equation in the $k - \omega$ model. In this equation β^* and σ^* are constants.

$$\frac{\partial k}{\partial t} + \bar{V}_i \frac{\partial k}{\partial x_j} = \frac{1}{\rho} \tau_{ij} \frac{\partial \bar{V}_i}{\partial x_j} - \beta^* k \omega + \frac{\partial}{\partial x_j} \left((\nu + \sigma^* \nu_t) \frac{\partial k}{\partial x_j} \right) \quad (\text{A.18})$$

In Equation A.17, a partial differential equation for the specific dissipation rate ω needs to be formulated for closing the system. To do that, Wilcox *et al* used again the sum of the physical quantities influencing turbulence in a flow (see Equation A.101) applied on the specific dissipation rate [318]. Here a strong hypothesis is made on the fact that the physical quantities governing the apparition of turbulence (*i.e.* the turbulence kinetic energy k) are the same governing the dissipation (*i.e.* the specific dissipation rate ω). Each terms are then extended through a dimensional analysis. Equation A.19 shows the final partial differential equation used for finding ω .

$$\underbrace{\frac{\partial \omega}{\partial t} + \bar{V}_i \frac{\partial \omega}{\partial x_j}}_{\text{Convection}} = \underbrace{\frac{1}{\rho} \alpha \frac{\omega}{k} \tau_{ij} \frac{\partial \bar{V}_i}{\partial x_j}}_{\text{Production}} - \underbrace{\beta \omega^2}_{\text{Dissipation}} + \underbrace{\frac{\partial}{\partial x_j} \left((\nu + \sigma \nu_t) \frac{\partial \omega}{\partial x_j} \right)}_{\text{Molecular diffusion + Turbulent transport + Pressure diffusion}} \quad (\text{A.19})$$

In the $k - \omega$ model, there are 5 closures coefficients that needs to be found β^* , σ^* , α , β and α . For finding them, the strategy is similar to what has been done in the Spalart-Allmaras model, set the values of these coefficients for various observed turbulence properties in various types of flows, and verify that the Equation with these coefficients verify

the different boundary conditions and is close to the empirical results. Those coefficients have been set by looking at log-law layers of free-shear layers and boundary layers. The values of those coefficients are given in Equation A.20.

$$\alpha = 5/9, \quad \beta = 3/40, \quad \beta^* = 9/100, \quad \sigma = 1/2, \quad \sigma^* = 1/2 \quad (\text{A.20})$$

A.3 k-epsilon turbulence model

On the basis the work of Chou [317], Jones and Launder [319] developed the Standard $k - \epsilon$ model. This first model was full of unknown coefficients and was applicable only to a limited range of flows. Later, Launder and Sharma [321] modified the original model for it to match with various types of flows. This last model is world widely known as the standard $k - \epsilon$ model. It is until today, the most popular and most used model in industrial and research problems dealing with turbulence. The main relations used for being able to construct the model were found through dimensional analysis, and looks similar to the ones used for the $k - \omega$ model (see Equation A.20). Equation A.21 presents the relations between ν_t , k , l and ϵ . In this Equation, a relation for determining ω is also present despite its absence in the final differential equations. In this Equation, the constant C_μ is the same as the one presented in the Prandtl-Kolmogorov equation (see Equation A.94).

$$\nu_t = C_\mu k^2 / \epsilon, \quad l = C_{mu} k^{3/2} / \epsilon, \quad \omega = \epsilon / (C_\mu k) \quad (\text{A.21})$$

The first transport equation of this model is the turbulence energy equation depicted in Equation A.97. For an easier understanding, this Equation is given back below (see Equation A.22).

$$\underbrace{\frac{\partial k}{\partial t} + \bar{V}_i \frac{\partial k}{\partial x_j}}_{\text{Convection}} = \underbrace{\frac{1}{\rho} \tau_{ij} \frac{\partial \bar{V}_i}{\partial x_j}}_{\text{Production}} - \underbrace{\epsilon}_{\text{Dissipation}} + \underbrace{\frac{\partial}{\partial x_j} \left((\nu + \nu_t / \sigma_k) \frac{\partial k}{\partial x_j} \right)}_{\text{Molecular diffusion + Turbulent transport + Pressure diffusion}} \quad (\text{A.22})$$

The second transport equation is built for the dissipation rate ϵ . On the contrary of Spalart-Allmaras and Wilcox, this equation is not built to be dimensionally homogeneous, they are derived from Equation from equation A.23. The $k - \epsilon$ model has revolutionised

the study of turbulence, and became the most popular turbulence model, because of the building of this equation. In this equation $N(v_i)$ is called the Navier-Stokes operator, it is mainly the Navier-Stokes equations written in the form $f(v_i, \nu, \rho) = 0$. From these equations, Launder *et al* showed for the first time that in turbulence modeling any quantity can be modeled through transport equations similar to Navier-Stokes equations. From the time-averaging of the Navier-Stokes equations, Launder *et al* arrived mathematically at a form where there was a balance of Convection, Production, Dissipation, Molecular diffusion and Turbulent transport for dissipation. This approach gave rise to further investigations and enhancements of various two equations models.

$$\begin{aligned}
2\nu \frac{\partial v'_i}{\partial x_j} \frac{\partial}{\partial x_j} [N(v_i)] &= 0 \\
N(v_i) &= \frac{\partial v_i}{\partial t} + v_j \left(\frac{\partial v_i}{\partial x_j} \right) + \frac{1}{\rho} \frac{\partial P}{\partial x_i} - \nu \frac{\partial^2 v_i}{\partial x_j^2} \\
N(v_i) &= 0
\end{aligned} \tag{A.23}$$

After many mathematical derivations and empirical identifications detailed in [318], the final transport equation for the dissipation has the following form (see Equation A.24). One can note that this final form is very similar to the $k - \omega$ model exposed earlier.

$$\underbrace{\frac{\partial \epsilon}{\partial t} + \bar{V}_i \frac{\partial \epsilon}{\partial x_j}}_{\text{Convection}} = \underbrace{\frac{1}{\rho} C_{\epsilon 1} \frac{\epsilon}{k} \tau_{ij} \frac{\partial \bar{V}_i}{\partial x_j}}_{\text{Production}} - \underbrace{C_{\epsilon 2} \frac{\epsilon^2}{k}}_{\text{Dissipation}} + \underbrace{\frac{\partial}{\partial x_j} \left((\nu + \nu_t / \sigma_\epsilon) \frac{\partial \epsilon}{\partial x_j} \right)}_{\text{Molecular diffusion + Turbulent transport}} \tag{A.24}$$

As it was the case for the previous models, there are now closure constants to determine for having a usable model. Those constants are 5 in number: $C_{\epsilon 1}$, $C_{\epsilon 2}$, C_μ , σ_k and σ_ϵ . As it was the case for other models, the values of these coefficients were determined by setting their values in a way that the results obtained with this model matches empirical turbulence data in various types of flows. The coefficients given in Equation A.25 were set in a similar way that the $k - \omega$ coefficients were determined: by looking at the log-law region properties of a free shear layer and a boundary layer.

$$C_{\epsilon 1} = 1.44, \quad C_{\epsilon 2} = 1.92, \quad C_\mu = 0.09, \quad \sigma_k = 1.0, \quad \sigma_\epsilon = 1.3 \tag{A.25}$$

BIBLIOGRAPHY

- [1] J Tournadre, « Anthropogenic pressure on the open ocean: The growth », *Geophysical Research Letters*, vol. 41, 22, pp. 7924–7932, 2014, ISSN: 00948276. DOI: 10.1002/2014GL061786.Marine.
- [2] IMO, « Fourth IMO Greenhouse Gas Study », *International Maritime Organization*, 11, pp. 951–952, 2021, ISSN: 1098-6596. arXiv: arXiv:1011.1669v3.
- [3] D. Rutherford, X. Mao, L. Osipova, and B. Comer, « Limiting engine power to reduce CO2 emissions from existing ships », *ICCT Working Paper 2020-01, February*, pp. 1–16, 2020.
- [4] *The Development of Foiling Sailboats | Yacht Racing Inspiration | Ancasta*. [Online]. Available: <https://ancasta.com/features-and-articles/the-development-of-foiling-sailboats/> (visited on 01/06/2022).
- [5] A. Giallanza, G. Marannano, F. Morace, and V. Ruggiero, « Numerical and experimental analysis of a high innovative hydrofoil », *International Journal on Interactive Design and Manufacturing (IJIDeM)*, 0123456789, 2019, ISSN: 1955-2505. DOI: 10.1007/s12008-019-00616-0. [Online]. Available: <https://doi.org/10.1007/s12008-019-00616-0>.
- [6] R. Vos, Z. Gürdal, and M. Abdalla, « Mechanism for warp-controlled twist of a morphing wing », *Journal of Aircraft*, vol. 47, 2, pp. 450–457, 2010, ISSN: 15333868. DOI: 10.2514/1.39328.
- [7] R. Pecora, « Morphing wing flaps for large civil aircraft: Evolution of a smart technology across the Clean Sky program », *Chinese Journal of Aeronautics*, vol. 34, 7, pp. 13–28, 2021, ISSN: 10009361. DOI: 10.1016/j.cja.2020.08.004. [Online]. Available: <https://doi.org/10.1016/j.cja.2020.08.004>.
- [8] J Vale, A. Leite, F Lau, and A. Suleman, « Aero-structural optimization and performance evaluation of a morphing wing with variable span and camber », *Journal of Intelligent Material Systems and Structures*, vol. 22, 10, pp. 1057–1073, 2011, ISSN: 1045389X. DOI: 10.1177/1045389X11416031.

-
- [9] M. A. Fatiha, B. Augier, F. Deniset, P. Casari, and J. A. Astolfi, « Morphing hydrofoil model driven by compliant composite structure and internal pressure », *Journal of Marine Science and Engineering*, vol. 7, 12, 2019, ISSN: 20771312. DOI: 10.3390/JMSE7120423.
- [10] M. Sacher, M. Durand, É. Berrini, *et al.*, « Flexible hydrofoil optimization for the 35th America's Cup with constrained EGO method », *Ocean Engineering*, vol. 157, September 2017, pp. 62–72, 2018, ISSN: 00298018. DOI: 10.1016/j.oceaneng.2018.03.047.
- [11] *Morgan Motor Company Hydrofoil on Behance*. [Online]. Available: <https://www.behance.net/gallery/57410013/Morgan-Motor-Company-Hydrofoil> (visited on 05/11/2022).
- [12] G. Wolberg, « Image morphing: A survey », *Visual Computer*, vol. 14, 8-9, pp. 360–372, 1998, ISSN: 01782789. DOI: 10.1007/s003710050148.
- [13] F. Ballarin, A. D'Amario, S. Perotto, and G. Rozza, « A POD-selective inverse distance weighting method for fast parametrized shape morphing », *International Journal for Numerical Methods in Engineering*, vol. 117, 8, pp. 860–884, 2019, ISSN: 10970207. DOI: 10.1002/nme.5982. arXiv: 1710.09243.
- [14] M. Tezzele, N. Demo, A. Mola, and G. Rozza, « PyGeM: Python Geometrical Morphing », *Software Impacts*, vol. 7, November 2020, p. 100 047, 2021, ISSN: 26659638. DOI: 10.1016/j.simpa.2020.100047. [Online]. Available: <https://doi.org/10.1016/j.simpa.2020.100047>.
- [15] F. Aimedee, G. Gogu, J. S. Dai, C. Bouzgarrou, and N. Bouton, « Systematization of morphing in reconfigurable mechanisms », *Mechanism and Machine Theory*, vol. 96, pp. 215–224, 2016, ISSN: 0094114X. DOI: 10.1016/j.mechmachtheory.2015.07.009.
- [16] P. Portela, P. Camanho, P. Weaver, and I. Bond, « Analysis of morphing, multi stable structures actuated by piezoelectric patches », *Computers and Structures*, vol. 86, 3-5, pp. 347–356, 2008, ISSN: 00457949. DOI: 10.1016/j.compstruc.2007.01.032.
- [17] S. Daynes, A. Grisdale, A. Seddon, and R. Trask, « Morphing structures using soft polymers for active deployment », *Smart Materials and Structures*, vol. 23, 1, 2014, ISSN: 09641726. DOI: 10.1088/0964-1726/23/1/012001.

-
- [18] N. Sekularac, J. Ivanovic-Sekularac, and J. Cikić-Tovarović, « Folded structures in modern architecture », *Facta universitatis - series: Architecture and Civil Engineering*, vol. 10, 1, pp. 1–16, 2012, ISSN: 0354-4605. DOI: 10.2298/fuace1201001s.
- [19] I. A. Doroftei, C. Bujoreanu, and I. Doroftei, « An Overview on the Applications of Mechanisms in Architecture. Part II: Foldable Plate Structures », *IOP Conference Series: Materials Science and Engineering*, vol. 444, 5, 2018, ISSN: 1757899X. DOI: 10.1088/1757-899X/444/5/052019.
- [20] K. Miura and M. Natori, « 2-D array experiment on board a space flyer unit », *Space Solar Power Review*, vol. 5, 4, pp. 345–356, 1985.
- [21] S. Sareh and J. Rossiter, « Kirigami artificial muscles with complex biologically inspired morphologies », *Smart Materials and Structures*, vol. 22, 1, 2013, ISSN: 09641726. DOI: 10.1088/0964-1726/22/1/014004.
- [22] S. Shian, K. Bertoldi, and D. R. Clarke, « Dielectric Elastomer Based "grippers" for Soft Robotics », *Advanced Materials*, vol. 27, 43, pp. 6814–6819, 2015, ISSN: 15214095. DOI: 10.1002/adma.201503078.
- [23] W. Crooks, G. Vukasin, M. O’Sullivan, W. Messner, and C. Rogers, « Fin Ray® effect inspired soft robotic gripper: From the robosoft grand challenge toward optimization », *Frontiers Robotics AI*, vol. 3, NOV, pp. 1–9, 2016, ISSN: 22969144. DOI: 10.3389/frobt.2016.00070.
- [24] K. R. Olympio and F. Gandhi, « Zero poisson’s ratio cellular honeycombs for flex skins undergoing one-dimensional morphing », *Journal of Intelligent Material Systems and Structures*, vol. 21, 17, pp. 1737–1753, 2010, ISSN: 1045389X. DOI: 10.1177/1045389X09355664.
- [25] W. Raither, M. Heymanns, A. Bergamini, and P. Ermanni, « Morphing wing structure with controllable twist based on adaptive bending-twist coupling », *Smart Materials and Structures*, vol. 22, 6, 2013, ISSN: 09641726. DOI: 10.1088/0964-1726/22/6/065017.
- [26] F. Hueber, G. Caponnetto, and C. Poloni, « A Passively Morphing Trailing Edge Concept for Sailing Hydrofoil », *June*, pp. 1–11, 2017. DOI: 10.20944/preprints201706.0080.v1. [Online]. Available: www.preprints.org.

-
- [27] N. Hagemeister and R. G. J. Flay, « Velocity Prediction of Wing-Sailed Hydrofoiling Catamarans », *Journal of Sailing Technology*, vol. 4, 01, pp. 66–83, 2019. DOI: 10.5957/jst.2019.4.1.66.
- [28] K. Graf, O. Freiheit, P. Schlockermann, and J. C. Mense, « VPP-Driven Sail and Foil Trim Optimization for the Olympic NACRA 17 Foiling Catamaran », *Journal of Sailing Technology*, vol. 5, 01, pp. 61–81, 2020. DOI: 10.5957/jst/2020.5.1.61.
- [29] J. J. Bertin and R. M. Cummings, *Aerodynamics for Engineers*. Pearson Education, 2013, ISBN: 9780133379235. [Online]. Available: <https://books.google.fr/books?id=CcgvAAAAQBAJ>.
- [30] *Pinterest*. [Online]. Available: <https://www.pinterest.fr/pin/241364861251989670/> (visited on 11/03/2021).
- [31] H. Sogukpinar, « Numerical simulation of 4-Digit inclined NACA 00XX airfoils to find optimum angle of attack for airplane wing », *Uludag University Journal of The Faculty of Engineering*, vol. 22, 1, pp. 169–169, 2017, ISSN: 2148-4147. DOI: 10.17482/uumfd.309470.
- [32] B. Jenett, S. Calisch, D. Cellucci, *et al.*, « Digital Morphing Wing: Active Wing Shaping Concept Using Composite Lattice-Based Cellular Structures », *Soft Robotics*, vol. 4, 1, pp. 33–48, 2017, ISSN: 21695172. DOI: 10.1089/soro.2016.0032.
- [33] K. Tuncay, « 2-D and 3-D assesment of cambered and symmetric airfoils: a CFD 2-D and 3-D assesment of cambered and symmetric airfoils », Ph.D. dissertation, 2009.
- [34] J. Winslow, H. Otsuka, B. Govindarajan, and I. Chopra, « Basic understanding of airfoil characteristics at low Reynolds numbers (104–105) », *Journal of Aircraft*, vol. 55, 3, pp. 1050–1061, 2018, ISSN: 15333868. DOI: 10.2514/1.C034415.
- [35] Y. Zhang, A. O’Neill, L. N. Cattafesta, *et al.*, « Assessment of noise reduction concepts for leading-edge slat noise », *2018 AIAA/CEAS Aeroacoustics Conference*, June, 2018. DOI: 10.2514/6.2018-3461.
- [36] D. Li, S. Zhao, A. Da Ronch, *et al.*, *A review of modelling and analysis of morphing wings*, 2018. DOI: 10.1016/j.paerosci.2018.06.002. [Online]. Available: <https://doi.org/10.1016/j.paerosci.2018.06.002>.

-
- [37] A. V. Popov, M. Labib, J. Fays, and R. M. Botez, « Closed-loop control simulations on a morphing wing », *Journal of Aircraft*, vol. 45, 5, pp. 1794–1803, 2008, ISSN: 00218669. DOI: 10.2514/1.37073.
- [38] H. P. Monner, M Kintscher, T Lorkowski, and S Storm, « Design of a smart droop nose as leading edge high lift system for transportation aircrafts », in *Collection of Technical Papers - AIAA/ASME/ASCE/AHS/ASC Structures, Structural Dynamics and Materials Conference*, 2009, pp. 1–10, ISBN: 9781563479731. DOI: 10.2514/6.2009-2128.
- [39] L. F. Campanile and D. Sachau, « Belt-rib concept: a structronic approach to variable camber », *Journal of Intelligent Material Systems and Structures*, vol. 11, 3, pp. 215–224, 2000, ISSN: 1045389X. DOI: 10.1106/6H4B-HBW3-VDJ8-NB8A.
- [40] C. Deutsch, J. Kutteneuler, and T. Melin, « Glider performance analysis and intermediate-fidelity modelling of underwater vehicles », *Ocean Engineering*, vol. 210, May, p. 107 567, 2020, ISSN: 00298018. DOI: 10.1016/j.oceaneng.2020.107567. [Online]. Available: <https://doi.org/10.1016/j.oceaneng.2020.107567>.
- [41] R. D. Vocke, C. S. Kothera, and N. M. Wereley, « Development of a quasi-static span-extending blade tip for a morphing helicopter rotor », *Journal of Aircraft*, vol. 52, 3, pp. 792–804, 2015, ISSN: 15333868. DOI: 10.2514/1.C032729.
- [42] D. Falanga, K. Kleber, S. Mintchev, D. Floreano, and D. Scaramuzza, « The Foldable Drone: A Morphing Quadrotor That Can Squeeze and Fly », *IEEE Robotics and Automation Letters*, vol. 4, 2, pp. 209–216, 2019, ISSN: 23773766. DOI: 10.1109/LRA.2018.2885575.
- [43] M. Di Luca, S Mintchev, G Heitz, F Noca, and D Floreano, « Bioinspired morphing wings for extended flight envelope and roll control of small drones », *Interface Focus*, vol. 7, 1, 2017, ISSN: 20428901. DOI: 10.1098/rsfs.2016.0092.
- [44] R. Siddall, A. Ortega Ancel, and M. Kovač, « Wind and water tunnel testing of a morphing aquatic micro air vehicle », *Interface Focus*, vol. 7, 1, 2017, ISSN: 20428901. DOI: 10.1098/rsfs.2016.0085.
- [45] *RoboSwift*. [Online]. Available: <https://www.roboswift.nl/?page=news{\&}lang=en> (visited on 11/08/2021).

-
- [46] T. Li and L. Wang, « Bending behavior of sandwich composite structures with tunable 3D-printed core materials », *Composite Structures*, vol. 175, *May*, pp. 46–57, 2017, ISSN: 02638223. DOI: 10.1016/j.compstruct.2017.05.001. [Online]. Available: <http://dx.doi.org/10.1016/j.compstruct.2017.05.001>.
- [47] D. Bornengo, F. Scarpa, and C. Remillat, « Evaluation of hexagonal chiral structure for morphine airfoil concept », *Proceedings of the Institution of Mechanical Engineers, Part G: Journal of Aerospace Engineering*, vol. 219, *3*, pp. 185–192, 2005, ISSN: 09544100. DOI: 10.1243/095441005X30216.
- [48] A. Airoidi, M. Crespi, G. Quaranti, and G. Sala, « Design of a Morphing Airfoil with Composite Chiral Structure », *Journal of Aircraft*, vol. 49, *4*, pp. 1008–1019, 2012, ISSN: 0021-8669. DOI: 10.2514/1.C031486. [Online]. Available: <http://arc.aiaa.org/doi/10.2514/1.C031486>.
- [49] Les Sables Vendée Journal, *Vendée Globe : mais au fait, c'est quoi un foil ?*, 2020. [Online]. Available: https://actu.fr/pays-de-la-loire/les-sables-d-olonne{_}85194/vendee-globe-mais-au-fait-c-est-quoi-un-foil{_}37626174.html.
- [50] TAHE, *T windfoil TWF / TAHE*, 2022. [Online]. Available: https://tahesport.com/fr{_}tahe{_}fr/t-wind-foil-one-design-107418 (visited on 02/01/2022).
- [51] *Hydrofoil water taxi Sea Bubble zero emissions concept*. [Online]. Available: <https://www.iims.org.uk/hydrofoil-water-taxi-sea-bubble-zero-emissions-concept/> (visited on 02/24/2022).
- [52] M. Grabow, V. Keryvin, A. Marchandise, *et al.*, « Influence of the manufacturing process on the interlaminar tensile strength of thick unidirectional continuous epoxy/carbon fibre composites », *Composites Part A: Applied Science and Manufacturing*, vol. 154, *November 2021*, p. 106754, 2022, ISSN: 1359835X. DOI: 10.1016/j.compositesa.2021.106754. [Online]. Available: <https://doi.org/10.1016/j.compositesa.2021.106754>.
- [53] C. Lothode, M. Durand, A. Leroyer, *et al.*, « Fluid structure interaction analysis of an hydrofoil », *Computational Methods in Marine Engineering V - Proceedings of the 5th International Conference on Computational Methods in Marine Engineering, MARINE 2013*, pp. 491–501, 2013.
- [54] S. Minko, « Configuration of the mechanical structure and flap », Ph.D. dissertation, KTH Stockholm, 2019, p. 37.

-
- [55] F. Mohammed Arab, « Contrôle actif par pression interne des performances hydrodynamiques et de l'apparition de la cavitation d'un hydrofoil composite déformable en composite », Theses, Université de Bretagne occidentale - Brest, 2020. [Online]. Available: <https://tel.archives-ouvertes.fr/tel-03457841>.
- [56] K. A. Mørch, « Cavitation inception from bubble nuclei », *Interface Focus*, vol. 5, 5, pp. 1–13, 2015, ISSN: 20428901. DOI: 10.1098/rsfs.2015.0006.
- [57] C. E. Brennen, *Cavitation and bubble dynamics*. 2013, pp. 1–249, ISBN: 9781107338760. DOI: 10.1017/CBO9781107338760.
- [58] G. Wang and M. Ostoja-Starzewski, « Large eddy simulation of a sheet/cloud cavitation on a NACA0015 hydrofoil », *Applied Mathematical Modelling*, vol. 31, 3, pp. 417–447, 2007, ISSN: 0307904X. DOI: 10.1016/j.apm.2005.11.019.
- [59] E. J. Foeth, C. W. Van Doorne, T. Van Terwisga, and B. Wieneke, « Time resolved PIV and flow visualization of 3D sheet cavitation », *Experiments in Fluids*, vol. 40, 4, pp. 503–513, 2006, ISSN: 07234864. DOI: 10.1007/s00348-005-0082-9.
- [60] R. E. A. Arndt, « Cavitation in », 2002.
- [61] Y. A. Pishchalnikov, O. A. Sapozhnikov, M. R. Bailey, *et al.*, « Cavitation bubble cluster activity in the breakage of kidney stones by lithotripter shockwaves », *Journal of Endourology*, vol. 17, 7, pp. 435–446, 2003, ISSN: 08927790. DOI: 10.1089/089277903769013568.
- [62] M. Bhatt and K. Mahesh, « LES of turbulent cavitating flows using the homogeneous mixture model », Ph.D. dissertation, 2020. DOI: 10.13140/RG.2.2.25806.69442.
- [63] E. Korkut and M. Atlar, « On the importance of the effect of turbulence in cavitation inception tests of marine propellers », *Proceedings of the Royal Society A: Mathematical, Physical and Engineering Sciences*, vol. 458, 2017, pp. 29–48, 2002, ISSN: 13645021. DOI: 10.1098/rspa.2001.0852.
- [64] C. E. Brennen, « An Introduction to Cavitation Fundamentals », *WIMRC Forum*, July, pp. 1–17, 2011. [Online]. Available: <http://authors.library.caltech.edu/28373/>.
- [65] J.-B. Leroux, J.-A. Astolfi, and J.-Y. Billard, « An experimental investigation of partial cavitation on a two dimensional hydrofoil », *4th International Symposium on Cavitation*, 1998, pp. 2–9, 2001.

-
- [66] C. Liu, Q. Yan, and H. G. Wood, « Numerical investigation of passive cavitation control using a slot on a three-dimensional hydrofoil », *International Journal of Numerical Methods for Heat and Fluid Flow*, vol. 30, 7, pp. 3585–3605, 2020, ISSN: 09615539. DOI: 10.1108/HFF-05-2019-0395.
- [67] E. Kadivar, M. V. Timoshevskiy, K. S. Pervunin, and O. el Moctar, « Cavitation control using Cylindrical Cavitating-bubble Generators (CCGs): Experiments on a benchmark CAV2003 hydrofoil », *International Journal of Multiphase Flow*, vol. 125, p. 103 186, 2020, ISSN: 03019322. DOI: 10.1016/j.ijmultiphaseflow.2019.103186. [Online]. Available: <https://doi.org/10.1016/j.ijmultiphaseflow.2019.103186>.
- [68] W. Wang, T. Tang, Q. D. Zhang, *et al.*, « Effect of water injection on the cavitation control:experiments on a NACA66 (MOD) hydrofoil », *Acta Mechanica Sinica/Lixue Xuebao*, vol. 36, 5, pp. 999–1017, 2020, ISSN: 16143116. DOI: 10.1007/s10409-020-00983-y.
- [69] A. Spadoni and M. Ruzzene, « Numerical and experimental analysis of the static compliance of chiral truss-core airfoils », *Journal of Mechanics of Materials and Structures*, vol. 2, 5, pp. 965–981, 2007.
- [70] R. D. VockeIII, C. S. Kothera, B. K. S. Woods, and N. S. Wereley, « Development and Testing of a Span-Extending Morphing Wing », *Journal of Intelligent Material Systems and Structures*, vol. 22, June, pp. 879–890, 2011. DOI: 10.1177/1045389X11411121.
- [71] H. P. Monner, « Realization of an optimized wing camber by using formvariable flap structures », *Aerospace Science and Technology*, vol. 5, 7, pp. 445–455, 2001, ISSN: 12709638. DOI: 10.1016/S1270-9638(01)01118-X.
- [72] F. Gandhi and P. Anusonti-Inthra, « Skin design studies for variable camber morphing airfoils », *Smart Materials and Structures*, vol. 17, 1, 2008, ISSN: 09641726. DOI: 10.1088/0964-1726/17/01/015025.
- [73] M. Eugeni, F. Saltari, and F. Mastroddi, « Structural damping models for passive aeroelastic control », *Aerospace Science and Technology*, vol. 118, p. 107 011, 2021, ISSN: 12709638. DOI: 10.1016/j.ast.2021.107011. [Online]. Available: <https://doi.org/10.1016/j.ast.2021.107011>.

-
- [74] H. P. Monner, E. Breitbach, T. Bein, and H. Hanselka, « Design aspects of the adaptive wing - the elastic trailing edge and the local spoiler bump », *Aeronautical Journal*, vol. 104, 1032, pp. 89–95, 2000, ISSN: 00019240.
- [75] L. D. Peel, J. Mejia, B. Narvaez, K. Thompson, and M. Lingala, « Development of a simple morphing wing using elastomeric composites as skins and actuators », *Journal of Mechanical Design, Transactions of the ASME*, vol. 131, 9, pp. 0910 031–0910 038, 2009, ISSN: 10500472. DOI: 10.1115/1.3159043.
- [76] H. Heo, J. Ju, and D. M. Kim, « Compliant cellular structures: Application to a passive morphing airfoil », *Composite Structures*, vol. 106, December, pp. 560–569, 2013, ISSN: 02638223. DOI: 10.1016/j.compstruct.2013.07.013. [Online]. Available: <http://dx.doi.org/10.1016/j.compstruct.2013.07.013>.
- [77] J. B. Bai, D. Chen, J. J. Xiong, and R. A. Shenoi, « A corrugated flexible composite skin for morphing applications », *Composites Part B: Engineering*, vol. 131, pp. 134–143, 2017, ISSN: 13598368. DOI: 10.1016/j.compositesb.2017.07.056. [Online]. Available: <https://doi.org/10.1016/j.compositesb.2017.07.056>.
- [78] D. Coutu, V. Brailovski, and P. Terriault, « Optimized design of an active extradors structure for an experimental morphing laminar wing », *Aerospace Science and Technology*, vol. 14, 7, pp. 451–458, 2010, ISSN: 12709638. DOI: 10.1016/j.ast.2010.01.009. [Online]. Available: <http://dx.doi.org/10.1016/j.ast.2010.01.009>.
- [79] S. Courchesne, A. V. Popov, and R. M. Botez, « New aeroelastic studies for a morphing wing », *48th AIAA Aerospace Sciences Meeting Including the New Horizons Forum and Aerospace Exposition, January*, pp. 1–8, 2010, ISSN: 20668201. DOI: 10.13111/2066-8201.2012.4.2.2.
- [80] H. P. Monner, J. Riemenschneider, and M. Kintscher, « Groundtest of a composite smart droop nose », *Collection of Technical Papers - AIAA/ASME/ASCE/AHS/ASC Structures, Structural Dynamics and Materials Conference, April 2012*, pp. 1–7, 2012, ISSN: 02734508. DOI: 10.2514/6.2012-1580.
- [81] M. Kintscher, J. Kirn, S. Storm, and F. Peter, « Smart Intelligent Aircraft Structures (SARISTU) », *Smart Intelligent Aircraft Structures (SARISTU)*, 2016. DOI: 10.1007/978-3-319-22413-8.

-
- [82] Y. LI, W. GE, J. ZHOU, *et al.*, « Design and experiment of concentrated flexibility-based variable camber morphing wing », *Chinese Journal of Aeronautics*, May, pp. 1–15, 2021, ISSN: 10009361. DOI: 10.1016/j.cja.2021.04.030. [Online]. Available: <https://doi.org/10.1016/j.cja.2021.04.030>.
- [83] O. J. Ohanian III, E. D. Karni, C. C. Olien, *et al.*, « Piezoelectric composite morphing control surfaces for unmanned aerial vehicles », *Sensors and Smart Structures Technologies for Civil, Mechanical, and Aerospace Systems 2011*, vol. 7981, 79815K, 2011, ISSN: 0277786X. DOI: 10.1117/12.881770.
- [84] D. Communier, R. M. Botez, and T. Wong, *Design and validation of a new morphing camber system by testing in the price-païdoussis subsonic wind tunnel*, 2020. DOI: 10.3390/aerospace7030023.
- [85] F. K. Straub, D. K. Kennedy, D. B. Domzalski, *et al.*, « Smart Material-actuated Rotor Technolnnogy - SMART », *Journal of Intelligent Material Systems and Structures*, vol. 15, 4, pp. 249–260, 2004, ISSN: 1045389X. DOI: 10.1177/1045389X04042795.
- [86] M. A. Castillo-Acero, C. Cuerno-Rejado, and M. A. Gómez-Tierno, « Morphing structure for a rudder », *Aeronautical Journal*, vol. 120, 1230, pp. 1291–1314, 2016, ISSN: 00019240. DOI: 10.1017/aer.2016.54.
- [87] A. Hasse, I. Zuest, and L. F. Campanile, « Modal synthesis of belt-rib structures », *Proceedings of the Institution of Mechanical Engineers, Part C: Journal of Mechanical Engineering Science*, vol. 225, 3, pp. 722–732, 2011, ISSN: 09544062. DOI: 10.1243/09544062JMES2329.
- [88] K. Taguchi, K. Fukunishi, S. Takazawa, Y. Sunada, and T. Imamura, « Experimental Study about the Deformation and Aerodynamic Characteristics of the Passive Morphing Airfoil * », vol. 63, 1, pp. 18–23, 2020.
- [89] J. Sun, Q. Guan, Y. Liu, and J. Leng, « Morphing aircraft based on smart materials and structures: A state-of-the-art review », *Journal of Intelligent Material Systems and Structures*, vol. 27, 17, pp. 2289–2312, 2016, ISSN: 15308138. DOI: 10.1177/1045389X16629569.
- [90] O. Ohanian, B. David, S. Taylor, *et al.*, « Piezoelectric Morphing versus Servo-Actuated MAV Control Surfaces, Part II: Flight Testing », in *51st AIAA Aerospace Sciences Meeting including the New Horizons Forum and Aerospace Exposition*.

-
2013. DOI: 10.2514/6.2013-767. [Online]. Available: <https://arc.aiaa.org/doi/abs/10.2514/6.2013-767>.
- [91] O. Bilgen, M. I. Friswell, K. B. Kochersberger, and D. J. Inman, « Surface actuated variable-camber and variable-twist morphing wings using piezocomposites », *Collection of Technical Papers - AIAA/ASME/ASCE/AHS/ASC Structures, Structural Dynamics and Materials Conference, April*, pp. 1–13, 2011, ISSN: 02734508. DOI: 10.2514/6.2011-2072.
- [92] M. Bodaghi, R. Noroozi, A. Zolfagharian, M. Fotouhi, and S. Norouzi, « 4D printing self-morphing structures », *Materials*, vol. 12, 8, 2019, ISSN: 19961944. DOI: 10.3390/ma12081353.
- [93] G. Chabaud, M. Castro, C. Denoual, and A. Le Duigou, « Hygromechanical properties of 3D printed continuous carbon and glass fibre reinforced polyamide composite for outdoor structural applications », *Additive Manufacturing*, vol. 26, January, pp. 94–105, 2019, ISSN: 22148604. DOI: 10.1016/j.addma.2019.01.005. [Online]. Available: <https://doi.org/10.1016/j.addma.2019.01.005>.
- [94] Y. C. Cheng, H. C. Lu, X. Lee, H. Zeng, and A. Priimagi, « Kirigami-Based Light-Induced Shape-Morphing and Locomotion », *Advanced Materials*, vol. 32, 7, 2020, ISSN: 15214095. DOI: 10.1002/adma.201906233.
- [95] D. Prall and R. S. Lakes, « Properties of a chiral honeycomb with a Poisson's Ratio of -1 », *Int. J. Mech. Sc.*, vol. 39, 3, pp. 305–314, 1997.
- [96] A. Spadoni and M. Ruzzene, « Static aeroelastic response of chiral-core airfoils », *Journal of Intelligent Material Systems and Structures*, vol. 18, 10, pp. 1067–1075, 2007, ISSN: 1045389X. DOI: 10.1177/1045389X06072361.
- [97] D. T. Grant, M. Abdulrahim, and R. Lind, « Design and analysis of biomimetic joints for morphing of micro air vehicles », *Bioinspiration and Biomimetics*, vol. 5, 4, 2010, ISSN: 17483182. DOI: 10.1088/1748-3182/5/4/045007.
- [98] N. Ma, X. Zhou, G. He, and J. Yu, « Design and analysis of a bat-like active morphing wing mechanism », in *Proceedings of the ASME Design Engineering Technical Conference*, vol. 5A-2016, 2016, ISBN: 9780791850152. DOI: 10.1115/DETC2016-59111.

-
- [99] K Saito, T Tachi, T Fujikawa, R Niiyama, and Y Kawahara, « Deployable Structures Inspired by Insect Wing Folding », in *Origami 7: Proceedings from the seventh meeting of Origami*, 2018, pp. 747–762.
- [100] R. E. Murray, D. A. Doman, and M. J. Pegg, « Finite element modeling and effects of material uncertainties in a composite laminate with bend-twist coupling », *Composite Structures*, vol. 121, pp. 362–376, 2015, ISSN: 02638223. DOI: 10.1016/j.compstruct.2014.11.035. [Online]. Available: <http://dx.doi.org/10.1016/j.compstruct.2014.11.035>.
- [101] R. Nicholls-Lee, S. Turnock, and S. Boyd, « Performance prediction of a free stream tidal turbine with composite bend-twist coupled blades », *2nd International Conference on Ocean Energy, October*, pp. 1–9, 2008. [Online]. Available: <http://eprints.soton.ac.uk/66466/>.
- [102] G. W. Milton, *The Theory of Composites* (Cambridge Monographs on Applied and Computational Mathematics). Cambridge University Press, 2002. DOI: 10.1017/CBO9780511613357.
- [103] R. W. Vesel and J. J. McNamara, « Performance enhancement and load reduction of a 5MW wind turbine blade », *Renewable Energy*, vol. 66, pp. 391–401, 2014, ISSN: 09601481. DOI: 10.1016/j.renene.2013.12.019. [Online]. Available: <http://dx.doi.org/10.1016/j.renene.2013.12.019>.
- [104] J. Boddapati, S. Mohanty, and R. K. Annabattula, « An analytical model for shape morphing through combined bending and twisting in piezo composites », *Mechanics of Materials*, vol. 144, November 2019, p. 103 350, 2020, ISSN: 01676636. DOI: 10.1016/j.mechmat.2020.103350. [Online]. Available: <https://doi.org/10.1016/j.mechmat.2020.103350>.
- [105] S. M. Smith, J. A. Venning, D. R. Giosio, P. A. Brandner, B. W. Pearce, and Y. L. Young, « Cloud Cavitation Behavior on a Hydrofoil Due to Fluid-Structure Interaction », *Journal of Fluids Engineering*, vol. 141, 4, 2019, ISSN: 0098-2202. DOI: 10.1115/1.4042067. [Online]. Available: <https://doi.org/10.1115/1.4042067>.
- [106] C.-S. Lee, B.-K. Ahn, J.-M. Han, and J.-H. Kim, « Propeller tip vortex cavitation control and induced noise suppression by water injection », *Journal of Marine Science and Technology*, vol. 23, 3, pp. 453–463, 2018, ISSN: 1437-8213. DOI: 10.1007/s00773-017-0484-4. [Online]. Available: <https://doi.org/10.1007/s00773-017-0484-4>.

-
- [107] L. Pernod, A. Ducoin, H. Le Sourné, J. A. Astolfi, and P. Casari, « Experimental and numerical investigation of the fluid-structure interaction on a flexible composite hydrofoil under viscous flows », *Ocean Engineering*, vol. 194, *October*, 2019, ISSN: 00298018. DOI: 10.1016/j.oceaneng.2019.106647.
- [108] L. J. Gibson and M. F. Ashby, « Cellular Solids: Structure and Properties », 1997. DOI: 10.1017/CBO9781139878326. [Online]. Available: <https://www.cambridge.org/core/product/BC25789552BAA8E3CAD5E1D105612AB5>.
- [109] D. Bhate, C. Penick, L. Ferry, and C. Lee, « Classification and Selection of Cellular Materials in Mechanical Design: Engineering and Biomimetic Approaches », *Designs*, vol. 3, 1, p. 19, 2019, ISSN: 2411-9660. DOI: 10.3390/designs3010019.
- [110] R. L. Lincoln, F. Scarpa, V. P. Ting, and R. S. Trask, « Multifunctional composites: a metamaterial perspective », *Multifunctional Materials*, vol. 2, 4, p. 043 001, 2019. DOI: 10.1088/2399-7532/ab5242.
- [111] G. Rosi and N. Auffray, « Continuum modelling of frequency dependent acoustic beam focussing and steering in hexagonal lattices », *European Journal of Mechanics, A/Solids*, vol. 77, *June*, p. 103 803, 2019, ISSN: 09977538. DOI: 10.1016/j.euromechsol.2019.103803. [Online]. Available: <https://doi.org/10.1016/j.euromechsol.2019.103803>.
- [112] P. Bollen, N. Quiévy, I. Huynen, *et al.*, « Multifunctional architected materials for electromagnetic absorption », *Scripta Materialia*, vol. 68, 1, pp. 50–54, 2013, ISSN: 13596462. DOI: 10.1016/j.scriptamat.2012.05.011.
- [113] J. Ma, X. Wang, W. Cao, *et al.*, « A facile fabrication and highly tunable microwave absorption of 3D flower-like Co₃O₄-rGO hybrid-architectures », *Chemical Engineering Journal*, vol. 339, *February*, pp. 487–498, 2018, ISSN: 13858947. DOI: 10.1016/j.cej.2018.01.152. [Online]. Available: <https://doi.org/10.1016/j.cej.2018.01.152>.
- [114] R. M. Neville, F. Scarpa, and A. Pirrera, « Shape morphing Kirigami mechanical metamaterials », *Scientific Reports*, vol. 6, *August 2015*, pp. 1–12, 2016, ISSN: 20452322. DOI: 10.1038/srep31067.
- [115] H. M. Kolken and A. A. Zadpoor, *Auxetic mechanical metamaterials*, 2017. DOI: 10.1039/c6ra27333e.

-
- [116] X. Yu, J. Zhou, H. Liang, Z. Jiang, and L. Wu, « Mechanical metamaterials associated with stiffness, rigidity and compressibility: A brief review », *Progress in Materials Science*, vol. 94, pp. 114–173, 2018, ISSN: 00796425. DOI: 10.1016/j.pmatsci.2017.12.003. [Online]. Available: <https://doi.org/10.1016/j.pmatsci.2017.12.003>.
- [117] A. Krzyzak, M. Mazur, M. Gajewski, K. Drozd, A. Komorek, and P. Przybyłek, « Sandwich Structured Composites for Aeronautics: Methods of Manufacturing Affecting Some Mechanical Properties », *International Journal of Aerospace Engineering*, vol. 2016, 2016, ISSN: 16875974. DOI: 10.1155/2016/7816912.
- [118] A. P. Mouritz, E. Gellert, P. Burchill, and K. Challis, « Review of advanced composite structures for naval ships and submarines », *Composite Structures*, vol. 53, 1, pp. 21–42, 2001, ISSN: 02638223. DOI: 10.1016/S0263-8223(00)00175-6.
- [119] H. Toftegaard and A. Lystrup, « Design and test of lightweight sandwich T-joint for naval ships », *Composites Part A: Applied Science and Manufacturing*, vol. 36, 8, pp. 1055–1065, 2005, ISSN: 1359835X. DOI: 10.1016/j.compositesa.2004.10.031.
- [120] C. A. Ulven and U. K. Vaidya, « Post-fire low velocity impact response of marine grade sandwich composites », *Composites Part A: Applied Science and Manufacturing*, vol. 37, 7, pp. 997–1004, 2006, ISSN: 1359835X. DOI: 10.1016/j.compositesa.2005.03.001.
- [121] A. Launay, V. Keryvin, J. C. Grandidier, P. Y. Mechin, and R. Balze, « Design of a set-up for measuring the residual compressive strength after high load and high cycle compression fatigue on CFRP », *Composite Structures*, vol. 286, January, p. 115 294, 2022, ISSN: 02638223. DOI: 10.1016/j.compstruct.2022.115294. [Online]. Available: <https://doi.org/10.1016/j.compstruct.2022.115294>.
- [122] J. M. Patel and B. A. Modi, « Stiffness and thermal analysis of doubly curve sandwich panel for an automobile application », *Procedia Engineering*, vol. 51, *NViCONE 2012*, pp. 655–664, 2013, ISSN: 18777058. DOI: 10.1016/j.proeng.2013.01.093. [Online]. Available: <http://dx.doi.org/10.1016/j.proeng.2013.01.093>.
- [123] A. Sunanda and M. S. Nayak, « Analysis of NACA 2412 for Automobile Rear Spoiler Using Composite Material », *International Journal of Emerging Technology and Advanced Engineering*, vol. 3, 1, pp. 236–242, 2013.

-
- [124] N. Fatima and G. Newaz, « Mechanical And Electro-Chemical Investigation Of Carbon Farbric/epoxy And Aluminum Foam Sandwich Composite Beams », Ph.D. dissertation, 2013. DOI: 10.13140/RG.2.2.33666.71365.
- [125] M. Montemurro, A. Catapano, and D. Doroszewski, « A multi-scale approach for the simultaneous shape and material optimisation of sandwich panels with cellular core », *Composites Part B: Engineering*, vol. 91, pp. 458–472, 2016, ISSN: 13598368. DOI: 10.1016/j.compositesb.2016.01.030. [Online]. Available: <http://dx.doi.org/10.1016/j.compositesb.2016.01.030>.
- [126] A. Catapano and M. Montemurro, « A multi-scale approach for the optimum design of sandwich plates with honeycomb core. Part II: The optimisation strategy », *Composite Structures*, vol. 118, 1, pp. 677–690, 2014, ISSN: 02638223. DOI: 10.1016/j.compstruct.2014.07.058. [Online]. Available: <http://dx.doi.org/10.1016/j.compstruct.2014.07.058>.
- [127] J. Zhang and J. Yanagimoto, « Design of bendable sandwich sheets with 3D printed CFRP cores via multi-stage topology optimization », *COMPOSITE STRUCTURE*, p. 115 372, 2022, ISSN: 0263-8223. DOI: 10.1016/j.compstruct.2022.115372. [Online]. Available: <https://doi.org/10.1016/j.compstruct.2022.115372>.
- [128] W. Hou, Y. Shen, K. Jiang, and C. Wang, « Study on mechanical properties of carbon fiber honeycomb curved sandwich structure and its application in engine hood », *Composite Structures*, vol. 286, *April 2021*, p. 115 302, 2022, ISSN: 02638223. DOI: 10.1016/j.compstruct.2022.115302. [Online]. Available: <https://doi.org/10.1016/j.compstruct.2022.115302>.
- [129] J. Zhang, W. Huang, F. Miao, J. Du, and H. Sun, « Plastic behavior of sandwich beams with fiber metal laminate face-sheets and metal foam core: Combined local denting and overall deformation », *Thin-Walled Structures*, vol. 173, *December 2021*, p. 108 973, 2022, ISSN: 02638231. DOI: 10.1016/j.tws.2022.108973. [Online]. Available: <https://doi.org/10.1016/j.tws.2022.108973>.
- [130] M. Ma, W. Yao, W. Jiang, *et al.*, « Fatigue of composite honeycomb sandwich panels under random vibration load », *Composite Structures*, vol. 286, *December 2021*, p. 115 296, 2022, ISSN: 02638223. DOI: 10.1016/j.compstruct.2022.115296. [Online]. Available: <https://doi.org/10.1016/j.compstruct.2022.115296>.

-
- [131] H. Qin, G. Sanjaya, and Y. Tang, « Research on the distribution and evolution of weathering failure of stacked wall and sandwich wall under freeze–thaw cycles », *Engineering Failure Analysis*, vol. 135, *October 2021*, p. 106–109, 2022, ISSN: 13506307. DOI: 10.1016/j.engfailanal.2022.106109. [Online]. Available: <https://doi.org/10.1016/j.engfailanal.2022.106109>.
- [132] S. Hou, S. Zhao, L. Ren, X. Han, and Q. Li, « Crashworthiness optimization of corrugated sandwich panels », *Materials and Design*, vol. 51, *October*, pp. 1071–1084, 2013, ISSN: 18734197. DOI: 10.1016/j.matdes.2013.04.086. [Online]. Available: <http://dx.doi.org/10.1016/j.matdes.2013.04.086>.
- [133] L. Yang, O. L. A. Harrysson, D. Cormier, H. A. West, C. M. Park, and K. Peters, « Design Of Auxetic Sandwich Panels For Structural Applications Design Of Auxetic Sandwich Panels For Structural Applications », 2013.
- [134] H. Yazdani Sarvestani, A. H. Akbarzadeh, A. Mirbolghasemi, and K. Hermenean, « 3D printed meta-sandwich structures: Failure mechanism, energy absorption and multi-hit capability », *Materials and Design*, vol. 160, pp. 179–193, 2018, ISSN: 18734197. DOI: 10.1016/j.matdes.2018.08.061. [Online]. Available: <https://doi.org/10.1016/j.matdes.2018.08.061>.
- [135] S. Hou, T. Li, Z. Jia, and L. Wang, « Mechanical properties of sandwich composites with 3d-printed auxetic and non-auxetic lattice cores under low velocity impact », *Materials and Design*, vol. 160, *December*, pp. 1305–1321, 2018, ISSN: 18734197. DOI: 10.1016/j.matdes.2018.11.002. [Online]. Available: <https://doi.org/10.1016/j.matdes.2018.11.002>.
- [136] C. Combescure, R. S. Elliott, and N. Triantafyllidis, « Deformation patterns and their stability in finitely strained circular cell honeycombs », *Journal of the Mechanics and Physics of Solids*, vol. 142, p. 103976, 2020, ISSN: 00225096. DOI: 10.1016/j.jmps.2020.103976. [Online]. Available: <https://doi.org/10.1016/j.jmps.2020.103976>.
- [137] Z. Vangelatos, G. X. Gu, and C. P. Grigoropoulos, « Architected metamaterials with tailored 3D buckling mechanisms at the microscale », *Extreme Mechanics Letters*, vol. 33, p. 100580, 2019, ISSN: 23524316. DOI: 10.1016/j.eml.2019.100580. [Online]. Available: <https://doi.org/10.1016/j.eml.2019.100580>.

-
- [138] W. Liu, H. Li, J. Zhang, and Y. Bai, « In-plane mechanics of a novel cellular structure for multiple morphing applications », *Composite Structures*, vol. 207, *September 2018*, pp. 598–611, 2019, ISSN: 02638223. DOI: 10.1016/j.compstruct.2018.08.096. [Online]. Available: <https://doi.org/10.1016/j.compstruct.2018.08.096>.
- [139] J. Qiu, C. Wang, C. Huang, H. Ji, and Z. Xu, « Smart skin and actuators for morphing structures », *Procedia IUTAM*, vol. 10, pp. 427–441, 2014, ISSN: 22109838. DOI: 10.1016/j.piutam.2014.01.037. [Online]. Available: <http://dx.doi.org/10.1016/j.piutam.2014.01.037>.
- [140] H. V. Wang and D. W. Rosen, « Detc2006-99661 an Automated Design Synthesis Method for Compliant Mechanisms With », pp. 1–9, 2006.
- [141] D. M. Elzey, A. Y. N. Sofla, and H. N. G. Wadley, « A bio-inspired high-authority actuator for shape morphing structures », *Smart Structures and Materials 2003: Active Materials: Behavior and Mechanics*, vol. 5053, p. 92, 2003, ISSN: 0277786X. DOI: 10.1117/12.484745.
- [142] M. H. Fu, O. T. Xu, L. L. Hu, and T. X. Yu, « Nonlinear shear modulus of re-entrant hexagonal honeycombs under large deformation », *International Journal of Solids and Structures*, vol. 80, pp. 284–296, 2016, ISSN: 00207683. DOI: 10.1016/j.ijsolstr.2015.11.015.
- [143] J. Yvonnet, *Computational Homogenization of Heterogeneous Materials with Finite Elements*, 1st ed., Springer, Ed. Springer, Cham, 2019, p. 223. DOI: <https://doi.org/10.1007/978-3-030-18383-7>.
- [144] C. Czech, « Design of Meta-Materials Outside the Homogenization Limit Using Multiscale Analysis and Topology Optimization », Ph.D. dissertation, 2012, pp. 10–13, 112–116.
- [145] J. Dirrenberger, S. Forest, D. Jeulin, and C. Colin, « Homogenization of periodic auxetic materials », *Procedia Engineering*, vol. 10, pp. 1847–1852, 2011, ISSN: 18777058. DOI: 10.1016/j.proeng.2011.04.307.
- [146] A. Bacigalupo and L. Gambarotta, « Homogenization of periodic hexa- and tetra-chiral cellular solids », *Composite Structures*, vol. 116, 1, pp. 461–476, 2014, ISSN: 02638223. DOI: 10.1016/j.compstruct.2014.05.033.
- [147] *Micromechanics Plugin for Abaqus*. [Online]. Available: <https://www.linkedin.com/pulse/micromechanics-plugin-abaqus-ross-mclendon> (visited on 02/17/2022).

-
- [148] M. M. S. Al-Hamzawi and S. Szávai, « Optimization of weight and elastic properties for unidirectional glass fiber reinforced composites », *Multidiszciplináris tudományok*, vol. 11, 5, pp. 206–214, 2021, ISSN: 20629737. DOI: 10.35925/j.multi.2021.5.21.
- [149] K. Yang, Q. Jiang, X. Ma, and X. Xia, « Simulation of 3D Cutting Process of SiCp/Al Composites », vol. 166, *Amcce*, pp. 510–513, 2018. DOI: 10.2991/amcce-18.2018.88.
- [150] A. R. Zamani, L. Sanguigno, and A. R. Maligno, « Finite Element Modelling of a 3D Woven Composite for Automotive Applications », *International Journal of Mechanical and Materials Engineering*, vol. 14, 11, pp. 546–552, 2020. [Online]. Available: <https://publications.waset.org/vol/167>.
- [151] A. Catapano and M. Montemurro, « A multi-scale approach for the optimum design of sandwich plates with honeycomb core. Part I: Homogenisation of core properties », *Composite Structures*, vol. 118, 1, pp. 664–676, 2014, ISSN: 02638223. DOI: 10.1016/j.compstruct.2014.07.057. [Online]. Available: <http://dx.doi.org/10.1016/j.compstruct.2014.07.057>.
- [152] O. Al-Ketan, R. Rowshan, and R. K. Abu Al-Rub, « Topology-mechanical property relationship of 3D printed strut, skeletal, and sheet based periodic metallic cellular materials », *Additive Manufacturing*, vol. 19, pp. 167–183, 2018, ISSN: 22148604. DOI: 10.1016/j.addma.2017.12.006. [Online]. Available: <http://dx.doi.org/10.1016/j.addma.2017.12.006>.
- [153] C. B. Williams, J. K. Cochran, and D. W. Rosen, « Additive manufacturing of metallic cellular materials via three-dimensional printing », *International Journal of Advanced Manufacturing Technology*, vol. 53, 1-4, pp. 231–239, 2011, ISSN: 02683768. DOI: 10.1007/s00170-010-2812-2.
- [154] M. Dallago, S. Raghavendra, V. Luchin, G. Zappini, D. Pasini, and M. Benedetti, « The role of node fillet, unit-cell size and strut orientation on the fatigue strength of Ti-6Al-4V lattice materials additively manufactured via laser powder bed fusion », *International Journal of Fatigue*, vol. 142, *September 2020*, p. 105946, 2021, ISSN: 01421123. DOI: 10.1016/j.ijfatigue.2020.105946. [Online]. Available: <https://doi.org/10.1016/j.ijfatigue.2020.105946>.

-
- [155] A. Aversa, G. Marchese, M. Lorusso, *et al.*, « Microstructural and Mechanical Characterization of Aluminum Matrix Composites Produced by Laser Powder Bed Fusion », 2017. DOI: 10.1002/adem.201700180. [Online]. Available: <http://www.aem-journal.com>.
- [156] Z. Hou, X. Tian, J. Zhang, *et al.*, « Design and 3D printing of continuous fiber reinforced heterogeneous composites », *Composite Structures*, vol. 237, August 2019, p. 111 945, 2020, ISSN: 02638223. DOI: 10.1016/j.compstruct.2020.111945. [Online]. Available: <https://doi.org/10.1016/j.compstruct.2020.111945>.
- [157] S. M. Kabir, K. Mathur, and A. F. M. Seyam, « A critical review on 3D printed continuous fiber-reinforced composites: History, mechanism, materials and properties », *Composite Structures*, vol. 232, August 2019, p. 111 476, 2020, ISSN: 02638223. DOI: 10.1016/j.compstruct.2019.111476. [Online]. Available: <https://doi.org/10.1016/j.compstruct.2019.111476>.
- [158] J.-p. Carmona, « Mémoire de maîtrise », Ph.D. dissertation, Ecole polytechnique de Montreal, 2016, p. 134.
- [159] S Rohde, J Cantrell, A Jerez, *et al.*, « Experimental Characterization of the Shear Properties of 3D-Printed ABS and Polycarbonate Parts », *Experimental Mechanics*, vol. 58, 6, pp. 871–884, 2018, ISSN: 17412765. DOI: 10.1007/s11340-017-0343-6.
- [160] N. A. B. Sukindar, M. K. A. M. A. Bin, B. T. Hang Tuah Bin, C. N. A. J. Binti, and M. I. S. I. Bin, « Analysis on the impact process parameters on tensile strength using 3d printer repetier-host software », *ARPJN Journal of Engineering and Applied Sciences*, vol. 12, 10, pp. 3341–3346, 2017, ISSN: 18196608.
- [161] A. R. Torrado Perez, D. A. Roberson, and R. B Wicker, *Fracture surface analysis of 3D-printed tensile specimens of novel ABS-based materials*, 2014. DOI: 10.1007/s11668-014-9803-9.
- [162] S. Khan, K. Joshi, and S. Deshmukh, « A comprehensive review on effect of printing parameters on mechanical properties of FDM printed parts », *Materials Today: Proceedings*, vol. 50, pp. 2119–2127, 2022, ISSN: 22147853. DOI: 10.1016/j.matpr.2021.09.433. [Online]. Available: <https://doi.org/10.1016/j.matpr.2021.09.433>.
- [163] K. V. Wong and A. Hernandez, « A Review of Additive Manufacturing », *ISRN Mechanical Engineering*, vol. 2012, pp. 1–10, 2012, ISSN: 2090-5130. DOI: 10.5402/2012/208760.

-
- [164] J. Dulieu-Barton and M. Fulton, « Mechanical Properties of a Typical Stereolithography Resin », *Strain*, vol. 36, pp. 81–87, 2000. DOI: 10.1111/j.1475-1305.2000.tb01177.x.
- [165] K. Szykiedans and W. Credo, « Mechanical properties of FDM and SLA low-cost 3-D prints », *Procedia Engineering*, vol. 136, pp. 257–262, 2016, ISSN: 18777058. DOI: 10.1016/j.proeng.2016.01.207. [Online]. Available: <http://dx.doi.org/10.1016/j.proeng.2016.01.207>.
- [166] B. Vieira Magaldi, M. De Oliveira Da Costa, R. M. D. S. Thiré, and A. C. ARAUJO, « Comparison of the porosity of scaffolds manufactured by two additive manufacturing technologies: SLA and FDM », in *24th International Congress of Mechanical Engineering*, Curitiba, Brazil, 2018. [Online]. Available: <https://hal.archives-ouvertes.fr/hal-03226784>.
- [167] T. Csenge and K. Norbert Kovács, « Characterization of short fiber-reinforced polylactic acid composites produced with Fused Filament Fabrication (FFF) », *IOP Conference Series: Materials Science and Engineering*, vol. 903, 1, 2020, ISSN: 1757899X. DOI: 10.1088/1757-899X/903/1/012031.
- [168] Y. Sano, R. Matsuzaki, M. Ueda, A. Todoroki, and Y. Hirano, « 3D printing of discontinuous and continuous fibre composites using stereolithography », *Additive Manufacturing*, vol. 24, October, pp. 521–527, 2018, ISSN: 22148604. DOI: 10.1016/j.addma.2018.10.033. [Online]. Available: <https://doi.org/10.1016/j.addma.2018.10.033>.
- [169] H. Eng, S. Maleksaeedi, S. Yu, *et al.*, « 3D Stereolithography of Polymer Composites Reinforced with Orientated Nanoclay », *Procedia Engineering*, vol. 216, 2017, pp. 1–7, 2017, ISSN: 18777058. DOI: 10.1016/j.proeng.2018.02.080.
- [170] A. Adumitroaie, F. Antonov, A. Khaziev, A. Azarov, M. Golubev, and V. V. Vasiliev, « Novel continuous fiber bi-matrix composite 3-D printing technology », *Materials*, vol. 12, 18, pp. 1–10, 2019, ISSN: 19961944. DOI: 10.3390/ma12183011.
- [171] S. Kasmi, G. Ginoux, S. Allaoui, and S. Alix, « Investigation of 3D printing strategy on the mechanical performance of coextruded continuous carbon fiber reinforced PETG », *Journal of Applied Polymer Science*, vol. 138, 37, pp. 1–15, 2021, ISSN: 10974628. DOI: 10.1002/app.50955.

-
- [172] A. V. Azarov, F. K. Antonov, V. V. Vasil'ev, *et al.*, « Development of a two-matrix composite material fabricated by 3D printing », *Polymer Science - Series D*, vol. 10, 1, pp. 87–90, 2017, ISSN: 19954220. DOI: 10.1134/S1995421217010026.
- [173] M. Dryzek and E. Dryzek, « Positron annihilation lifetime spectroscopy of ABS objects manufactured by fused deposition modelling », *Acta Physica Polonica A*, vol. 132, 5, pp. 1506–1508, 2017, ISSN: 1898794X. DOI: 10.12693/APhysPolA.132.1506.
- [174] G. Chabaud, « 3D and 4D printing of high performance continuous synthetic and natural fibre composites for structural and morphing applications », Theses, Université de Bretagne Sud, 2020. [Online]. Available: <https://tel.archives-ouvertes.fr/tel-03217124>.
- [175] D. D. Hernandez, « Factors affecting dimensional precision of consumer 3D printing », *International Journal of Aviation, Aeronautics, and Aerospace*, vol. 2, 4, 2015, ISSN: 23746793. DOI: 10.15394/ijaaa.2015.1085.
- [176] K. G. Christiyan, U. Chandrasekhar, and K. Venkateswarlu, « A study on the influence of process parameters on the Mechanical Properties of 3D printed ABS composite », *IOP Conference Series: Materials Science and Engineering*, vol. 114, 1, 2016, ISSN: 1757899X. DOI: 10.1088/1757-899X/114/1/012109.
- [177] O. S. Es-Said, J. Foyos, R. Noorani, M. Mendelson, R. Marloth, and B. A. Pregger, « Effect of layer orientation on mechanical properties of rapid prototyped samples », *Materials and Manufacturing Processes*, vol. 15, 1, pp. 107–122, 2000, ISSN: 10426914. DOI: 10.1080/10426910008912976.
- [178] M. S. Alsoofi and A. E. Elsayed, « Warping deformation of desktop 3D printed parts manufactured by open source fused deposition modeling (FDM) system », *International Journal of Mechanical and Mechatronics Engineering*, vol. 17, 4, pp. 7–16, 2017, ISSN: 2077124X.
- [179] S. S. Haque, « Minimizing Stringing Issues In FDM Printing », *December*, 2020. [Online]. Available: <https://www.researchgate.net/publication/346563712>.
- [180] *Print Quality Guide*. [Online]. Available: <https://www.simplify3d.com/support/print-quality-troubleshooting/> (visited on 03/03/2022).
- [181] *Some musings on retracts / Sublime Layers*. [Online]. Available: <https://www.sublimelayers.com/2016/10/some-musings-on-retracts.html> (visited on 05/18/2022).

-
- [182] *Selecting the optimal shell and infill parameters for FDM 3D printing | Hubs*. [Online]. Available: <https://www.hubs.com/knowledge-base/selecting-optimal-shell-and-infill-parameters-fdm-3d-printing/> (visited on 05/18/2022).
- [183] *The DIY 3D Printer Life – Part 1: Cooling – Norwegian Creations*. [Online]. Available: <https://www.norwegiancreations.com/2017/03/the-diy-3dprinter-life-part-1cooling/> (visited on 05/18/2022).
- [184] *Best Layer Height for 3D Printing | Quality, Speed, etc.* [Online]. Available: <https://the3dprinterbee.com/best-layer-height-3d-printing/> (visited on 05/18/2022).
- [185] *The importance of the type of infill in 3D printing*. [Online]. Available: https://filament2print.com/gb/blog/71{_}importance-infill-3d-printing.html (visited on 05/18/2022).
- [186] B. Msallem, S. Neha, C. Shuaishuai, F. S. Halbeisen, and F. M. T. Hans-Florian Zeilhofer, « Evaluation of the Dimensional Accuracy of 3D-Printed Anatomical Mandibular Models Using », *Journal of Clinical Medicine*, vol. 9, 3, pp. 1–18, 2020.
- [187] R. Quelho de Macedo, R. T. L. Ferreira, and K. Jayachandran, « Determination of mechanical properties of FFF 3D printed material by assessing void volume fraction, cooling rate and residual thermal stresses », *Rapid Prototyping Journal*, vol. 25, 10, pp. 1661–1683, 2019, ISSN: 13552546. DOI: 10.1108/RPJ-08-2018-0192.
- [188] S. H. Ahn, M. Montero, D. Odell, S. Roundy, and P. K. Wright, « Anisotropic material properties of fused deposition modeling ABS », *Rapid Prototyping Journal*, vol. 8, 4, pp. 248–257, 2002, ISSN: 13552546. DOI: 10.1108/13552540210441166.
- [189] J. J. Laureto and J. M. Pearce, « Anisotropic mechanical property variance between ASTM D638-14 type i and type iv fused filament fabricated specimens », *Polymer Testing*, vol. 68, April, pp. 294–301, 2018, ISSN: 01429418. DOI: 10.1016/j.polymeresting.2018.04.029. [Online]. Available: <https://doi.org/10.1016/j.polymeresting.2018.04.029>.
- [190] R. Zou, Y. Xia, S. Liu, *et al.*, « Isotropic and anisotropic elasticity and yielding of 3D printed material », *Composites Part B: Engineering*, vol. 99, pp. 506–513, 2016, ISSN: 13598368. DOI: 10.1016/j.compositesb.2016.06.009. [Online]. Available: <http://dx.doi.org/10.1016/j.compositesb.2016.06.009>.

-
- [191] M. Fernandez-Vicente, W. Calle, S. Ferrandiz, and A. Conejero, « Effect of Infill Parameters on Tensile Mechanical Behavior in Desktop 3D Printing », *3D Printing and Additive Manufacturing*, vol. 3, 3, pp. 183–192, 2016, ISSN: 23297670. DOI: 10.1089/3dp.2015.0036.
- [192] I. J. Solomon, P. Sevel, and J. Gunasekaran, « A review on the various processing parameters in FDM », *Materials Today: Proceedings*, vol. 37, Part 2, pp. 509–514, 2020, ISSN: 22147853. DOI: 10.1016/j.matpr.2020.05.484. [Online]. Available: <https://doi.org/10.1016/j.matpr.2020.05.484>.
- [193] C. K. Yeoh, C. S. Cheah, R. Pushpanathan, C. C. Song, M. A. Tan, and P. L. Teh, « Effect of infill pattern on mechanical properties of 3D printed PLA and cPLA », *IOP Conference Series: Materials Science and Engineering*, vol. 957, 1, 2020, ISSN: 1757899X. DOI: 10.1088/1757-899X/957/1/012064.
- [194] B. M. Tymrak, M. Kreiger, and J. M. Pearce, « Mechanical properties of components fabricated with open-source 3-D printers under realistic environmental conditions », *Materials and Design*, vol. 58, pp. 242–246, 2014, ISSN: 18734197. DOI: 10.1016/j.matdes.2014.02.038. [Online]. Available: <http://dx.doi.org/10.1016/j.matdes.2014.02.038>.
- [195] T. Letcher, R. Behzad, and J. Sina, « Experimental Study of Mechanical Properties of Additively », *Proceedings of the ASME 2015 International Mechanical Engineering Congress and Exposition IMECE2015*, pp. 1–8, 2015.
- [196] A. W. Fatimatuzahraa, B. Farahaina, and W. A. Yusoff, « The effect of employing different raster orientations on the mechanical properties and microstructure of Fused Deposition Modeling parts », *ISBEIA 2011 - 2011 IEEE Symposium on Business, Engineering and Industrial Applications*, pp. 22–27, 2011. DOI: 10.1109/ISBEIA.2011.6088811.
- [197] J. F. Rodriguez, J. P. Thomas, J. E. Renaud, and Â. F. Rodrõ, « Mechanical behavior of acrylonitrile butadiene styrene (ABS) fused deposition materials . Experimental investigation », vol. 7, 3, pp. 148–158, 2001.
- [198] C. O. Balderrama-Armendariz, E. MacDonald, D. A. Roberson, *et al.*, « Folding behavior of thermoplastic hinges fabricated with polymer extrusion additive manufacturing », *International Journal of Advanced Manufacturing Technology*, vol. 105, 1-4, pp. 233–245, 2019, ISSN: 14333015. DOI: 10.1007/s00170-019-04196-x.

-
- [199] S. Phani, R. Butler, S. Habgood, and C. Bowen, « Analysis of Wing Morphing via Frame Buckling », *February 2014*, 2008. DOI: 10.2514/6.2008-1792.
- [200] *Le matériau Ultimaker CPE : des impressions robustes et aux dimensions précises*. [Online]. Available: <https://ultimaker.com/fr/materials/cpe> (visited on 05/18/2022).
- [201] J. C. Maxwell, « On the calculation of the equilibrium and stiffness of frames », *The London, Edinburgh, and Dublin Philosophical Magazine and Journal of Science*, vol. 27, 182, pp. 294–299, 1864.
- [202] A. Lanzotti, M. Grasso, G. Staiano, and M. Martorelli, « The impact of process parameters on mechanical properties of parts fabricated in PLA with an open-source 3-D printer », *Rapid Prototyping Journal*, vol. 21, 5, pp. 604–617, 2015, ISSN: 13552546. DOI: 10.1108/RPJ-09-2014-0135.
- [203] A. L. Slonov, A. A. Khashirov, A. A. Zhansitov, E. V. Rzhetskaya, and S. Y. Khashirova, « The influence of the 3D-printing technology on the physical and mechanical properties of polyphenylene sulfone », *Rapid Prototyping Journal*, vol. 24, 7, pp. 1124–1130, 2018, ISSN: 13552546. DOI: 10.1108/RPJ-03-2017-0045.
- [204] M. R. Khosravani and T. Reinicke, « Effects of raster layup and printing speed on strength of 3D-printed structural components », *Procedia Structural Integrity*, vol. 28, pp. 720–725, 2020, ISSN: 24523216. DOI: 10.1016/j.prostr.2020.10.083. [Online]. Available: <https://doi.org/10.1016/j.prostr.2020.10.083>.
- [205] E. Cuan-Urquizo, E. Barocio, V. Tejada-Ortigoza, R. B. Pipes, C. A. Rodriguez, and A. Roman-Flores, « Characterization of the mechanical properties of FFF structures and materials: A review on the experimental, computational and theoretical approaches », *Materials*, vol. 16, 6, 2019, ISSN: 19961944. DOI: 10.3390/ma12060895.
- [206] I. Durgun and R. Ertan, « Experimental investigation of FDM process for improvement of mechanical properties and production cost », *Rapid Prototyping Journal*, vol. 20, 3, pp. 228–235, 2014, ISSN: 13552546. DOI: 10.1108/RPJ-10-2012-0091.
- [207] A. Spadoni and M. Ruzzene, « Static aeroelastic behavior of a chiral-core airfoil objectives & motivation », in *16th International Conference on Adaptive Structures Technologies (ICAST)*, 2005, pp. 1–23, ISBN: 1932078576.

-
- [208] C. W. Smith, J. N. Grima, and K. E. Evans, « Novel mechanism for generating auxetic behaviour in reticulated foams: Missing rib foam model », *Acta Materialia*, vol. 48, 17, pp. 4349–4356, 2000, ISSN: 13596454. DOI: 10.1016/S1359-6454(00)00269-X.
- [209] J. X. Qiao and C. Q. Chen, « Impact resistance of uniform and functionally graded auxetic double arrowhead honeycombs », *International Journal of Impact Engineering*, vol. 83, pp. 47–58, 2015, ISSN: 0734743X. DOI: 10.1016/j.ijimpeng.2015.04.005. [Online]. Available: <http://dx.doi.org/10.1016/j.ijimpeng.2015.04.005>.
- [210] X. T. Wang, B. Wang, Z. H. Wen, and L. Ma, « Fabrication and mechanical properties of CFRP composite three-dimensional double-arrow-head auxetic structures », *Composites Science and Technology*, vol. 164, May, pp. 92–102, 2018, ISSN: 02663538. DOI: 10.1016/j.compscitech.2018.05.014.
- [211] P. Bettini, A. Airoidi, G. Sala, L. D. Landro, M. Ruzzene, and A. Spadoni, « Composite chiral structures for morphing airfoils: Numerical analyses and development of a manufacturing process », *Composites Part B: Engineering*, vol. 41, 2, pp. 133–147, 2010, ISSN: 13598368. DOI: 10.1016/j.compositesb.2009.10.005. [Online]. Available: <http://dx.doi.org/10.1016/j.compositesb.2009.10.005>.
- [212] J. Huang, Q. Zhang, F. Scarpa, Y. Liu, and J. Leng, « Bending and benchmark of zero Poisson’s ratio cellular structures », *Composite Structures*, vol. 152, pp. 729–736, 2016, ISSN: 02638223. DOI: 10.1016/j.compstruct.2016.05.078. [Online]. Available: <http://dx.doi.org/10.1016/j.compstruct.2016.05.078>.
- [213] S. Murugan and M. I. Friswell, « Morphing wing flexible skins with curvilinear fiber composites », *Composite Structures*, vol. 99, pp. 69–75, 2013, ISSN: 02638223. DOI: 10.1016/j.compstruct.2012.11.026. [Online]. Available: <http://dx.doi.org/10.1016/j.compstruct.2012.11.026>.
- [214] NASA, *2D NACA 0012 Airfoil Validation*. [Online]. Available: https://turbmodels.larc.nasa.gov/naca0012{_}val.html (visited on 09/23/2021).
- [215] G. De Nayer, « Interaction fluide-structure pour les corps élancés », Ph.D. dissertation, 2008, 1 vol. (282 f.) [Online]. Available: <http://www.theses.fr/2008NANT2090>.
- [216] G. Hou, J. Wang, and A. Layton, « Numerical methods for fluid-structure interaction - A review », *Communications in Computational Physics*, vol. 12, 2, pp. 337–377, 2012, ISSN: 18152406. DOI: 10.4208/cicp.291210.290411s.

-
- [217] B. Hübner, E. Walhorn, and D. Dinkler, « A monolithic approach to fluid-structure interaction using space-time finite elements », *Computer Methods in Applied Mechanics and Engineering*, vol. 193, 23-26, pp. 2087–2104, 2004, ISSN: 00457825. DOI: 10.1016/j.cma.2004.01.024.
- [218] E. Walhorn, A. Kölke, B. Hübner, and D. Dinkler, « Fluid-structure coupling within a monolithic model involving free surface flows », *Computers and Structures*, vol. 83, 25-26, pp. 2100–2111, 2005, ISSN: 00457949. DOI: 10.1016/j.compstruc.2005.03.010.
- [219] T. Wick, « Flapping and contact FSI computations with the fluid-solid interface-tracking/interface-capturing technique and mesh adaptivity », *Computational Mechanics*, vol. 53, 1, pp. 29–43, 2014, ISSN: 01787675. DOI: 10.1007/s00466-013-0890-3.
- [220] U. M. Mayer, A. Popp, A. Gerstenberger, and W. A. Wall, « 3D fluid-structure-contact interaction based on a combined XFEM FSI and dual mortar contact approach », *Computational Mechanics*, vol. 46, 1, pp. 53–67, 2010, ISSN: 01787675. DOI: 10.1007/s00466-010-0486-0.
- [221] C. A. Felippa, K. C. Park, and M. R. Ross, « A classification of interface treatments for FSI », in *Fluid structure interaction II*, Springer, 2011, pp. 27–51.
- [222] Y. Wang, P. K. Jimack, M. A. Walkley, and O. Pironneau, « An energy stable one-field monolithic arbitrary Lagrangian–Eulerian formulation for fluid–structure interaction », *Journal of Fluids and Structures*, vol. 98, pp. 1–25, 2020, ISSN: 10958622. DOI: 10.1016/j.jfluidstructs.2020.103117. arXiv: 2003.03819.
- [223] Z. Huang, Y. Xiong, and Y. Xu, « The simulation of deformation and vibration characteristics of a flexible hydrofoil based on static and transient FSI », *Ocean Engineering*, vol. 182, August 2018, pp. 61–74, 2019, ISSN: 00298018. DOI: 10.1016/j.oceaneng.2019.04.028.
- [224] N. Di Cesare, « Développement d’une nouvelle méthode metaheuristique pour l’optimisation topologique des structures et des metamatériaux », Theses, Université de Technologie de Belfort-Montbéliard, 2016. [Online]. Available: <https://hal.archives-ouvertes.fr/tel-01576611>.

-
- [225] I. Koc, Y. Atay, and I. Babaoglu, « Discrete tree seed algorithm for urban land readjustment », *Engineering Applications of Artificial Intelligence*, vol. 112, February, p. 104783, 2022, ISSN: 09521976. DOI: 10.1016/j.engappai.2022.104783. [Online]. Available: <https://doi.org/10.1016/j.engappai.2022.104783>.
- [226] S. Li, Y. Wei, X. Liu, and H. Zhu, « A New Fast Ant Colony Optimization Algorithm : The Saltatory Evolution Ant Colony Optimization Algorithm », 2022.
- [227] J. Yu, G. Liu, J. Xu, *et al.*, « A Hybrid Multi-Target Path Planning Algorithm for Unmanned Cruise Ship in an Unknown Obstacle Environment », pp. 1–26, 2022.
- [228] T. P. Ribeiro, L. F. Bernardo, and J. M. Andrade, « Topology optimisation in structural steel design for additive manufacturing », *Applied Sciences (Switzerland)*, vol. 11, 5, pp. 1–66, 2021, ISSN: 20763417. DOI: 10.3390/app11052112.
- [229] S Nadarajah and A Jameson, « Studies of the Continuous and Discrete Adjoint Approaches to Viscous Automatic Aerodynamic Shape Optimization 15th AIAA Computational Fluid Dynamics Conference For permission to copy or republish , contact the American Institute of Aeronautics and Astronautics », *AIAA Journal*, p. 2530, 2001.
- [230] M. Topaç, H. Enginar, and N. Kuralay, « Reduction of Stress Concentration at the Corner Bends of the Anti-Roll Bar by Using Parametric Optimisation », *Mathematical and Computational Applications*, vol. 16, 2011. DOI: 10.3390/mca16010148.
- [231] R. Paz, M. D. Monzón, B. González, E. Pei, G. Winter, and F. Ortega, « Lightweight parametric optimisation method for cellular structures in additive manufactured parts », *International Journal for Simulation and Multidisciplinary Design Optimization*, vol. 7, A6, 2016, ISSN: 1779-627X. DOI: 10.1051/smdo/2016009.
- [232] H. R. Boucekara, A. Kedous-Lebouc, J. P. Yonnet, and C. Chillet, « Multiobjective optimization of AMR systems », *International Journal of Refrigeration*, vol. 37, 1, pp. 63–71, 2014, ISSN: 01407007. DOI: 10.1016/j.ijrefrig.2013.09.009. [Online]. Available: <http://dx.doi.org/10.1016/j.ijrefrig.2013.09.009>.
- [233] Y. Cherruault, « A New Method for Global Optimisation (Alienor) », *Kybernetes*, vol. 19, 3, pp. 19–32, 1990, ISSN: 0368492X. DOI: 10.1108/eb005845.
- [234] S. Klein, J. P. Plum, M. Staring, and M. A. Viergever, « Adaptive stochastic gradient descent optimisation for image registration », *International Journal of Computer Vision*, vol. 81, 3, pp. 227–239, 2009, ISSN: 09205691. DOI: 10.1007/s11263-008-0168-y.

-
- [235] B. Wilson and M. Leimeister, « Gradient descent in hyperbolic space », pp. 1–10, 2018. arXiv: 1805.08207. [Online]. Available: <http://arxiv.org/abs/1805.08207>.
- [236] S. Flennerhag, A. A. Rusu, R. Pascanu, F. Visin, H. Yin, and R. Hadsell, « Meta-Learning with Warped Gradient Descent », pp. 1–28, 2019. arXiv: 1909.00025. [Online]. Available: <http://arxiv.org/abs/1909.00025>.
- [237] S. Ruder, « An overview of gradient descent optimization algorithms », pp. 1–14, 2016. arXiv: 1609.04747. [Online]. Available: <http://arxiv.org/abs/1609.04747>.
- [238] Y. Qiao, B. Van Lew, B. P. Lelieveldt, and M. Staring, « Fast automatic step size estimation for gradient descent optimization of image registration », *IEEE Transactions on Medical Imaging*, vol. 35, 2, pp. 391–403, 2016, ISSN: 1558254X. DOI: 10.1109/TMI.2015.2476354.
- [239] P. S. Stanimirović and M. B. Miladinović, « Accelerated gradient descent methods with line search », *Numerical Algorithms*, vol. 54, 4, pp. 503–520, 2010, ISSN: 10171398. DOI: 10.1007/s11075-009-9350-8.
- [240] W. A. Gardner, « Learning characteristics of stochastic-gradient-descent algorithms: A general study, analysis, and critique », *Signal Processing*, vol. 6, 2, pp. 113–133, 1984, ISSN: 01651684. DOI: 10.1016/0165-1684(84)90013-6.
- [241] J. Tondut, C. Ollier, N. Cesare, J. C. Roux, and S. Ronel, « An automatic kriging machine learning method to calibrate meta-heuristic algorithms for solving optimization problems », *Engineering Applications of Artificial Intelligence*, vol. 113, p. 104940, 2022. DOI: 10.1016/j.engappai.2022.104940.
- [242] M. Dorigo, « Optimization, Learning and Natural Algorithms », Politecnico di Milano, 1995. [Online]. Available: <https://ci.nii.ac.jp/naid/10027800670/en/>.
- [243] M. Dorigo, V. Maniezzo, and A. Colorni, « Ant system: Optimization by a colony of cooperating agents », *IEEE Transactions on Systems, Man, and Cybernetics, Part B: Cybernetics*, vol. 26, 1, pp. 29–41, 1996, ISSN: 10834419. DOI: 10.1109/3477.484436.
- [244] C. Blum, « Ant colony optimization: Introduction and recent trends », *Physics of Life Reviews*, vol. 2, 4, pp. 353–373, 2005, ISSN: 15710645. DOI: 10.1016/j.plrev.2005.10.001.

-
- [245] K. Mayilvaganam, A. Shrivastava, and P. Rajagopal, « An optimal coverage path plan for an autonomous vehicle based on polygon decomposition and ant colony optimisation », *Ocean Engineering*, vol. 252, *April*, p. 111 101, 2022, ISSN: 0029-8018. DOI: 10.1016/j.oceaneng.2022.111101. [Online]. Available: <https://doi.org/10.1016/j.oceaneng.2022.111101>.
- [246] M. S. Iqbal, M. M. Kabir, A. S. Surja, and A. Rouf, « Solar Radiation Prediction using Ant Colony Optimization and Artificial Neural Network », *European Journal of Engineering and Technology Research*, vol. 7, 2, pp. 99–111, 2022.
- [247] S. Katoch, S. S. Chauhan, and V. Kumar, *A review on genetic algorithm: past, present, and future*. Multimedia Tools and Applications, 2021, vol. 80, pp. 8091–8126, ISBN: 1104202010139. DOI: 10.1007/s11042-020-10139-6.
- [248] Y. Wang, G. Shi, and K. Hirayama, « Many-Objective Container Stowage Optimization Based on Improved NSGA-III », 2022.
- [249] S. Grubeša and J. Stama, « Use of Genetic Algorithms for Design an FPGA-Integrated Acoustic Camera », 2022.
- [250] N. Di Cesare, D Chamoret, and M Domaszewski, « A new hybrid PSO algorithm based on a stochastic Markov chain model », *Advances in Engineering Software*, vol. 90, pp. 127–137, 2015, ISSN: 18735339. DOI: 10.1016/j.advengsoft.2015.08.005. [Online]. Available: <http://dx.doi.org/10.1016/j.advengsoft.2015.08.005>.
- [251] N. Di Cesare and M. Domaszewski, « A new hybrid topology optimization method based on I-PR-PSO and ESO. Application to continuum structural mechanics », *Computers and Structures*, vol. 212, pp. 311–326, 2019, ISSN: 00457949. DOI: 10.1016/j.compstruc.2018.11.006.
- [252] K. Rameshkumar and C. Rajendran, « A novel discrete PSO algorithm for solving job shop scheduling problem to minimize makespan », *IOP Conference Series: Materials Science and Engineering*, vol. 310, 1, 2018, ISSN: 1757899X. DOI: 10.1088/1757-899X/310/1/012143.
- [253] W. Deng, R. Yao, H. Zhao, X. Yang, and G. Li, « A novel intelligent diagnosis method using optimal LS-SVM with improved PSO algorithm », *Soft Computing*, vol. 23, 7, pp. 2445–2462, 2019, ISSN: 14337479. DOI: 10.1007/s00500-017-2940-9. [Online]. Available: <https://doi.org/10.1007/s00500-017-2940-9>.

-
- [254] J Wu, C. H. Zhang, and N. X. Cui, « PSO algorithm-based parameter optimization for HEV powertrain and its control strategy », *International Journal of Automotive Technology*, vol. 9, 1, pp. 53–59, 2008, ISSN: 1976-3832. DOI: 10.1007/s12239-008-0007-8. [Online]. Available: <https://doi.org/10.1007/s12239-008-0007-8>.
- [255] S. Strasser, R. Goodman, J. Sheppard, and S. Butcher, « A New Discrete Particle Swarm Optimization Algorithm », *Genetic and Evolutionary Computation Conference (GECCO)*, pp. 53–60, 2016. DOI: 10.1145/2908812.2908935. [Online]. Available: <http://dx.doi.org/10.1145/2908812.2908935>.
- [256] K. Socha and M. Dorigo, « Ant colony optimization for continuous domains », *European Journal of Operational Research*, vol. 185, 3, pp. 1155–1173, 2008, ISSN: 03772217. DOI: 10.1016/j.ejor.2006.06.046.
- [257] D. Bunnag and M. Sun, « Genetic algorithm for constrained global optimization in continuous variables », *Applied Mathematics and Computation*, vol. 171, 1, pp. 604–636, 2005, ISSN: 00963003. DOI: 10.1016/j.amc.2005.01.075.
- [258] R. Chelouah and P. Siarry, « Continuous genetic algorithm designed for the global optimization of multimodal functions », *Journal of Heuristics*, vol. 6, 2, pp. 191–213, 2000, ISSN: 13811231. DOI: 10.1023/A:1009626110229.
- [259] *pyswarm* · *PyPI*. [Online]. Available: <https://pypi.org/project/pyswarm/> (visited on 04/12/2022).
- [260] L. James V. Miranda, « PySwarms: a research toolkit for Particle Swarm Optimization in Python », *The Journal of Open Source Software*, vol. 3, 21, p. 433, 2018. DOI: 10.21105/JOSS.00433.
- [261] C. W. Reynolds, « Flocks-Hers-and-Schools », *Computer Graphics*, vol. 21, 4, pp. 25–34, 1987.
- [262] F. Nédélec, T. Surrey, and E. Karsenti, « Self-organisation and forces in the microtubule cytoskeleton », *Current Opinion in Cell Biology*, vol. 15, 1, pp. 118–124, 2003, ISSN: 09550674. DOI: 10.1016/S0955-0674(02)00014-5.
- [263] S. Kalantari, E. Nazemi, and B. Masoumi, « Emergence phenomena in self-organizing systems: a systematic literature review of concepts, researches, and future prospects », *Journal of Organizational Computing and Electronic Commerce*, vol. 30, 3, pp. 224–265, 2020, ISSN: 10919392. DOI: 10.1080/10919392.2020.1748977. [Online]. Available: <https://doi.org/10.1080/10919392.2020.1748977>.

-
- [264] J Kennedy and R Eberhart, « Particle swarm optimization », in *Proceedings of ICNN'95 - International Conference on Neural Networks*, vol. 4, 1995, 1942–1948 vol.4. DOI: 10.1109/ICNN.1995.488968.
- [265] Y Shi and R Eberhart, « A modified particle swarm optimizer », in *1998 IEEE International Conference on Evolutionary Computation Proceedings. IEEE World Congress on Computational Intelligence (Cat. No.98TH8360)*, 1998, pp. 69–73. DOI: 10.1109/ICEC.1998.699146.
- [266] J. Kennedy and R. Mendes, « Population structure and particle swarm performance », *Proceedings of the 2002 Congress on Evolutionary Computation, CEC 2002*, vol. 2, May, pp. 1671–1676, 2002. DOI: 10.1109/CEC.2002.1004493.
- [267] R Eberhart and J Kennedy, « A new optimizer using particle swarm theory », in *MHS'95. Proceedings of the Sixth International Symposium on Micro Machine and Human Science*, 1995, pp. 39–43. DOI: 10.1109/MHS.1995.494215.
- [268] H. Khakzad, Y. Karami, and S. S. Arab, « Accelerating Protein Structure Prediction using Particle Swarm Optimization on GPU », 2015. DOI: 10.13140/RG.2.1.2094.9607.
- [269] P. N. Suganthan, « Particle swarm optimiser with neighbourhood operator », in *Proceedings of the 1999 Congress on Evolutionary Computation-CEC99 (Cat. No. 99TH8406)*, vol. 3, 1999, 1958–1962 Vol. 3. DOI: 10.1109/CEC.1999.785514.
- [270] S Janson and M Middendorf, « A hierarchical particle swarm optimizer », in *The 2003 Congress on Evolutionary Computation, 2003. CEC '03.*, vol. 2, 2003, 770–776 Vol.2. DOI: 10.1109/CEC.2003.1299745.
- [271] A Ratnaweera, S. K. Halgamuge, and H. C. Watson, « Self-organizing hierarchical particle swarm optimizer with time-varying acceleration coefficients », *IEEE Transactions on Evolutionary Computation*, vol. 8, 3, pp. 240–255, 2004. DOI: 10.1109/TEVC.2004.826071.
- [272] B. Cichocki, B. U. Felderhof, K. Hinsen, E. Wajnryb, and J. Bławdziewicz, « Friction and mobility of many spheres in Stokes flow », *The Journal of Chemical Physics*, vol. 100, 5, pp. 3780–3790, 1994, ISSN: 00219606. DOI: 10.1063/1.466366.
- [273] S. Taneda, *Visualization of Separating Stokes Flows*, 1979. DOI: 10.1143/JPSJ.46.1935.

-
- [274] F. M. White, *Fluid Mechanics* (McGraw-Hill series in mechanical engineering). McGraw Hill, 2011, ISBN: 9780073529349.
- [275] K. Yousefi and A. Razeghi, « Determination of the critical reynolds number for flow over symmetric NACA airfoils », *AIAA Aerospace Sciences Meeting, 2018, 210059*, pp. 1–11, 2018. DOI: 10.2514/6.2018-0818.
- [276] A. Macchi, H. Bi, J. R. Grace, C. A. McKnight, and L. Hackman, « Dimensional hydrodynamic similitude in three-phase fluidized beds », *Chemical Engineering Science*, vol. 56, 21-22, pp. 6039–6045, 2001, ISSN: 00092509. DOI: 10.1016/S0009-2509(01)00207-X.
- [277] S. Wilhelm, J. Jacob, and P. Sagaut, *A New Explicit Algebraic Wall Model for LES of Turbulent Flows Under Adverse Pressure Gradient*. Springer Netherlands, 2020, ISBN: 0123456789. DOI: 10.1007/s10494-020-00181-7. [Online]. Available: <https://doi.org/10.1007/s10494-020-00181-7>.
- [278] M. Zancanaro, M. Mrosek, G. Stabile, C. Othmer, and G. Rozza, « Hybrid neural network reduced order modelling for turbulent flows with geometric parameters », pp. 1–21, 2021. arXiv: arXiv:2107.09591v1.
- [279] P. R. Spalart, S. R. Allmaras, and J. Reno, « One-Equation Turbulence Model for Aerodynamic Flows », *30th Aerospace Sciences Meeting & Exhibit*, p. 23, 1992.
- [280] *On a teste un surf électrique volant sur La Seine - YouTube*. [Online]. Available: <https://www.youtube.com/watch?v=OOGKWI187fc> (visited on 09/21/2021).
- [281] *International Moth Speed Guide*. [Online]. Available: <https://www.northsails.com/sailing/en/resources/north-sails-international-moth-speed-guide> (visited on 09/21/2021).
- [282] J. Aguilar, A. Rubio-Clemente, L. Velasquez, and E. Chica, « Design and optimization of a multi-element hydrofoil for a horizontal-axis hydrokinetic turbine », *Energies*, vol. 12, 24, 2019, ISSN: 19961073. DOI: 10.3390/en12244679.
- [283] K. S. Lokesh, « Evaluation of Flexural Rigidity of PU- foam Cored Sandwich Structures », *International Journal of Scientific Research in Mechanical and Materials Engineering (IJSRMME)*, ISSN, pp. 435–2457, 2018.
- [284] A. Spadoni, M. Ruzzene, and F. Scarpa, « Global and local linear buckling behavior of a chiral cellular structure », *Physica Status Solidi (B) Basic Research*, vol. 242, 3, pp. 695–709, 2005, ISSN: 03701972. DOI: 10.1002/pssb.200460387.

-
- [285] X. Yu, J. Zhou, H. Liang, Z. Jiang, and L. Wu, « Mechanical metamaterials associated with stiffness, rigidity and compressibility: A brief review », *Progress in Materials Science*, vol. 94, pp. 114–173, 2018, ISSN: 00796425. DOI: 10.1016/j.pmatsci.2017.12.003. [Online]. Available: <https://doi.org/10.1016/j.pmatsci.2017.12.003>.
- [286] M. Spahic, N. Di Cesare, A. Le Duigou, and V. Keryvin, « Multi-scale analysis of the flexural behaviour of 3D printed cellular polymer materials: Comparison between morphing and sandwich beams », *Composite Structures*, vol. 273, June, p. 114 249, 2021, ISSN: 02638223. DOI: 10.1016/j.compstruct.2021.114249. [Online]. Available: <https://doi.org/10.1016/j.compstruct.2021.114249>.
- [287] S. Martínez-Aranda, A. Garcia-Gonzalez, L. Parras, *et al.*, « Comparison of the aerodynamic characteristics of the NACA0012 airfoil at low-to-moderate Reynolds numbers for any aspect ratio », *International Journal of Aerospace Sciences*, vol. 2016, 1, pp. 1–8, 2016. DOI: 10.5923/j.aerospace.20160401.01. [Online]. Available: <https://www.researchgate.net/publication/307943437>.
- [288] F. D. Reis and J. F. Ganghoffer, « Discrete homogenization of architected materials : Implementation of the method in a simulation tool for the systematic prediction of their effective elastic properties », *Technische Mechanik*, vol. 30, pp. 85–109, 2010.
- [289] F. Dos Reis and J. F. Ganghoffer, « Equivalent mechanical properties of auxetic lattices from discrete homogenization », *Computational Materials Science*, vol. 51, 1, pp. 314–321, 2012, ISSN: 09270256. DOI: 10.1016/j.commatsci.2011.07.014. [Online]. Available: <http://dx.doi.org/10.1016/j.commatsci.2011.07.014>.
- [290] A. S. Dalaq, D. W. Abueidda, R. K. Abu Al-Rub, and I. M. Jasiuk, « Finite element prediction of effective elastic properties of interpenetrating phase composites with architected 3D sheet reinforcements », *International Journal of Solids and Structures*, vol. 83, pp. 169–182, 2016, ISSN: 00207683. DOI: 10.1016/j.ijsolstr.2016.01.011. [Online]. Available: <http://dx.doi.org/10.1016/j.ijsolstr.2016.01.011>.
- [291] A. Clausen, F. Wang, J. S. Jensen, O. Sigmund, and J. A. Lewis, « Topology Optimized Architectures with Programmable Poisson’s Ratio over Large Deformations », *Advanced Materials*, vol. 27, 37, pp. 5523–5527, 2015, ISSN: 15214095. DOI: 10.1002/adma.201502485.

-
- [292] M. Osanov and J. K. Guest, « Topology Optimization for Architected Materials Design », *Annual Review of Materials Research*, vol. 46, pp. 211–233, 2016, ISSN: 15317331. DOI: 10.1146/annurev-matsci-070115-031826.
- [293] J. Xu, L. Gao, M. Xiao, J. Gao, and H. Li, « Isogeometric topology optimization for rational design of ultra-lightweight architected materials », *International Journal of Mechanical Sciences*, vol. 166, May 2019, 2020, ISSN: 00207403. DOI: 10.1016/j.ijmecsci.2019.105103.
- [294] S. Deck, « Numerical simulation of transonic buffet over a supercritical airfoil », *AIAA Journal*, vol. 43, 7, pp. 1556–1566, 2005, ISSN: 00011452. DOI: 10.2514/1.9885.
- [295] L. Bahi, J. M. Ross, and H. T. Nagamatsu, « Passive Shock Wave/Boundary Layer Control for Transonic Airfoil Drag Reduction. », *AIAA Paper*, 1983, ISSN: 01463705. DOI: 10.2514/6.1983-137.
- [296] N. Tillmark and P. H. Alfredsson, « Experiments on transition in plane Couette flow », *Journal of Fluid Mechanics*, vol. 235, pp. 89–102, 1992, ISSN: 14697645. DOI: 10.1017/S0022112092001046.
- [297] *Flow Properties of Polymers*, 2015. [Online]. Available: <http://polymerdatabase.com/polymerphysics/Viscosity2.html> (visited on 05/26/2021).
- [298] M. Gad-el Hak, « Technical forum », *Journal of Fluids Engineering*, vol. 117, pp. 3–5, 1995, ISSN: 02625091.
- [299] N. Massarotti, F. Arpino, R. W. Lewis, and P. Nithiarasu, « Explicit and semi-implicit CBS procedures for incompressible viscous flows », *International Journal for Numerical Methods in Engineering*, vol. 66, 10, pp. 1618–1640, 2006, ISSN: 00295981. DOI: 10.1002/nme.1700.
- [300] A. J. Chorin, « A numerical method for solving incompressible viscous flow problems », *Journal of Computational Physics*, vol. 2, 1, pp. 12–26, 1967, ISSN: 10902716. DOI: 10.1016/0021-9991(67)90037-X.
- [301] I. V. Kudryavtseva, S. V. Rykov, V. A. Rykov, and E. E. Ustyuzhanin, « A model system of the liquid density, the gas density and the pressure on the saturation line of SF6 », *Journal of Physics: Conference Series*, vol. 1385, 1, 2019, ISSN: 17426596. DOI: 10.1088/1742-6596/1385/1/012010.

-
- [302] P. R. Spalart, W. H. Jou, M. K. Strelets, and S. R. Allmaras, « Comments on the feasibility of LES for wings and on a hybrid RANS/LES approach », *Advances in DNS/LES*, vol. 1, JANUARY, pp. 4–8, 1997.
- [303] P. R. Spalart, *Trends in turbulence treatments*, 2000. DOI: 10.2514/6.2000-2306.
- [304] X. I. A. Yang and K. P. Griffin, « Grid-point and time-step requirements for direct numerical simulation and large-eddy simulation », *Physics of Fluids*, vol. 33, 1, p. 15 108, 2021. DOI: 10.1063/5.0036515. [Online]. Available: <https://doi.org/10.1063/5.0036515>.
- [305] P. Moin and K. Mahesh, « DIRECT NUMERICAL SIMULATION : A Tool in Turbulence Research », 1998.
- [306] W. Rodi and M. Asce, « Turbulence Modeling and Simulation in Hydraulics : A Historical Review », pp. 1–20, DOI: 10.1061/(ASCE)HY.1943-7900.0001288..
- [307] G. R. Tabor and M. H. Baba-ahmadi, « Computers & Fluids Inlet conditions for large eddy simulation : A review », *Computers and Fluids*, vol. 39, 4, pp. 553–567, 2010, ISSN: 0045-7930. DOI: 10.1016/j.compfluid.2009.10.007. [Online]. Available: <http://dx.doi.org/10.1016/j.compfluid.2009.10.007>.
- [308] *Turbulence models in CFD - RANS, DES, LES and DNS*. [Online]. Available: <https://www.idealsimulations.com/resources/turbulence-models-in-cfd/> (visited on 08/20/2021).
- [309] B. SMITH, « Application of turbulence modeling to the design of military aircraft », 1991. DOI: 10.2514/6.1991-513.
- [310] D. C. Wilcox, *Turbulence Modeling for CFD*. DCW Industries, Incorporated, 1994, ISBN: 9780963605108. [Online]. Available: <https://books.google.fr/books?id=VwIRAAAAMAAJ>.
- [311] G. S. Glushko, « Turbulent boundary layer on a flat plate in an incompressible fluid », in *Turbulentnyy pogranichnyy sloy na ploskoy plastine v neszhimayemoy zhidkost*, ASME-AMER SOC MECHANICAL ENG 345 E 47TH ST, NEW YORK, NY 10017, 1965.
- [312] H. W. Emmons, « Shear flow turbulence », in *Journal of Applied Mechanics-Transactions of the ASME*, ASME-AMER SOC MECHANICAL ENG 345 E 47TH ST, NEW YORK, NY 10017, vol. 21, 1954, p. 283.

-
- [313] M Wolfshtein, « Convection Processes in Turbulent Impinging Jets », Imperial College, Heat Transfer Section Report SF/R/2, 1967.
- [314] U. C. Goldberg, « Derivation and testing of a one-equation model based on two time scales », in *AIAA Journal*, vol. 29, 1991, pp. 1337–1340.
- [315] B. Baldwin and T. Barth, « A one-equation turbulence transport model for high Reynolds number wall-bounded flows », 1991. DOI: 10.2514/6.1991-610.
- [316] A. N. Kolmogorov, « Equations of turbulent motion in an incompressible fluid », *Proceedings of the USSR Academy of Sciences*, vol. 30, pp. 299–303, 1941.
- [317] P. Y. CHOU, « ON VELOCITY CORRELATIONS AND THE SOLUTIONS OF THE EQUATIONS OF TURBULENT FLUCTUATION », *Quarterly of Applied Mathematics*, vol. 3, 1, pp. 38–54, 1945, ISSN: 0033569X, 15524485. [Online]. Available: <http://www.jstor.org/stable/43633490>.
- [318] D. C. Wilcox, « Reassessment of the scale-determining equation for advanced turbulence models », *AIAA Journal*, vol. 26, 11, pp. 1299–1310, 1988, ISSN: 00011452. DOI: 10.2514/3.10041.
- [319] W. P. Jones and B. E. Launder, « The prediction of laminarization with a two-equation model of turbulence », *International Journal of Heat and Mass Transfer*, vol. 15, 2, pp. 301–314, 1972, ISSN: 0017-9310. DOI: [https://doi.org/10.1016/0017-9310\(72\)90076-2](https://doi.org/10.1016/0017-9310(72)90076-2). [Online]. Available: <https://www.sciencedirect.com/science/article/pii/0017931072900762>.
- [320] F. R. Menter, « Two-equation eddy-viscosity turbulence models for engineering applications », *AIAA Journal*, vol. 32, 8, pp. 1598–1605, 1994, ISSN: 00011452. DOI: 10.2514/3.12149.
- [321] B. E. Launder and B. I. Sharma, « Application of the energy-dissipation model of turbulence to the calculation of flow near a spinning disc », *Letters in Heat and Mass Transfer*, vol. 1, 2, pp. 131–137, 1974, ISSN: 0094-4548. DOI: [https://doi.org/10.1016/0094-4548\(74\)90150-7](https://doi.org/10.1016/0094-4548(74)90150-7). [Online]. Available: <https://www.sciencedirect.com/science/article/pii/0094454874901507>.
- [322] Y. Nagano and M Tagawa, « An Improwed k-e Model for K) », *Journal of Fluids Engineering*, vol. 112, March 1990, pp. 111–117, 2015.

Titre : Optimisation paramétrique de matériaux architecturés imprimés 3D : application au morphing des appendices de navire

Mot clés : Morphing, Matériaux architecturés, Interaction fluide-structure, Impression 3D, Homogénéisation, Analyse multi-échelle

Résumé : Dans le domaine de la course au large, Les hydrofoils sont utilisés pour augmenter la vitesse maximale des bateaux. Cet appendice agit comme une aile d'avion et permet au bateau de surélever sa coque au-dessus de l'eau et de ne reposer que sur ses hydrofoils. Cependant, les hydrofoils connaissent des limitations, la principale étant la difficulté d'adapter leurs propriétés hydrodynamiques aux changements d'environnement. Cette limitation les rends parfois sous-performants. L'objectif de cette thèse a donc été de permettre à un hydrofoil de modifier passivement et de façon autonome sa géométrie dans le but de maximiser ses propriétés hydrodynamiques. Pour réaliser ce but, un concept de morphing passif composé d'une âme faite de matériaux architecturés et d'une peau conti-

nue a été étudié. L'objectif de cette thèse a été d'identifier et d'optimiser les différents paramètres permettant de piloter la déformation passive de cet hydrofoil cellulaire. Pour faire cela, les travaux de cette thèse ont été divisés en deux parties. Premièrement, une analyse multi-échelle expérimentale et numérique a permis d'identifier les différents paramètres pilotant la déformation de l'hydrofoil. Dans un second temps, une interaction fluide-structure et un programme d'optimisation paramétrique ont permis d'étudier les intervalles d'adaptabilité de ce concept et d'assurer l'impression 3D polymère de cet hydrofoil. Les résultats obtenus lors de cette thèse ont montré que, lors du morphing, la rigidité de la peau de l'hydrofoil est le paramètre clé gouvernant le morphing de cet hydrofoil.

Title: Parametric optimisation of 3D-printed architected materials: application to boat's morphing appendages

Keywords: Morphing, architected materials, fluid-structure interaction, 3D printing, Homogenisation, Multi-scale analysis

Abstract: In the domain of yacht racing, hydrofoils are used for increasing the maximal velocity of the yacht. This appendage operates as an aircraft's wing, it raises the yacht's hull above the water's surface and withstands the yacht's weight. Nevertheless, hydrofoils face limitations, the main being its inability to adapt their hydrodynamic properties to changes in the environment. This issue makes them underperformant. The objective of this thesis was to provide the capacity to a hydrofoil to modify passively and autonomously its geometry in order to maximise its aerodynamic properties. In order to attain this goal, a passive morphing was studied. This concept is made out of two elements: a continuous skin and a cellular

core. Thus, the objective of this thesis was to identify and optimise the different parameters governing the passive deformation of this cellular hydrofoil. To do that, the work was divided in two major parts. The first one consisted in an experimental and numerical multi-scale analysis that aims to identify the different parameters governing the deformation of the hydrofoil. The second one consisted in developing a fluid-structure interaction and a parametric optimisation program for studying the interval of tailorability of this concept and insure that the hydrofoil is 3D-printable. The results obtained in this thesis showed that, the skin's rigidity is the main parameter governing the hydrofoil's morphing.